Geotechnical Bearing Capacity of Timber Piles in the City of Amsterdam

Derivation of bearing capacity prediction factors based on static load tests conducted on instrumented timber piles.

S. Honardar

TU Delft Deltares
Gemeente Amsterdam
Gemeente Rotterdam

Geotechnical Bearing Capacity of Timber Piles in the City of Amsterdam

Derivation of bearing capacity prediction factors based on static load tests conducted on instrumented timber piles.

by

S. Honardar

in fulfilment of the requirements for the degree of
Master of Science
at the Delft University of Technology,
to be defended publicly on November 20, 2020.

Student number:	4291255	
Project duration:	February, 2020 – November, 2020	
Thesis Committee:	Dr. ir. M. (Mandy) Korff	*TU Delft, Geo-Engineering*
	ir. D.A. (Dirk) de Lange	*Deltares, Geo Unit*
	Prof. Dr. K. G. (Kenneth) Gavin	*TU Delft, Geo-Engineering*
	Dr. ir. G. J. P. (Geert) Ravenshorst	*TU Delft, Engineering Structures*
	Dr. ir. R. (Rodriaan) Spruit	*Ingenieursbureau Rotterdam*
	ir. M. A. (Martin) op de Kelder	*Ingenieursbureau Amsterdam*
	ing. E. (Erik) Hutcheson	*Ingenieursbureau Amsterdam*

Delft University of Technology
Faculty of Civil Engineering and Geo-Scinces
Master Applied Earth Sciences

TU Delft | Delft University of Technology | Faculty of Civil Engineering and Geo-Sciences | Master Track Geo-Engineering

Deltares | Gemeente Amsterdam | Gemeente Rotterdam

Preface

This thesis serves the purpose of outlining research and analysis carried out by a student from Delft University of Technology. The document before you is written in fulfilment of the requirements for the degree of Master of Science in Geotechnical Engineering at the faculty of Civil Engineering and Geo-sciences. The conducted research is supported by Delft University of Technology, Deltares, the Municipality of Amsterdam and the Municipality of Rotterdam.

The main focus of this thesis is the assessment of the geotechnical bearing capacity of timber piles in Amsterdam. The research is carried out in order to have a better understanding of the geotechnical bearing capacity of wooden piles. This plays a significant role in the assessment of structural integrity and safety for quay walls and bridges in the city of Amsterdam. For this purpose, a series of piles are instrumented with optical fiber sensors and loaded axially in a testing ground located in Overamstel, Amsterdam.

Readers interested in gaining more insight regarding the geotechnical bearing capacity of timber piles may refer to the contents of this report. For more details on the conducted analysis, refer to the final chapter and appendices of this report. Those interested in obtaining further information may contact the author and the corresponding supervisors.

Delft, November 2020

Acknowledgements

This document is the final product of 9 months of research and analysis as part of graduation work carried out at Deltares and Delft University of Technology. This research was further supported by the engineering firms of the municipalities of Rotterdam and Amsterdam. The formulation of this document would not have been possible without the supervision and support of my graduation committee, and those who arranged the logistics and supplied me with necessary information throughout the duration of this project.

I would like to thank my direct supervisor at Deltares, Dirk de Lange, for his constant presence, willingness to help and incredibly valuable knowledge that he has passed on to me. I would also like to express my gratitude to Mandy Korff for her constructive feedback and guidance throughout the entire project. The conducted analysis would have been impossible without the much appreciated efforts and assistance of Rodriaan Spruit. Furthermore, I would like to thank Ken Gavin and Geert Ravenshorst for their willingness to help and their continuous presence during feedback sessions. Moreover, I am grateful to Erik Hutcheson, Martin op de Kelder, Willem van Bommel and Hans Landwehr for providing technical support and sharing their knowledge on the specifics of the project with me.

Finally, I would like to express my appreciation to my parents, Sara and Kiamars, for their never ending support and for always driving me forward to learn and achieve more. I would also like to thank Ellie, for her support, patience and taking time to discuss the project with me. Many thanks to Munta for sharing his opinion and insight. Last but not least, I am grateful for the support and motivation I've received from my friends and colleagues at the university and Deltares.

S. Honardar
Delft, November 2020

Abstract

In the city of Amsterdam, a large number of structures, such as houses, bridges and quay walls, are founded on wooden piles. In order to gain insight into the safety of such structures, assessment of the foundations is required. As part of an experimental framework assessing the safety of bridges and quay walls in the city of Amsterdam, a number of piles are instrumented with fiber optic sensors and load tested in compression. These tests aim to provide detailed information on the behaviour of timber piles subjected to loading. This information can be used to determine the geotechnical bearing capacity of such piles. An in-depth analysis is conducted on 8 timber piles tested within this framework.

The current Dutch practice for predicting the bearing capacity of piles consists of a CPT-based method using correlation factors which relate the capacity of the pile to the surrounding soils. In order to appropriately predict the bearing capacity of timber piles in Amsterdam, the analysis aims to derive such correlation factors based on several aspects. These aspects consist of pile specifics such as wood type, effects of residual loads and pile geometry.

The recorded data in the form of applied loads, displacements and strains are assessed with regards to validity and usability. The geometry of the tested piles and their mechanical properties are evaluated based on field measurements and the strain readings at the pile head exposed above the surface level. This is followed by a consideration of residual loads and their effect on the load distribution through the pile. Upon determination of true loads, the analysis continues to correlate the distribution to the CPT results in order to derive correlation factors.

The conducted analysis has resulted in a variation of outcomes. Without including the effects of residual loads, an average base resistance of 130 kN is observed. This measure has a extent of variation of 36 %. This variation stems from the differences between the analyzed piles, most significantly the diameter of each pile, and the difference in loading schemes. Upon inclusion of residual loads the average true base resistance increases to a value of 188 kN. The average shaft capacities in the bearing sand layer for scenarios excluding and including residual effects are 48 and 60 kN respectively. The base resistance and shaft capacities obtained through this analysis have ultimately resulted in the derivation of representative alpha factors for timber piles.

The correlation factor α_p is derived using three cone resistance averaging techniques. The three averaging methods used in this analysis are Koppejan, LCPC and the alternative averaging method developed by de Boorder. The Koppejan method has consistently resulted in the highest derived α_p factors with values of 1.09 and 1.61 for scenarios excluding and including residual loads respectively. The LCPC method indicated the highest cone resistance averages for each pile and has resulted in an average α_p of 0.60 without

consideration of residual effects. The method of de Boorder indicates an average factor of 0.72 for this scenario. Inclusion of residual loads raises these factors to 0.88 and 1.07 for LCPC and de Boorder respectively.

The scenario excluding residual effects has resulted in an average α_s of 0.009 for the bearing sand layer. Upon inclusion of residual loads, the derived α_s factor for the first sand layer amounts to 0.012. This increase in shear forces is also observed in the Pleistocene peat layer. Therefore, residual loads redistribute the capacity of the piles by increasing the shaft resistance in the bearing sand and Pleistocene peat, while simultaneously decreasing the shear stresses in the Holocene layers above.

Conclusively, timber pile characteristics such as variation in geometry and mechanical properties have significant effects on the capacity of the piles. Additionally, these variations result in fluctuations in the calculated load distribution along the pile. Local smoothing of these fluctuations results in higher apparent loads, most specifically at the pile base. Therefore, smoothing algorithms are not implemented in this analysis. The variation in diameter along the entire length of each pile directly affects the load distribution. Despite this influence, no particular trend is observed for the variation of α_p factors with respect to pile tip diameter. An apparent relationship between the tapering of the pile in the bearing sand layer and the derived α_s factors suggests that tapering effectively increases the shear forces along the shaft in that layer. It is also observed that the variation in stiffness along the length of the pile has significant influence on the shear stresses acting on the pile shaft. Further research on the variation of stiffness in wooden piles is therefore highly recommended.

Furthermore, the usage of fiber optic sensors on wooden piles has proven to be effective. The variation in local behaviour of wood is clearly illustrated through the conducted analysis. As a consequence of the biological nature of wood, the local behaviour of wooden piles is best captured by sensing technologies measuring strains at high spatial frequencies.

List of Figures

List of Tables

List of Symbols

Symbol	Description	Unit
A	Area	m^2
a	Coefficient of quadratic fit to strain readings	PN/m^4
b	Coefficient of quadratic fit to strain readings	GN/m^2
CoV	Coefficient of variation	%
C_ε	Constant coefficient for changes in strain	-
D	Diameter	m
E	Modulus of Elasticity	GPa
F	Load	kN
L	Length	m
MOE_{dyn}	Dynamic Modulus of Elasticity	GPa
O	Perimeter	m
q_c	Cone resistance	MPa
$q_{c,avg}$	Average cone resistance obtained using an averaging method	MPa
Q_b	Pile base Capacity	kN
$Q_{b,max}$	Ultimate pile base Capacity	kN
Q_s	Pile shaft capacity	kN
Q_T	Total pile capacity	kN
$soru$	Displacement	mm
u_b	Base displacement	mm
u_H	Head displacement	mm
$v(\varepsilon)$	Brillouin scattering frequency	Hz
α_p	Reduction factor for base capacity	$-$
α_s	Reduction factor for shaft capacity	$-$
γ	Volumetric Weight	kN/m^3
ΔL	Deformation/Compression	m
ΔL_i	Length increment	m
ε	Strain	$\mu\varepsilon, -$
ε_{res}	Residual strain	$\mu\varepsilon, -$
ε_H	Strain while pile is hanging	$\mu\varepsilon, -$
ε_S	Strain while pile is standing	$\mu\varepsilon, -$
ε_{AD}	Strains measured after installation	$\mu\varepsilon, -$
ε_{BT}	Strains measured before load test	$\mu\varepsilon, -$
μ	Mean value	-
ρ	Density	kg/m^3
σ	Standard deviation	-
σ_i	Nodal stress	-
σ_T	Total stress	kPa
σ_N	Normal stress	kPa

Abbreviations

Abbreviation	Description
CPT	Cone Penetration Test
FOS	Fiber Optic Sensors
NAP	Amsterdam Ordnance Datum ("Normaal Amsterdams Peil" in Dutch)
LCPC	Laboratoire Central des Ponts et Chausees
LVDT	Linear Variable Differential Transformer
SPT	Standard Penetration Test

Contents

Chapter 1

Introduction

1.1 Problem Description

Timber piles have been used in the city of Amsterdam as a means to create foundations for structures since before the 17th century. A large portion of bridges and quay walls in this city have wooden pile as foundations. As a consequence of several processes such as aging and deterioration of these piles, as well as changes in infrastructure through the years, the need to assess the safety and integrity of these foundations has risen.

In order to assess the safety of such structures, efficient and appropriate means of evaluation must be developed. The assessment of timber piles is a complex matter due to their biological nature and the consequential variability. The heterogeneity of this material is influential with regards to the strength characteristics of a pile. Additionally, the geotechnical parameters affecting the bearing capacity of such piles require further research and clarification.

1.2 Project Background

In order to assess the safety of structures found on timber piles, the city of Amsterdam has formulated an assessment program titled "Structural Safety of Bridges". As part of this program, an experimental framework is set up concerned with the geotechnical capacity of timber pile foundations. This framework aims to evaluate the bearing capacity of timber piled foundations under 250 bridges and 200 kilometers of quay walls in Amsterdam.

To accurately predict the bearing capacity of these foundations, 27 new timber piles are instrumented with fiber optic sensors as part of this experimental framework. Sixteen of these piles were tested in compression and strain measurements were recorded using the sensors.

The current practice of predicting the bearing capacity of timber piles consists of a CPT-based method with correlation factors relating base resistance and shaft capacity to the surrounding soils. This method can further be evaluated by deriving the true load distribution in timber piles that are load tested. The usage of fiber optic sensors allows for discretized measurements of strains along the length of a pile. Correlation of the corresponding load distributions with the surrounding soil may lead to improvements in the method of prediction.

1.3 Scope and Objectives

The main research question of this thesis is formulated as: "**What is the geotechnical bearing capacity of timber piles in Amsterdam**?". The objective of this question is to determine the best means to predict the bearing capacity of wooden piles in the lithological setting of Amsterdam. In order to achieve this objective, the following questions are to be answered.

- Are there specific characteristics of timber piles that affect the behaviour of a pile subjected to axial loads?
- What are the effects of residual loads on timber piles?
- What alpha factors can be used to predict the bearing capacity of timber piles, using different cone resistance averaging techniques?
- How effective is the usage of fiber optic sensing on wooden piles?

The scope of this project is focused on timber piles with with wood types and lengths that are typical of piles used in Amsterdam. The derived results are however applicable to timber piles installed in soil settings similar to that of Amsterdam. The analysis only focuses on piles loaded in compression. The study includes the effect of residual loads on timber piles. Additional aspects such as wood degradation, pile group effects and lateral loading of timber piles are not included in the conducted analysis.

As part of the aforementioned experimental framework, other tests have been conducted on similar piles. These tests consist of, but are not limited to, evaluation of the effect of negative skin friction, load tests in tension and laboratory tests that are to be conducted in the future. These additional experiments are not analysed in this thesis.

1.4 Outline

The structure of this report is as follows. Chapter 2 illustrates the necessary background information and literature research conducted as part of this thesis. The study elaborates on aspects such as characteristics of wooden piles, usage of fiber optics as sensing technologies, a description of the bearing capacity prediction method and an elaboration on the concept of residual loads. Additionally, the geological sphere of the city and a description of previously performed pile load tests are provided. Chapter 3 describes the experimental framework and provides an overview of the data that is made available to this project.

The fourth chapter elaborates on the methods used to derive results from the data obtained through fiber optic sensors installed on the tested piles. The methodology is separated into sections outlining the approach to determine the most influential aspects such as residual loads and the methods used to account for pile stiffness. Finally, chapter 4 also outlines the process through which the load distribution along the pile is determined, followed by the steps necessary to determine correlation factors between loads and the cone resistance profile of the surrounding soil.

Chapter 5 focuses on the analysis and illustrates the results of this project. As the first step, the fiber readings are assessed and the correlation between strains and loads is described. This is followed by the determination of residual loads and a description of

the pile behaviour as a consequence of loading. The resultant load distributions and their correlations with the CPT profiles follows. Finally, the chapter concludes the analysis by discussing the variation in results and illustrating representative calculation factors based on a statistical analysis.

The sixth chapter of this report provides a discussion and evaluation of the calculation factors derived. This discussion focuses on the main factors influencing the results and the extent to which the outcomes are reliable. This chapter is followed by a series of conclusions drawn based on the analysis and the assessment of the research approach. Finally, recommendations are provided regarding future analysis of similar projects and as a reflection on the approach and methodology used in this project.

Chapter 2

Literature Study

This chapter outlines the literature study conducted to evaluate the geotechnical bearing capacity of wooden piles in Amsterdam. The main objective of this study is highlight background information to support assumptions and methods throughout the project

In foundation engineering, piles are commonly used for the purpose of increasing the load-bearing capacity of a foundation, as well as reducing the settlement of the foundation (Reese et al., 2006). The principle as to how piles accomplish this revolves around the concept of load distribution. Upon application of load on the pile head, the forces distributed through the pile can be divided into two separate entities, namely friction along the shaft of the pile and resistance at the pile tip. The summation of the two components, defines the extent to which the pile can bear loads. Figure 2.1 illustrates a schematized form of this concept by separating the two forms of resistances.

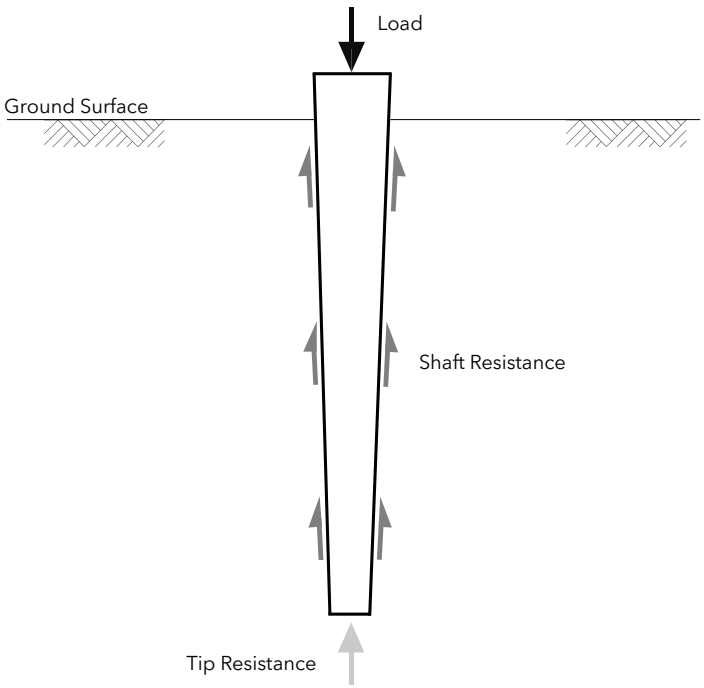

Figure 2.1: Base and shaft resistance of a pile loaded in compression

2.1 Bearing Capacity of Piles

In order to gain insight into a piles behaviour when it is subjected to loading, a load test can be conducted. The derivation of pile capacity, based on a pile load test, is governed by the load-displacement relationship. Figure 2.2 illustrates a loading scheme with the response of the pile both in terms of head and base displacement. In this example, the pile is loaded in compression and upon reaching a certain applied force, the loading step is maintained. The duration of a load step is governed by the displacement rate. Once the settlement rate reaches a particular threshold known as the creep-criterion, the load is to be altered. The pile is then unloaded which results in positive response in terms of displacement. However, upon unloading, the pile does not displace back to its original position as a certain measure of permanent displacement has taken place. This is followed by application of another a load step which consequently displaces the pile head and base relative to the previously attained permanent displacement.

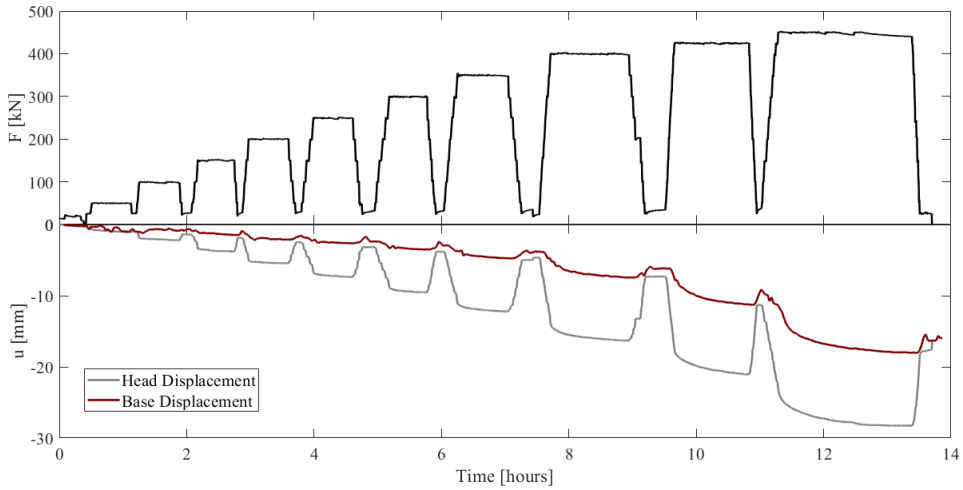

Figure 2.2: Pile response to loading in terms of head and base displacement

It is therefore important to note that a load test is designed to include information on load steps, the duration of each load step, application of load cycles, displacements and creep. Based on this information, a load-displacement relationship can be obtained through which the ultimate capacity of a pile is determined. Figure 2.3 illustrates a typical and idealized load settlement curve for a pile. The point at which the base capacity is mobilized is defined at a base displacement of 10% of the pile base diameter (Normcommissie 351 006 "Geotechniek", 2016). This only applies to soil-displacements piles loaded in compression. The ultimate base capacity of the pile, $Q_{b,ult}$, is highlighted in this figure.

For piled foundations, several evaluation methods have been developed through history. As mentioned previously, the bearing capacity of a pile is in principal the summation of the shaft and tip resistance. Therefore, the general form of every prediction method for the bearing capacity of a pile can be expressed as equation 2.1, where Q_T is the total bearing capacity and Q_s and Q_b are the shaft and base capacities respectively.

$$Q_T = Q_s + Q_b \tag{2.1}$$

Currently in Dutch practice, cone penetration test (CPT) based methods are exclusively used to estimate the pile capacity. This thesis focuses only on CPT-based prediction methods but provides a description of several methods in Appendix A.1. The prediction method used in the analysis is further discussed in section 2.4.

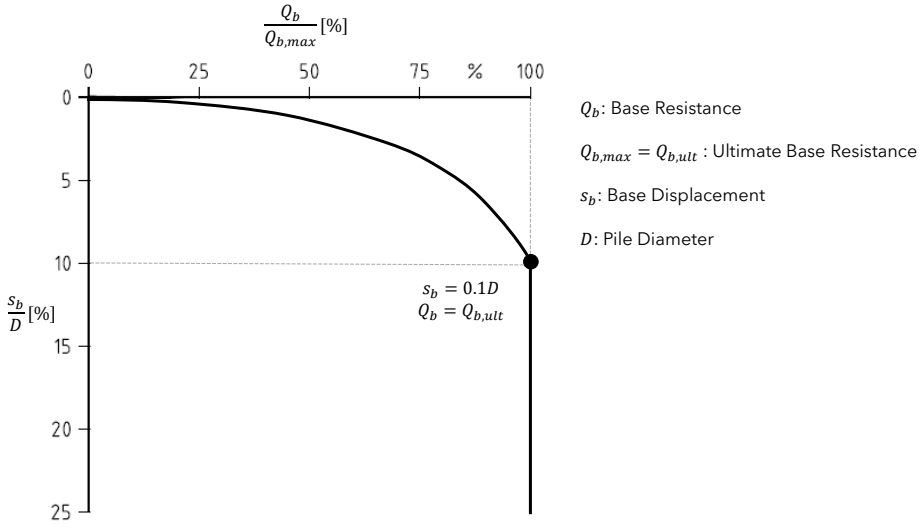

Figure 2.3: General load displacement curve for driven piles illustrating ultimate pile capacity
Adapted from Normcommissie 351 006 "Geotechniek". (2016). *Nen9997-1* (tech. rep.). NEN

2.2 Timber Piles

The most relevant characteristics of timer piles are discussed in this section. The study only focuses on characteristics that are taken into account in this test. The study does not illustrate information on topics such as degradation or specific effects of internal fibers. Such characteristics are briefly discussed in Appendix A.3.

2.2.1 Background and Common Use

General Characteristics and Wood Structure

Any form of wood taken from a tree can be categorized as either conifer or deciduous. These families are also known as soft and hard woods respectively. This categorization may be misleading as it portrays softwoods to be weaker than hardwoods. This is however not the case, as the main difference between the two categories is their density. Conifer wood is widely used in construction. This thesis studies the characteristics and behaviour of coniferous woods, as the majority of timber piles used in Amsterdam are taken from coniferous trees. More specifically, the most common wood species used as timber piles in Amsterdam consist of pine (Dutch: grenen) and spruce (Dutch: vuren). The load bearing behaviour of both pine and spruce timber piles are further analysed in Chapter 5.

Timber consists of cells, composed of wood substance, that are cemented together by lignin. Each of the composing fibers is different from the other in terms of size, density and orientation (Hansen, 1948). Considering this fact, one can conclude that aspects such as specific gravity and density of wooden materials vary from one sample to the other. Since both specific gravity and density have an effect on the strength of the material (Hansen, 1948), these properties must be taken into account when analyzing the capacity to which a pile can bear forces. As a consequence of applying forces that exceed this bearing capacity, plastic deformation and irreversible destruction of fibers and structures of the inner bindings of the wood can occur.

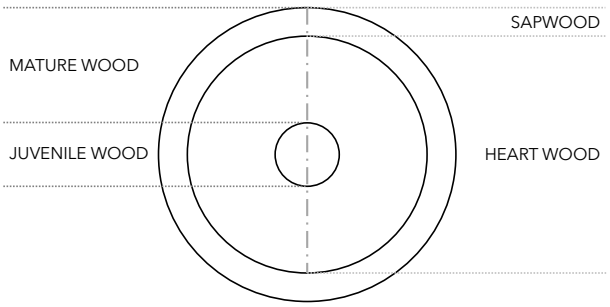

Figure 2.4: Internal structure of wood - base of the trunk

The internal structure of the original trunk is also an important aspect to take into consideration. Figure 2.4 illustrates a generalization of the internal structure of a wooden trunk at the base of the tree. The divisions of sapwood, heartwood, juvenile wood and mature wood are applicable to all types of timber. Heartwood is the central portion that consists entirely of inactive tissues and serves as the strengthening agent to the tree trunk.

The outer portion called sapwood, contains living cells and is lighter in color. Neither of the two entities is necessarily stronger than the other but sapwood is prone to decay much more than heartwood.

In addition to this separation between the outer shell and the core piece, the trunk can be separated into juvenile and mature wood. This division is illustrated in Figure 2.5. Figure 2.5 also illustrates a combination of the two categories for all parts.

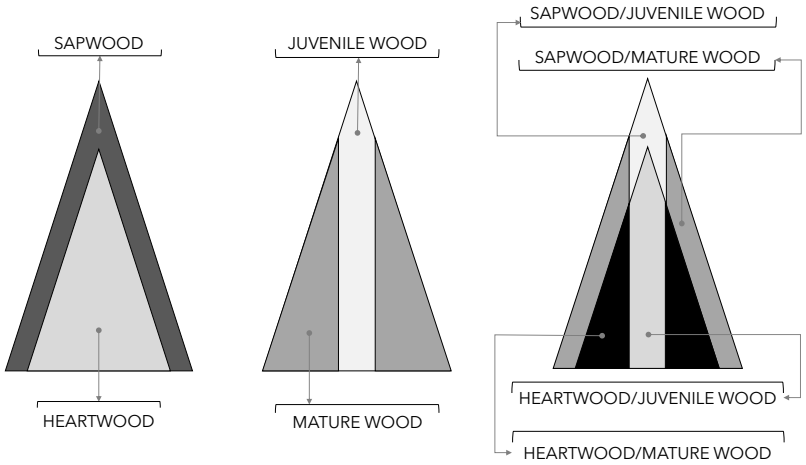

Figure 2.5: Division of parts of a trunk.
Adapted from Latinga, C. (2015). *De resterende (geotechnische) draagkracht van bestaande houten funderingspalen.* TU Eindhoven

The density of each division can be different from the other. It is also important to note that the geometry of each division is highly variable along the length of the pile. This is due to the tapering nature of a growing tree. Since a tree grows in the shape of a cone, some sections may even be absent (Latinga, 2015).

Conclusively, it can be stated that this natural variability caused by the division of parts and tapering of a tree trunk creates a rather complex nature for wooden piles. The effect of this inhomogeneity with regards to mechanical properties is further discussed in section 2.2.4.

Background and History

Timber piles have been used in construction for centuries and are one of the oldest means of creating foundations for structures. The oldest existing piled foundations in the city of Amsterdam date back to the 17^{th} century (Korff, 2012). Prior to the 17^{th} century, timber piles were in use more in the form of friction piles as the extent of pile driving was limited. Towards the end of the 17^{th} century, a setup was developed to hammer such piles deep enough to reach a bearing stratum. This setup consisted of a tripod and a weight of approximately 250 to 300 kilograms that was lifted by several people and dropped on the pile head. With the invention of the steam engine, pile installation was revolutionized, as steam engines were utilized for pile driving to deeper levels. Figure 2.6a illustrates the installation method prior to the usage of steam engines and Figure 2.6b shows the usage of steam engines for driving timber piles in the Netherlands.

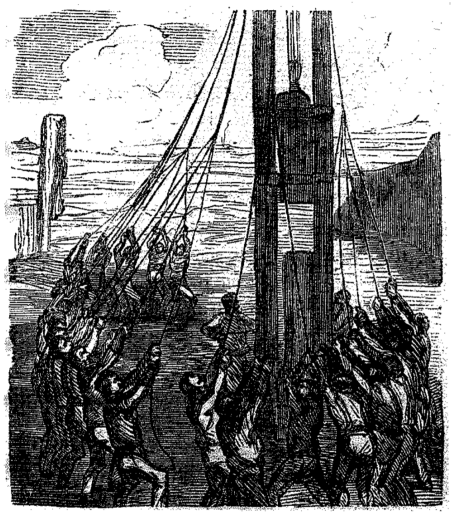

(a) Pile hammering in the 17th century. Reprinted from Wennekes, E., & Grijp, L. (2002). *De hele dag maar op en neer. over heien, heiliedjes en hoofdstedelijke muziekgebouwen.* Meertens Instituut i.s.m. Het Muziekgebouw

(b) Usage of the steam engine for pile driving. Photo taken by Jacob Olie, 1891, Reprinted from Korff, M. (2012). *Response of piled buildings to the construction of deep excavations* (Doctoral dissertation). University of Cambridge. IOS Press BV

Figure 2.6: Means of Pile Installation in the 17th Century

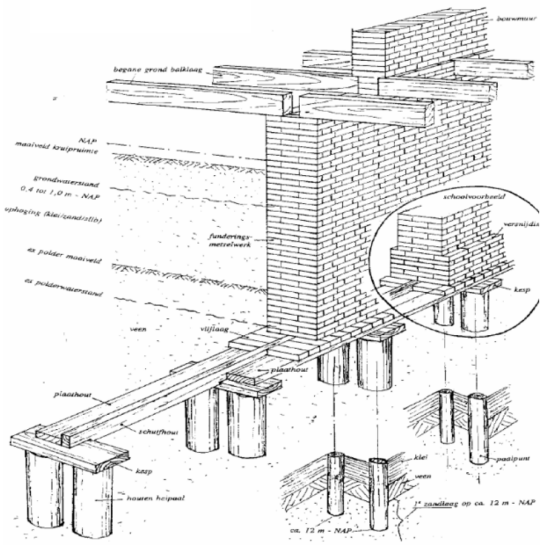

Figure 2.7: Typical timber piled foundation system in Amsterdam.
Reprinted from Zantkuijl, H. J. (1993). *Bouwen in amsterdam - het woonhuis in de stad.* Architectura & Natura.

The base level of timber piles in Amsterdam is typically defined by the term "tocht". This term is indicative, in theory, of 25 centimeters of insertion into the first sand layer. This measure of insertion was previously defined as a calendar. A calendar was defined as 30 drops of driving weight on top of the pile. Currently, the definition of calendar is based on the pile settlement. A calendar is therefore, effectively, defined as 25 centimeters

of settlement. Piles in Amsterdam are typically inserted 25 to 50 centimeters below the top of the first sand layer (Spruit & Hutcheson, 2019).

In the past, the main advantages of using wooden piles consisted of low initial costs, easy handling and resistance to decay if fully submerged (Kumar, 2010). Wooden piles have a typical head diameter of 300 to 500 millimeters and base diameter of 120 to 230 millimeter as generally used around the globe (Kumar, 2010). However, piles specifically used in Amsterdam are believed to have typical diameters ranging from 180 to 200 millimeters at the head and 120 to 140 millimeters at the base (Zantkuijl, 1993). The usage of timber piles in Amsterdam was well-established by the beginning of the 18^{th} century and by the 1800's, the so-called Amsterdam foundation with round timber piles was common. Figure 2.7 illustrates the typical wooden pile foundation system in Amsterdam. It

The variation of geometrical attributes for timber piles in Amsterdam gives insight into the complexity of drawing locally applicable conclusions regarding the bearing capacity. In 1974, 1616 piles were extracted as part of the Dapperbuurt extracted piles data-set. Another data-set for extracted piles, collected by Frans Sas, contains pile specifics for 1110 extracted timber piles. An insightful statistical analysis was carried out by Van Daatselaar, 2019, illustrating the variation of geometrical attributes of the piles. Figure 2.8 illustrates these variations with information from the Dapperbuurt data-set, Frans Sas data-set and a combination of the two.

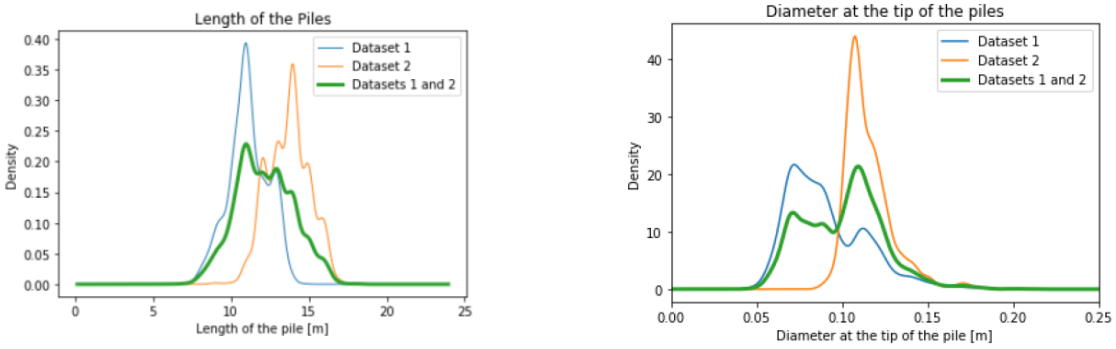

(a) Pile lengths

(b) Pile base diameters

Figure 2.8: PDFs for pile characteristics in Amsterdam based on the Dapperbuurt and Frans Sas data-sets for extracted piles.
Reprinted from Van Daatselaar, F. J. (2019). *The geotechnical bearing capacity of old timber piles.* TU Delft

2.2.2 Tapering

Tapering in piles has a direct effect on their bearing capacity and resistance behaviour. For instance, an increase in the degree of tapering may result in higher skin friction (Manandhar & Yasufuku, 2013). It was shown by Manandhar (2010) that tapering can be responsible for an increase in normalised skin friction and horizontal stresses. It is of significance to note that tapering causes a difference in shaft friction between scenarios where the pile is loaded in compression and in tension (Korff, 2012).

The effect of tapering on the bearing capacity of piles is analysed using small-scale model tests by Manandhar and Yasufuku, 2013. One of the findings of this research is that the effective radius of the influence zone around the pile shaft increases with an increase in the tapering angle. In order to appropriately consider the influence of tapering on the

bearing capacity of timber piles, a tapering angle or a series of discretized measurements of geometry need to be taken into account. The theory of cavity expansion has been used to include this effect and to predict both the end bearing and the shaft resistance of tapered piles (Manandhar & Yasufuku, 2013). The addition of tapering as a factor to the cavity expansion theory, results in an expansion of the diameter to which the influence zone of the pile extends.

The average tapering of piles in the city of Amsterdam is assumed to amount to approximately 8 millimeters per meter length. This is derived from information contained within the aforementioned data-sets of extracted piles. Figure 2.9 illustrates the variation in tapering between piles extracted in different parts of Amsterdam. As can be seen, the difference in tapering between piles is relatively small.

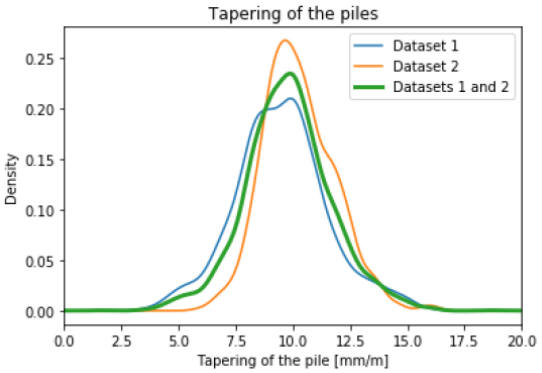

Figure 2.9: PDFs for pile tapering in Amsterdam
Reprinted from Van Daatselaar, F. J. (2019). *The geotechnical bearing capacity of old timber piles.* TU Delft

Experiments have shown that the tapering of piles can result in the increase of axial capacity (Wei, 1998). Figure 2.10 illustrates an example of such experiments where the shaft resistance of a tapered pile and a straight sided pile under compression are compared. This is believed to be only one of the advantages of tapered piles. Observations regarding the shaft friction indicated that the resistance of the shaft in tapered piles is up to 40% higher than that of a straight sided pile. It has also been observed that with increasing taper angle, the friction along the shaft increases (Wei, 1998).

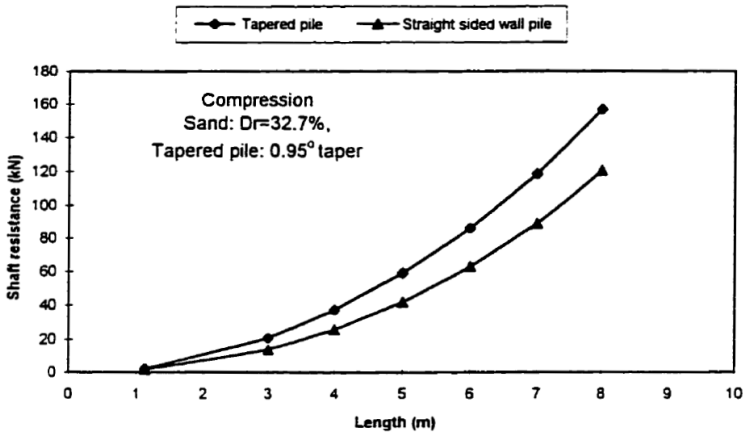

Figure 2.10: Comparison of shaft resistance for tapered and straight piles
Reprinted from Wei, J. (1998). *Experimental investigation of tapered piles.* University of Western Ontario

2.2.3 Effect of Moisture Content and Temperature

Another significant factor affecting both the strength and the deformation of wood is the moisture content. Hansen (1948) indicates that depending on relative humidity and temperature of the atmosphere, wood tends to attain a specific moisture content that is in equilibrium with the surroundings. Fiber saturation is defined as the full saturation of cell walls. The strength properties of wood increase when it is dried below this saturation point (Hansen, 1948).

Most mechanical properties tend to increase with a decrease in moisture content (Green et al., 1999). The point at which the mechanical properties of timber begin to change when a specimen is dried is called the intersection moisture content. The typical values for this property are 21 to 24 % for pine woods and 27 % for spruce species. Changes in temperature also result in alterations of the mechanical properties in wood. Generally, these properties tend to decrease upon heating and increase when cooling (Green et al., 1999). The changes and behaviour are however highly dependent on the moisture content of the specimen. More information and illustrations of these factors are shown in Appendix A.3.

It is of great relevance to this thesis that moisture content heavily affects the compressive strength and modulus of elasticity of timber (Aicher & Stapf, 2016). The importance stems from the potential changes in moisture content upon pile installation. Additionally, the moisture content present in the pile before installation affects any form of reference measurement. A study has proven that larger reduction factors must be applied to spruce wooden piles with high moisture contents. This is especially applicable to trunks loaded in compression (Aicher & Stapf, 2016). The effect of moisture content and temperature are not studied in this thesis in a detailed manner. The aim of this illustration is to elaborate on the potential of variation due to changes in circumstances at the test location.

2.2.4 Natural Variability in Mechanical Properties

Wood is a highly variable and heterogeneous material due to it's biological origin. Endless research has been conducted to determine patterns of variability and correlation between properties yet some aspects remain random (Catera & Morlier, 1994). Despite this fact, research has provided insight into certain aspects which can be explained in a deterministic manner. However, aspects such as the variation of the modulus of elasticity along the length of a trunk does not follow a consistent trend (Green et al., 1999). The natural variability in mechanical properties results in behavioural complexity and ambiguities with regards to drawing conclusions.

Wood can be described as an orthotropic material, meaning it has three mutual planes of elastic symmetry perpendicular to one another (Green et al., 1999). In the direction of each of these axes, the mechanical properties are unique and independent. The longitudinal direction is known as the grain. This is the direction in which the fiber grows. Specific natural growth characteristics of trees have great influence on mechanical properties. These growth characteristics consist of, but are not limited to, aspects such as the existence of cross-grain, knots and branches. The term cross-grain is related to the angle at which the slope of the grain is. The term knot is indicative of the location at which a branch is incorporated into the trunk of a tree. This entity acts as an interruption to continuity and alters the fiber direction, hence affecting mechanical properties locally (Green et al., 1999).

The ambiguity and variability of mechanical properties, most significantly the modulus of elasticity, play a major role in the analysis of wooden piles. The usage of an average modulus of elasticity for a timber pile is common practice but it is significant to consider the variation in stiffness that is caused by the biological nature of wood.

2.3 Fiber Optics and Data Interpretation

2.3.1 Optical Fiber Sensors

Fiber optic sensors (FOS) have grown in maturity and popularity over the last years (Bersan et al., 2018). Recently, the usage of "distributed sensing" in the civil engineering and construction industry has proven to be a significant and effective tool for conducting measurements (De Battista et al., 2016). This tool is rapidly replacing the conventional local sensor systems which is capable of measuring a physical entity at a single point in space. This replacement is intuitively a positive change as continuous means of measuring are far more effective, both in practicality and in costs, than the installment of numerous point sensors.

FOSs are particularly useful due to a series of advantages in comparison with other sensing technologies. Specifically, FOSs have proven to be appropriately usable in harsh environments. These sensors feature characteristics such as intrinsic immunity to electromagnetic interference, flexibility and low operational and elemental costs. Another advantage of such sensors is their ability to be easily multiplexed in order to enable the user to conduct measurements over long distances or at large numbers of nodes. As a result of using FOSs, mechanical properties of the tested pile can be determined. For instance, strain distributions during a compression test can give detailed indications of stiffness variation along the length of a specimen. Additionally, a detailed distribution of strains and soil-structure interactions at the interface can also be measured and estimated before installation.

Fiber optic sensors can be generally categorized into three main categories, namely, point sensors, quasi-distributed sensors and fully distributed sensors. The more prominent form of distributed sensors are called distributed fiber optic sensors, DFOS for short. Application of distributed optical fiber sensors to monitor the mechanical performance of driven piles is shaping to become common practice (Hong et al., 2016). These systems work off of the photonic principle of measuring alterations of molecular structures of glass along the fiber. In pile testing, such alterations are in relation to changes in strain and/or temperature.

Examples of fully distributed sensors are BOTDR (Brillouin Optical Time Domain Reflectometry) and BOTDA (Brillouin Optical Time Domain Analysis) sensors. These sensors are capable of providing continuous strain and temperature distribution profiles of monitored structures. It has been observed that DFOS systems, specifically BOTDA and BOTDR sensors, are capable of delivering reliable information (De Battista et al., 2016). Despite the reliability of the delivered results, it can also be seen that more information is provided in comparison with the point sensor system. In order to interpret data obtained through fiber optic sensing, it is essential to have an understanding of the mathematical background of FOSs.

2.3.2 Mathematical Basics of Fiber Optic Sensing

The fundamentals of measurements for BOTDA/BOTDR sensors revolve around the concept of scattering frequencies measured in the time domain. Equation 2.2 illustrates the principle of frequency obtainment as a function of strains.

$$v(\epsilon) = v(0)(1 + C_\varepsilon \times \varepsilon) \tag{2.2}$$

Where v_ε is the Brillouin scattering frequency, $v(0)$ is the reference frequency and C_ε is the constant coefficient corresponding to changes in strain.

Using the scattering frequency, the deformation, stresses and other phenomena in piles can be determined as illustrated in equations 2.3 to 2.9.

$$\Delta L_i = L_i \varepsilon_i \tag{2.3}$$

$$\Delta L = \sum_{i=1}^{n} L_i \varepsilon_i \tag{2.4}$$

For each element the axial stress and the related forces at each end can be calculated as follows; (σ_i is axial stress, E_s is the elastic modulus and A is the cross sectional area of the pile)

$$\sigma_i = E_s \varepsilon_i \tag{2.5}$$

$$F_i = \sigma_i A = E_s \varepsilon_i A \tag{2.6}$$

$$F_{i-1} = \sigma_{i-1} A = E_s \varepsilon_{i-1} A \tag{2.7}$$

Frictional force F_{s_i} and shear stress τ_i between the pile and the soil can be calculated by; (O is the perimeter).

$$F_{s_i} = F_i - F_{i-1} \tag{2.8}$$

$$\tau_i = \frac{F_{s_i}}{O L_i} \tag{2.9}$$

Table 2.1: Parameter description for equations 2.2 to 2.9

Parameter	**Description**
L_i	Nodal Length
ε_i	Nodal Strain Measurement
σ	Stress
A	Cross-sectional area
E	Modulus of Elasticity
F_i	Nodal Force
F_{s_i}	Frictional Force
τ	Shear Stress
O	Perimeter

2.4 CPT Based Methods

As mentioned in section 2.1, this report focuses on a CPT based calculation method as illustrated in equations 2.10 and 2.11.

$$Q_T = Q_b + Q_s \tag{2.10}$$

$$Q_T = q_{c,avg} \cdot \alpha_p \cdot A + \sum q_c \cdot \alpha_s \cdot O \cdot \Delta L \tag{2.11}$$

Table 2.2: Parameter description for equations 2.10 and 2.11

Parameter	Description	Unit
Q_T	Total bearing capacity	$[kN]$
Q_b	Pile base capacity	$[kN]$
Q_s	Pile shaft Capacity	$[kN]$
A	Cross-sectional area of pile base	$[m^2]$
α_p	Correction factor for base capacity	[-]
α_s	Correction factor for shaft capacity	[-]
$q_{c,avg}$	Average cone resistance determined using an averaging method	$[kPa]$
ΔL	A segment of length over which a specific cone resistance acts	$[m]$
O	Perimeter of pile over the length ΔL	$[m]$
q_c	Averaged cone resistance at acting over the depth of ΔL	$[kPa]$

The method above predicts the total capacity of a pile based on CPT value. The average cone resistance $q_{c,avg}$ can be determined through several methods. Such methods aim to obtain a representative value for the determination of pile capacity while including several factors. These factors consist of, but are not limited to zone of pile influence, layering in the soil system and installation effects. The most commonly used methods to determine the average cone resistance are Koppejan and LCPC, also known as the French method. In Dutch practice, the Koppejan method is used which is also known as the 4D-8D method (Van Mierloo & Koppejan, 1952).

The alpha factors in equation 2.11 have been points of discussion for years. It has been argued that α_p can be a constant entity if the appropriate averaging method is used for the cone resistance (Randolph, 2003).

2.4.1 CPT Averaging Methods

As previously mentioned, the most commonly used averaging methods for determining the average cone resistance for base capacity predictions are Koppejan and LCPC. In this section, the two averaging methods are discussed alongside the alternative method of De Boorder, 2019.

Koppejan

The Koppejan method is the main method of determining $q_{c,avg}$ used in Dutch practice. The averaged cone resistance obtained through this method is multiplied by an α_p factor, which has a value of 0.7 in the Dutch norm. This set of norms imposes an upper limit

of $q_{c,av} = 15MPa$ for driven piles (Normcommissie 351 006 "Geotechniek", 2016). The method's aim is to return an average cone resistance based on values above the pile tip at a distance of 8 times the pile diameter (8D) and 0.7 to 4 times the diameter (0.7D-4D) below the pile tip. This method is governed by equation 2.12 where $q_{c,avg}$ is the average cone resistance for the prediction of base capacity.

$$q_{c,avg} = \frac{1}{2}\left[\frac{q_{c,I} + q_{c,II}}{2} + q_{c,III}\right] \tag{2.12}$$

The procedure through which $q_{c,I}$, $q_{c,II}$ and $q_{c,III}$ are obtained is schematized in Figure 2.11. $q_{c,I}$ is the minimum arithmetic average of cone resistance below the pile tip over a depth of 0.7 to 4 times the diameter. $q_{c,II}$ is also an arithmetic average over the same depth as $q_{c,I}$ but following a minimum path rule. And finally, $q_{c,III}$ is an average of q_c following a minimum path rule over a distance of 8D above the pile tip level.

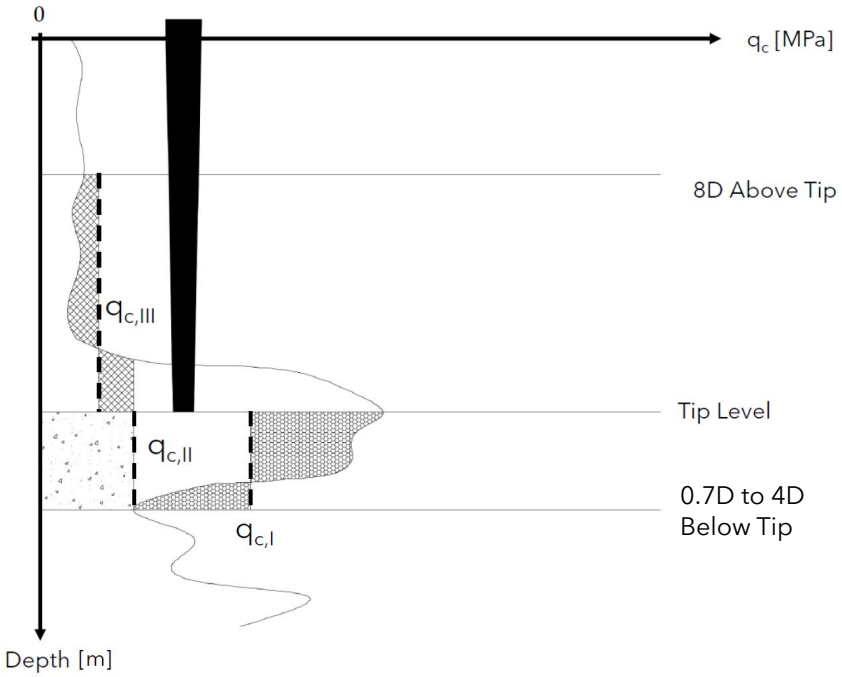

Figure 2.11: The Koppejan averaging method

It is of interest to note that the method of Koppejan results in conservative cone resistance values (De Boorder, 2019). The application of this method in practice has been a point of discussion and much research has been done to develop more representative and accurate methods of averaging.

LCPC

Also known as the French method, the LCPC method is another arithmetic averaging method proven to be effective and used commonly around the world (Bustamante & Gianeselli, 1982). The average cone resistance is evaluated over a depth of 1.5D above and below the pile tip level. The averaging procedure is divided into three steps. First, an arithmetic average of cone resistance, $q_{c,mean}$, is calculated over a depth of 1.5 times the pile diameter above and below the tip level. This is followed by the elimination of all q_c

values lower than $0.7q_{c,mean}$ or higher than $1.3q_{c,mean}$. An equivalent arithmetic average cone resistance, $q_{c,eq}$, is then calculated from the remaining cone resistance values over the zones that were not eliminated. This process is illustrated in Figure 2.12 where ultimately $q_{c,eq}$ is equal to $q_{c,avg}$.

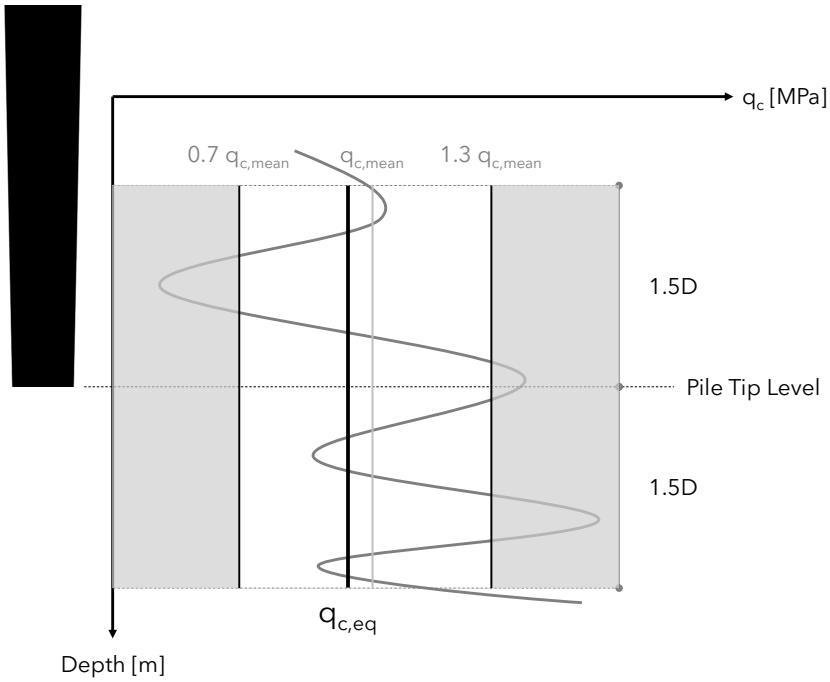

Figure 2.12: The LCPC averaging method where $q_{c,eq} = q_{c,avg}$

De Boorder, 2019

A new alternative averaging method is introduced by De Boorder, 2019, which consists of a weighted averaging formulation. Equations 2.13 and 2.14 illustrate the principles behind this method. The formulation depends on the distance from the pile tip and a comparison of soil and pile-tip stiffness.

$$q_{c,avg} = \sum \left(q_{c,j} \frac{w_{T,j}}{\sum w_{T,j}} \right) \tag{2.13}$$

$$q_{c,avg} = \sum \left(q_{c,j} \frac{w_{d,j} \cdot w_{qc,j}}{\sum w_{d,j} \cdot w_{qc,j}} \right) \tag{2.14}$$

Table 2.3: Parameter description for de Boorder averaging method
Adapted from De Boorder, M. (2019). *Development of a new cpt averaging technique and review of existing cpt based methods for the calculation of total pile capacity.* TU Delft

Parameter	Description
$q_{c,j}$	Cone resistance at a point
$w_{T,j}$	Total weight of q_c at a point i.e. $w_{d,j} \cdot w_{qc,j}$
$w_{d,j}$	Weight of a point related to its distance to the pile tip
$w_{qc,j}$	Weight of a point related to the stiffness ratio $\frac{q_{c,tip}}{q_{c,j}}$
s	Reshape factor for weight related to the stiffness ratio

This method, like Koppejan and LCPC, enables the user to include soil transition zones and considers thin soil lenses. The capturing of transition zones is a significant advantage of this method. Overall, upon calibration of this method with the application of several averaging techniques to pile load test results, the formulation has delivered promising and valuable results that can be used in the future.

Evaluation of Averaging Methods

A comparison of the aforementioned averaging methods was carried out by De Boorder, 2019. As mentioned previously, the method of Koppejan tends to be conservative and presents representative values in layered soil systems. However, Koppejan falls short when the embedment of the pile in a strong soil layer is less than 8 times the diameter. This method is conservative in essence as it follows a minimum path rule. The French method delivers representative values in uniform soils but tends to overestimate the strength in layered soils. Neither LCPC nor Koppejan are capable of capturing the effect of transition zones. The alternative method of De Boorder, 2019 has proven to capture transition zones and thin lenses. All three of the mentioned methods are used in the analysis that follows in the 5^{th} chapter.

2.5 Residual Loads and True Load Distribution

This section aims to illustrate the fundamental aspects behind residual loads and their effect on the bearing capacity of piles as a consequence of load distribution. This is significant with regards to instrumented pile load testing as the opportunity of determining the true load distribution is realized through instrumentation.

2.5.1 Conceptual Definition of Residual Loads

It is important to consider the null state or a no-load condition of a pile in order to have an appropriate understanding of the load distribution upon loading. A zero or initial reading of gauges on an instrumented pile is however not representative of a no-load condition (Fellenius, 2002b). There are existing loads in the pile upon installation before the loading process begins. Such loads are considered as results from so called locked in strains. These locked in strains are the source of locked in stresses which are in line with the concept of having residual loads.

Upon driving a pile for installation, residual loads are to fully develop after the driving force is removed. Residual compressive stresses remain at the base and are balanced by the negative skin friction of the shaft. With the existence of these stresses, it can be concluded that the pile is never truly unloaded (Xu, 2007).

Fellenius (2015) defines residual loads as the axial force that is present in the pile when the pile is not statically loaded in a test. The development of this load occurs at two main stages, namely, the completion of driving and during the recovery of the surrounding soil (Fellenius, 2015). Figure 2.13 illustrates the load distribution upon development of residual loads. A neutral plane, or equilibrium point, exists in this profile which is indicative of the position at which the shaft resistance and the relative movement between the pile and the surrounding soil are zero (Lie & Zhang, 2012).

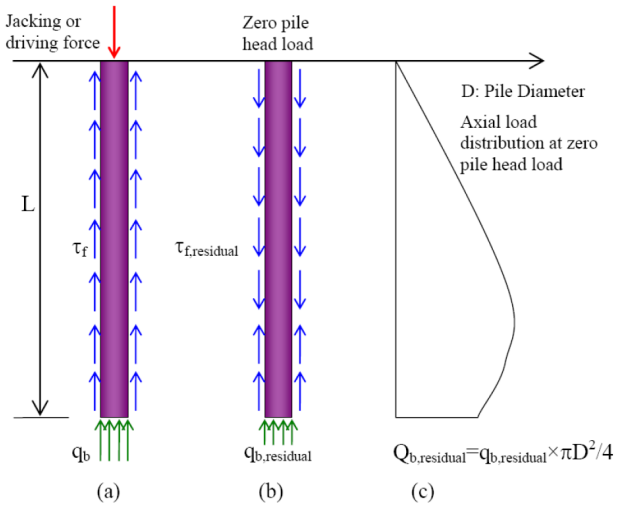

Figure 2.13: Development of residual stresses. (a) pile during driving. (b) residual stresses upon removal of head load, and (c) scheme of load distribution.
Reprinted from Xu, X. (2007). *Investigation of the end bearing performance of displacement piles in sand* (Doctoral dissertation)

It is therefore of great significance to consider residual loads and their effect in order

to have a complete picture of true load distribution. The effect of residual loads on this distribution is illustrated in the following section.

2.5.2 Influence of Residual Loads on Measurements

The effect of residual loads on load distribution and determination of bearing capacity can be observed using results illustrated by Gregersen et al. (1975). A series of static loading tests were conducted on instrumented piles and the set-up was devised to take residual loads into account. This means that measurements were conducted before the start of the static loading test. Ultimately the results shown in Figure 2.14 were obtained.

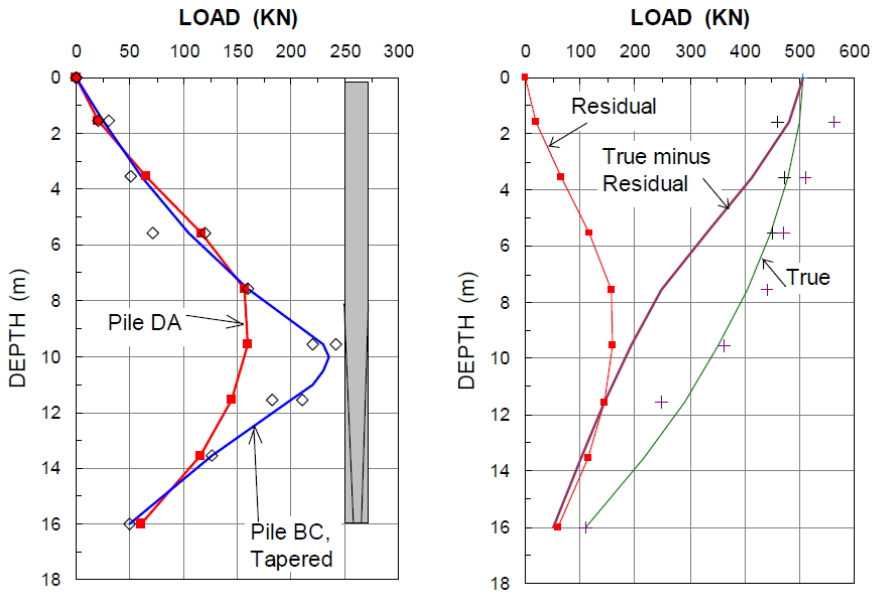

Figure 2.14: Left: Distribution of residual loads in piles BC and DA before the start of the test. Right: Load and resistance distribution in pile DA during the test.
Derived from Gregersen et al., 1975 and reprinted from Fellenius, B. (2002a). Determining the true distributions of load in instrumented piles. https://doi.org/10.1061/40601(256)104

Zeroing measurements on strain gauges at the beginning of a test results in the "S" shaped curve that is labeled as 'True minus Residual' in Figure 2.14. As this figure shows, the true minus residual load distribution versus depth is unrepresentative of how the load actually propagates through the pile. Therefore, it is essential to consider locked in strains and forces in order to obtain the true load distribution throughout a pile.

Other case studies illustrating this fact are presented by Fellenius (2002a). Conclusively, it is clear that without consideration of residual loads, one is unable to derive realistic and appropriate results from pile load tests (Fellenius, 2002a). Dismissal of residual loads results in an over-prediction of shaft capacity and an under-predication of base resistance. As a consequence of the aforementioned aspects, any derivation of a bearing capacity calculation method must include the effect of residual loads and all load distributions must take locked in forces into account.

Fellenius et al., 2000 conducted experiments on instrumented piles tapered at the bottom and straight along the top portion of the pile. The experiments illustrate that the equilibrium plane is positioned within the tapered portion of the pile (Fellenius et al., 2000). As illustrated in Figure 2.15, the corresponding load to measured strains at the mid-point of the tapered section is equal to the residual load before the test.

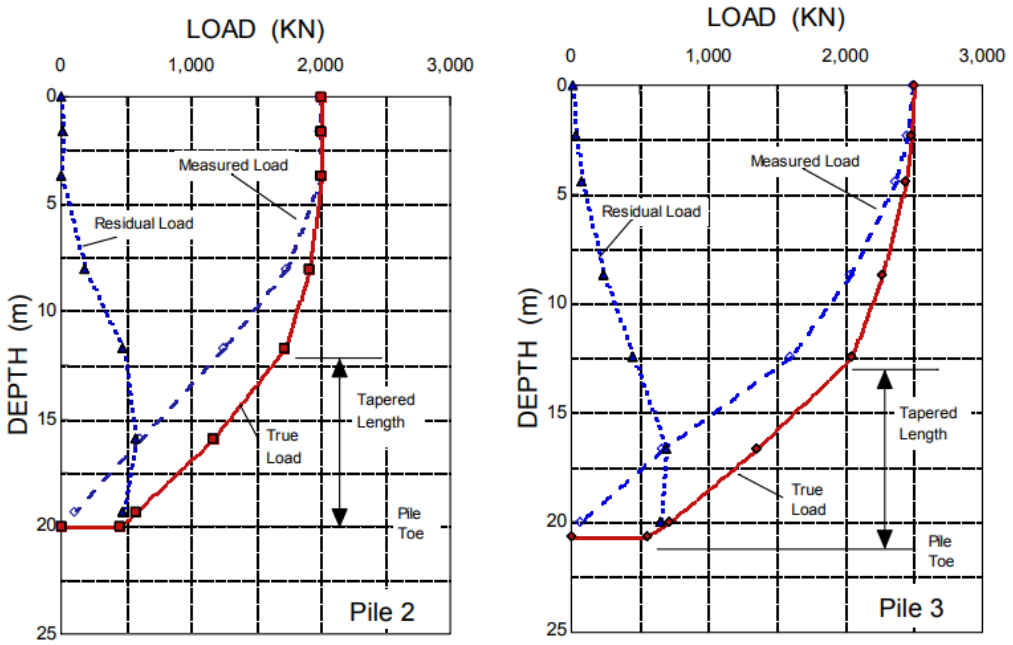

Figure 2.15: Distribution of measured load, true load, and residual load on tapered piles reprinted from Fellenius, B., Brusey, W., & Pepe, F. (2000). Soil set-up, variable concrete modulus, and residual load for tapered instrumented piles in sand. https://doi.org/10.1061/40486(300)6

2.6 Geological Sphere of Amsterdam

The geology of the Netherlands is governed by the melting of glaciers and rises in the sea levels during the early stages of the Quaternary era. The subsurface of the Netherlands mostly consists of formations deposited during the Holocene and Pleistocene time periods. In Amsterdam, the first 20 or so metres of the subsurface, consists of several formations deposited during the Holocene and the Boxtel formation. The Boxtel formation consists of sand layers (Keijer, 2015). The so-called first and second sand layers of Amsterdam are from this formation and were deposited in the mid-Pleistocene.

A decrease in the sea level due to regression during the late Pleistocene allowed for vegetation to grow. This process formed a peat layer on top of the first sand layer. This was followed by a transgression which resulted in the deposition of the Holocene formations. The formations deposited during the Holocene period consist of both continental and marine deposits. This is due to fluctuations in the sea-level which resulted in the formation of extensive clay layers and a somewhat thin sand-clay lens at around 7 to 8 meters below the Amsterdam Ordnance Datum (NAP) (de Gans, 2011). The Holocene clay layer is topped with another peat layer belonging to the Nieuwkoop formation. In most parts of Amsterdam, a sand-fill is present on top of the soft soil. The general soil profile in Amsterdam is illustrated in Figure 2.16.

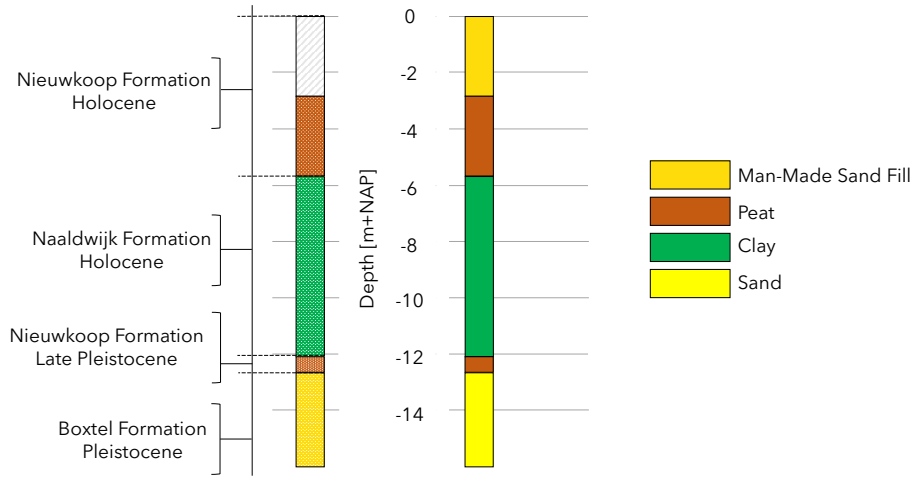

Figure 2.16: Typical soil profile and formations for Amsterdam
adapted from de Gans, W. (2011). *De bodem onder amsterdam: Een geologische stadswandeling* (1st Edition). TNO

The lithology in Amsterdam is of great significance to an analysis of bearing capacity. The variation in the soft layers has direct influence on the shaft capacity of piles. The most important factors causing variation within the subsurface of Amsterdam are the rivers IJ and Amstel. The erosion of the Holocene clay layers and its replacement with river sand and clay deposits are significant in the areas close to the rivers. Another significant aspect is the variation in depth of the sand layer which acts as the bearing stratum to piles. As illustrated in Figure 2.17, the top of the first sand layer may vary between -10 meters to -13.5 meters with respect to NAP. Typical cone resistance values for this layer vary between 12 to 20 MPa.

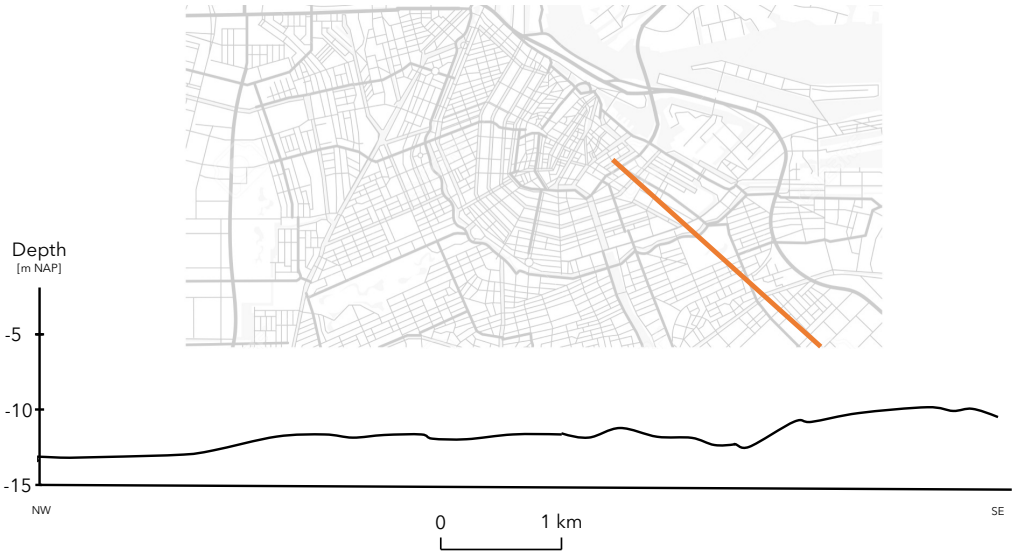

Figure 2.17: Top of the first sand layer
adapted from de Gans, W. (2011). *De bodem onder amsterdam: Een geologische stadswandeling* (1st Edition). TNO

Conclusively, it is important to note that the top fill layer which is present throughout the city is highly variable. It is also of significance that the soft layers above the first sand layer are highly variable both in thickness and in properties. These aspects, alongside the embedment of the piles, are of great influence to the bearing capacity of timber piles in Amsterdam.

2.7 Previous Pile Load Tests on Timber Piles in Amsterdam

As part of the North-South metro line project in Amsterdam, new timber piles were loaded in compression to have a better understanding of the settlement behaviour. Through these tests, it was determined that the theoretical bearing capacity of such piles varied between 177 to 265 kN (Van der Stoel, 2001). Aside from these test, a series of tests were conducted in Dapperbuurt, Amsterdam. The main goal of this program was the assessment of the timber pile foundation quality in the 1960's.

Korff (2012) dedicates a chapter to the Dapperbuurt pile load tests on timber piles under demolished buildings. In this dissertation it is indicated that a series of tests were conducted on Pine timber piles from demolished houses in 2nd van Swindenstraat and on additionally installed driven piles. The piles from the demolished houses aged between 70 to 100 years. The average pile head diameter in the area was between 220 to 225 millimeters whereas the average toe diameter amounted to about 110 millimeters. Therefore, there is a resulting average taper of approximately 10.5 mm/m. The average tapering in the Holocene layer is 9.1 mm/m. Pile spacing varies between 0.6 meters to 0.9 meters. The soil conditions at the testing and foundation site are summarized in Table 2.4. The peat layer above the foundation sand layer separates the aquifer from the phreatic level above.

Table 2.4: Characteristics of soil layers from tests
Based on Hoekstra and Bokhoven, 1974; adapted from Korff, 2012

Layer	**Soil Type**	**Top of Layer [NAP]**	γ_{sat} $[kN/m^3]$	**φ' [degrees]**
1	Sand, Fill	0	17	25
2	Peat	-4.0	11	-
3	Clay	-6.0	16	-
4	Sand, Clay	-7.0	18.5	27
5	Clay, Peat	-9.5	15	-
6	Peat	-12.0	11	-
7	Sand	-12.2	18	33

Ultimately, the bearing capacity of the new timber piles varied between 260 to 270 kN. The research illustrates that the shaft friction amounts to 8.8 kN/m in the Holocene layer. Additionally, a shaft friction of 59 kN in the sand layer is observed for a typical embedment of 25 to 50 centimeters. The base resistance varies between 90 to 100 kN. Comparison between old and new piles led to the observation that the shaft friction of old piles were 40% lower than that of new piles.

Considering the fact that this project and the Dapperbuurt tests both include an analysis on new piles, the bearing capacities can be compared. The soil conditions and the effect of different soil layers can also be compared. The comparison depends on site conditions, pile characteristics and the applied loads during tests. Additional information such as a CPT from the test locations and load-settlement curves are provided in Appendix A.4.

Chapter 3

Test and Data Description

The purpose of this chapter is to outline the experimental framework of this project and to provide an overview of the data obtained from the experiments.

3.1 Experimental Framework

As part of the 'Structural Safety of Bridges' program (Programma Constructieve Veiligheid Bruggen (PCVB)), all road traffic bridges managed by the municipality of Amsterdam are analysed in terms of structural safety (Spruit & Hutcheson, 2019). This analysis is based on the rating of structural safety guidelines which are based on the construction decree of 2012 and the corresponding norms. As part of this program, an assessment framework is developed for bridges, namely Toetsingskader Amsterdamse Bruggen (TAB) (Spruit & Hutcheson, 2019).

One part of the TAB program consists of an evaluation of the timber pile foundations under approximately 250 bridges and 200 kilometers of quay walls. This research aims to determine more efficient and appropriate means of evaluation for such constructions. The overall framework is divided into two aspects namely, evaluation of parameters affecting the strength of the piles, and evaluation of the geotechnical parameters affecting the geotechnical bearing capacity.

As to achieve the overall goal, a series of new timber piles were made available to the project to be tested in several settings. The choice of piles is based on several aspects. The test framework aims to analyze the effect of certain phenomena that are variable between piles in order to draw applicable and concrete conclusions. The most significant aspects are the variation in insertion depth, variation in wood type, influence of moisture content and variation in mechanical properties. The aim of the tests conducted is to determine the pile bearing parameters for the pile base and shaft in the soil profile of Amsterdam. The effect of negative sleeve friction and deterioration of the wood are also aspects to be observed. The initial thought process behind the framework of the load tests and their purpose is outlined below (Spruit & Hutcheson, 2019).

1. On the basis of CPT results the geotechnical bearing capacity of the piles is predicted.

2. Series of load tests, tension tests and negative skin friction tests are conducted. The results are compared to the theoretically calculated bearing capacity of each pile.

3. Differences in results are outlined using calculations based on the measured entities such as deformation of the pile, shaft friction, soil pressure and water pressures.

4. Based on these aspects, the necessary parameters and safety factors of the relevant norms are analysed.

3.1.1 Research and Test Method

In order to achieve appropriate derivations of pile capacity prediction factors, a total of 27 piles were made available to this project and instrumented with fiber optics. Sixteen of these piles were installed in the grounds of a test site in Overamstel, Amsterdam to be tested in compression. Four piles were tested in a rapid load test and left under load for months. Four other piles were tested in tension. The site conditions are ideal as there is little spatial variability in terms of the soil profile. This thesis focuses on the load tests in compression. The following steps illustrate a generalization of the different phases of the test framework.

Preparation

1. Installation locations are determined.

2. Per pile location, 2 CPT and 1 CPTu at a distance of 1 meter from the pile are carried out.

3. The piles are laid horizontally on supporting tripods.

4. Grooves are sawed onto the edges of two perpendicular planes of the wood (Figure E.4).

5. Using a caliper, the piles are marked at their tapered end so that a diameter of approximately 15 centimeters is ensured. The extra wood is to be sawed off.

6. Above said tip level, using a drilling frame, a loop is drilled through the core of the wood to loop the fiber through. This is illustrated in Figure 3.1.

7. The piles are instrumented with sensing fibers in the grooves by gluing.

8. The circumference of the piles is measured at every 0.5 to 1 meter length.

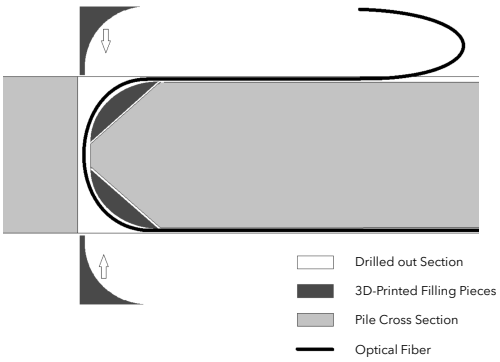

Figure 3.1: Cross section of fiber loop at pile tip
adapted from Spruit, R. (2020). *Feitenrapportage proefbelastingen op houten palen* (tech. rep.). IB Gemeente Rotterdam

It is important to note that two sets of sensing fibers are installed for each pile. One set, labeled North-South, loops 2 centimeters above the pile tip. The other set, labeled East-West, is located 4 centimeters above the tip level.

Reference Measurements and Pile Installation

1. The instrumentation is connected to OmniSense Dual system to read measurements.
2. Reference measurements are conducted on the pile as glue control, lying down, standing on a steel element and finally hanging from a crane.
3. The top fill sand layer is pre-drilled (Figure E.5,left).
4. The piles are driven into the soil body (Figure E.5,right).
5. A frame is installed on top of the piles. This frame imposes vertical loads. The design for this setup is illustrated in Figure 3.2.

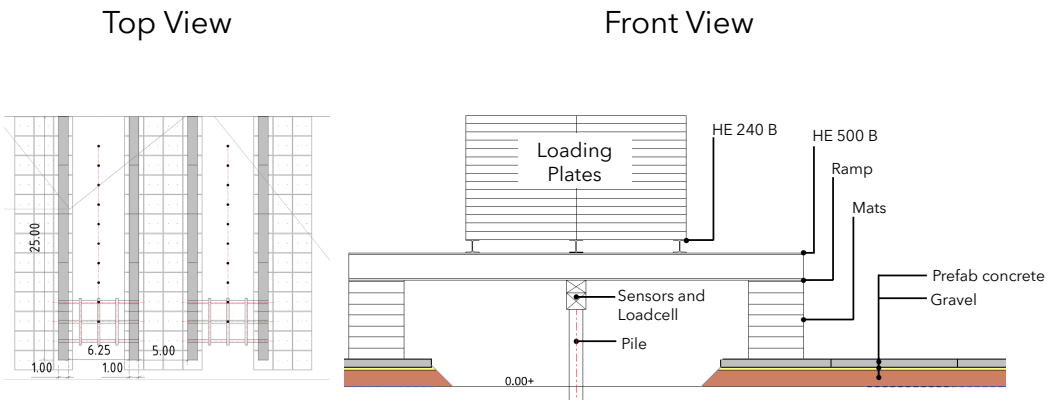

Figure 3.2: Design of loading frame
Courtesy of Engineering Firm of Municipality of Amsterdam

Load Tests

1. The load-cell and displacement sensors (LVDT's) are installed on the pile head alongside a loading plate and hydraulic jack which all-together weigh about 70 kilograms.
2. The piles are loaded using pumps increasing oil pressures in tubes connected to the load-cell. This is done manually and the pressure is monitored at all times.
3. The displacement of the pile, both vertically and horizontally, is also monitored throughout.
4. Two piles are tested simultaneously under each frame (refer to Figure 3.2 top view).
5. Piles are loaded and unloaded and the creep rate is evaluated during each load-step to alter the loading scheme if need be. Loading schemes are summarized in Appendix D.

3.1.2 Pile Specifications

Physical and Mechanical Specifications

As mentioned previously, the data-sets of extracted piles in Amsterdam indicated an average pile head diameter of 250 millimeters, average tapering of 10.26 mm/m, range of pile lengths varying between 12.25 to 15.5 meters and pile tip diameters varying between 125 to 150 millimeters (Korff, 2012; Van Daatselaar, 2019).

Table 3.1: Dimensions and properties of tested piles

ID	**Wood Type**	**Debarking**	$\mathbf{D_{Head}}$ [mm]	$\mathbf{D_{Tip}}$ [mm]	$\boldsymbol{L}$ [mm]	$\boldsymbol{MOE_{dyn}}$ [GPa]
572	S	H	296.0	147.1	14.3	13.42
177	S	H	284.9	150.2	14.3	13.99
397	S	H	311.9	139.1	14.4	16.55
564	S	H	273.7	142.3	14.3	14.51
195	S	M	241.9	131.8	14.4	11.43
175	S	H	288.1	159.2	13.9	16.99
643	P	M	218.0	146.4	14.5	12.07
183	S	H	283.3	155.3	14.4	10.44
594	P	M	215.8	141.6	14.3	10.79
179	S	H	267.4	155.7	14.1	13.65
592	P	M	227.0	141.3	14.2	12.60
398	S	H	267.4	142.6	13.8	12.06
164	S	M	261.0	136.9	14.3	15.35
576	P	M	206.9	131.1	14.1	14.52
573	P	M	248.3	158.2	14.3	14.00
191	S	H	276.9	140.4	13.5	16.90
596	P	M	220.9	141.6	14.6	10.25
399	S	M	251.5	145.1	14.4	18.26
172	S	M	245.1	144.2	14.1	12.06
590	P	M	211.7	144.8	14.3	12.88
566	S	M	232.4	146.1	13.8	13.47
581	P	M	234.0	150.6	14.8	14.41
595	P	M	203.7	131.8	14.2	9.82
570	S	H	292.8	148.0	13.8	14.12
162	S	H	292.8	147.7	13.7	14.44
187	S	H	302.4	143.9	14.0	13.23
567	S	H	270.6	146.1	14.1	13.78
Average			**256.5**	**144.8**	**14.2**	**13.6**

Table 3.1 illustrates the physical and mechanical specifications of the piles that were made available to this project. As mentioned previously, the wood type of the piles was chosen so that both pine and spruce species would be available. The wood type of each pile is indicated by letters "S" and "P" for spruce and pine respectively. The debarking method of each pile is indicated by letters "M" and "H" for mechanically debarked and debarking by hand respectively. The piles were debarked over their entire length. Debarking of piles has direct effect on the surface roughness of the pile shaft. This surface roughness ultimately may have effects on the shaft friction of the pile.

As shown in Table 3.1, the dimensions of the piles are more or less comparable to those included in the extracted piles data set. The average diameter is on the far end of the range of pile diameters used in the city. The resultant average tapering is 8 mm/m.

Aside from the volumetric and dimensional aspects of the piles, the elastic moduli are also specific to each pile. Ravenshorst (2019) states through personal communication that a series of tests were conducted on the tested piles in order to determine the dynamic elastic modulus of each pile. It has been proven that dynamic moduli of elasticity are higher than static E-moduli (Raymond et al., 2007). In a general sense, the static moduli amount to 92 to 95% of the values obtained for dynamic moduli (Ravenshorst, 2015). Raymond et al., 2007 illustrated through experiments that static stiffness of wood ranges between 89.1 to 89.9% of the dynamic E-moduli. The distribution and configuration of this measure of stiffness throughout the length of the piles are aspects that need further consideration. The values obtained from the dynamic tests are also illustrated in table 3.1. The acquired stiffness measures vary between 9 to 17 GPa and is 13.6 GPa on average.

Instrumentation

All piles aside from one, with ID number 183, are instrumented with BOTDA fiber optics. Pile 183 is instrumented with BOTDR instead. The specifications consist of aspects such as spatial resolution of 25 centimeters and a strain resolution of 10 $\mu m/m$. The sensors are capable of measuring the stress distribution over the pile as a function of distance and applied load.

3.2 Overview of Available Data

From the 16 instrumented piles loaded in compression, a total of 8 are analysed in this project. These piles are chosen as a result of data-assessment and based on their representativeness. For a complete overview of all tested piles, refer to Appendix D. A detailed overview alongside an assessment of the strain readings for each of the aforementioned 8 piles are included in this section. This is followed by an overview of preliminary results such as illustrations of reference measurements, strain readings throughout the load test and the difference between measuring channels.

3.2.1 Overview of Analysed Piles

As mentioned previously, within the test frame, the variation of wood type and installation depth are factors that must be analysed. Based on this, three categories of tested piles are defined.

- Category A: Spruce - 1 calendar
- Category B: Spruce - 2 calendars
- Category C: Pine - 2 calendars

Tables 3.2 shows an overview of the specifications of the analysed piles.

Table 3.2: Specifications of analysed piles

Pile ID	**Category**	**NAP Head[m]**	**NAP Tip[m]**	**D_{tip} [m]**
164	A	2.004	-12.296	0.137
175	A	1.683	-12.227	0.159
398	B	1.496	-12.324	0.143
397	B	2.283	-12.127	0.139
573	C	1.861	-12.439	0.158
592	C	1.395	-12.805	0.141
576	C	1.584	-12.536	0.131
594	C	1.515	-12.775	0.142

Aside from the geometrical attributes illustrated in Table 3.1, each pile has segmented measurements of its perimeter. The measurements were conducted at spatial resolutions of 0.5 to 1 meter. These measurements provide a much more accurate representation of the tapering of each pile.

3.2.2 Site-Investigation Data

As mentioned previously, the test site is ideal due to its lack of subsurface spatial variability. A total of 36 CPT tests were carried out which showed very little variability throughout the testing grounds. Figure 3.3 illustrates this condition while Figure 3.4 shows the representative soil profile and corresponding CPT of the test ground.

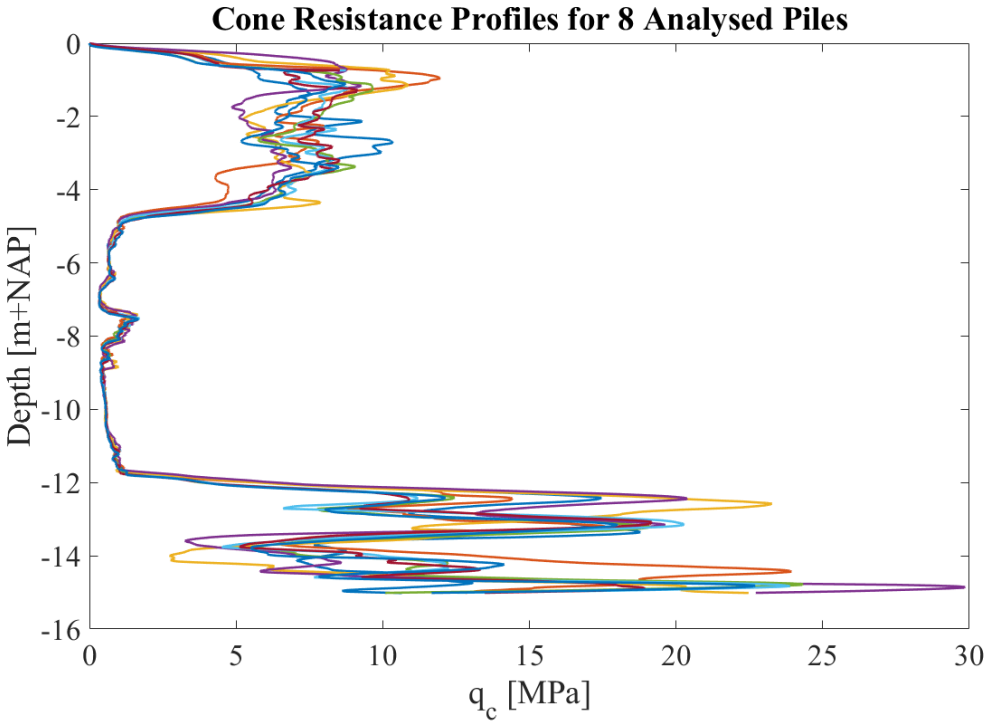

Figure 3.3: Cone resistance of all CPT profiles in Overamstel

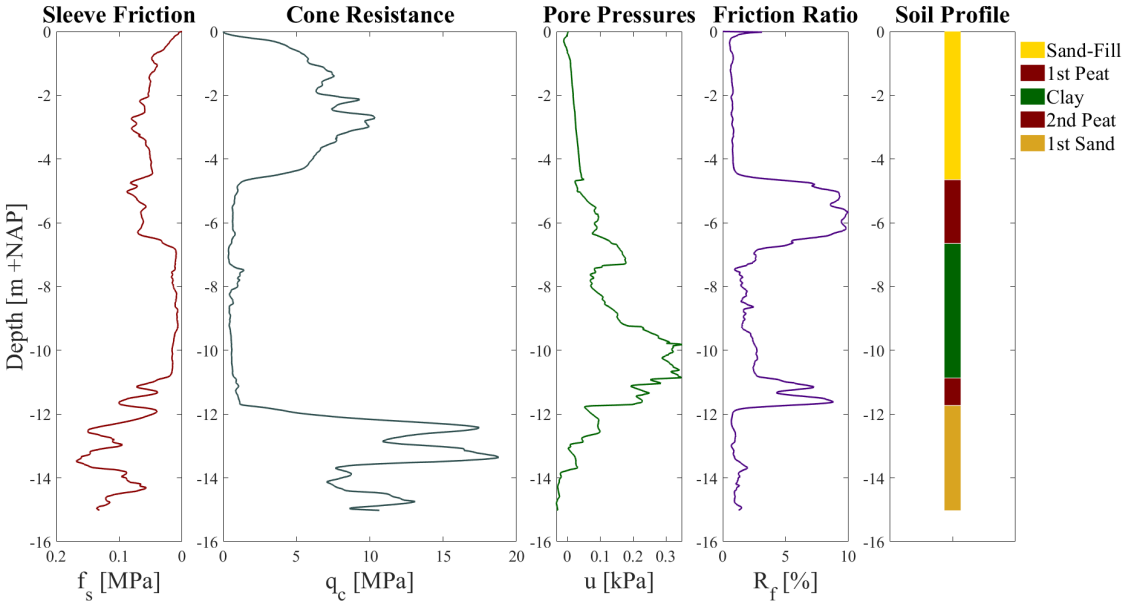

Figure 3.4: Representative soil profile and CPT of testing grounds

In addition to the cone penetration tests, a borehole sample was collected up to a depth of 19 meters below NAP. The average volumetric weights and undrained shear strength of the soft soil layers are generalized in table 3.3. Laboratory results do not include information for the bearing sand layer.

Table 3.3: Characteristics of soil layers, test site Overamstel

Soil Type	**Top of Layer [NAP]**	γ_{sat} $[kN/m^3]$	γ_d $[kN/m^3]$	$c_u[kPa]$
Holocene Peat	-4.8	10.1	2.1	38.6
Holocene Clay	-6.4	14.2	11.0	22.0
Pleistocene Peat	-11.5	10.8	2.9	49.0

It is important to note that the top sand-fill layer is pre-drilled before pile installation. This pre-drilling is significant as it disturbs the frictional properties of the sand layer. Appendices B and B.2 contain more information on the details of the present lithology. The soil properties alongside images of the sampled borehole are also included in Appendix B.

3.2.3 Strain Readings

As mentioned previously, the piles are instrumented in quadrants, meaning two loops of fibers are installed on 4 sides of each pile. There are 2 channels, labeled North-South and East-West. The fibers measure strains simultaneously and can therefore be averaged. The spatial resolution of each fiber is 25 centimeters. Considering the fact that strain is stiffness dependent, any variation of stiffness in the wood is taken into account at each measuring point. Since the fibers cover four sides of each pile, any sort of deformation due to installation, most significantly bending, would also be taken into account.

Since the two fibers are to be averaged, it is of great significance to have an idea of what the effective length of the fiber is. The effective length is indicative of the length to which the fiber is delivering valid readings symmetrically. This concept alongside the orientation of the fibers in cross-section form are illustrated in Figure 3.5.

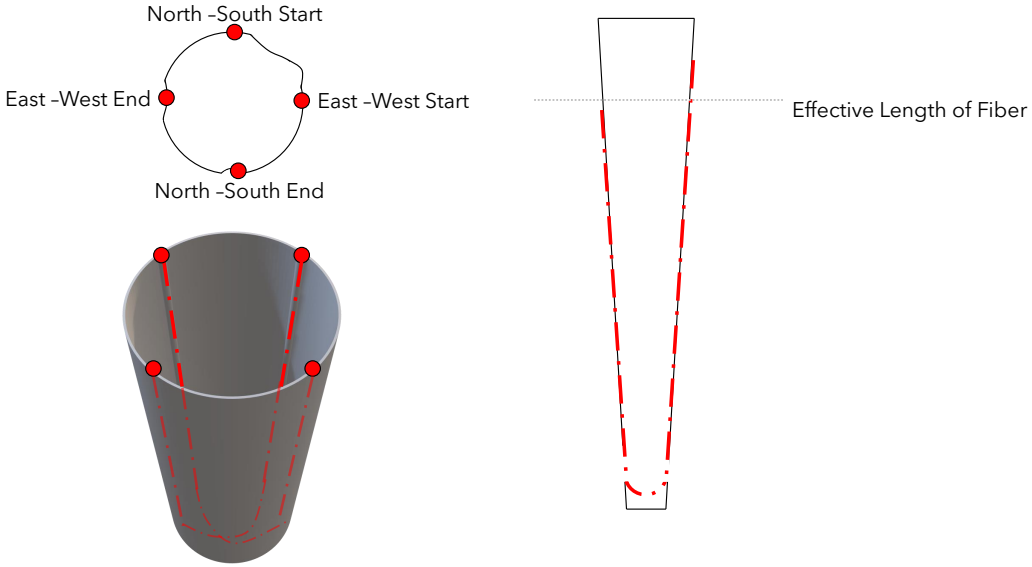

Figure 3.5: Fiber orientation and effective fiber length

As mentioned previously, before the load tests are conducted, a series of strain readings were conducted with the pile hanging from a crane and standing on a beam element measuring its weight. These measurements alongside the load test readings are discussed in the following sections.

Reference Measurements

A series of different reference measurements were conducted in order to gain more insight into potential residual loads. These measurements consist of glue-control, hanging, standing and after installation phases. Figure 3.6 illustrates the first three reference measurements. The glue-control measurement is conducted while the pile is laid on its side. This measurement is not carried out for all piles as it was mostly carried out to ensure the functionality of the fibers. The data obtained for glue-control is not significant to the analysis. The measurements conducted during hanging and standing are however significant as they are governed by the weight of the pile.

Another reference measurement is the readings taken after installation of each pile. These readings are inclusive of any phenomena that might have taken effect during installation. As defined previously, residual loads begin to develop once the installation force is removed from the pile. Therefore, it is important to take the readings from after pile installation into account when analyzing locked in strains before the load test. Before the start of the application of forces during the load tests, strains are measured. This measurement, labeled as "before testing" is also important as the recordings may show developments of locked-in strains through time. The time gap between pile installation and load testing may result in relaxation of the pile and settlement of the surface which in turn may cause alterations in existing strains for each pile.

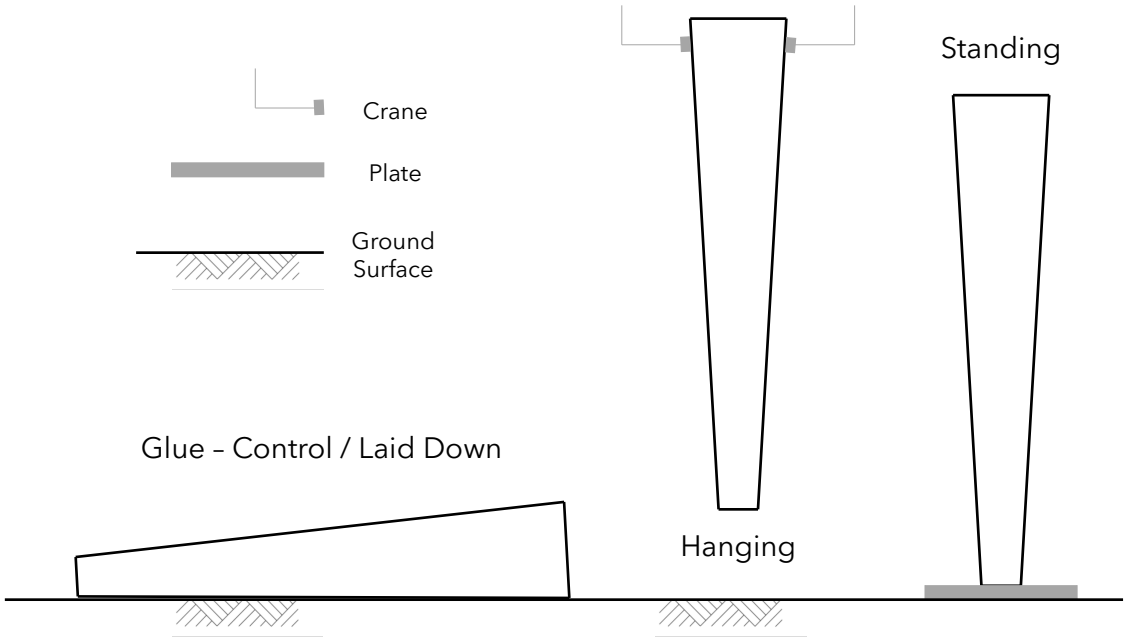

Figure 3.6: Illustration of reference measurements

Measurements During Load Test

Measurements during load tests are conducted through the N-S and E-W channels on an OmniSense Dual system with a spatial resolution of 25 centimeters and an accuracy of 10 micro-strain. The data is recorded for two simultaneous load tests on two separate piles. Therefore, a total of 4 readings are made at the same time per test. These measurements include the position of the measuring point, the time of the measurement and the recorded strain.

3.2.4 Load-Cell and LVDT Readings

A total of 2 LVDT sensors are installed on the pile head to record the displacement of the pile head. The sensors are installed parallel to the length axis of the pile in order to fully record the absolute displacement of the pile head. The accuracy of these sensors amounts to 0.01 mm. The displacement of the reference frame was also measured as part of the test but the data is not considered in this report. Figure 3.7 illustrates the used load-cell and LVDT sensors that are installed on the pile head. The utilized load has an accuracy of approximately 1 kN.

(a) Load-cell and LVDT's on pile head

(b) LVDT's on Reference Frame

Figure 3.7: Load-cell and LVDT sensors installed on pile head and reference frame
Courtesy of IB Gemeente Rotterdam, taken by Rodriaan Spruit (2019)

Further illustration on test site conditions and provided data are provided in Appendices B, D and E.

Chapter 4

Methodology

This chapter illustrates the methodology that forms the basis of calculations conducted during the analysis. The most significant steps taken to determine the end result are outlined here.

4.1 Assessment of Strain Readings and Load Cell Data

4.1.1 Determination of Pile Tip Location

In order to calculate the effective length of each fiber, the measuring position at the pile tip must be determined. Figure 3.5 illustrated that the length of the installed fiber may be longer one one side and that simply dividing the measurement points in two does not represent the pile tip. This determination is a manual process which involves checking the symmetry of the measurements. This is done through trial and error and visual inspection of the symmetry of strain readings with respect to measuring positions. This procedure must be carried out for both the reference measurements and the load test readings as the process of installation may damage fibers that need to be repaired. This procedure is crucial to the assessment of strain readings and is further discussed in section 5.1.1

4.1.2 Definition of Reference Point for Strain Readings

The raw data obtained through the OmniSense Dual system requires further analysis. Once the pile tip is determined and the symmetry of measurements with respect to the pile length axis is ensured, the strains can be averaged over the two sides of each fiber channel. Before this averaging, the strains are assessed to ensure no discontinuities are observed in the raw data. This assessment is discussed in section 5.1.

4.1.3 Definition of Reference Point for Load Cell and LVDT readings

All LVDT and load-cell measurements are zeroed out before the beginning of the test by the operators. This ensures the process of obtaining absolute measures of force applied and displacement of the pile head.

4.2 Determination of Residual Loads

As illustrated in section 2.5, locked-in strains can develop after the installation of a pile. The reference measurements introduced in section 3.2.3 are the key component to the determination of residual loads. In order to remove the effect of the buoyant weight of the pile on the distribution of strains, the reference measurements taken during hanging or standing can be subtracted from other strain readings. The effect of the installation procedure on the pile instead of locked-in strains is captured by measurements conducted after driving and before the start of a load test.

Negative strain is indicative of compression in the strain readings used in the analysis. It is important to note the significance of the behaviour of the pile above the pre-drilled sand layer. Due to the disturbance of the frictional properties of this layer, the measured strains after installation and before testing may be ambiguous. This ambiguity is due to the fact that the fibers are exposed to more external factors in this section of the pile. The correction of these strains for the cross-sectional area includes the effect of tapering and variation of pile dimensions.

Different scenarios for the definition of residual strains can be considered. Several scenarios as to how the locked-in strains must be considered were formed. The most significant aspects that were considered are the inclusion of installation effects and the removal of the buoyant weight of the pile. Equations 4.1 and 4.2 illustrate the two main scenarios considered in the analysis. In order to dismiss the effect of the buoyant weight of the pile, the hanging strains are subtracted from the locked-in strains in the pile. The difference between the after-installation strains and readings taken before the start of a load test is related to the occurrence of time dependent phenomena (refer to Appendix A.2.1) and potential surface settlements. Other influential factors to strain development consist of changes in temperature and moisture content. Therefore, both of the scenarios are analysed in order to determine the true residual load locked into the pile before the start of the load test. Each Scenario is evaluated and the resultant residual loads are discussed in section 5.3.

$$\varepsilon_{Res} = \varepsilon_{AD} - \varepsilon_{H} \tag{4.1}$$

$$\varepsilon_{Res} = \varepsilon_{BT} - \varepsilon_{H} \tag{4.2}$$

Table 4.1: Parameter description for equations 4.1 and 4.2

Parameter	Description	Unit
ε_{Res}	Residual strains	$[\mu e]$
ε_{AD}	Reference strains: After driving	$[\mu e]$
ε_{BT}	Reference strains: Before load test	$[\mu e]$
ε_{H}	Reference strains: Hanging	$[\mu e]$

4.3 Determination of Pile Stiffness

As mentioned in sections 2.2.4 and 2.2.3, several factors can affect the mechanical properties of wood. One of the most relevant properties of piles to a load distribution analysis is the modulus of elasticity or stiffness of the pile. Three means of acquiring a representative stiffness for all piles in this project are discussed in this section.

4.3.1 Dynamic Modulus of Elasticity

As mentioned in section 3.1.2, the dynamic moduli of elasticity were measured for all piles that are part the experimental framework. This data was obtained through the application of vibratory stress waves to the entire pile. As mentioned before, the values for stiffness obtained through dynamic tests are generally higher than static E-moduli. The obtained results from the conducted dynamic tests, alongside their static stiffness equivalents, are taken into consideration in the analysis. The dynamic E-Moduli of the analysed piles are shown in Appendix A.5, table A.4. The following equation illustrates the means of measuring this modulus, where ρ and v are the density of the pile and the velocity of the stress wave respectively.

$$MOE_{dyn} = \rho \cdot v^2 \tag{4.3}$$

4.3.2 Measurements on Pile Head

Considering the fact that the pile head is above ground surface, the static stiffness of the pile can be calculated using the strain readings. It can also be argued that due to the disturbance of the upper fill sand layer and its apparent lack of friction, strain readings in that section of the pile can also be used to derive the E-modulus. These readings were manually checked to ensure consistency. This process is simply carried out as shown in equations 4.4 and 4.5.

$$\sigma_N = \frac{F}{A} = E \cdot \varepsilon \tag{4.4}$$

$$E = \frac{F}{A \cdot \varepsilon} \tag{4.5}$$

The equations above hold for a linear-elastic model. In equation 4.5, the force F is the absolute load on the pile head recorded by the load cell. Therefore, if strains corrected for area are plotted against the force applied on the pile tip during loading stages, the slope of the fit through 0 would indicate the E-modulus of the pile head. An example of this process is illustrated in Figure 4.1. It is important to note that the illustrated linear fit is based on the concept of having a constant load applied on the pile head. If the loading and unloading of the pile are to be considered, non-linear behaviour may be observed. Figure 4.2 illustrates the entirety of the loading process for the same set of data illustrated in Figure 4.1. As can be seen, in such cases, it is more appropriate to utilize a quadratic fit to relate the absolute top load to the corresponding strain readings.

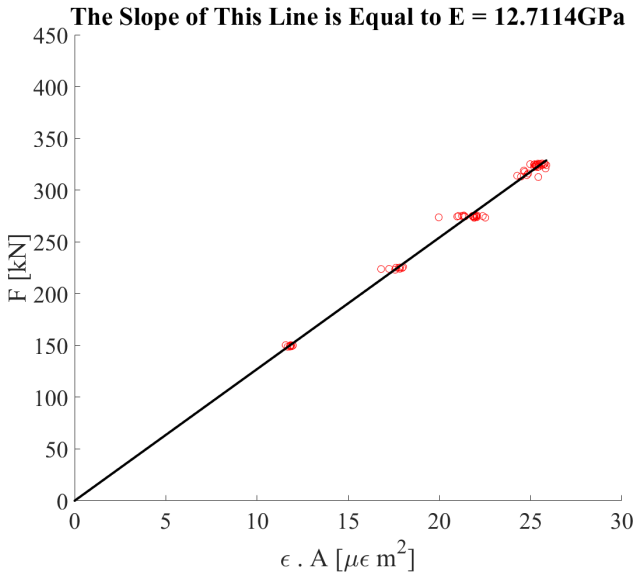

Figure 4.1: Example of E-modulus as a fit slope

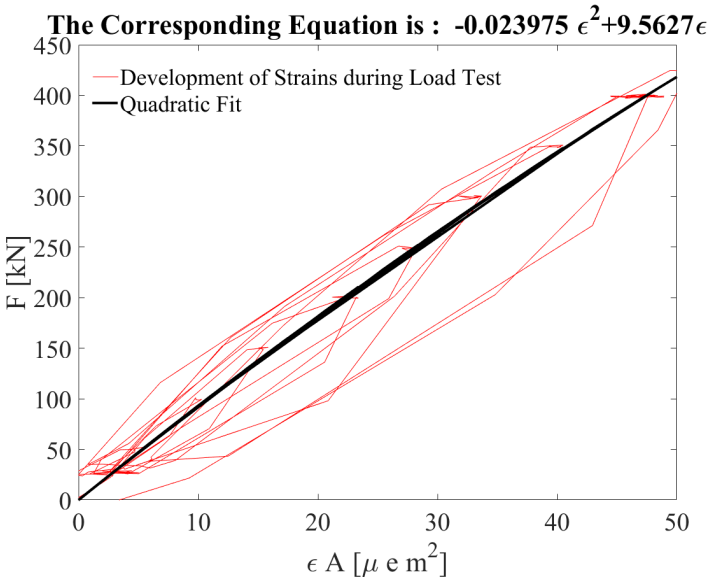

Figure 4.2: Example of correlation between load and strain as a quadratic fit

By using a quadratic fit as the correlation between strains and forces, the effect of non-linearity of strain developments is taken into account. Equation 4.6 illustrates the means to calculated loads given a quadratic correlation of the form $y = ax^2 + bx + c$. Considering the assumption of a zero state for both load and strains, the remainder of the fit equation, i.e. c, amounts to zero.

$$F = a(\varepsilon \cdot A)^2 + b(\varepsilon \cdot A) \tag{4.6}$$

Other methods of determining the E-modulus of piles are further discussed in Appendix A.5. These methods were discarded for several reasons, which is further explained in the appendix.

4.4 Determination of Loads

The conversion of discrete strain readings to a continuous distribution of stress requires a number of steps to be taken. These steps and the mathematical fundamentals behind them are discussed in this section.

4.4.1 Pile Geometry

Variations in cross-sectional and circumferential areas along the length of the pile are defining factors in the determination of loads. The geometry of the analysed piles are complex and variable due to the biological nature of wood. As mentioned in section 3.2.1, each pile has segmented measurements of its perimeter at a spatial resolution of 0.5 or 1 meter. Therefore the circumference of the pile can be interpolated between each measured point. Since the spatial resolution of the fiber readings amounts to 0.25 meters, for each measuring point on the fiber, a diameter can be assigned based on the interpolated perimeter data.

4.4.2 Conversion of Strains to Forces

As illustrated in section 2.3, discrete strain readings can be converted to loads using the governing mechanical equations. It must be noted that a discrete, or nodal, measurement is the average of recordings over a certain spatial frequency. Figure 4.3 illustrates a visualization of a pile, segmented into nodes of measurement. The pile is discretized in n segments, each 0.25 meters long parallel to the length axis of the pile. At each upper and lower boundary of a segment, a recording of strain and diameter is available. Therefore there are $n + 1$ nodes at which measurements are taken. Given this, and the modulus of elasticity, the normal forces in the pile can be calculated as illustrated in equation 4.7, where ε_i and D_i are strain and diameter at a given node respectively.

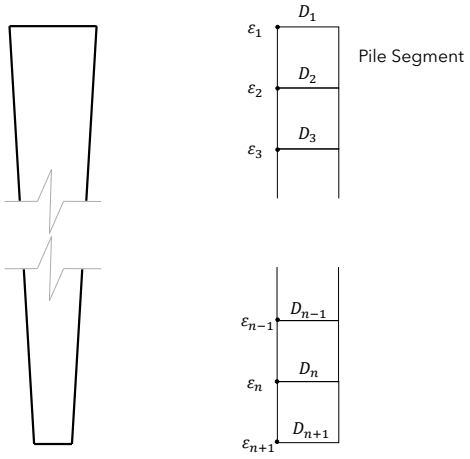

Figure 4.3: Discritization of a pile into nodes

$$F_i = EA_i\varepsilon_i = 0.25E\pi {D_i}^2\varepsilon_i \quad : i = [1, n+1] \tag{4.7}$$

4.4.3 Shear Forces

Since the force at each measuring node is determined through equation 4.7, the shear force along each segment can be calculated. This calculation is illustrated in equation 4.8, where τ_i is the shear force across L_j, the length of the segment. This length is constant, as the spatial resolution of the fibers is always 25 centimeters.

$$\tau_j = \frac{F_i - F_{i+1}}{L_j O_j} = \frac{F_i - F_{i+1}}{L_j \pi \frac{D_i + D_{i+1}}{2}} \quad : i = [1, n+1] \,\&\, j = [1, n] \tag{4.8}$$

4.4.4 Compression and Base Displacement

Given the average strain of each segment, the change in length for each segment can be determined. The multiplication of the strain of each segment with its length results in the change in length under load. Equations 4.9 and 4.10 illustrate the calculation of compression for each segment.

$$\varepsilon_j = \frac{\Delta L_j}{L_j} = \frac{\varepsilon_i + \varepsilon_{i+1}}{2} \quad : i = [1, n+1] \,\&\, j = [1, n] \tag{4.9}$$

$$\Delta L_j = \varepsilon_j L_j \quad : j = [1, n] \tag{4.10}$$

As mentioned before, the head displacement of the pile, $u_H[m]$ is recorded by LVDT displacement sensors. Subtraction of the total change in length from head displacement results in the pile base displacement. It is important to note that this can only be applied to segments of the pile to which the fiber is connected. The deformation of the segments without sensors is not considered.

$$u_b = u_H - \Sigma \Delta L_j \quad : j = [1, n] \tag{4.11}$$

4.5 Correlation with CPT Profiles

4.5.1 Definition of Soil Layers

As illustrated in Figure 3.4, the soil unit at the test site consists of an alternation of peat, clay and sandy soils. Based on the CPT data, the soil system is divided into separate layers. This division is based on values recorded for cone resistance and sleeve friction. The criteria for defining the separate soil layers is illustrated in Table 4.2.

Table 4.2: CPT criteria for layer definition
Modified from Robertson, 2016 and adapted to CPT conducted in Overamstel in accordance to the borehole data.

Soil Type	q_c **[MPa]**	f_s **[MPa]**
Peat	less than 1.71	more than 0.03
Clay	less than 1.71	less than 0.03
Sand	more than 1.71	N/A

It is important to note that this criterion is only applicable and specific to this project. This method is further discussed in section 5.6. The average cone resistance for the base capacity of each pile is must also be determined. The three averaging methods mentioned in section 2.4.1 are used in this analysis to determine $q_{c,avg}$.

4.5.2 Determination of Alpha Factors

As illustrated in section 2.4, equation 2.11, the correction factors α_s and α_p are units that correlate CPT readings and a pile's geometry to its bearing capacity. The first step to determine the α factors, is to calculate the base and shaft resistance of the pile based on strain readings. Equations 4.12 to 4.14 illustrate the steps taken to determine both alpha factors. In order to determine the base capacity, the measured force at the pile tip, i.e. node $n+1$, is considered upon a base displacement of 0.1D. The distance between this measuring node and the pile tip is approximately 3 centimeters.

$$Q_{b,0.1D} = F_{n+1,0.1D} = EA\varepsilon_{n+1,0.1D} \tag{4.12}$$

For the determination of shaft capacity, the procedure takes place per defined soil unit. Since each soil unit has specific frictional characteristics, separate α_s factors must be derived for each of them. Equation 4.13 illustrates this procedure where k is the index at which a soil layer begins and l is representative of the point where that soil layer ends.

$$Q_{s,0.1D} = \frac{F_{k,0.1D} - F_{l,0.1D}}{(l-k)L_j\pi\frac{D_k+D_l}{2}} \tag{4.13}$$

Once the base and shaft capacity are determined based on strain readings, the alpha factors can be determined as illustrated in equations 4.14 Separate α_s factors can be derived for each soil unit of length L and average cone resistance of q_c.

$$\alpha_p = \frac{Q_{b,0.1D}}{q_{c,avg}A} \quad \& \quad \alpha_s = \frac{Q_{s,0.1D}}{q_c\pi DL} \tag{4.14}$$

Chapter 5

Analysis

This chapter illustrates the results obtained through the computational procedure outlined in Chapter 4. In order to elaborate on the means of analysis in a representative manner, the results for three piles, one from each category, are illustrated and discussed. These three piles are identified with ID numbers 164, 398 and 573. Illustration of results for all other piles are shown in Appendix C. Furthermore, a simple statistical analysis is conducted to provide more insight into the variation of results.

5.1 Fiber Assessment and Pile Geometry

5.1.1 Determination of Pile Tip

The first step to this analysis is the determination of the measuring node corresponding to the pile tip. As illustrated in section 3.2.3, Figure 3.5, the fiber can measure over a larger length on one side of the pile compared to the other. Therefore, dividing the fiber length in two and assuming symmetry is not appropriate. The determination of the pile tip is a manual procedure that is required for each fiber on each pile. Figure 5.1 illustrates an example of readings from the North-South fiber on pile 164.

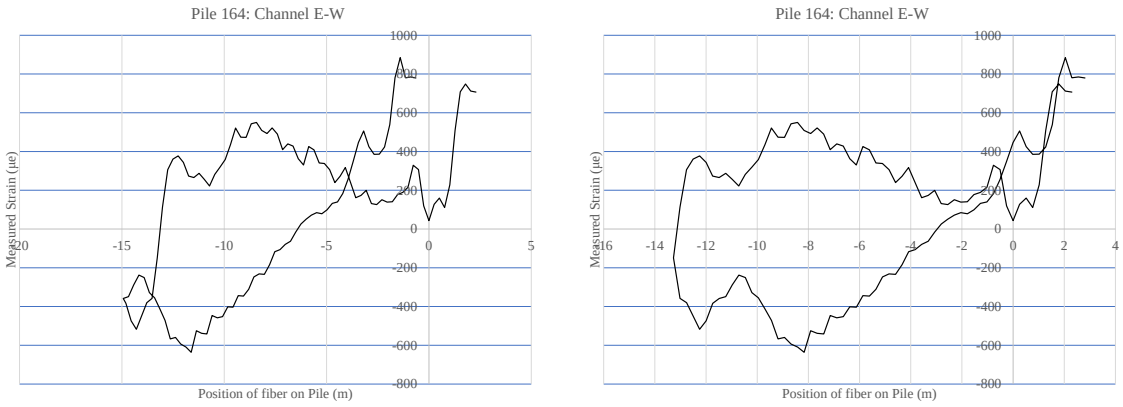

(a) Tip level chosen as half of fiber length

(b) Tip level determined correctly

Figure 5.1: Evaluation of measurement node corresponding to pile tip

The tip level is considered as the halfway node along the entire fiber in Figure 5.1a. On the other hand, Figure 5.1b illustrates the strain distribution when the correct tip level is determined. This process ensures the symmetry of the measurements over each side of the pile. This node is determined through trial and error and wiggle-matching.

Once the location of the pile tip is determined, readings from each side of the pile can be averaged to obtain a singular profile of strain readings for each fiber. This is followed by averaging the two fibers resulting in a unique strain distribution along the length of the pile. As mentioned in section 3.1.1, the fibers N-S and E-W loop at 2 and 4 centimeters above the pile tip respectively. This difference in positioning is insignificant due to the spatial resolution of strain recordings (25 centimeters) and the large length of the piles.

5.1.2 Assessment of Fiber Readings

Once the measuring node at the pile tip is determined, the strain readings during the load test are assessed with regard to symmetry. The readings are also assessed with regard to data quality. Figure 5.2 illustrates the readings from both N-S and E-W fibers on piles 164 and 573.

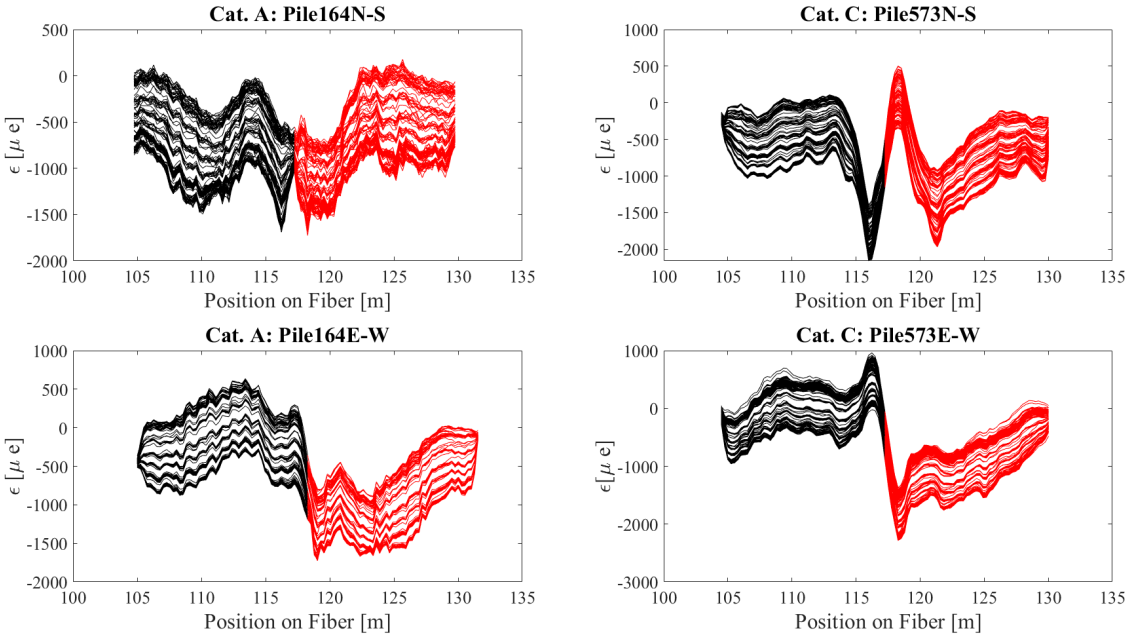

Figure 5.2: Raw strains recorded during load tests on piles 164 and 573

The measuring position corresponding to the pile tip is located in between the readings illustrated in red and black colors. As illustrated, for several fibers, the direction of measurement on one side of the pile differs from the opposing side. This results in readings of opposite sign and should therefore be avoided. Zeroing out all readings by subtracting the first reading in time eliminates the effect of measuring direction. The resultant readings are symmetric strain measurements along the length axis of the pile. The process of zeroing all readings results in dismissal of locked-in strains. Figure 5.3 illustrates the result of referencing all readings to a zero state.

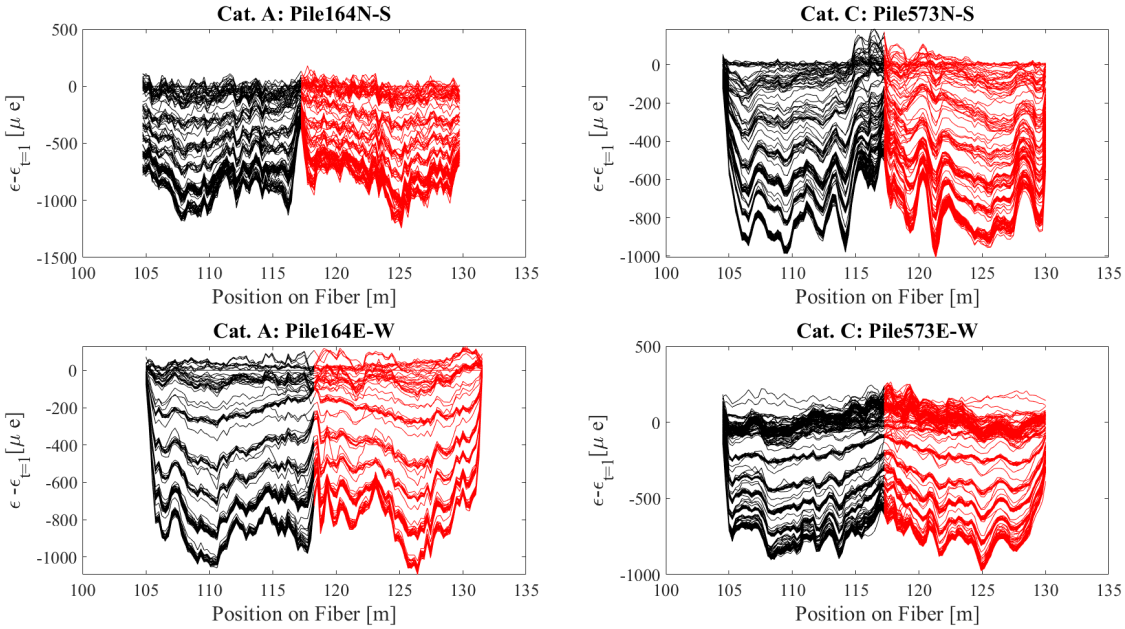

Figure 5.3: Referenced strains recorded during load tests on piles 164 and 573

All analysed piles, aside from pile 398, are assessed using an average of both the N-S and E-W channels. Pile 398 is assessed using only the N-S fiber as the E-W fiber on this pile was damaged due to the pile tip splitting (Spruit, 2020). Other instrumented piles are also assessed with regards to the delivered data. This assessment is summarised in Appendix D, Figure D.3.

Table 5.1 illustrates the assessment of each fiber channel for each pile. The starting point indicates the location at which the first valid measurement is taken. In other words, the starting point is the beginning of the effective length of the fiber (L_{fiber}). The total effective length of measurements is therefore the smallest fiber length between the two channels. The strains are averaged over this length to provide a singular distribution of strain over the length of the pile. The raw readings and the referenced readings for other piles are illustrated in Appendix C.2. All depths and locations are with respect to NAP. A more detailed assessment of the fibers is illustrated in Appendix D, Figure D.4.

Table 5.1: Assessment of fiber channels

Pile		**Surface Level**	**FIBER N-S**		**FIBER E-W**	
ID	Category	$+mNAP$	$L_{fiber}[m]$	Start $[m+NAP]$	$L_{fiber}[m]$	Start $[m+NAP]$
164	A	0.04	12.506	0.21	13.018	0.722
175	A	0.015	12.762	0.535	11.996	-0.231
398	B	0.035	12.762	0.438	N/A	N/A
397	B	0.03	13.017	0.89	13.017	0.89
573	C	0.02	12.762	0.323	12.762	0.323
592	C	0.015	13.272	0.467	13.018	0.213
573	C	0.02	12.507	-0.029	12.507	-0.029
594	C	0.005	12.762	-0.013	13.018	0.243

5.1.3 Discretization of Pile Geometry

The circumference of each pile was measured at every meter of length. Some piles include measurements of their perimeter for every 50 centimeters. Interpolation of geometry between these measurements results in a continuous profile of the pile diameter. Figure 5.4 illustrates the measured diameter alongside the interpolated diameter profile for piles 164, 398 and 573.

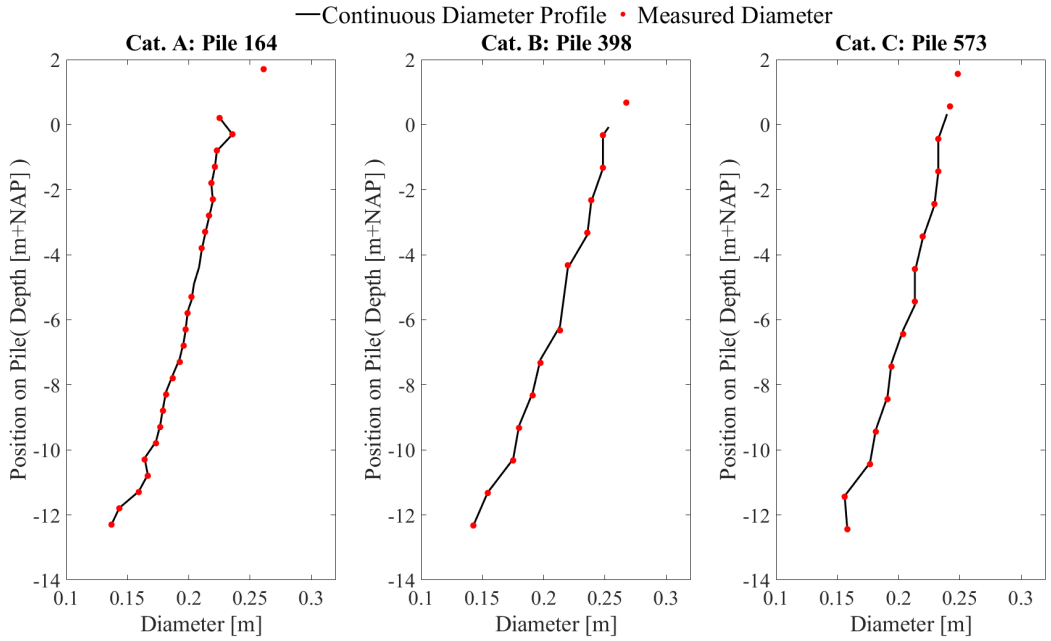

Figure 5.4: Continuous diameter profile of piles 164, 398 and 573

As can be seen, tapering of the piles is not constant along the length of the pile. The illustrated profile covers the effective measuring length of the pile. This variation in diameter, and therefore cross-section, contributes to variation of load distribution in the pile. It is important to note that the slope of a fit through the illustrated data gives an indication of the rate of decrease in diameter.

5.2 Consideration of Pile Stiffness

Section 4.3 elaborated on the different approaches to evaluate the stiffness for each tested pile. The dynamic E-moduli measured before the installation of piles is used as a reference point for the derivation of static stiffness. As mentioned before, the pile head is always above the surface level and in contact with the load cell. Additionally, the first four meters of the subsurface consists of pre-drilled soil. Therefore, this layer has unknown frictional properties due to the disturbance caused by pre-drilling. Consideration of developed strains in these sections of the pile as a result of the applied load enables one to derive a static modulus of elasticity.

In theory, the absence of load entails the absence of strain. Therefore, it can be concluded that the relationship between the applied load and measured strains is best described by considering a relationship fitted through zero and the readings excluding residual strains. This relationship is illustrated as a linear fit in Figure 5.5. The scattered data are strain readings corrected for area only during a load-step with a constant load. The relationship between values derived through this method and the dynamic E-moduli is illustrated in Appendix A.5, Figure A.14.

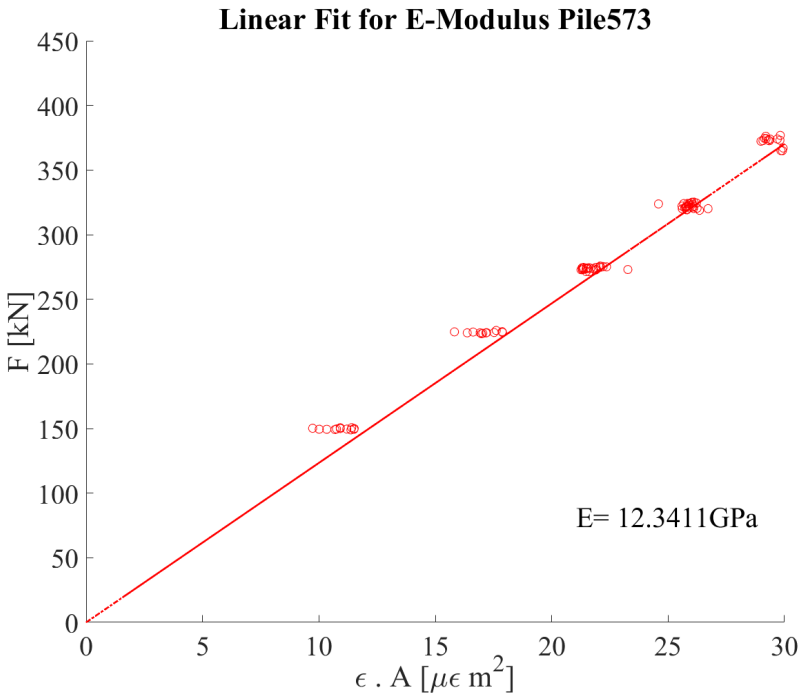

Figure 5.5: Linear fit for determination of E-Modulus: Pile 573

However upon further inspection, it is noticeable that the extent of linearity for strain development during the load-test decreases as the load increases. Figure 5.6 illustrates the hysteretic behaviour of the pile head subjected to loading. As shown in Figure 5.6, the relationship is not as linear as previously illustrated. As discussed in section 4.3.2, a quadratic relationship can be determined between the applied load and strains corrected for area. Fitting a quadratic fit through the non-linear development of strains results in a more accurate correlation of strains and loads.

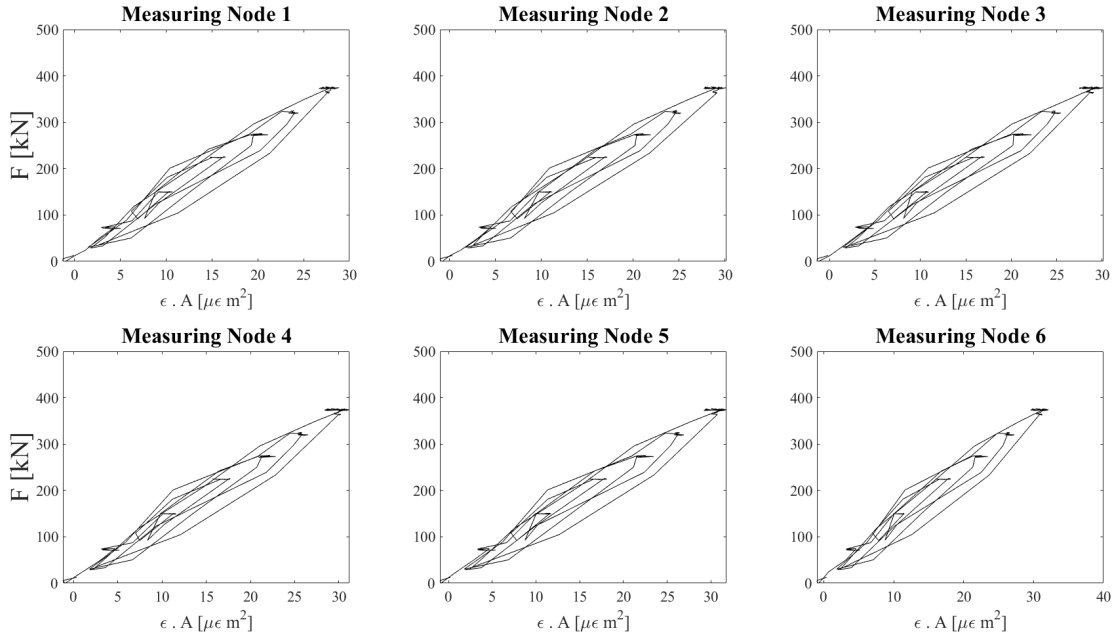

Figure 5.6: Hysteretic and non-linear behaviour of pile head subjected to load: Pile 573

The comparison between the linear and quadratic fits is illustrated in Figure 5.7. As can be seen, the quadratic fit covers the loading stages much more accurately than the linear fit, especially at lower loads. Therefore, relating strains to loads through fitted quadratic relationships is more favourable.

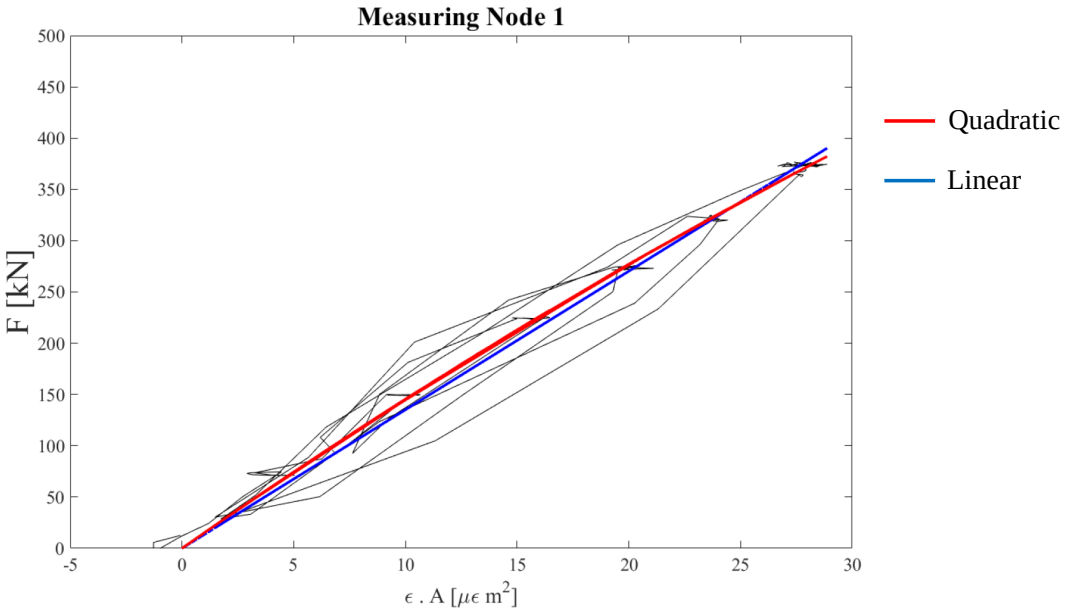

Figure 5.7: Comparison of quadratic and linear fit: Pile 573

The quadratic relationships obtained as discussed above are purely based on the first 5 measuring nodes at the pile head. Considering the fact that variability in stiffness through the length of the pile might be a highly influential factor, perhaps it is better to have a

more transparent approach to the consideration of stiffness. Considering the uncertainty regarding variation of stiffness through the length of each pile, the approach to utilize the quadratic fit relationships can be simplified. The coefficients used to convert strains to loads, namely a and b in equation 4.6, can be averaged for each wood type. Equations 5.1 and 5.2 illustrate the relationships used to derive loads based on strain readings for the spruce and pine samples respectively. It is important to note that both categories A and B utilize equation 5.1.

$$F_{A,B} = -0.0432 \cdot \varepsilon^2 \cdot A^2 + 11.11 \cdot \varepsilon \cdot A \tag{5.1}$$

$$F_C = -0.0328 \cdot \varepsilon^2 \cdot A^2 + 13.92 \cdot \varepsilon \cdot A \tag{5.2}$$

The variability of stiffness through the length of the pile can be roughly observed through the Fellenius method of stiffness determination. This is illustrated in Appendix A.5. The importance and effect of this potential variability is further discussed in section 6.2.1. Results obtained for other methods of stiffness determination are also illustrated in Appendix A.5. The quadratic relationships obtained for each pile are illustrated in Appendix C.3.

5.3 Residual Load Profiles

As defined in section 4.2, two different scenarios for the analysis of residual loads are defined. Figure 5.8 illustrates these scenarios for piles 164, 398 and 573. In this figure ε_{AD}, ε_{BT} and ε_{H} are representative of strain measurements recorded after installation, before load testing and during hanging respectively.

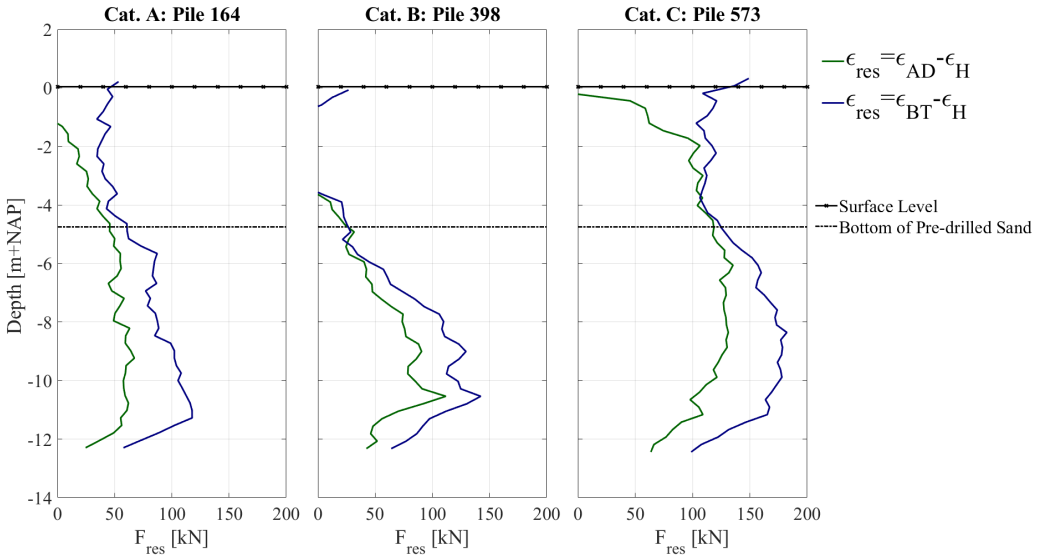

Figure 5.8: Residual load profiles for piles 164, 398 and 573

It can be seen that the locked-in loads have increased through time as a consequence of additional strain development. The additional strains can occur due to a number of reasons. Factors such as changes in moisture content or temperature can potentially contribute to this development. However, it is impossible to pinpoint the mechanism that results in this behaviour.

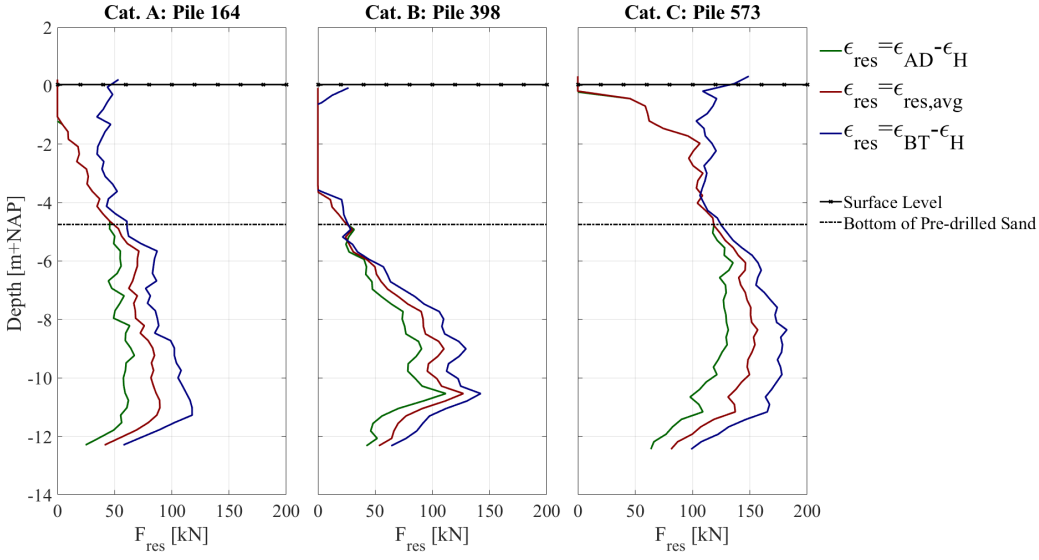

Figure 5.9: Residual load Profiles including interpolated residuals

The recordings before the test indicate higher strains near the pile head. The concept of residual loads is not applicable to the pile head above the surface. This concept is also not physically accurate for the section of the pile in the sand fill as pre-drilling disturbs the soil-structure interface. Upon inspection of residual load for all piles, it was discovered that the readings after installation have extreme fluctuations at times (Appendix C.4).

Since the exact cause of additional strain developments from the "AD" to the "BT" stage cannot be fully explained, choosing the readings before testing as residual strains adds uncertainty to the analysis. In order to dismiss the effect of high strains at the pile head and to balance the distribution of strains between the "AD" and "BT" stages, an averaging algorithm is developed to create a representative estimation of locked-in strains. This algorithm is based on engineering judgement and aims to negate uncertainties and to be inclusive of installation effects. Figure 5.9 illustrates the resultant residual loads determined through this averaging algorithm. The strains and corresponding loads obtained through this method are added to all readings during the load test as residual loads.

5.4 Load-Displacement Profiles

The response of the piles to the applied load in the form of displacements is illustrated in Figures 5.10 to 5.12. These graphs illustrate the applied load on the pile head (F_H) and the corresponding head displacement (u_H) as a function of time. Alongside this, the response of the pile base in terms of loads (F_{b_0} and $F_{b_{res}}$) and displacements (u_b) are also illustrated. Addition of residual loads as a constant entity, increases the base response in terms of load by approximately 40, 46 and 77 kN for piles 164, 398 and 573 respectively. The displacement of the pile base is independent of residual loads.

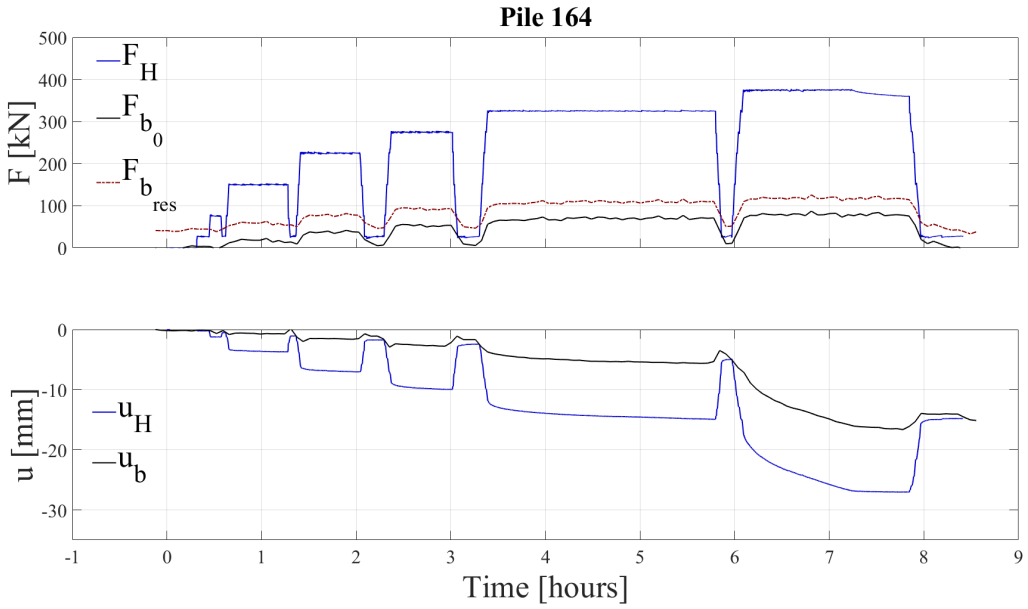

Figure 5.10: Pile response to loading, pile category A: 164

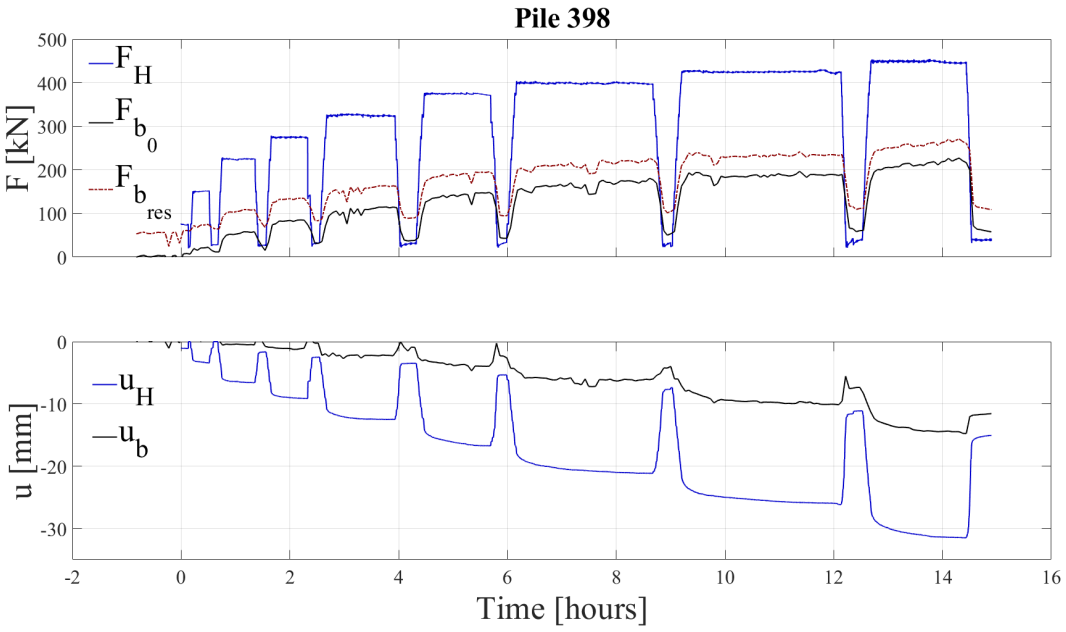

Figure 5.11: Pile response to loading, pile category B: 398

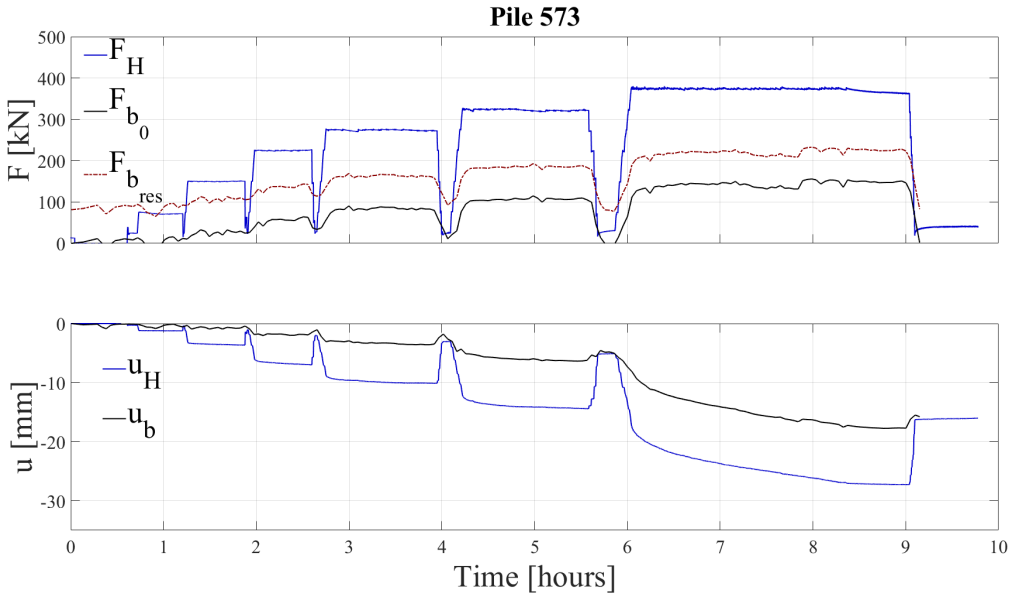

Figure 5.12: Pile response to loading, pile category C: 573

It is important to note that the data recorded by the load cell has a much higher time frequency than the strain readings. This difference in frequency results in slight misalignment of corresponding loads and displacements. This also results in fewer readings during unloading stages. Figure 5.13 illustrates the load displacement curves excluding the unloading and reloading steps for all piles.

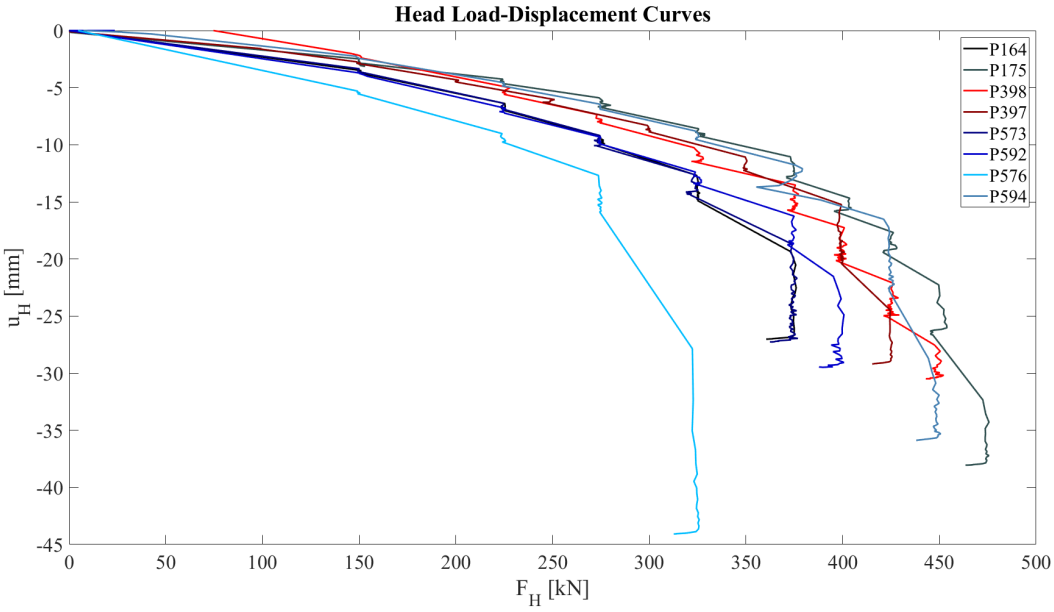

Figure 5.13: Load displacement curves all piles

Figure 5.13 illustrates how similarly piles 573 and 592 behave. Bot of these piles are from category C. The behaviour of pile 576 is incomparable to the other piles. This is due to the fact that it has the smallest diameter both at the base and the head of the pile. The

two piles from category A also behave similarly. The maximum displacement of each pile and the corresponding loads are illustrated in table 5.2. The maximum displacement is not pre-determined and is purely derived from the results obtained through the analysis.

Table 5.2: Loads and displacement at maximum base displacement

Pile		$u_{H,max}$	$u_{b,max}$	F_H	F_{b_0}	$F_{b_{res}}$	Tip Level	Depth in Sand
ID	**Category**	[mm]	[mm]	[kN]	[kN]	[kN]	[m NAP]	[m]
164	A	27.0	16.6	361	78	117	-12.3	0.6
175	A	38.0	27.2	465	160	192	-12.2	0.5
398	B	30.5	14.7	443	217	261	-12.3	0.6
397	B	29.2	19.2	416	99	162	-12.1	0.4
573	C	27.2	17.7	365	147	224	-12.5	0.6
592	C	29.3	17.9	392	131	218	-12.7	0.9
576	C	44.1	34.7	314	77	133	-12.6	0.7
594	C	35.9	25.7	438	127	194	-12.8	0.9

A base displacement of 0.1D is a pivotal point in this analysis as it is assumed to define the ultimate state from which bearing capacities can be determined. The displacements and corresponding loads at this point are illustrated in table 5.3.

Table 5.3: Loads and displacement at 0.1D base displacement

Pile		$\mathbf{D_{tip}}$	u_H	$u_{b_{0.1D}}$	F_H	F_{b_0}	$F_{b_{res}}$	Tip Level
ID	**Category**	[mm]	[mm]	[mm]	[kN]	[kN]	[kN]	[m NAP]
164	A	137	24.4	13.6	373	76	115	-12.3
175	A	159	26.2	15.9	451	162	195	-12.2
398	B	143	30.0	14.3	448	212	256	-12.3
397	B	139	24.5	14.6	424	91	154	-12.1
573	C	158	25.4	15.8	373	139	217	-12.5
592	C	141	26.5	14.4	399	157	243	-12.7
576	C	131	27.9	18.1	322	77	132	-12.5
594	C	142	28.7	18.7	444	124	190	-12.8

The high values for pile 398 may be due to the lack of compensation for bending effects, as only a single loop of fibers is used, i.e. the North-South channel. Perhaps data from the East-West channel will balance out the recordings at the pile tip once averaged with the high recordings of the N-S fiber. Figure 5.14 illustrates the base displacement versus the corresponding base resistance for all piles. The difference between ultimate capacity and the capacity defined by a base displacement of 0.1D is clear in this illustration. Upon comparing the loads and displacements illustrated in Tables 5.2 and 5.3 an estimate of the remaining capacity can be made. This comparison, alongside the asymptotic behaviour of the pile base shown in Figure 5.14, results in remaining capacities between 2 to 25 kN. The maximum value of this measure amounts to approximately 15%, which can be dismissed as most piles do not have much remaining capacity after reaching a base displacement of 0.1D.

The illustrated loads and displacements are used to determine the bearing capacity of each pile. However, before the immediate correlation of loads with CPT profiles, a more detailed analysis of the load distribution in each pile is necessary. The following sections illustrate the load distribution and the determination of alpha factors. The load displacement profiles of all piles are included in Appendix C.5.

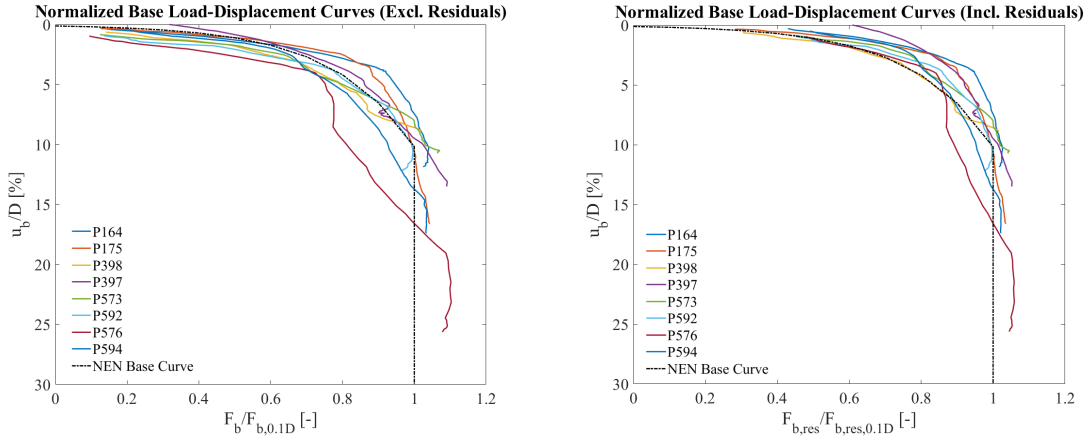

(a) Normalized Base Load-Displacement Curves (excl. Residuals)

(b) Normalized Base Load-Displacement Curves (incl. Residuals)

Figure 5.14: Normalized Base-Load Displacement Curves

5.5 Resultant Load Distributions

The distribution of load along the length of the pile defines the behaviour of the pile per soil layer. Figures 5.15 to 5.17 illustrate the load distribution per load step for piles 164, 398 and 573.

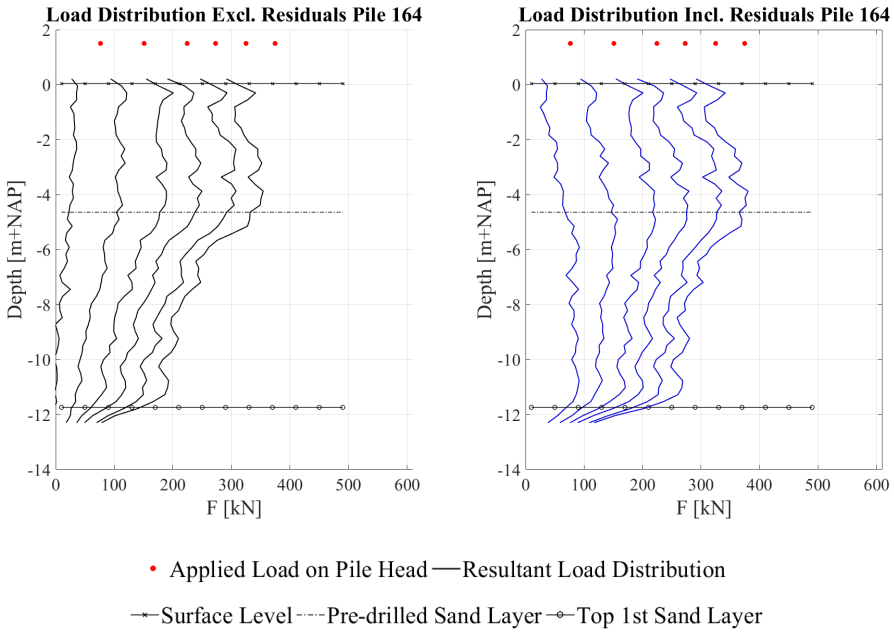

Figure 5.15: Resultant load distributions-Category B: Pile 164

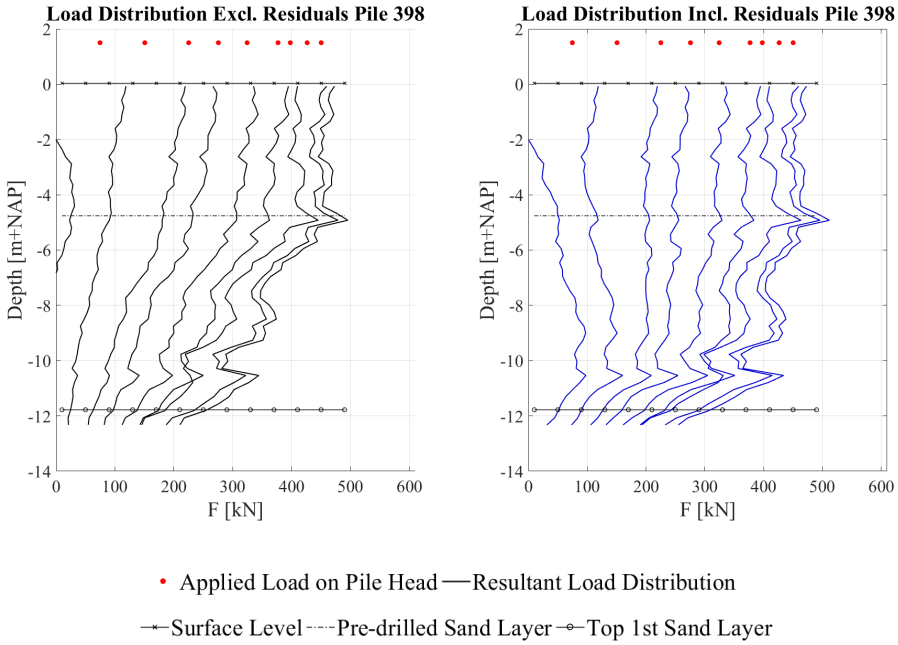

Figure 5.16: Resultant load distributions-Category B: Pile 398

As can be seen, the inclusion of residual loads increases both the base force and the shear forces near the pile tip. The top sand fill layer is indicated as the apparent loads in this layer are often not representative of real load distributions, due to the pre-drilling of the layer.

The fluctuations near the -10 meter mark in Figure 5.16 can be due to several reasons. The measured perimeter near this section of pile 398 seems to be increasing as illustrated in Figure 5.4. However, since the perimeter of the pile was only measured at a spatial frequency of 1 meter, no exact justification can be made based on the pile geometry. It can be suggested that at this specific section of the pile, a large branch may have existed, increasing its local stiffness, which is not currently taken into account.

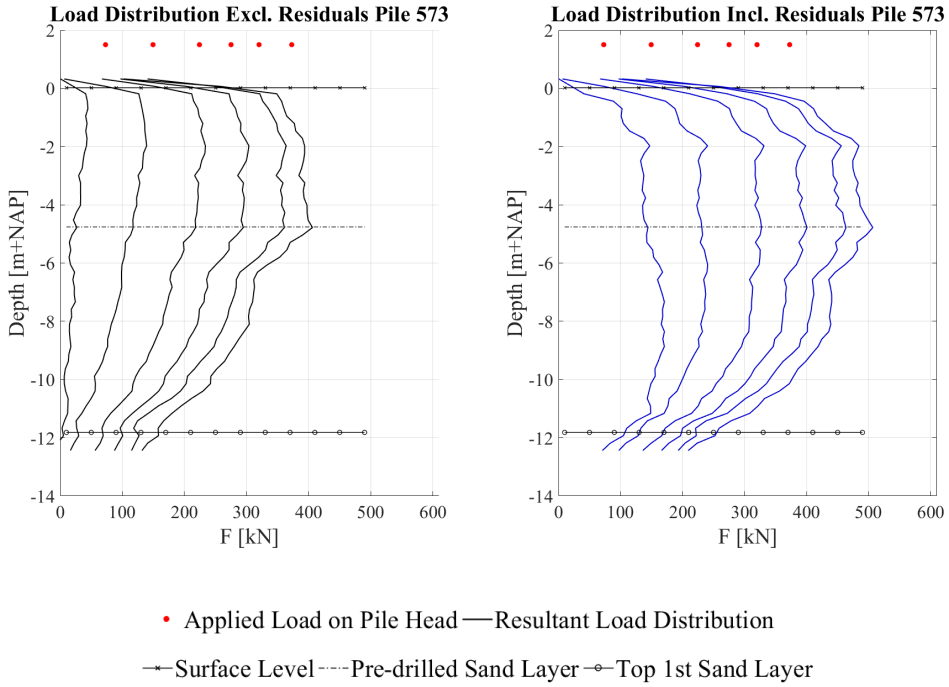

Figure 5.17: Resultant load distributions-Category C: Pile 573

Overall, the observed fluctuations in strain readings, and the corresponding load profiles, are due to several reasons. The natural variation of the specimen as well as the ambiguity of true stiffness are contributing factors.

The addition of residual loads generally results in a highly evident increase of loads between the -6 and -11 meter mark which are representative of the clay layer and the peat lens above the bearing sand. Based on the results illustrated in this section and section 5.4, the piles can be correlated with the surrounding soil body in a detailed manner. The load distributions of all piles are illustrated in Appendix C.6. The correlation of the observed pile behaviour and the CPT profiles are discussed in the following section.

5.6 Evaluation of Alpha Factors

This section focuses on the derivation of alpha factors introduced in section 2.4. These factors are obtained through correlating the load distribution to the cone resistance along the length of the pile. As previously mentioned, each pile has 3 CPT profiles which are averaged. The factor α_p is acquired using three different cone resistance averaging methods. The correlation factor α_s is a result of correlation of shear forces across the length of each soil layer with the corresponding averaged cone resistance. The following sub-sections illustrate the means of obtaining such factors and the results.

5.6.1 Alpha-p

As mentioned in section 2.4, there are several averaging techniques for determining the average cone resistance for base capacity calculations. This project uses the method of Koppejan, the LCPC method and the method of de Boorder to obtain $q_{c,avg}$. Figure 5.18 illustrates the load distribution along the length of pile 164 at a base displacement of 0.1D. The load profiles are based on strains measured during the load test and a profile including the effect of residual loads. In addition to this, the cone resistance of the surrounding soil is presented. The averaged cone resistance obtained through each averaging method is illustrated at the base level of the pile.

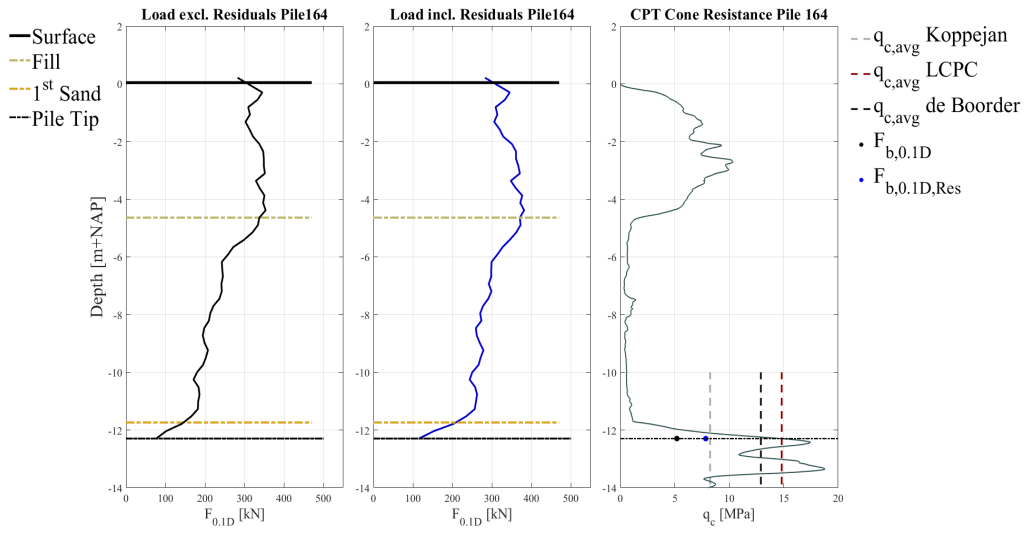

Figure 5.18: Determination of Alpha-p factor-Category A: Pile 164

Equation 5.3 illustrates the means to obtain the α_p from the results illustrated in Figure 5.18. The same process is applied to all analysed piles. The illustrations of the load profiles corresponding to 0.1D of base displacement are shown in Appendix C.7, alongside the cone resistance of the surrounding soil. Table 5.4 outlines the factors derived per method.

$$\alpha_p = \frac{Q_b}{q_{c,avg} \cdot A_b} = \frac{F_{b,0.1D}}{q_{c,avg} \cdot A_b} \tag{5.3}$$

Table 5.4: Derived α_p factors with base load excluding residuals

Pile		Koppejan		LCPC		de Boorder	
ID	**Category**	$q_{c,avg}$ [MPa]	$\alpha_{p,K}$	$q_{c,avg}$ [MPa]	$\alpha_{p,LCPC}$	$q_{c,avg}$ [MPa]	$\alpha_{p,dB}$
164	A	8.24	0.631	14.82	0.351	12.90	0.403
175	A	6.57	1.244	11.98	0.682	10.48	0.780
398	B	10.61	1.252	15.21	0.873	14.95	0.888
397	B	6.81	0.880	9.32	0.643	9.63	0.623
573	C	6.10	1.166	14.99	0.475	10.62	0.670
592	C	6.03	1.660	12.88	0.777	9.14	1.110
576	C	7.13	0.799	15.10	0.378	10.54	0.541
594	C	7.25	1.086	12.44	0.633	9.73	0.810

Table 5.5: Derived α_p factors with base load including residuals

Pile		Koppejan		LCPC		de Boorder	
ID	**Category**	$q_{c,avg}$ [MPa]	$\alpha_{p,K}$	$q_{c,avg}$ [MPa]	$\alpha_{p,LCPC}$	$q_{c,avg}$ [MPa]	$\alpha_{p,dB}$
164	A	8.24	0.952	14.82	0.530	12.90	0.608
175	A	6.57	1.492	11.98	0.818	10.48	0.935
398	B	10.61	1.514	15.21	1.056	14.95	1.075
397	B	6.81	1.494	9.32	1.02	9.63	1.057
573	C	6.10	1.810	14.99	0.737	10.62	1.041
592	C	6.03	2.571	12.88	1.203	9.14	1.696
576	C	7.13	1.378	15.10	0.651	10.54	0.933
594	C	7.25	1.670	12.44	0.974	9.73	1.244

The demonstration of base loads in table 5.3 clearly shows that the inclusion of residual loads increases the true load experienced by the pile base. The consequence of higher base loads can be observed in the factors illustrated in Table 5.5. The variation for these factors and the importance of the spread is discussed in sections 5.7 and 6.2.

5.6.2 Alpha-s

The determination of α_s for pile 164 is illustrated in Figure 5.19 as an example. The soil categorization illustrated in section 4.5 is applied to each CPT and the corresponding loads at the top and bottom of each soil layer are considered for the calculation of shear forces. The cone resistance in each soil layer is arithmetically averaged and correlated with the difference in force normalized by the circumferential area of each section of the pile. This results in an α_s factor for each soil layer.

The residual loads illustrated in section 5.3 have a reoccurring trend of increasing towards the end of the soft layers and decreasing when approaching the sand body. This trend results in lower α_s factors in case of inclusion of residual loads for the first two soft layers of peat and clay. The transition of the second peat layer to the sand body is often the peak of the developed residual load, which sometimes results in higher factors for this layer in comparison to the scenario excluding residual loads. The layer boundaries and corresponding alpha factors for all piles are further illustrated in Appendix C.7. Table 5.6

shows the shaft resistance factors obtained for the bearing sand layer. The factors derived for the soft Holocene layer are illustrated in Table 5.7.

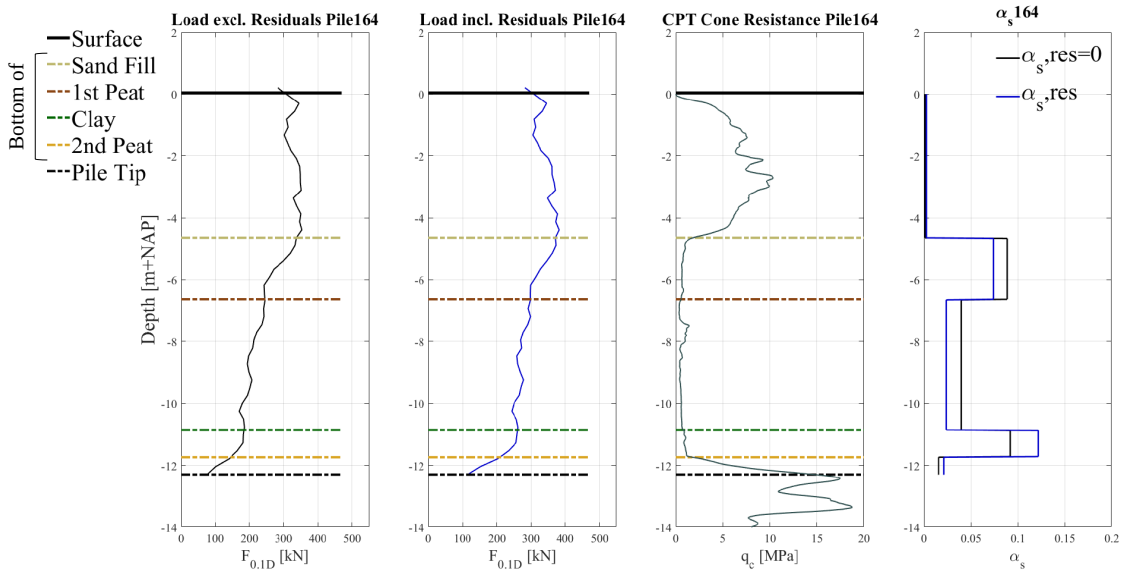

Figure 5.19: Determination of Alpha-s factor-Category A: Pile 164

As can be seen in the results illustrated in tables 5.6 and 5.7, the addition of residual loads leads to noticeable changes in shear forces. It has been observed that residual loads increase with depth in the soft layers and decrease when approaching the bearing sand. This effect is noticeable as the α_s factors for the soft layers generally decrease for the first peat and clay layers but increase for the second peat layer. The shear forces are strictly calculated based on the difference in forces at the top and bottom margin of each defined soil layer. Fluctuations in measurements of strains may result in higher or lower differences of load for each section. As mentioned previously, these fluctuations are due to several factors such as sudden changes in pile geometry or the existence of features that alter mechanical and strength properties.

Table 5.6: Derived α_s factors for bearing sand layer

Pile		α_{s_S}	α_{s_S}
ID	**Category**	**Excl. Residuals**	**Incl. Residuals**
164	A	0.016	0.021
175	A	0.003	0.007
398	B	0.010	0.012
397	B	0.009	0.011
573	C	0.005	0.008
592	C	0.013	0.018
576	C	0.010	0.007
594	C	0.006	0.008

Table 5.7: Derived α_s factors for soft layers

Pile		Excl. Residuals			Incl. Residuals		
ID	**Category**	$\alpha_{s_{P1}}$	α_{s_C}	$\alpha_{s_{P2}}$	$\alpha_{s_{P1}}$	α_{s_C}	$\alpha_{s_{P2}}$
164	A	0.089	0.039	0.039	0.075	0.024	0.024
175	A	0.079	0.077	0.077	0.055	0.102	0.102
398	B	0.107	0.041	0.041	0.089	0.024	0.024
397	B	0.059	0.091	0.091	0.050	0.087	0.087
573	C	0.076	0.082	0.082	0.057	0.081	0.080
592	C	0.075	0.095	0.095	0.056	0.087	0.087
576	C	0.032	0.056	0.057	0.022	0.046	0.046
594	C	0.034	0.068	0.068	0.028	0.070	0.070

The variation in alpha factors alongside the mean values for each averaging method are presented in the following section. Section 6.1 further elaborates on the reliability and potential application of these factors.

5.6.3 Influential Pile Characteristics and Soil Conditions

Figures 5.20 to 5.22 illustrate the influence of diameter and insertion depth on the derived α_p factors. As can be seen in Figure 5.20, no particular relationship between diameter and α_p can be observed. This is most likely due to the lack of data. The influence of insertion depth, L_i in the sand layer is illustrated in Figure 5.21 while Figure 5.22 shows the relationship of the derived factors with the ratio of L_i/D. The method of de Boorder illustrates a clearer depth dependency in comparison to the other two methods. The illustration shows that with higher ratios of embedment to tip diameter, higher α_p factors are calculated.

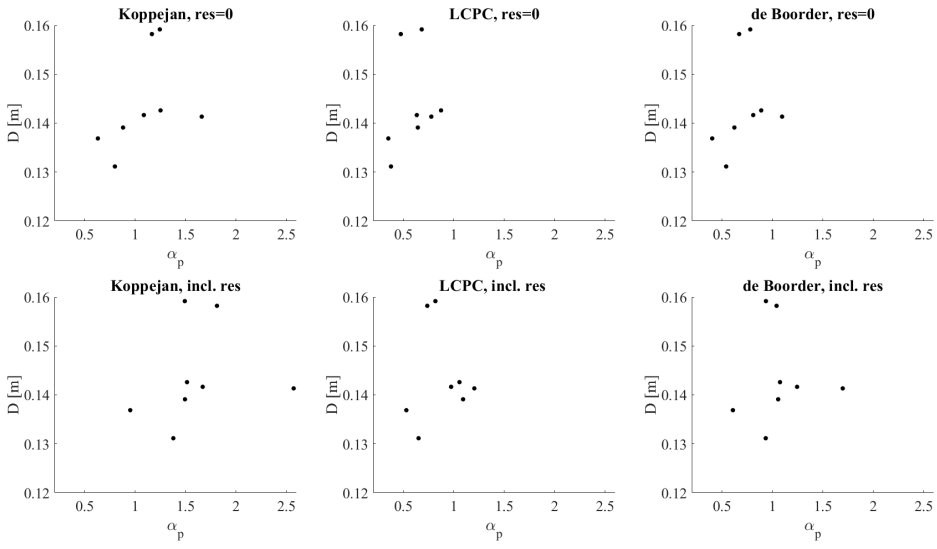

Figure 5.20: α_p vs diameter

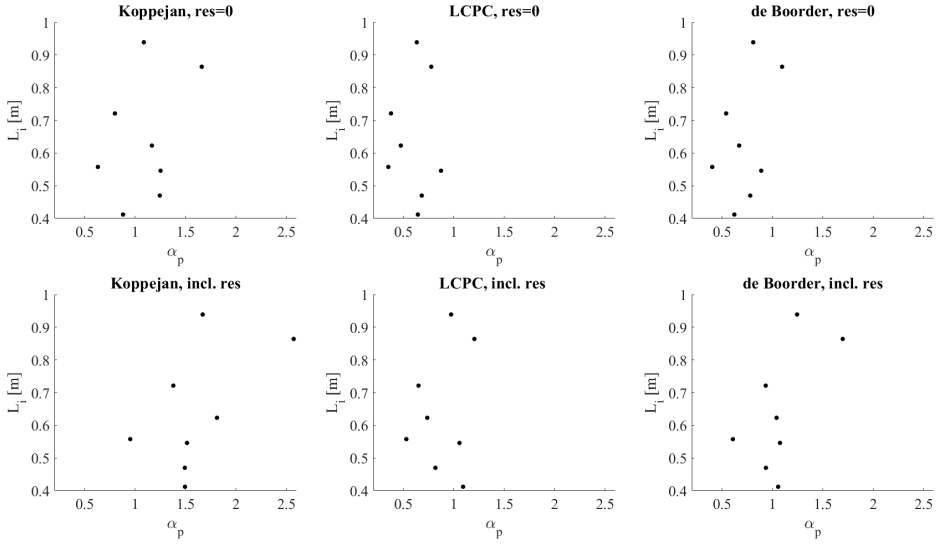

Figure 5.21: α_p vs insertion in bearing sand

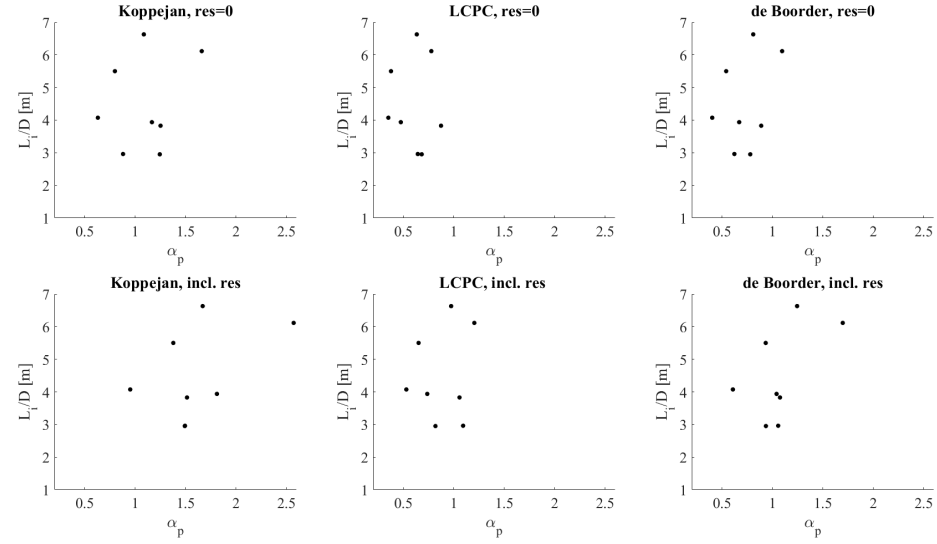

Figure 5.22: α_p vs L_i/D

In addition, the influence of insertion depth and L_i/D ratio on shear stresses in the sand layer is analysed. This is done by inspecting potential relationships between the derived α_s factors and the aforementioned aspects. However, no particular relationship was observed. The lack of correlation between these entities is further illustrated in Appendix C.7, Figures C.49 and C.50. Furthermore, the influence of tapering on the derived α_s factors is analysed. As illustrated in Figure 5.23, tapering of the pile in the bearing sand layer seems to increase shear forces.

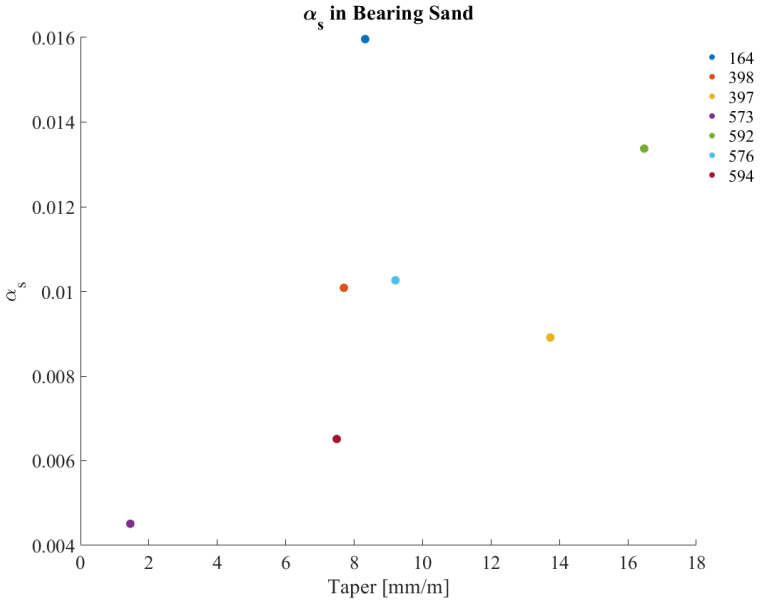

Figure 5.23: α_s vs pile taper in the bearing sand layer [mm/m]

Figure 5.24 illustrates the relationship between derived α_p factors and $q_{c,avg}$ obtained through the methods of Koppejan, LCPC and de Boorder. As can be seen, the methods of Koppejan and de Boorder illustrate a somewhat clear relationship with α_p factors decreasing as the average cone resistance increases. The LCPC method has a less clear relationship in comparison with the other two methods.

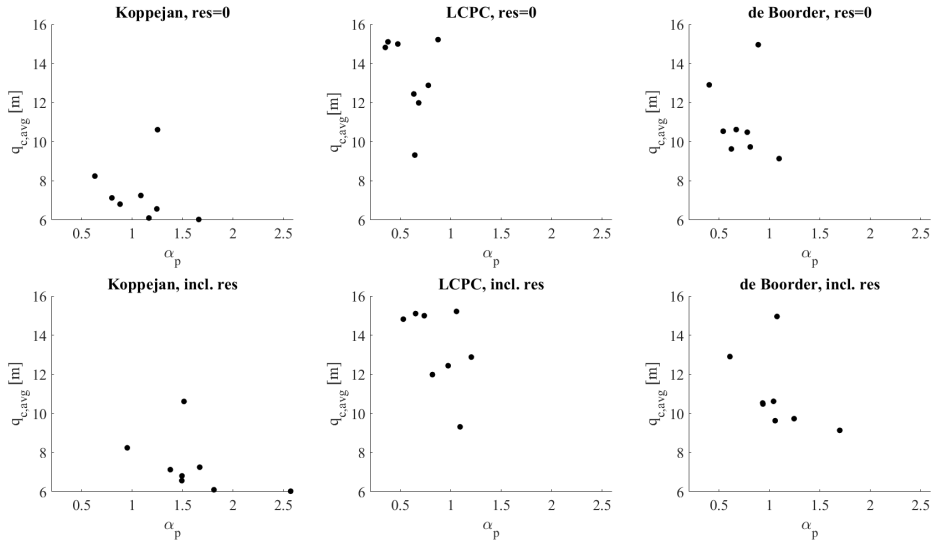

Figure 5.24: α_p vs $q_{c,avg}$

5.7 Statistical Analysis

This section aims to illustrate the variation of results obtained. The most relevant aspects such as pile characteristics, average cone resistance and alpha factors are discussed.

5.7.1 Variation of Pile Attributes

The discretization of pile geometry was discussed in section 5.1.3. It was shown that the variation of pile circumference does not have a particular trend and hence the definition of a singular taper for each pile is not representative of its actual geometry. This is applicable to piles used in the past as well as new piles. The natural variability in pile geometry would only be achieved through detailed debarking and sawing of the pile. Despite how a singular value of taper is not representative of the true geometry of these piles, the averaged tapering and diameter of all piles is illustrated in Table 5.8.

Table 5.8: Statistics of pile geometry

	μ	σ	CoV
Taper [mm/m]	8	2	0.30
Tip Diameter [mm]	144	10	0.07

The dynamic E-moduli of all piles were determined before their arrival at the test site. The variation of these measurements are illustrated in Figure 5.25. As can be seen, the pine samples have higher dynamic E-moduli. The variation of the measurements for pines is also less than those of the spruce samples. Therefore, it is safe to assume that the pine samples have higher static E-moduli as well. However, this cannot be confirmed unless static E-moduli of these samples are determined through laboratory testing. Upon assessment of the coefficients of the quadratic correlation between strains and forces, it can be seen that the pine samples have higher coefficients.

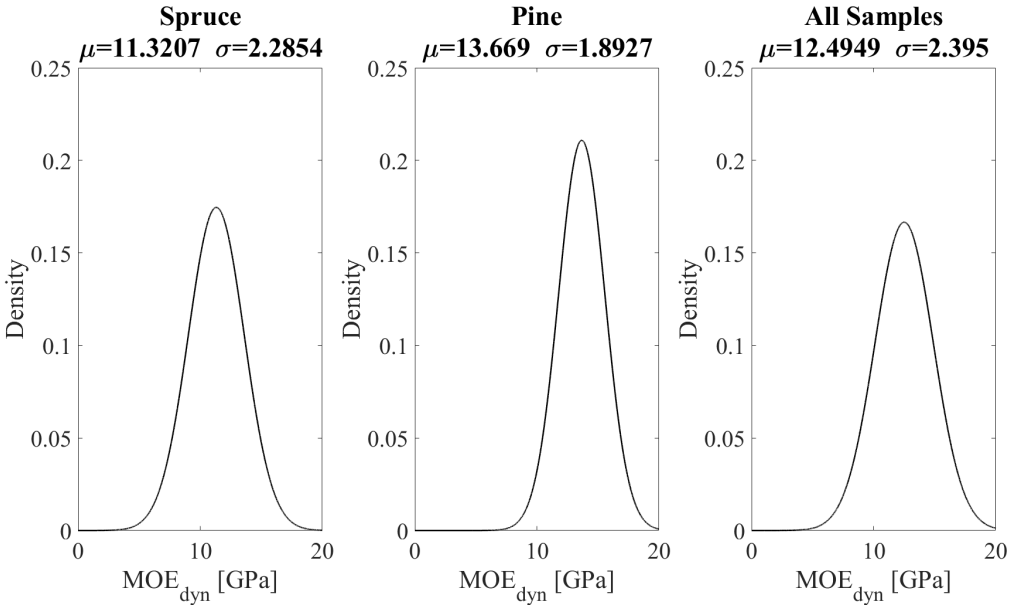

Figure 5.25: Variation of MOEdyn

5.7.2 Variation of Average Cone Resistance

The three methods used to determine the average cone resistance for the calculation of base capacities resulted in a variety of results. As expected, the Koppejan method delivered the lowest estimations. The influence of the soft layers above the bearing sand layer is highly influential in this case. The variation in the average cone resistance obtained through each method is illustrated in Figure 5.26.

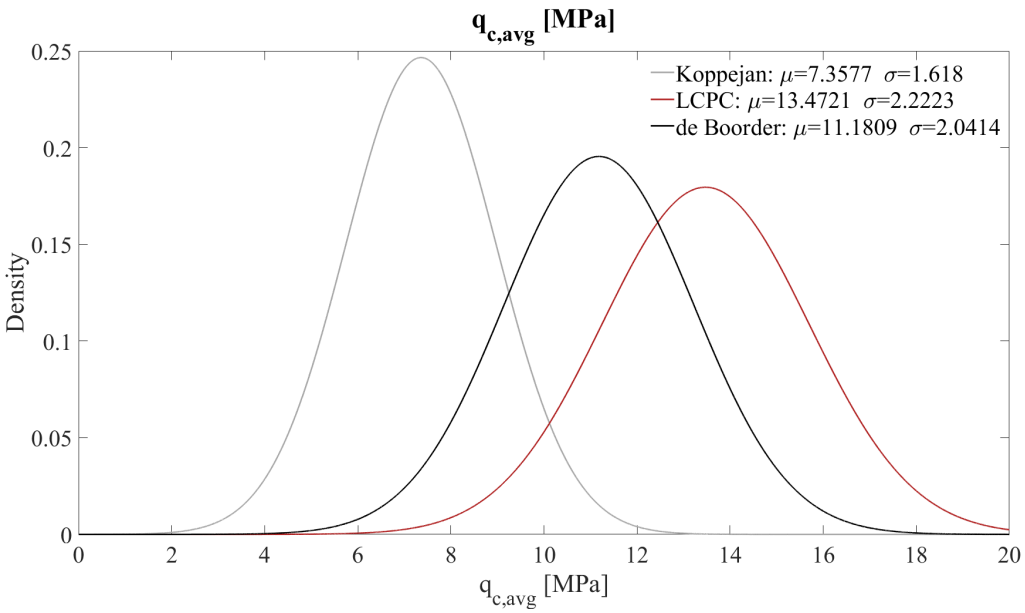

Figure 5.26: Variation of average cone resistance

It is evident that the resultant $q_{c,avg}$ values for the Koppejan method have the least variation. This method results in a spread of values from 6.02 to 10.61 MPa, with a variation of 15.2%. The LCPC and de Boorder method have higher coefficients of variation, namely 16.5% and 18.0%. The results from each method have significant effects on the derivation of the base resistance and its corresponding correlation factor, α_p.

5.7.3 Variation of Alpha Factors

Analyzing the variation in derived alpha factors can result in the definition of a representative value for estimating the bearing capacity of timber piles in similar soil conditions. Figure 5.27 illustrates the probability density functions for α_p based on base loads excluding residual effects. As can be seen, the factors derived based on the LCPC averaging technique have the least spread and variation. This is logical, as the zone of interest for this averaging technique is limited to 1.5D above and below the pile tip. The small zone of interest, alongside the dismissal of values below the $0.7q_{c,mean}$ (refer to section 2.4.1) results in more similarity between averaged cone resistances.

The method of De Boorder, 2019 has a variation of 29.6%. The Koppejan method, with a coefficient of variation of 29.4%, results in the highest mean alpha factor. This is expected, as the average cone resistances calculated using this method are lower than the other two. The same trends can be observed in Figure 5.28 which illustrates the variation in α_p based on base loads including residual forces.

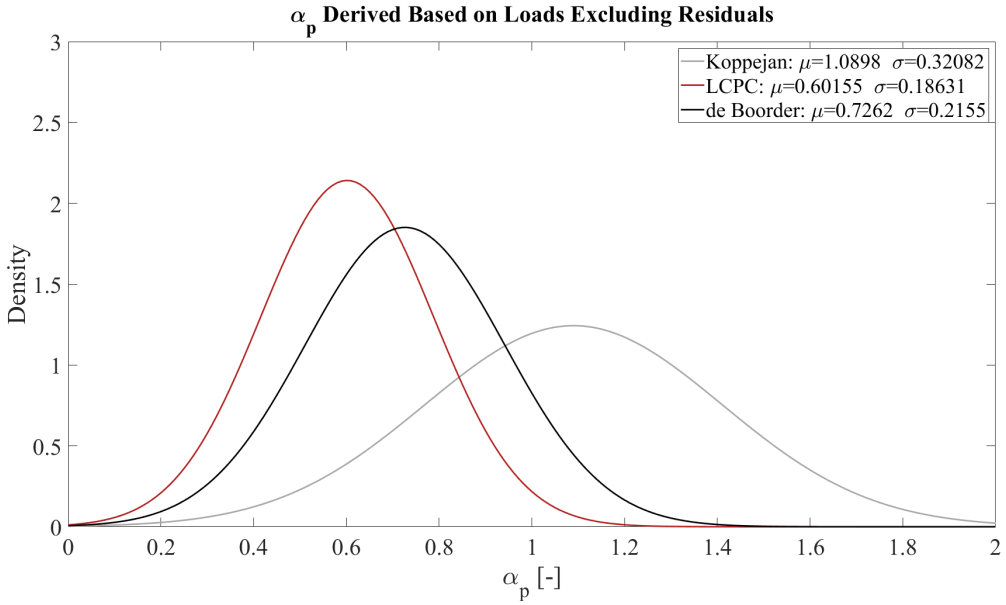

Figure 5.27: Variation of $\alpha_{p,0}$

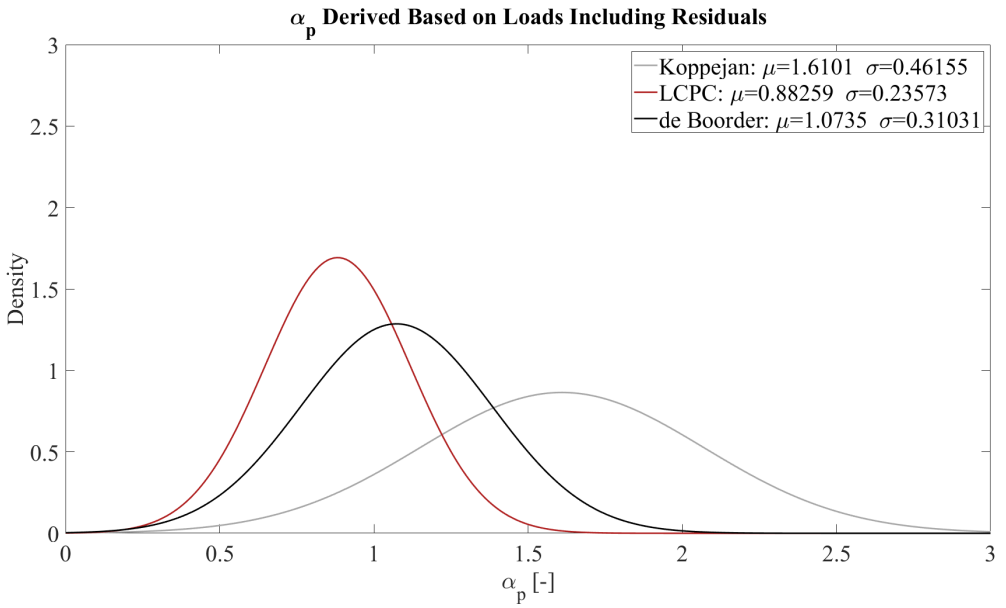

Figure 5.28: Variation of $\alpha_{p,res}$

The value used in the Dutch norm ($\alpha_p = 0.7$ for Koppejan) is approximately at the 10 percentile mark of the distribution illustrated in Figure 5.28. Therefore this value lies within the range of $\mu - 2\sigma$ in this distribution. When taking residual loads into account, the LCPC method has a variation of 26.7%, while the method of Koppejan has a variation of 28.66%. The representative mean for this method is rather high in comparison to factors used in the Dutch norm. The method of de Boorder has a variation of 29.0% and results in a mean value of 1.09.

The variation of the α_s factors for each layer is illustrated in Figure 5.29. The two lines indicate the scenario including and excluding residual loads. As discussed in the

previous section, in the first two soft layers the factors decrease upon adding residual loads. The factors for friction in the bearing sand layer vary between 0.005 and 0.018.

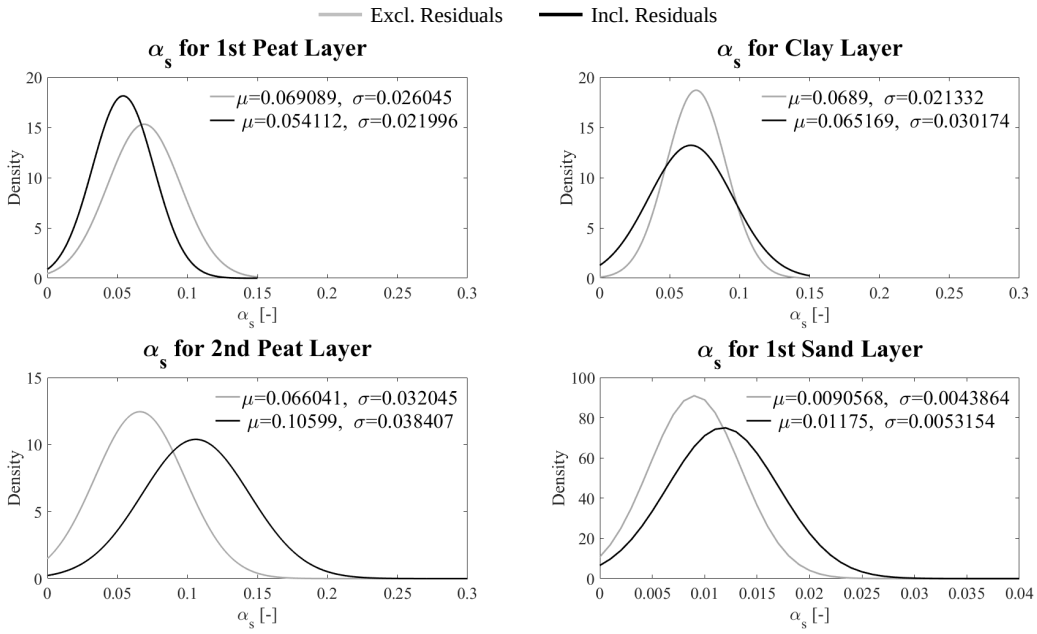

Figure 5.29: Variation of α_s ($\alpha_s = 0.012$ for bearing sand in the Dutch norm)

Given an appropriate and accurate averaging method, a singular alpha factor should be representative for the calculation of a particular pile type. The following tables illustrate the mean values for alpha factors based on results obtained in this project.

Table 5.9: Mean α_p Factors for Timber Piles

	Koppejan	LCPC	de Boorder
α_p excl. Residuals	1.09	0.60	0.72
α_p incl. Residuals	1.61	0.88	1.07

Table 5.10: Averaged α_s Factors for Timber Piles

	Bearing Sand Layer	Holocene Peat	Holocene Clay	Pleistocene Peat
α_s excl. Residuals	0.009	0.069	0.069	0.066
α_s incl. Residuals	0.012	0.054	0.065	0.10

Chapter 6

Discussion

Chapter 6 reflects on the results obtained through the analysis. Aspects such as the reliability of the computational procedure, the availability and validity of the data and the necessity for further research are discussed in this chapter. Additionally, a comparison is made between the results of this project and observations from the Dapperbuurt load tests. Finally, the chapter elaborates more on the potential for a more representative set of calculation factors for timber piles in accordance to the Dutch norm.

6.1 Evaluation of Available Data

6.1.1 Evaluation of Strain Readings

It is evident that the readings on some piles, for instance pile 397, include fluctuations that might be perceived as noise. The fluctuations could be caused by noise in the data but other factors may also result in this trend. For instance, the natural variability of wood and the existence of external factors such as branches, variations in temperature and moisture content, human error in installation or the attachment of the fiber to the surface could also contribute to the observed fluctuations in readings.

Uncertainty caused by the installation of fiber optic sensors consists of several aspects. Firstly, the tightening of fibers around the loop and in the groves to ensure attachment may lock strains in the fiber itself. The potential of residual strains from the attachment of the fiber and the application of glue may affect the measurements conducted.

The occurrence of such fluctuations does not dismiss the integrity of the test or the results thereof. However, for the derivation of shear forces, the fluctuations may be of influence. As mentioned previously, the difference in force at the border of each section of the pile is chosen at two nodes. Fluctuations in the readings may cause this calculation to be flawed as one node may be subjected to more shift in the data than the other.

In order to evaluate the effect of fluctuations, the data was smoothed using several methods such as averaging of peak envelops and utilizing a Savitzky-Golay filter. The smoothing of the data resulted in a decrease in shear stresses along the pile. This resulted in higher apparent loads at the base which ultimately contributed more to uncertainty. This is illustrated in Figure 6.1 Therefore, the smoothing of the data was dismissed in order to have a more transparent approach to the analysis.

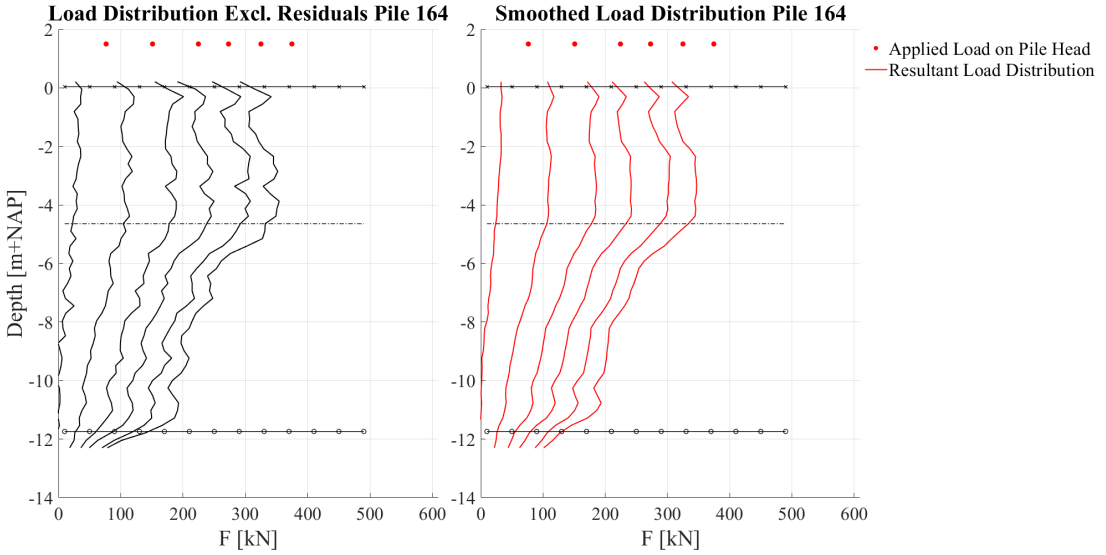

Figure 6.1: Pure and smoothed load distributions-Category A: Pile 164

Additionally, it is important to note that the entirety of the interpretation is dependent on the deduction of the measuring node at the pile tip. This process is manual and is subjected to human error. The symmetry of the measurements must be maintained with respect to the pile tip. This symmetry must apply to all sets of measurements, including reference strains. It was noticed that an error in this evaluation can lead to differences of up to 100 kN of additional base loads.

The averaging of two fibers serves the purpose of negating bending effects to an acceptable degree. The usage of only one fiber channel, for instance pile 398, may result in the lack of compensation for such effects. Often it is noticed that when a certain point on the pile is experiencing high amounts of strain, the opposing side compensates for the effect by registering less deformation. Therefore, it can be noted that the best approach is averaging all fibers. The averaging of fibers installed on each quadrant of each pile results in a more representative strain profile in comparison with a scenario where only a singular fiber is used for interpretation.

6.1.2 Evaluation of Pile Geometry

The circumference of the pile was measured at spatial resolutions of 0.5 to 1 meter for different piles. Upon inspection of the piles, the variation of circumference, especially for piles debarked by hand, is obvious and evident to the naked eye. It is also important to note that the area of the pile at each measuring node is calculated as though the pile has a circular cross-section. This is however an assumption and is not truly the case. The cross-section of the pile is best described by an irregular circle. The discretized geometry of the pile is based on the circumference measurements before pile installation. This irregularity in geometry may also be a factor of uncertainty as the actual cross-sectional area that experiences a certain amount of load may be less than what is calculated. Therefore, stresses might be higher than what the results indicate.

This derivation of segmented measures of diameter is based on a linear interpolation between the measured points and the assumption that the geometry is described by a

circular cross-section. Therefore, there is a chance that, at certain measuring nodes, the true diameter is different from what is interpolated.

6.1.3 Framework Logistics and Measurement Frequency

The initial framework consisted of analyzing piles installed at 1 and 2 calendars in the bearing sand layer. This insertion depth was to be maintained during the installation process. However, it has been observed that the insertion depth of the piles in the sand layer is always more than 1 calendar (25 centimetres). The embedment of each pile in the bearing sand layer is summarized in table 5.2. As a consequence of this, the comparison between the three categories is narrowed down to comparing the piles only based on wood type.

As mentioned in section 5.4, the frequency at which the strains are measured is much lower than the readings from the load cell. Often, during unloading/reloading stages, there are only a handful of strain readings. This may lead to a minimal amount of discrepancy in the correspondence of loads and strains in time. However, as illustrated previously, this difference in time is insignificant. In order to ensure validity, the time indicating maximum displacements and displacements of 0.1D were manually checked.

6.2 Discussion on Reliability and Certainty of Results

6.2.1 Discussion on Pile Stiffness

It has been observed that the effect of stiffness on the load distribution can be significant. Figure 6.2 illustrates an arbitrary scenario for pile 164. This illustration consists of the load distribution determined through the quadratic relationship described in the previous sections as a dashed black line. The other scenarios, as indicated in the legend of this figure, are scenarios of varying measures of stiffness over the length of the pile. This variation consists of a 15 % difference in stiffness between the pile head and the pile base. In other words, in the first scenario, the pile head has a stiffness that is 15% higher than the base and vice versa for the following scenario. As can be seen, the difference is not severe in terms of the loads at the pile base. However, the rate of decrease in load, which is a significant factor in deriving shear forces, is variable. The chosen 15 % of increase or decrease does not have a particular justification. This illustration only serves to elaborate on the importance of the effect of the modulus of elasticity on the results.

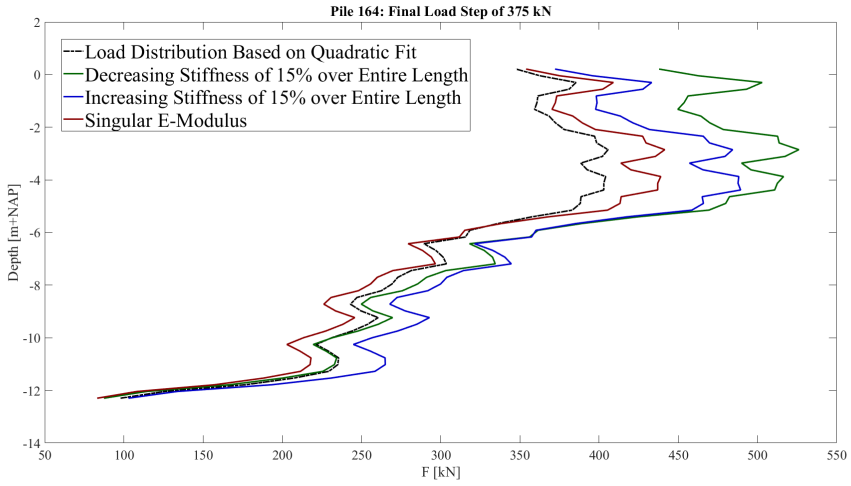

Figure 6.2: Comparison of variation in E-modulus-Category A: Pile 164

It is therefore significant to have a more concrete discretization of E-modulus along the length of the pile. A more accurate set of data regarding the distribution of stiffness in each pile may also result in negation of fluctuations. The existence of features such as branches and knots should also be further investigated in order to understand their effect with regards to local load distribution. The features contribute to local stiffness which can only be measured using high resolution sensing technologies. It is therefore significant to create a test framework with which the stiffness of the pile can be measured locally using the fiber optics which have already been installed.

It has been observed that the pine specimens are stiffer than the spruce piles. The categorization is therefore significant in this regard as it features a clear difference in load distribution between pile types. This observation holds for all methods used to derive stiffness or correlations between loads and strains. As illustrated in section 5.4, Figure 5.13, the pine specimens behave similarly and seem to have the same stiffness slope in relation to the load displacement curves. This further confirms the assignment of a singular relationship between loads and strains to each wood type.

In order to evaluate the variation of stiffness throughout the pile, it is essential to have segments of representative piles tested statically. The evaluation of segmented measures of stiffness can contribute to the derivation of calculation factors as it will refine the load distribution throughout the pile more accurately. This procedure is currently being pursued and the resultant variation of E-moduli will be made available to the overall experimental framework, at a later stage.

6.2.2 Reference Measurements and Residual Loads

As illustrated in section 5.3, there was an increase in strains over time. The difference between locked-in strains after pile installation and before the load test amount to approximately 100 micro-strains at the base and up to 120 micro-strains in the clay layer. The observed increase could be due to several factors. The recovery of shear surfaces by the surrounding soil as a time dependent effect can be a viable explanation. This is followed by potential surface settlements. However, no actual records of such a phenomenon is available. Another explanation could be the dissipation of pore pressures after the installation of the pile. The radial dispersion of pore pressures through time may have resulted in the consolidation of the softer layers, resulting in an increase in locked-in strains. Another significant factor may be the alterations in moisture content and changes in temperature. Such changes in time may contribute to the development of additional strains.

It has also been observed that the residual loads increase gradually till the -9 meter NAP mark and begin to decrease towards the pile tip. This phenomenon seems to result in lower shear forces upon inclusion of residual loads. These loads have an average contribution of 70 kN to the base capacity.

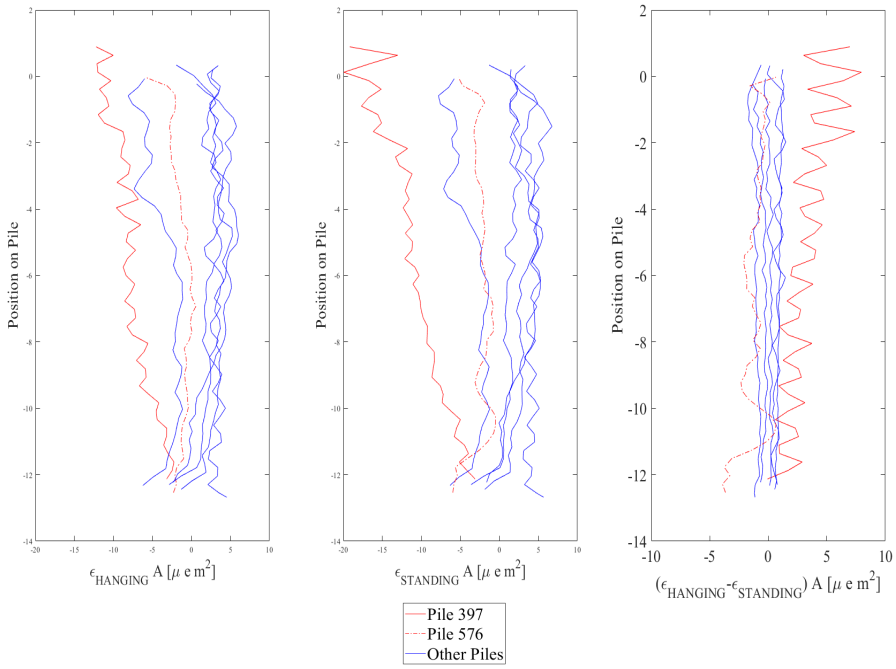

Figure 6.3: Reference measurements all piles

It is important to note that for a number of piles, the reference strains measured during hanging and standing are particularly noisy. Theoretically, the subtraction of

hanging and standing strains should result in a constant distribution along the pile length. As illustrated in Figure 6.3, this is not the case for piles 398 and 576. This raises the question of whether the results obtained for these piles upon inclusion of residual loads is flawed. Factors such as moisture content or temperature at the moment of conducting these measurements may cause this irregularity.

The derivation of the alternative residual strains, based on measurements conducted after pile installation and before the test, serves the purpose of creating more transparency in the analysis. This method includes both measurements and negates strange behaviour in the sand-fill layer by dismissing high strains at the pile head. This method also resulted in more uniformity between the residual strain profiles for each pile group.

6.2.3 Discussion on Interpretation of Load Tests

There are certain factors that affect the reliability of the results illustrated in Chapter 5. As mentioned in the previous sections, aspects such as strain readings and variation in stiffness are potential components that may affect the validity of the obtained results. Aside from the aforementioned data related uncertainties, other factors may contribute negatively to the reliability of the derived measures.

The fibers are installed in such a way that symmetry can be maintained in reference to the pile tip and the length axis of the pile. As mentioned in section 4.4.2, nodal or discrete measurements of strain are averages at a spatial frequency of 25 centimeters. This could mean that at the pile tip, there may or may not be a specific nodal measurement of strain. This can result in asymmetry of readings, which ultimately affects the averaging of strains over the length of the pile. The accuracy of the derived load distributions slightly decreases as a consequence of this spatial resolution.However, the extent of accuracy defined in this analysis is also a matter of perspective. Overall, measurements conducted at a frequency of 25 centimeters over a total length that almost amounts to 15 meters can justify dismissal of this lack of accuracy.

Due to the measurement frequency and time discrepancy between the load cell readings and the strain measurements, certain derivations are not particularly precise. For instance, the moment at which 0.1D displacement of the pile base has taken place is not correctly recorded for piles 576 and 594. Therefore, for these piles, the closest and most representative moment in time is used as the deriving moment rather than the actual displacement of 0.1D. As mentioned previously, pile 576 has the smallest diameter and as a consequence of this, the pile settled very quickly under a final load step of 325 kN.

6.2.4 Concluding Discussion of Derived Correlation Factors

The variation in α_p factors derived from the test results is illustrated in section 5.7. As mentioned in section 2.4.1, the average value for LCPC is obtained over a distance of 1.5D above and below the pile tip. Given the relatively small diameters of the tested piles, and the fundamentals of this averaging technique, the least variation in α_p factors derived based on this method is to be expected. The average cone resistances obtained through the Koppejan method is particularly low for pile 576 which results in a much higher α_p factor in comparison to the rest of the piles.

The inclusion of residual loads naturally results in higher derivations for α_p. The factors derived through the Koppejan method are much higher than the other two methods.

This is due to the effect of 8 meters of soft soils with low cone resistances above the bearing sand layer. No clear trend was observed between α_p and diameter; ratio of insertion in bearing layer to diameter or average cone resistance.

Variation of α_s factors for the bearing sand layer are also affected by the inclusion of residual loads. This increase indicates that there is more development of strains at the top of the sand layer than the pile tip. The correlation factors for the Holocene peat and clay layer decrease upon inclusion of residual loads. This is due to more strain development at the lower boundary of the clay layer as locked in strains in comparison to the top peat layer. The frictional contribution of the clay layer is higher than anticipated.

In order to evaluate the derived factors, the mean α_s's were incorporated with the cone resistance to develop an expected load distribution based on the soil conditions. This is illustrated in Figure 6.4 for the scenario excluding residual loads. Alongside this, the measured load distribution in the pile is also illustrated as means of comparison. This comparison assumes that the load distribution in the pile head and in the pre-drilled sand layer is equal to that of the load applied at the pile head. As can be seen, for all piles aside from 397 and 594, the load profiles and the correlated cone resistances are very similar. This not only validates the results for these piles with regards to the derived α_s factors, but confirms that the base resistance is appropriately measured.

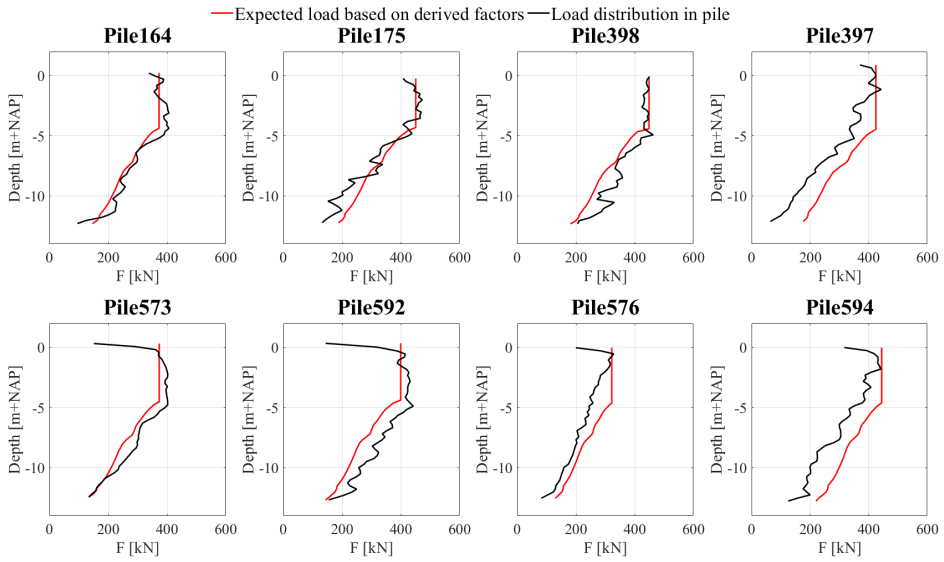

Figure 6.4: Comparison using representative α_s - Excluding residual loads

Figure 6.5 illustrates the same comparison for the scenario including residuals. In this case, the α_s factors are less for the Holocene layer but higher in the bearing sand. The correlation with the cone resistance is in line with the measured base resistances as the lines meet at the base for most piles. The variations illustrated here are most likely due to the pile-specific residual loads that are included. The uncertainty regarding the strains measured during hanging is most likely the factor causing this difference.

It is important to note the effect of pile stiffness on the illustrated results and comparison. As illustrated previously, the rate of load reduction towards the pile tip changes depending on the distribution of stiffness. This has direct effect on the shear forces that are calculated for each pile. Therefore, it is necessary to consider this distribution and to

conduct further research in order to validate the extent of reliability for results derived in this analysis.

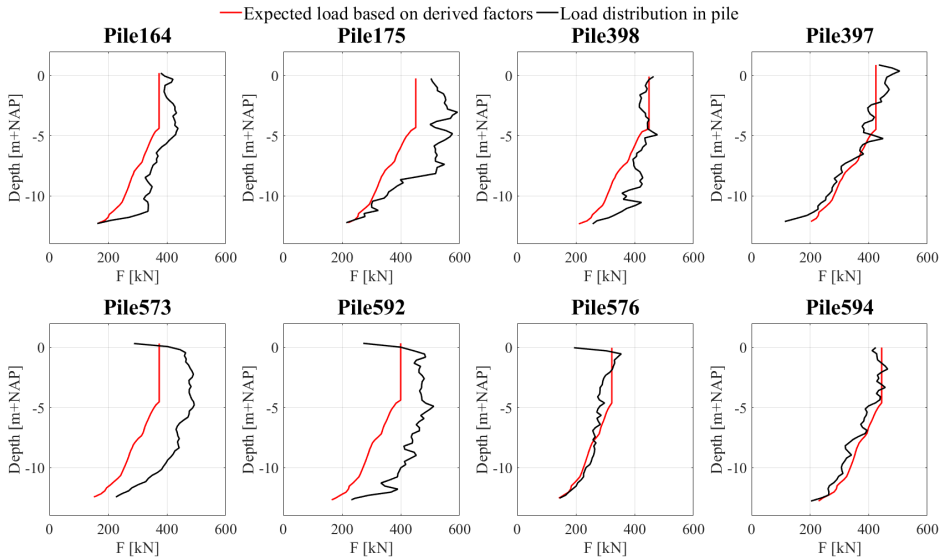

Figure 6.5: Comparison using representative α_s - including residual loads

In order to check the viability of the derived average factors, the total capacity for each pile can be calculated for both scenarios. In principle, the total capacity should be equal for both scenarios as inclusion of residual loads only redistributes the capacity. Table 6.1 illustrates this comparison between the two scenarios using their average representative factors. The obtained results are based on α_p factors derived using the Koppejan method. The shaft capacity in the upper sand layer is calculated using an α_s factor of 0.005 and is added to the total capacity. These measures are then compared to the load at a base displacement of 0.1D recorded by the load-cell. As can be seen, the calculated capacities and measured loads are mostly similar, which results in normalized loads very close to 1.0. The slight differences is most likely due to the previously mentioned uncertainties.

Table 6.1: Total capacity for scenario excluding and including residual loads

Pile		164	175	398	397	573	592	576	594
Category		A	A	B	B	C	C	C	C
Q_T [kN]	Excl. Residauls	355	404	390	415	375	391	320	367
Q_T [kN]	Incl. Residauls	367	410	396	425	383	407	333	385
Q_T [kN]	Load-cell	373	451	448	424	373	399	322	444

It is therefore advisable to use the derived set of factors in correlation with the CPT profile as the total capacities calculated are in line with one another. Additionally, the total capacities calculated using the derived factors are similar to the measured capacities for both scenario's shown in table 6.1.

6.3 Comparison to Norms and Previous Tests

6.3.1 Comparison of Correlation Factors to the Dutch Norm

The method utilized in the Dutch norm suggests an α_p factor of 0.70 using the method of Koppejan, for tapered timber piles installed through pile driving. The implementation of this factor has been in place since 2016. Before this time, the factor used for correlating cone resistance to base capacity was 1.00. The average factor derived in this report through the Koppejan method is 1.09. This factor increases to 1.61 upon inclusion of residual loads. This is significantly higher than the value indicated in the Dutch Norm.

This norm also provides α_s factors for different soil types. For driven piles in sand, the indicated factor is 0.012 for friction in the bearing layer. However, the method used in the norms dismisses the frictional contribution of peat and indicates an α_s factor between 0.02 and 0.03 for clayey soils. The α_s derived in this project is 0.009 for friction in the sand layer. This factor increases to 0.012 when residual loads are included. The consideration of frictional properties of the soft layers above the foundation layer is crucial. This is especially applicable to the peat lens above the first sand layer which has a high frictional contribution. The frictional contribution of the soft soil layers should therefore be considered when assessing the bearing capacity of timber piles.

6.3.2 Comparison to Previous Pile Load Tests on Timber Piles

As mentioned in section 2.7, a set of new timber piles were installed in Swindenstraat, Amsterdam as part of the Dapperbuurt pile load tests. These new piles had diameters of 13 centimeters and were loaded in compression and tension. Two of these piles were installed using casings to evaluate the pile behaviour in the bearing sand layer. The other two piles were installed without casings which are comparable to piles used in this project. The ultimate failure capacity in compression for the piles installed without casing ranged between 260 to 270 kN. The base capacity for these piles was calculated as 89 and 109 kN for a relative displacement of 10 to 15 millimeters. The base capacities at failure were 110 and 114 kN. This ultimate capacity is calculated based on the determination of a shaft capacity of 150 and 156 kN for each pile respectively.

Figure 6.6 illustrates a comparison of the head load-displacement curves from Dapperbuurt and Overamstel. It is noticeable that the piles from each test set behave differently. This difference stems mostly from the differences in pile geometry and loading schemes. The piles in Overamstel are loaded to far higher loads and are instrumented more accurately as well.

Considering the fact that residual loads were not taken into account in the analysis of the Dapperbuurt tests, the comparison is only valid for the scenario excluding residual loads. The conducted analysis resulted in an average capacity of 270 kN along the entire length of the pile. The average shaft capacity in the bearing sand layer is 48 kN. The average base resistance for all piles is 130 kN. As can be seen, the results from the conducted tests at Overamstel are larger than those from the Dapperbuurt tests. The differences in the two tests can be summarized as below;

- The diameter of the piles used in this project are larger.
- The means of measurement used to collect the data analysed in this project are more accurate

as the piles from Dapperbuurt were not instrumented.

- Despite the extreme similarity of soil conditions, the Holocene layers at the Overamstel testing grounds seem to have higher undrained shear strengths and hence higher frictional properties.
- The loading schemes were different due to differences in pile geometry.

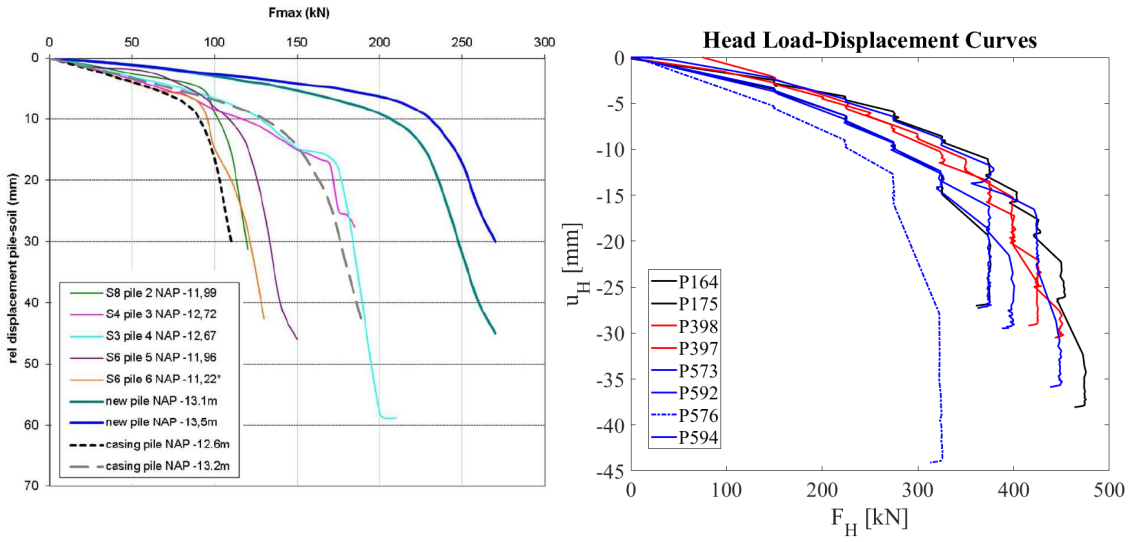

Figure 6.6: Comparison between the Dapperbuurt and Overamstel Load Tests

Chapter 7

Conclusion and Recommendations

7.1 Conclusion

As part of the safety assessment of bridges and quay walls founded on timber piles, an experimental framework was developed by the city of Amsterdam to evaluate the bearing capacity of such piles. As part of this experiment, a total of sixteen new timber piles are instrumented with fiber optic sensors and tested in compression to observe pile behaviour and their interaction with the surrounding soil. Eight of these piles are analysed in detail in order to determine calculation factors for predicting the bearing capacity using a CPT-based prediction method. The framework of this analysis consists of comparing two groups of piles based on their wood type, namely spruce and pine specimens.

In order to obtain representative correlation factors, a series of aspects are taken into consideration that form the basis of the analysis. The data obtained from the load tests is assessed with regards to validity and usability. This is followed by the determination of locked-in strains based on reference measurements conducted before and after pile installation. The geometry and strength properties of the piles are considered and a relationship to relate measured strains to loads is developed. The calculated load distribution is then correlated to CPT profiles to determine the appropriate correlation factors for each individual pile. A statistical analysis is conducted to evaluate the variation of the results and to derive representative correlation factors for predicting the bearing capacity of timber piles.

The analysis illustrates a variation of results that is affected by many different factors. It is observed that the pile geometry is highly variable for some of the piles. This variation in geometry stems from the biological nature of wood. Aside from geometry, the local variation of mechanical properties in wooden piles, most significantly stiffness, also have an effect on the distribution of loads through the pile. It has been observed that the pile head subjected to load has a hysteretic behaviour and is best described by a quadratic relationship correlating strains to loads. The application of a uniform quadratic equation for each category of piles results in a clearer and more transparent analysis. However, this application also dismisses the unique nature of each pile. Considering the fact that the local distribution of pile stiffness is yet unknown, this approach has proven to be the best option.

It has proven to be possible to derive residual loads using reference measurements of locked-in strains. A certain time effect is observed between measurements conducted after

installation and before the load tests. This time effect may be due to several reasons, such as the development of moisture content; changes in temperature; settlement of the surface and recovery of shear surfaces or dissipation of excess pore-pressures. However, the true identity of these phenomena cannot be pinpointed. Therefore, it is concluded that the measurements conducted after installation are more reliable as the process of excess strain development cannot be fully explained. As a consequence of this stigma, and in order to increase the extent of transparency in this analysis, an averaged residual strain profile has been devised. This derivation succeeds to negate extreme data fluctuations and dismisses unrealistically high strains in the pre-drilled sand fill layer and the pile head itself.

When inspecting the pile behaviour from the load-displacement curves, it is evident that all pine wood samples behave very similarly. Pile 576 is an exception, as it has the smallest diameter and settled significantly more during the load test. The piles from the spruce category initially behave in a similar manner but tend to deviate from each other at higher loads. However, the initial stiffness in loading is similar between piles from this category. This observation further confirms the viability of applying a singular relationship for deriving loads from strains to each pile type.

Correlation of load distributions to CPT profiles has resulted in a variation of α_p and α_s factors. The derivation of the base resistance correlation factor α_p consists of considering three cone resistance averaging techniques. The method of Koppejan consistently resulted in higher factors in comparison to LCPC and the method of de Boorder. The influence of the overlying soft layer in this averaging technique is much more prominent than the other two. The derived average correlation factors based on the Koppejan method are higher than values currently used in the Dutch norm. The shaft friction correlation factors are in line with values used in the norm for the bearing sand layer. However, for the calculation of the shaft friction in soft layers, the method presented in the norm is unrepresentative of load tests, as it dismisses peat layers and only serves to determine design values.

7.2 Assessment of Research Objectives

The main objective of this research was to determine the appropriate means to predict the bearing capacity of timber piles in the lithological setting of Amsterdam. This objective was achieved through observing the pile behaviour in each soil layer and the consideration of certain aspects such as timber properties and residual loads. In order to outline the assessment of this research, the following questions are answered.

Are there specific characteristics of timber piles that affect the behaviour of a pile subjected to loading?

The pile tapering, which is a natural characteristic of the analysed timber piles, has significant influence on the bearing capacity. This tapering increases the frictional forces along the pile shaft as a consequence of decreasing diameter. This is a result of differences of high normal loads applied to a decreasing circumferential area. Additionally, the variation in diameter causes fluctuations in the load distribution. These fluctuations do not dismiss the integrity of the derived load distribution, as conducted measurements are local at a spatial frequency of 25 centimeters. The locality of the measurements and the spatial resolution entails sufficient accuracy when compared to the length of the pile.

In addition to geometrical aspects specific to timber piles, the natural variability in fabric and mechanical properties also affect the behaviour of the pile. The variation of pile stiffness through the length of the pile significantly affects the distribution of loads. It is therefore important to conduct further research on the variation of properties in wooden piles. Aside from this variation, local features such as the existence of branches or knots affect the stiffness. These features are local and can be measured using the installed fiber optics. Evaluation of such features and their effects may alter the derived loads and corresponding correlations with soil conditions. In assessing existing structures, these aspects remain unknown and cannot be further analysed.

How do residual loads affect timber piles?

The effect of residual loads has proven to be significant as part of the analysis. Despite the uncertainty of the derivation of residual loads, the trend and effect they impose on the load distribution in each pile is important and noticeable. It is observed that locked-in strains have a trend of positively developing towards the interface between the soft soil and the bearing sand layer. Upon approaching this interface, the strains decrease towards the pile tip. This trend is occurring for all analysed piles. The equilibrium points of the residual plane seems to vary between the -8 to -9 meter mark with respect to NAP. Additionally, inclusion of residual loads results in alterations in the interpretation of total capacity. This alteration is best described by the redistribution of the total pile capacity by an increase of the base resistance and shaft resistance in the Pleistocene peat and bearing sand layer, and a simultaneous decrease of the shaft resistance in the upper Holocene layers. This is observed by the derivation of lower α_s factors for the scenario including residual loads.

What alpha factors can be used to predict the bearing capacity of timber piles, using different cone resistance averaging techniques?

The testing grounds for this project are ideal as very little spatial variability exists in the soft soil layers. The first sand layer in this field is also continuous and comparable for each pile. However, in some cases, as indicated by the variation in averaged cone resistance, the sand layer has higher values for cone resistance near the -13 meter mark.

This phenomenon leads to higher reaction forces at the pile base in comparison to others. This especially holds for pile 398. Additionally, the high shear forces in the soft layers may be due to the high undrained shear strengths of the clay (approximately 30 kPa).

As illustrated in section 6.2.4, the total capacities are similar for both scenarios (either including or excluding residual loads). The redistribution of capacity as a consequence of residual loads is a significant aspect that should not be dismissed. Therefore, it is advisable to predict the bearing capacity of timber piles using factors derived for the scenario including residual effects.

As a result of correlations between the derived load distribution and the soil conditions, it can be concluded that for prediction of shaft capacity in the sand layer, an α_s factor of 0.012 is appropriate. In order to estimate the frictional contribution of the peat and clay layers above the bearing sand, the application of respective factors 0.054 and 0.065 has proven to be effective. Additionally, the frictional contribution of the lower Pleistocene peat layer is best captured by using an α_s factor of 0.10. Due to the small spatial frequency of measurements, the derivation of this particular factor may be flawed as the soil layer is rather thin.

The correlation factor for prediction of base capacity has been derived for 3 averaging techniques. The method of Koppejan has resulted in α_p factors of 1.09 and 1.61 for scenarios excluding and including residual loads respectively. Considering the small ratio between pile diameters and the diameter of the CPT cone, the LCPC method has resulted in α_p factors of 0.6 and 0.88 with the least variation. Conclusively, for the prediction of base capacity, a correlation factor of 1.61 is effective and appropriate given an average cone resistance derived through the Koppejan method.

How effective is the usage of fiber optic sensing on wooden piles?

The usage of FOS on timber piles has proven to be effective. The nodal and discretized measurements of strain at such high spatial frequencies deems appropriate for a highly variable product such as wood. That being said, the biological nature of wood and the variation in parameters result in uncertainties that can be perceived as discrepancies with regards to the measurement technique. It is important to note the potentials of conducting staged measurements of strain such as hanging, standing and after installation. These reference measurements at such detail highlight significant information regarding characteristics of each pile.

The attachment of the fibers to the pile surface is ensured by gluing. Upon pile installation or loading this attachment may be compromised. Several fibers required reconnecting over the section exposed above ground surface after the piles were installed. More concise attachment of the fibers to the pile shaft, especially near the pile head, can be of great benefit to these tests. Correlation of applied loads to the pile head and elongation of the effective fiber length can further improve the results and provide more information on the pile head behaviour.

The installation of 2 fiber loops on 4 sides of each pile has also proven to be effective. This manner of sensing deformations negates effects of bending during installation and each side of the fiber compensates for discrepancies on the opposing side of the pile. However, as a consequence of the installation of these fibers, a certain amount of locked-in strains may exist in the fiber itself. These strains, although minimal, may affect the conducted measurements.

7.3 Recommendations

In addition to the methodology and analysis illustrated in this report, certain aspects regarding timber piles require further analysis and assessment. The most important aspect that requires further research is the distribution of stiffness through the pile. This measure significantly affects the interpretation of strains and the correlation to loads. In the case of analyzing data obtained through fiber optic sensing, the effect of local features such as knots and branches should be further studied. Such features introduce irregularities in readings that my be perceived as noise. It can therefore be suggested to utilize these sensors with higher spatial frequencies. Reducing the gap between measurements from 25 centimeters can be beneficial and may result in more clarity of the effect of the natural features of wood.

Furthermore, residual loads can be determined in a more appropriate manner. The re-evaluation of strain recordings after installation and further study the effect of time dependent behaviour may result in a more transparent derivation of residual loads.

Additionally, for prediction of bearing capacity, the frictional contribution of peat and clay layers requires more attention. The methods used in the Dutch norm undermines the effect of such layers. Moreover, the effect of friction fatigue can be further implemented into the derivation of shaft friction.

The effect of variation in lithology on the bearing capacity of timber piles may also be of interest for further investigation. By further investigating this variation (refer to section 2.6), more information may be obtained on the effect of soft soils on friction and the influence of insertion depth on pile base capacity.

The effect of pile groups also requires further analysis. Considering the format at which piles are installed in the city of Amsterdam, the effect of pile groups may be of significant effect to bearing capacity. Considering the installation patterns of new timber piles in the test grounds, perhaps this effect could be further evaluated.

In addition to the previously mentioned aspects, more observations on time-dependent phenomena (refer to Appendix A.2.1), negative skin friction and creep-settlement on the bearing capacity of such piles is required. For safety assessment of structures founded on timber piles in the city of Amsterdam, further observations on lateral loading is also required. Alongside this, more research on the effect of degradation for old timber piles is necessary, as this was not part of this test program.

Bibliography

Aicher, S., & Stapf, G. (2016). Compressive strength parallel to the fiber of spruce with high moisture content. *European Journal Wood Products*, (74), 527–542. https://doi.org/10.1007/s00107-015-1004-z

Bersan, S., Bergamo, O., Palmieri, L., Schenato, L., & Simonini, P. (2018). Distributed strain measurements in a cfa pile using high spatial resolution fibre optic sensors. *Engineering Structures*, *160*, 554–565. https://doi.org/10.1016/j.engstruct.2018.01.046

Bolton, M. (1986). Strength and dilatancy of sands. *Geotechnique*, *36*, 65–78. https://doi.org/10.1680/geot.1986.36.1.65

Bustamante, M., & Gianeselli, L. (1982). Bearing capacity predictions bymeans of static penetrometer cpt.

Catera, P., & Morlier, P. (1994). Variability of the mechanical properties of wood randomness and determinism. *Probabilities and Materials*.

De Battista, N., Kechavarzi, C., Seo, H., Soga, H., & Pennington, S. (2016). Distributed fibre optic sensors for measuring strain and temperature of cast-in-situ concrete test piles.

De Boorder, M. (2019). *Development of a new cpt averaging technique and review of existing cpt based methods for the calculation of total pile capacity*. TU Delft.

De Nicola, A., & Randolph, M. (1993). Tensile and compressive shaft capacity of piles in sand. *Journal of Geotechnical Engineering*, *119*(12), 1952–1973. https://doi.org/10.1061/(ASCE)0733-9410(1993)119:12(1952)

de Gans, W. (2011). *De bodem onder amsterdam: Een geologische stadswandeling* (1st Edition). TNO.

Fellenius, B. (2015). Static tests on instrumented piles affected by residual load. *DFI Journal: The Journal of the Deep Foundations Institute*, *9*, 11–20. https://doi.org/10.1179/1937525515Y.0000000001

Fellenius, B. (2002a). Determining the true distributions of load in instrumented piles. https://doi.org/10.1061/40601(256)104

Fellenius, B., Brusey, W., & Pepe, F. (2000). Soil set-up, variable concrete modulus, and residual load for tapered instrumented piles in sand. https://doi.org/10.1061/40486(300)6

Fellenius, B. (1989). Tangent modulus of piles determined from strain data. *the American Society of Civil Engineers, ASCE, Geotechnical Engineering Division, 1989 Foundation Congress*, *1*, 500–510.

Fellenius, B. (1991). Pile foundations, foundation engineering handbook. In H. Fang (Ed.). Van Nostrand Reinhold.

Fellenius, B. (2002b). Determining the resistance distribution in piles: Part i. notes on shift of no-load reading and residual load, *20*, 23–27.

Gard, W. (2019). Lecture cie4110: Wood structure and properties. Delft University of Technology.

Gavin, K., Jardine, R., Karlsrud, K., & Lehane, B. (2015). The effects of pile ageing on the shaft capacity of offshore piles in sand. https://doi.org/10.1201/b18442-8

Green, D. W., Winandy, J. E., & Kretschmann, D. E. (1999). *Mechanical properties of wood* (tech. rep.).

Gregersen, O., Aas, G., & DiBiagio, E. (1975). Load tests on friction piles in loose sand. *International Journal of Rock Mechanics and Mining Sciences & Geomechanics Abstracts*, *12*, 98–98. https://doi.org/10.1016/0148-9062(75)90484-2

Hannigan, P., Goble, G., Thendean, G., Likins, G., & Rausche, F. (2006). *Design and construction of driven pile foundations* (tech. rep.). National Highway Institute, U.S. Department of Transportation, Federal Highway Administration, Washington, DC 20590.

Hansen, H. (Ed.). (1948). *Timber engineers' handbook*. Wiley, New York.

Hoekstra, J., & Bokhoven, W. (1974). *Systematisch funderings onderzoek van de dapperbuurt ("systematic foundation research in the dapperbuurt")* (tech. rep.).

Hong, C.-Y., Zhang, Y.-F., & Liu, L. (2016). Application of distributed optical fiber sensor for monitoring the mechanical performance of a driven pile. *Measurement*, *88*. https://doi.org/10.1016/j.measurement.2016.03.052

Keijer, H. (2015). *1-2-3 geologie voor ingenieurs*. Koninklijk Instituut van Ingenieurs (KIVI).

Klaassen, R., den Nijs, P., & Beusekom, G. (2000). *Bacteriële aantasting van houten paalfunderingen: Literatuurstudie en inventarisatie van de nederlandse situatie* (2nd ed.).

Korff, M. (2012). *Response of piled buildings to the construction of deep excavations* (Doctoral dissertation). University of Cambridge. IOS Press BV.

Kumar, S. (2010). Geotechnical engineering handbook. In B. Das (Ed.). J. Ross Publishing, Inc.

Latinga, C. (2015). *De resterende (geotechnische) draagkracht van bestaande houten funderingspalen*. TU Eindhoven.

Lie, J., & Zhang, M. (2012). Measurement of residual force locked in open-ended pipe pile using fbg based sensors.

Manandhar, S. (2010). *Bearing capacity of tapered piles in sands* (Doctoral dissertation). Kyushu University.

Manandhar, S., & Yasufuku, N. (2013). Vertical bearing capacity of tapered piles in sands using cavity expansion theory. *Soils and Foundations*, *53*. https://doi.org/10.1016/j.sandf.2013.10.005

Meigh, A. (1987). *Cone penetration testing - methods and interpretation*. Construction Industry Research; Information Association (CIRIA).

Meyerhof, G. (1976). Bearing capacity and settlement of pile foundations. *Geotech. Eng. Div. ASCE*.

Nordlund, R. (1963). Bearing capacity of piles in cohesionless soils. *Soil Mech. Found. Div. ASCE*.

Normcommissie 351 006 "Geotechniek". (2016). *Nen9997-1* (tech. rep.). NEN.

Randolph, M. (2003). Science and empiricism in pile foundation design. *Géotechnique*, *53*(10), https://doi.org/10.1680/geot.2003.53.10.847, 847–875. https://doi.org/10.1680/geot.2003.53.10.847

Ravenshorst, G. (2019). Email: Elasticiteitmoduli houten palen.

Ravenshorst, G. (2015). *Species independent strength grading of structural timber* (Doctoral dissertation). TU Delft.

Raymond, C., Joe, B., Evans, R., & Dickson, R. (2007). Relationship between timber grade, static and dynamic modulus of elasticity, and silviscan properties for pinus radiata in new south wales. *Carolyn A Raymond*, *37*.

Reese, L., Isenhower, W., & Wang, S.-T. (2006). *Analysis and design of shallow and deep foundations*.

Robertson, P. (2016). Cpt-based soil behaviour type (sbt) classification system – an update. *Canadian Geotechnical Journal*, *53*. https://doi.org/10.1139/cgj-2016-0044

Spruit, R. (2020). *Feitenrapportage proefbelastingen op houten palen* (tech. rep.). IB Gemeente Rotterdam.

Spruit, R., & Hutcheson, E. (2019). *Draaiboek proefopstelling houten palen* (tech. rep.). IB Gemeente Amsterdam.

Tomlinson, M., & Woodward, J. (2008). *Pile design and construction practice* (fifth Edition). Taylor & Francis.

Van Daatselaar, F. J. (2019). *The geotechnical bearing capacity of old timber piles*. TU Delft.

Van der Stoel, A. (2001). *Grouting for pile foundation improvement* (Doctoral dissertation). TU Delft. Delft University Press.

Van Mierloo, W., & Koppejan, A. (1952). Lengte en draagvermogen van heipalen, vaststelling hiervan en enige daarbij verkregen ervaringen. *Bouw 1952*.

Vijayvergiya, V., & Focht, J. (1972). A new way to predict capacity of piles in clay. *Offshore Technology Confrence, Huston*.

Wei, J. (1998). *Experimental investigation of tapered piles*. University of Western Ontario.

Wennekes, E., & Grijp, L. (2002). *De hele dag maar op en neer. over heien, heiliedjes en hoofdstedelijke muziekgebouwen*. Meertens Instituut i.s.m. Het Muziekgebouw.

Xu, X. (2007). *Investigation of the end bearing performance of displacement piles in sand* (Doctoral dissertation).

Zantkuijl, H. J. (1993). *Bouwen in amsterdam - het woonhuis in de stad*. Architectura & Natura.

Appendices

Appendix A

Additional Background Information and Preliminary Results

A.1 Overview of Bearing Capacity Calculation Methods

The general form of load carrying capacity for a pile is formulated as illustrated in equation A.1, where Q_s and Q_b are load resistance due to friction, and at the pile tip respectively.

$$Q_T = Q_s + Q_b \tag{A.1}$$

The transfer of load through a pile, depending on arbitrary magnitudes of applied forces, is illustrated in Figure A.1. Upon application of load on top of the pile, a certain measure of "movement" and "insertion" must take place before both shaft friction and point resistance are fully mobilized. Literature has shown that, for soil-displacement piles, the required movement to mobilize Q_s amounts to an approximate measure of 5 to 8 millimeters whereas the movement required before the base capacity is mobilized is approximately 10% of the pile diameter (Kumar, 2010).

The general calculation method illustrated in equation A.1 can be reformulated into many different equations. Each existing prediction method consists of unique aspects that take specific factors into consideration. Different calculation methods utilize factors that can be related to site investigation findings such as CPT and SPT. The methods may also base the measurements on the stress regime that is present in the subsurface. The usage of parameters from a CPT is due to the fact that the driving of a cone penetrometer and a pile have similarities in behaviour. The main difference between the two is however the fact that driving a CPT into the ground is displacement-controlled, whereas the insertion of a pile is displacement controlled. This project focuses only on the CPT-based methods due to availability of data and common practice in the Netherlands. However, other methods are presented here as they were used throughout the project for confirmation and assessment of results. The different methods are discussed in the following sections.

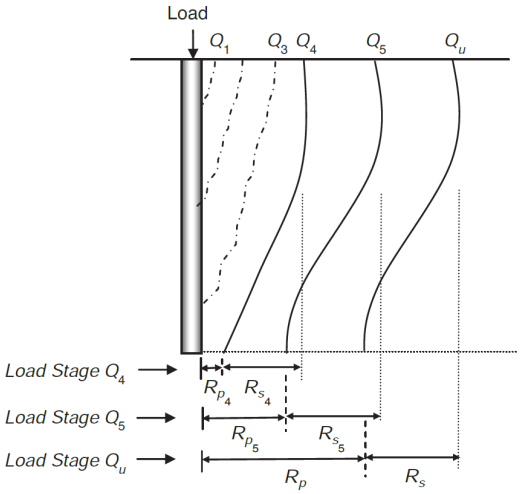

Figure A.1: Load Transfer Mechanism in Deep Foundations
Reprinted from Kumar, 2010

A.1.1 Overview of Available Prediction Methods

General Calculation for Cohesion-less Soils

The determination of the point capacity is illustrated as below where A_p is the pile tip area, q' is the effective overburden pressure, c is cohesion at pile tip and the N factors are bearing capacity factors related to length and diameter of piles.

$$q_p = cN_c^* + q'N_q^* \tag{A.2}$$

$$R_p = q_p A_p = (cN_c^* + q'N_q^*) \times A_p \tag{A.3}$$

Skin friction capacity is determined as below with $\delta = (0.5\ to\ 0.8)\phi$, the equation illustrates friction for a segment of the pile with a length of ΔL. K, p, and $(q')_z$ are the pressure coefficient, perimeter and effective vertical pressures respectively.

$$\Delta R_s = K \times (q')_z \times tan(\delta) \times p \times \Delta L \tag{A.4}$$

$$R_s = \sum \Delta R_s \tag{A.5}$$

Studies have illustrated that the unit frictional resistance of piles embedded in cohesion-less soils increases with depth (Kumar, 2010). This increase tends to plateau out after a certain depth and remain at a constant measure. This is illustrated in Figure A.2. This depth is referred to as critical depth and is observed to vary between 15 to 20 times the pile diameter.

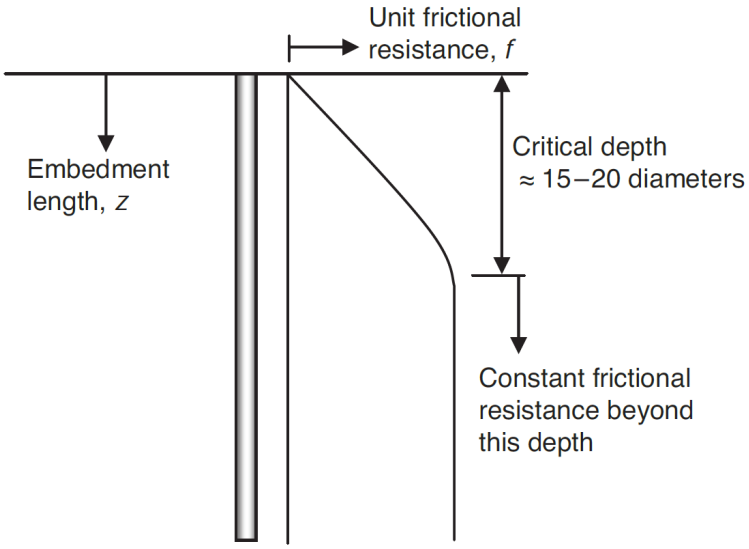

Figure A.2: Conceptualization of critical depth.
Reprinted from Kumar, 2010

It's stated that the K coefficient varies between 0.5 and 1.5 based on factors such as installation technique, roughness of the pile surface, type of soil, etc. The following values are commonly used in practice, despite the fact that K varies with depth, with $K_0 = 1 - sin(\phi)$. Equation A.6 is for bored or jetted piles, A.7 for low-displacement driven piles and A.8 for high-displacement driven piles.

$$K = K_0 \tag{A.6}$$

$$K \cong 1.4K_0 \tag{A.7}$$

$$K \cong 1.8K_0 \tag{A.8}$$

Meyerhof Method for Cohesion-less Soils

The method of Meyerhof (1976) relies on measures derived from standard penetration tests (SPTs). It was proposed by Meyerhof in 1976 that N_c^* and N_q^* are to be estimated from Figure A.3 and act as inputs for the following equation.

$$R_p = A_p \times (q' N_q^*) \tag{A.9}$$

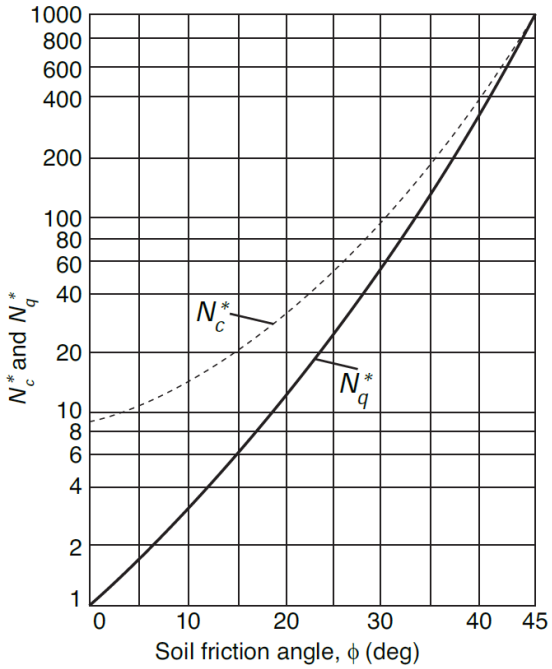

Figure A.3: Meyerhof, 1976 bearing capcaity factors
reprinted from Kumar, 2010

It was also observed that once the L_b/D ratio reaches a critical value, the point capacity reaches a limiting value in contrast with it's initial increase with depth. Therefore, based on field observations the limiting point capacity can be determined using;

$$(R_p)_lim = A_p \times (50 \times N_q^* tan(\phi)) \tag{A.10}$$

If the pile is embedded at least at a measure of $10D$, the point capacity can be determined using SPT data as below, where N_{cor} is the average corrected SPT N-value between $10D$ above and $3D$ below the pile tip.

$$R_p = A_p \times \left[40(N_{cor})\left(\frac{L}{D}\right)\right] \leq A_p \times [400(N_{cor})] \tag{A.11}$$

For the evaluation of skin friction, this method suggested the means of conducting calculations again based on SPT values.

$$R_s = \sum 2(N_{cor})pL \leq 100pL \tag{A.12}$$

Nordlund method for Cohesion-less Soils

Nordlund (1963) proposed this method which considers the increasing of skin friction along tapered piles and takes the mobilization of displaced soil volume into account. Figure A.4 Illustrates the schemitization of variables considered by Nordlund (1963).

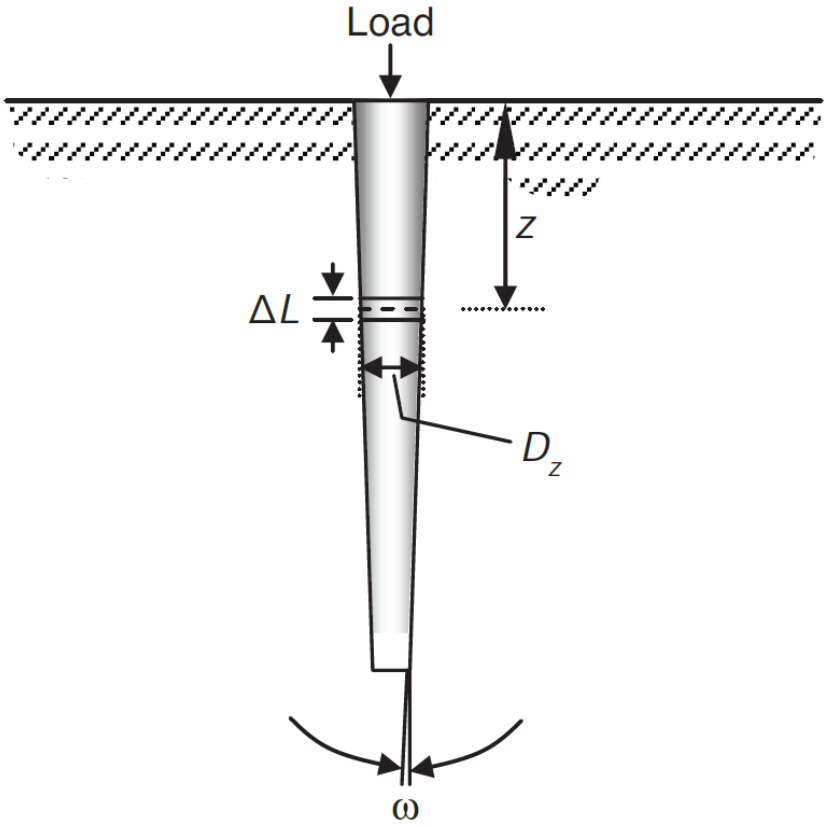

Figure A.4: Variables Considered by the Nordlund Method
reprinted from Kumar, 2010

The point capacity is to be estimated as below, where the factor α (dependent on ϕ and L/D) and N_q^*, a bearing capacity factor, can both be determined from charts shown in Figure A.5.

$$R_p = \alpha q' N_q^* A_p \tag{A.13}$$

The skin friction is proposed to be estimated using the equation illustrated below. In this formulation δ is the friction angle between the soil and pile material, ω is the pile taper angle with the vertical plane, z is the depth from the ground line, L is the length of the pile, ΔL is the pile length increment, K_δ is the coefficient of lateral earth pressure at depth z based on the angle of pile taper and displaced soil volume V, and C_F is the correction factor for K_δ when $\delta = \phi$.

$$R_s = \sum_{z=0}^{z=L} K_\delta C_F (q')_z \frac{sin(\delta + \omega)}{cos(\omega)} D - z\Delta L \tag{A.14}$$

The aforementioned coefficients are determined through a series of graphs as illustrated in Figure A.5.

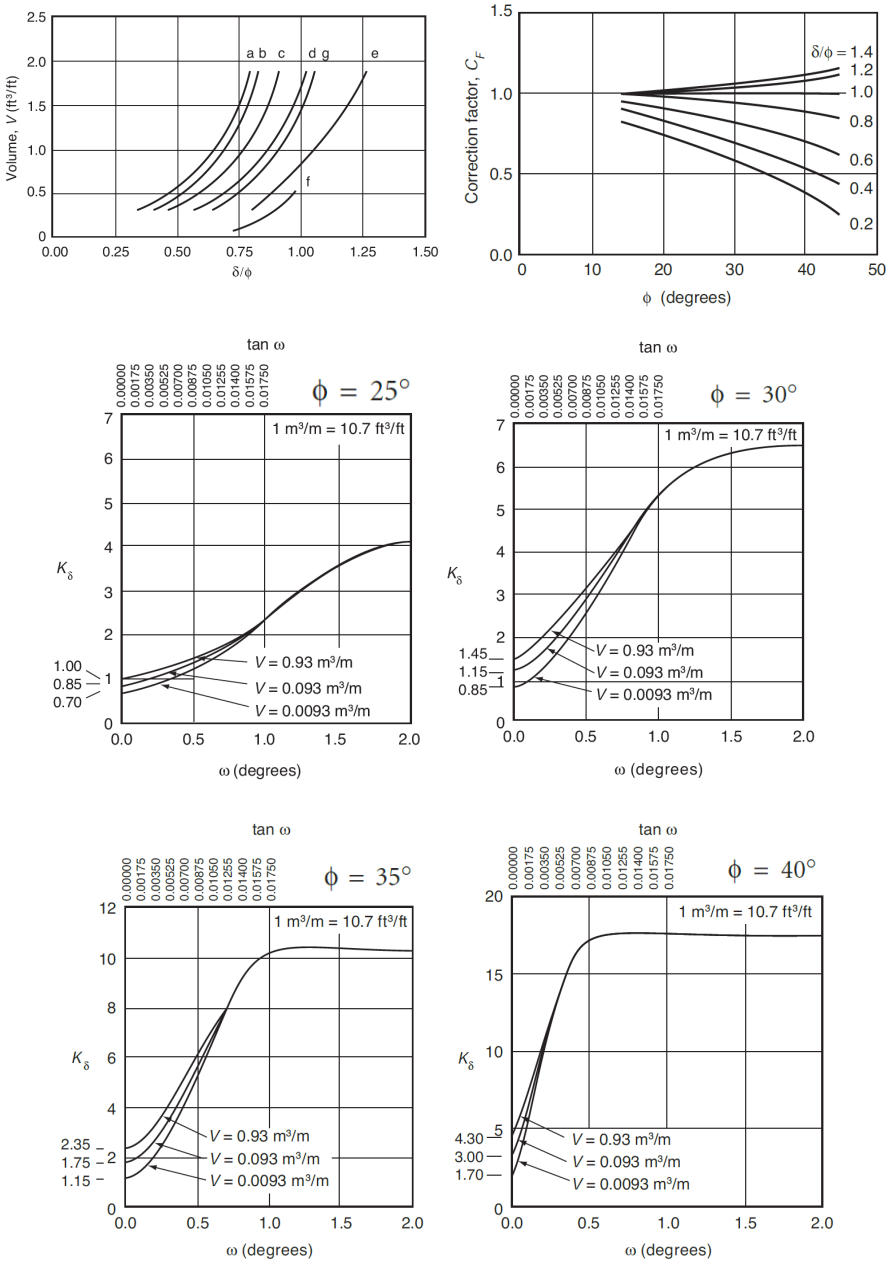

Figure A.5: Skin Friction Factor Determination for the Nordlund Method. Adapted from Hannigan et al., 2006 and reprinted from Kumar, S. (2010). Geotechnical engineering handbook. In B. Das (Ed.). J. Ross Publishing, Inc.

The Effective Stress Method

This method applies to both cohesive and cohesion-less soils. The point capacity determination illustrated below was proposed by Fellenius, 1991. The values of N_t can be found in Table A.1.

$$R_p = A_p \times (q' N_t) \tag{A.15}$$

Table A.1: N_t values for different soil types
Based on Fellenius, 1991; adapted from Hannigan et al., 2006

Soil Type	**Effective Soil Friction Angle φ**	**Bearing Capacity Coefficient N_t**
Clay	25-30	3-30
Silt	28-34	20-40
Sand	32-40	30-150
Gravel	35-45	60-300

The skin friction can be estimated as below. here the factor β is the Bjerrum-Burland coefficient. The values for this coefficient are presented in Table A.2.

$$R_s = \sum p \times \Delta L \times \beta \times (q')_z \tag{A.16}$$

Table A.2: β values for different soil types
Based on Fellenius, 1991; adapted from Hannigan et al., 2006

Soil Type	**Effective Soil Friction Angle φ**	**Beta Coefficient β**
Clay	25-30	0.23-0.40
Silt	28-34	0.27-0.50
Sand	32-40	0.30-0.60
Gravel	35-45	0.35-0.80

Shaft Friction Calculation Methods for Cohesive Soils

The basic rule for estimating skin friction can be applied to piles embedded in clays with a different approach to the determination of the unit friction factor f. The three most common methods for acquiring this unit are the *lambda*-, *alpha*- and *beta*-methods. The *beta*-method is the same as the effective stress method described previously.

$$R_s = \sigma p \Delta L f \tag{A.17}$$

λ-Method: According to this method, the skin friction in clays is determined through the equation below, which was proposed by Vijayvergiya and Focht, 1972. The factor λ is dependent on the embedment length of the pile and is determined using Figure A.6. p and L are the perimeter and length of the pile respectively, σ'_0 is the mean effective vertical stress and c_u is the undrained shear strength.

$$R_s = p \times L \times \lambda(\sigma'_0 + 2\bar{c}_u) \tag{A.18}$$

The effective stress and undrained shear strength for a multi-layered system can be calculated using weighted and linear average methods such as below;

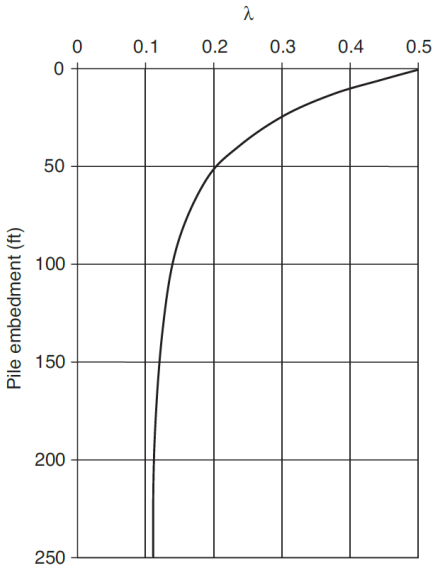

Figure A.6: Pile Embedment Length versus λ
Reprinted from Kumar, 2010, Data from Vijayvergiya and Focht, 1972

$$\bar{c}_u = \frac{c_{u_1} L_1 + c_{u_2} L_2 + c_{u_3} L_3 + ...}{L_1 + L_2 + L_3 + ...} \tag{A.19}$$

α-Method: According to this method the increment of skin friction can be calculated as below. This factor is dependent on strength of the clay, pile dimensions, roughness of the pile surface, installation method and time stages for installation.

$$\Delta R_s = p \times \Delta L \times \alpha \times c_u \tag{A.20}$$

$$R_s = \sum \Delta R_s = \sum p \times \Delta L \times \alpha \times c_u \tag{A.21}$$

Shaft Friction in Holocene Layer

Tomlinson and Woodward, 2008 suggest the a method below to calculate the shaft friction in the Holocene layer based on the undrained shear strength c_u, where h is the layer thickness and $\tau = \alpha \cdot c_u$.

$$R_s = \tau \cdot \pi \cdot D \cdot h \tag{A.22}$$

Meigh, 1987 suggest the following method to calculate the shaft resistance for a driven timber pile in cohesion-less soils, where q_c is the average cone resistance of the embedment.

$$R_s = \frac{q_c}{80} A_s \tag{A.23}$$

De Nicola and Randolph, 1993 suggests a reduction factor, R_t/R_c, for the shaft friction calculations in compress and tension. This is illustrated below where L/D is the slenderness of the pile, ν_p the Poisson's ratio of the pile, G_{ave} the average shear modulus of the sand, E_p the Young's modulus of the pile and δ is the interface friction angle. The reduction factor for the tests conducted here amount to an approximate value of 0.9.

$$\frac{R_t}{R_c} \approx (1 - 0.2log_{10}(\frac{100}{\frac{L}{D}}))(1 - 8\eta + 25\eta^2) \tag{A.24}$$

$$\eta = \nu_p \frac{L}{D} \frac{G_{ave}}{E_p} tan(\delta) \tag{A.25}$$

Ultimately, the factor 1.2 is taken between values in compression and tension (1.2 times the tension = compression).

Base Capacity in Foundation Layer

Tomlinson and Woodward, 2008 suggest the following method for the calculation of the base capacity where the factor N_q is based on the ratio of the pile diameter to depth of penetration and is dependent on the friction angle of the soil.

$$R_b = N_q \cdot \sigma'_{v0} \cdot A_b \tag{A.26}$$

A.2 Effect of Pile Driving on Pile Capacity

Pile driving often results in substantial disturbance and remolding of the surrounding soil and also changes in pore water pressure. Pile driving in cohesion-less soils tends to increase the relative density of loose and medium densely packed soils (Kumar, 2010).

Certain influential factors that affect the bearing capacity of piles are directly related to the installation procedure. These processes consist of but are not limited to cavity expansion, soil compaction, soil dilation, the restructuring of soil grains and residual loads. All but one of these phenomena are briefly discussed in order to paint a clearer picture of the different phenomena influencing the capacity of piles. The concept of residual loads are discussed in detail in section 2.5.

Compaction, Dilation and Restructuring of Soil Grains

Upon installation, the soil body surrounding the pile is to either dilate or compact, depending on the relative density and confining stress regime that is present (Bolton, 1986). Such changes are distinctly significant when analyzing the shaft capacity of a pile. The effect can be simply put as an increase in shear strength upon dilation and the opposite upon compaction. It is of significance however to note that at the base of the pile, the high stresses during driving result in compaction and crushing of the grains for the duration of the driving procedure.

Cavity Expansion

The theory of cavity expansion is best illustrated by Figure A.7. Throughout installation, the soil surrounding the pile is pushed outwards as illustrated in Figure A.7a. At the pile base, the displaced soil forms a spherical expansion and along the length of the pile, the expansion is cylindrical. This expansion, called cavity expansion, results in the occurrence of excess pore pressures around the pile , which ultimately results in a reduction in shear forces during installation (Randolph, 2003). The extent of this phenomena is dependent on soil properties and the installation method.

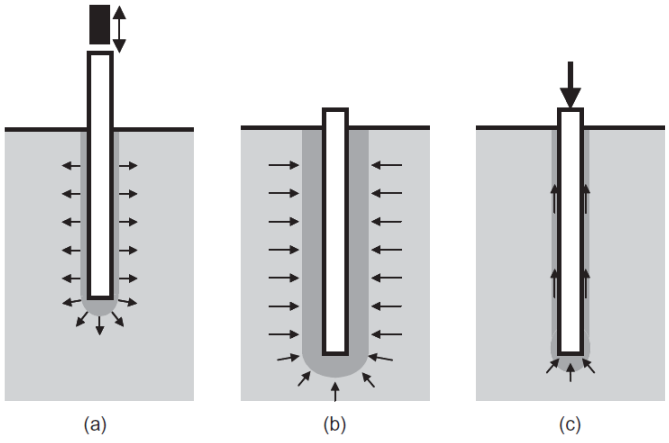

Figure A.7: Phases during History of Driven Piles
Reprinted from Randolph, 2003

A.2.1 Time Dependant Effects

Upon completion of pile installation, a series of processes take effect and begin developing. These processes are time dependent and influence the ultimate bearing capacity. One of the more significant processes occurring as a time dependent phenomena is the dissipation of excess pore pressures that were initiated during the installation process. This dissipation ultimately results in the consolidation of the soil body and is known as equalization (Randolph, 2003). This process is schematized in Figure A.7b.

Another time dependant effect can be described as a positive gain in pile capacity due to the recovery of the shear surface of the surrounding soil (Gavin et al., 2015). This phenomena mostly concerns the shaft capacity as the base capacity is prone to very little change through time (Gavin et al., 2015).

A.3 Additional Information on Wooden Piles

A.3.1 Internal Structure of Wood

Figure A.8 Illustrates the micro structure of a coniferous wood sample. The structure is consistent of long strands connected together small openings in the cell wall. These openings, called pits, allow for fluids to flow through cells.

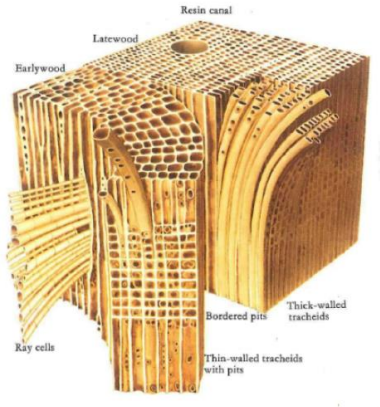

Figure A.8: Coniferous Wood Micro-structure.
Reprinted from Gard, 2019

A.3.2 Effect of Degradation

Van Daatselaar (2019) conducted a study on the effect of degradation on the bearing capacity of timber piles in Amsterdam. This study refers to Klaassen et al., 2000 to outline the general concept of bacterial decay on wooden piles. According to the conducted study, biological wood degradation can be categorized into two types. The categories of degradation are degradation due to fungi and degradation due to bacteria. Degradation due to fungi often occurs at the pile head as it can only develop due to alterations of the water level causing the pile to be above the groundwater table. This requirement is simply due to the fact that fungi require oxygen to trigger the degradation process.

Considering the fact that bacteria do not necessarily require oxygen for survival, they are capable of causing decay along the entire length of the pile. The study conducted by Van Daatselaar, 2019 therefore focuses mostly on this type of degradation as the piles that are studied are fully submerged and definitely under the existing groundwater table. It is important to note that degradation has no effect on the study conducted in this report as the piles have not been in the soil body long enough for bacterial decay to occur.

It has been stated in the past that bacterial degradation has no effect on the geotechnical bearing capacity of timber piles. However, tests performed in Dapperbuurt proved that the shaft friction of said old piles is 40% lower compared to new piles (Korff, 2012). Some argue that bacterial slime is the cause of this reduction in friction.

The results obtained from the conducted laboratory tests by Van Daatselaar (2019) do not show a significant alteration of friction angles for fresh samples and old samples.

A decrease in friction was noticed at the interface upon application of a slime layer to a fresh sample. Overall, there was no evident confirmation of a reduction in shaft friction through conducting laboratory tests. This seems to be mostly due to the logistics and the physicality of the test set-up. The experiment might therefore not be appropriate to draw conclusions from regarding the initial problem statement.

A.3.3 Wig-form Phenomena Upon Loading

The expansion of pile head in the form of separate wood fibers can be defined as a wig-forming phenomena. This phenomena occurs upon loading the pile excessively in load or time. This phenomena results in shortening and compression of the pile and can be avoided by means of cutting the pile head more appropriately and using a plate to cover the pile head sufficiently.

A.3.4 Effect of Moisture Content and Temperature

Figure A.9 A through C illustrates the effect of moisture content on wood. Figures D through F illustrate the effect of temperature on timber.

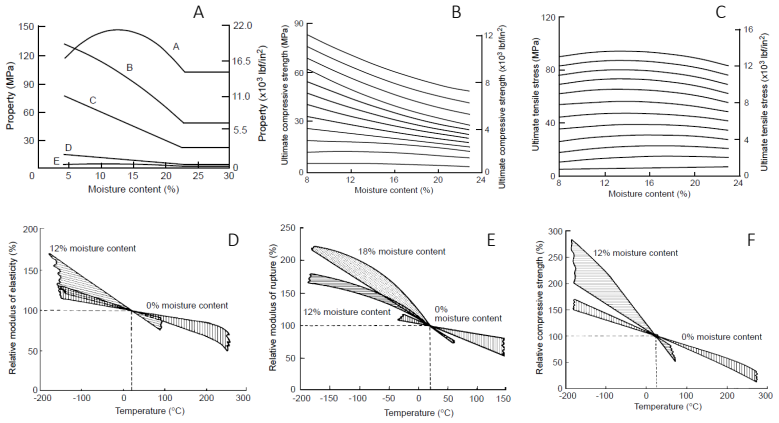

Figure A.9: Effect of Temperature and Moisture Content.
Reprinted from Green et al., 1999

In Figure A.9A, each curve is representative of a certain property. These properties are listed as below.

- A: Tension parallel to grain
- B: Bending
- C: Compression parallel to grain
- D: Compression perpendicular to grain
- E: Tension perpendicular to grain

A.4 Additional Information on Previous Pile Load Tests

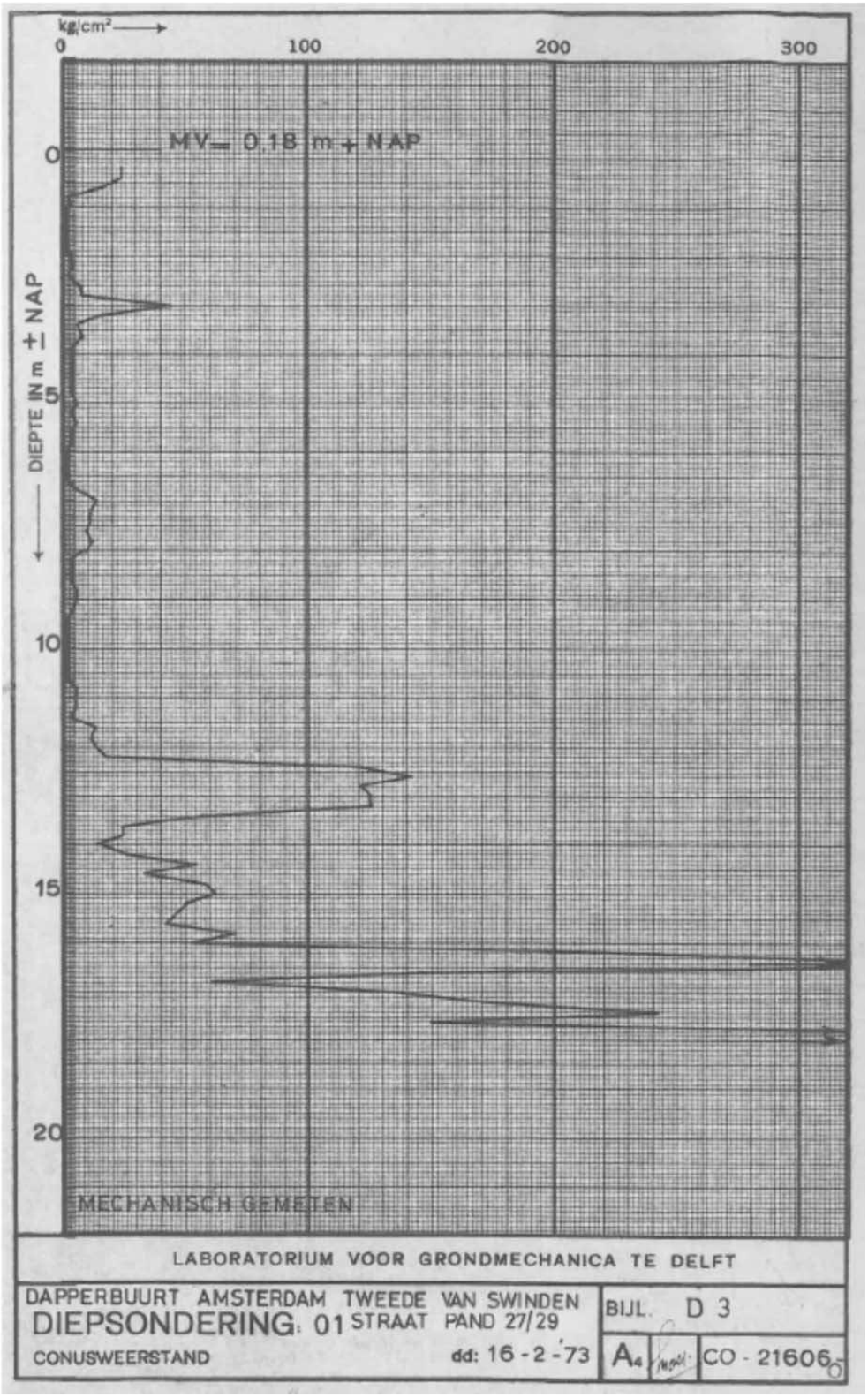

Figure A.10: CPT from Dapperbuurt Test Site
Reprinted from Korff, 2012

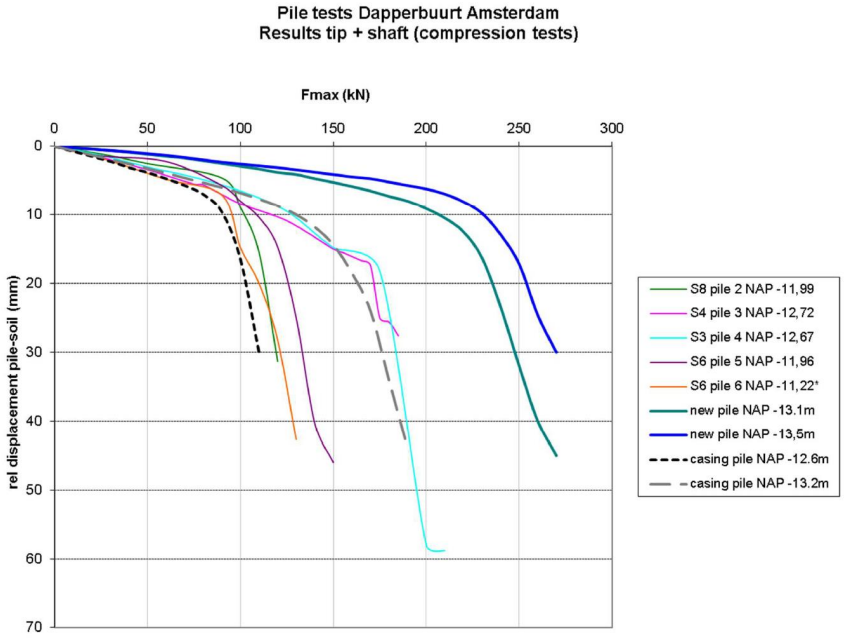

Figure A.11: Load-Displacement Curves in Compression - Dapperbuurt
Reprinted from Korff, 2012

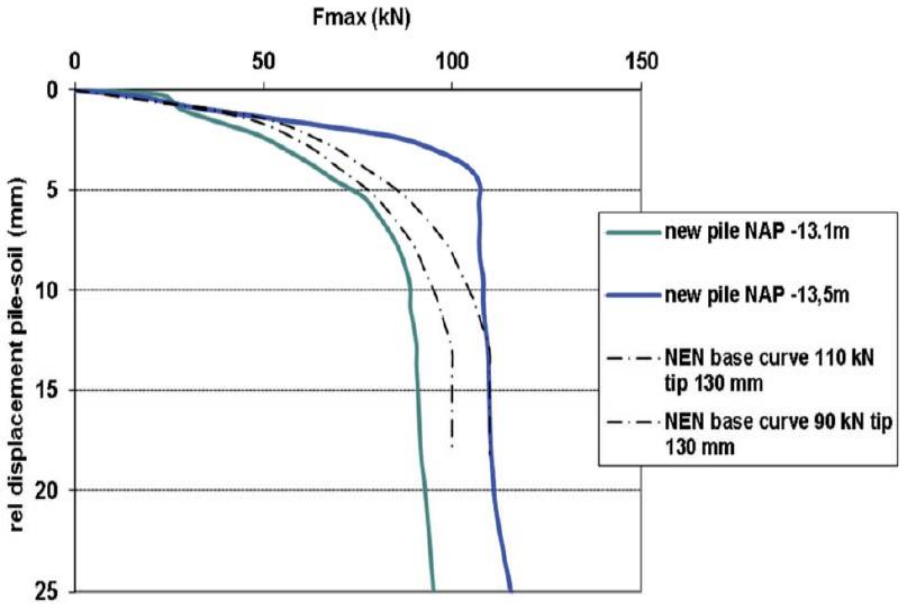

Figure A.12: Base Load-Displacement Curves in Compression - Dapperbuurt
Reprinted from Korff, 2012

A.5 Additional Information on Modulus of Elasticity

A.5.1 Determination of Modulus of Elasticity: Fellenius Method

Fellenius, 1989 introduced a method to determine the modulus of elasticity through obtaining a tangent line to the derivative of stress in terms of strain. This method is summarized in the following.

$$M = \frac{d\sigma}{d\varepsilon} = a\varepsilon + b \tag{A.27}$$

$$\sigma = a\varepsilon^2 + b\varepsilon \tag{A.28}$$

$$\sigma = E_s\varepsilon \tag{A.29}$$

$$E_s = 0.5a\varepsilon + b\varepsilon \tag{A.30}$$

Parameter Description for Equations A.27 to A.30

Parameter	**Description**	**Unit**
a	Slope of the tangent modulus line	$[GPa]$
b	y-Intercept of the tangent modulus line	$[kPa]$
M	Tangent stiffness	$[GPa]$
E_s	Secant stiffness	$[GPa]$
σ	Stress	$[kPa]$
ε	Measured strain	$[\mu e]$
$d\varepsilon = \varepsilon_{i+1} - \varepsilon_1$	Change of strain from one reading to the next	$[\mu e]$
$d\sigma = \sigma_{i+1} - \sigma_1$	Change of stress from one reading to the next	$[kPa]$

This method was used in the evaluation of pile stiffness moduli but was discarded. The resultant E-moduli had extremely high values for the intercept of the tangent line at the tip which could be due to lack of readings. Figure A.13 illustrates an example of this method conducted on pile 164. An estimate was made as an average a and b value based on weighted averaging for each segment of the pile. The resultant values were quite close to the dynamic E-moduli of the pile. These values are summarized in table A.3. This method was applied before the consideration of piles 398 and 397.

Table A.3: Resultant a and b Values for Fellenius's Method of Stiffness Determination

Pile	**Tangent**	
ID	a	b
164	-0.0063	13.607
175	-0.005	12.604
177	-0.0025	12.079
573	0.0	11.273
592	-0.0041	13.521
576	0.0	14.419

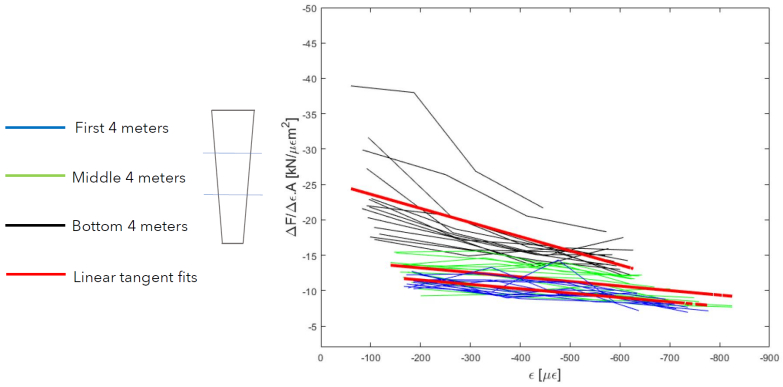

Figure A.13: Fellenius's Method of Stiffness Determination Applied to Pile 164

A.5.2 Dynamic Modulus of Elasticity

The dynamic E-moduli of the analyzed piles are summarized in the following table.

Table A.4: MOE_{dyn}

Pile ID	Category	MOE_{dyn}[GPA]
164	A	15.36
175	A	16.99
398	B	12.06
397	B	16.55
573	C	14.00
592	C	12.60
576	C	14.52
594	C	10.79

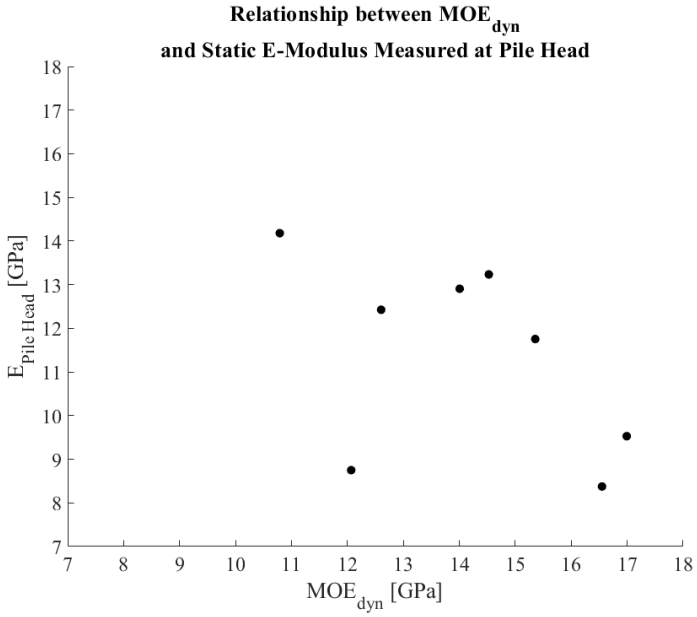

Figure A.14: Relationship between MOE_{dyn} and $E_{pile\ head}$

Appendix B

Lithology and Soil Conditions

B.1 Laboratory and Borehole Data

The following pages illustrate the borehole details taken from the test site.

Figure B.1: Borehole From Test Site 1

Figure B.2: Borehole From Test Site - 2

Dossiernummer: LAB2019-180

Projectnaam: Amsterdam Proeftuin MVB19090

Gemeente Rotterdam

Veld- en laboratoriummetingen Gww
Afdeling laboratorium

Boring: B01 - 1

mv m tov NAP: 0,03
X-coördinaat: 122861,99
Y-coördinaat: 483323,11

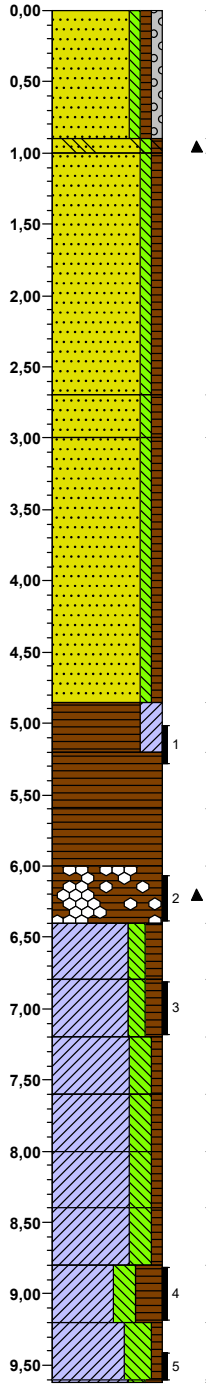

		mk	Yw [kN/m3]	Yd [kN/m3]	w [%]	n [%]	e	Sr [%]	cu [kPa]
0,03	Zand, matig fijn, zwak siltig, zwak humeus, zwak grindig								
-0,87									
-0,97	Zand, matig fijn, zwak siltig, zwak humeus, laagjes klei								
	Zand, matig fijn, zwak siltig, zwak humeus								
-2,67									
	Zand, matig grof, zwak siltig, zwak humeus								
-2,97									
	Zand, matig fijn, zwak siltig, zwak humeus								
-4,82									
	Veen, sterk kleïg	1	12,2	6	103,3				36
-5,17									
	Veen	1	10,2	2	410				47
-5,57									
	Veen	1	10,3	2	415				33
-5,97									
	Veen, sporen zand	1	9,8	2,4	308,3				
-6,37									
	Klei, matig siltig, matig humeus	1	15,4	9,3	65,6	64,9	1,85	94	23
-6,77									
	Klei, matig siltig, matig humeus								
-7,17									
	Klei, sterk siltig, zwak humeus	1	17,7	13,2	34,1	50,2	1,01	89,7	14
-7,57									
	Klei, sterk siltig, zwak humeus	1	17,8	13,3	33,8	49,8	0,99	90,3	15
-7,97									
	Klei, sterk siltig, zwak humeus	1	17,2	12,6	36,5	52,5	1,1	87,7	18
-8,37									
	Klei, sterk siltig, zwak humeus	1	17,5	13	34,6	50,9	1,04	88,3	11
-8,77									
	Klei, sterk siltig, uiterst humeus								
-9,17									
	Klei, uiterst siltig, zwak humeus	1	17,3	12,7	36,2	52,1	1,09	88,3	14
-9,59									
	Klei, matig siltig, matig humeus	1	14,4	8,6	67,4	67,5	2,08	85,9	29

Opdrachtgever: Gemeente Rotterdam		Uitwerkingsdatum: 16-10-2019	
Laborant: D.v.Mourik		Getekend volgens: NEN 5104	Schaal: 1: 50
Projectleider: D. Zandbergen		Printdatum: 19-10-2019	Pagina: 1 / 2

Dossiernummer: LAB2019-180

Projectnaam: Amsterdam Proeftuin MVB19090

Gemeente Rotterdam

Veld- en laboratoriummetingen Gww
Afdeling laboratorium

Boring: B01 - 2

mv m tov NAP: 0,03
X-coördinaat: 122861,99
Y-coördinaat: 483323,11

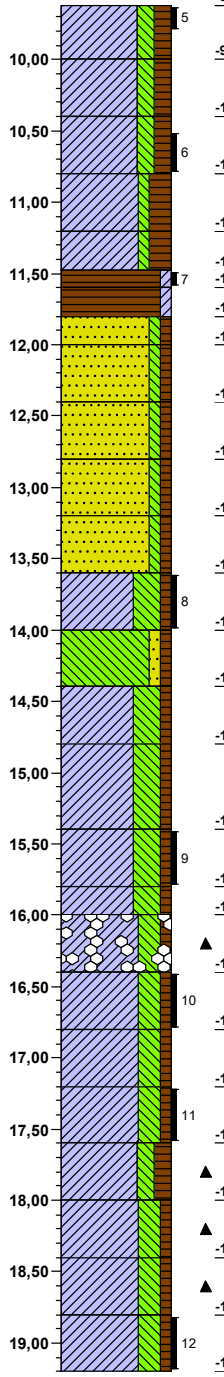

		mk	Yw [kN/m3]	Yd [kN/m3]	w [%]	n [%]	e	Sr [%]	cu [kPa]
-9,59									
	Klei, matig siltig, matig humeus	1	14,4	8,6	67,4	67,5	2,08	85,9	29
-9,97									
	Klei, matig siltig, matig humeus	1	15	8,7	72,4	67,2	2,05	93,8	28
-10,37									
	Klei, matig siltig, matig humeus	1	14,4	7,8	84,6	70,6	2,4	93,5	16
-10,77									
	Klei, zwak siltig, sterk humeus	1	12,3	5,5	123,6				36
-11,17									
	Klei, zwak siltig, sterk humeus	1	12,4	5,2	138,5				32
-11,45									
-11,57	Veen, zwak kleiïg								
-11,77	Veen, zwak kleiïg	1	10,8	2,9	272,4				49
-11,97	Zand, matig fijn, zwak siltig, zwak humeus	3							
	Zand, matig fijn, zwak siltig, zwak humeus	3							
-12,37									
	Zand, zeer fijn, zwak siltig, zwak humeus	3							
-12,77									
	Zand, zeer fijn, zwak siltig, zwak humeus	3							
-13,17									
	Zand, zeer fijn, zwak siltig, zwak humeus	3							
-13,57									
	Klei, uiterst siltig, zwak humeus								
-13,97									
	Leem, zwak zandig, zwak humeus	1	19,4	16,4	18,3	38,1	0,62	78,7	17
-14,37									
	Klei, uiterst siltig, zwak humeus	1	18,9	15,6	21,2	41,1	0,7	80,2	14
-14,77									
	Klei, uiterst siltig, zwak humeus	1	19	15,5	22,6	41,5	0,71	84,3	15
-15,37									
	Klei, uiterst siltig, zwak humeus								
-15,77									
-15,97	Klei, uiterst siltig, zwak humeus	1	18,3	14,3	28	46	0,85	86,9	11
	Klei, sterk siltig, zwak humeus, laagjes zand	1	16,9	12,6	34,1	52,5	1,1	82	22
-16,37									
	Klei, sterk siltig, zwak humeus								
-16,77									
	Klei, sterk siltig, zwak humeus	1	17,1	12,4	37,9	53,2	1,14	88,3	20
-17,17									
	Klei, sterk siltig, zwak humeus								
-17,57									
	Klei, matig siltig, matig humeus, zwak schelphoudend	1	15,5	10	55	62,3	1,65	88,3	44
-17,97									
	Klei, sterk siltig, zwak humeus, zwak schelphoudend	1	16,9	11,8	43,2	55,5	1,25	91,9	41
-18,37									
	Klei, sterk siltig, zwak humeus, zwak schelphoudend	1	16,7	11,9	40,3	55,1	1,23	87,1	15
-18,77									
	Klei, sterk siltig, zwak humeus								
-19,17									

Opdrachtgever: Gemeente Rotterdam		Uitwerkingsdatum: 16-10-2019	
Laborant: D.v.Mourik		Getekend volgens: NEN 5104	Schaal: 1: 50
Projectleider: D. Zandbergen		Printdatum: 19-10-2019	Pagina: 2 / 2

B.2 CPT's for Analyzed Piles

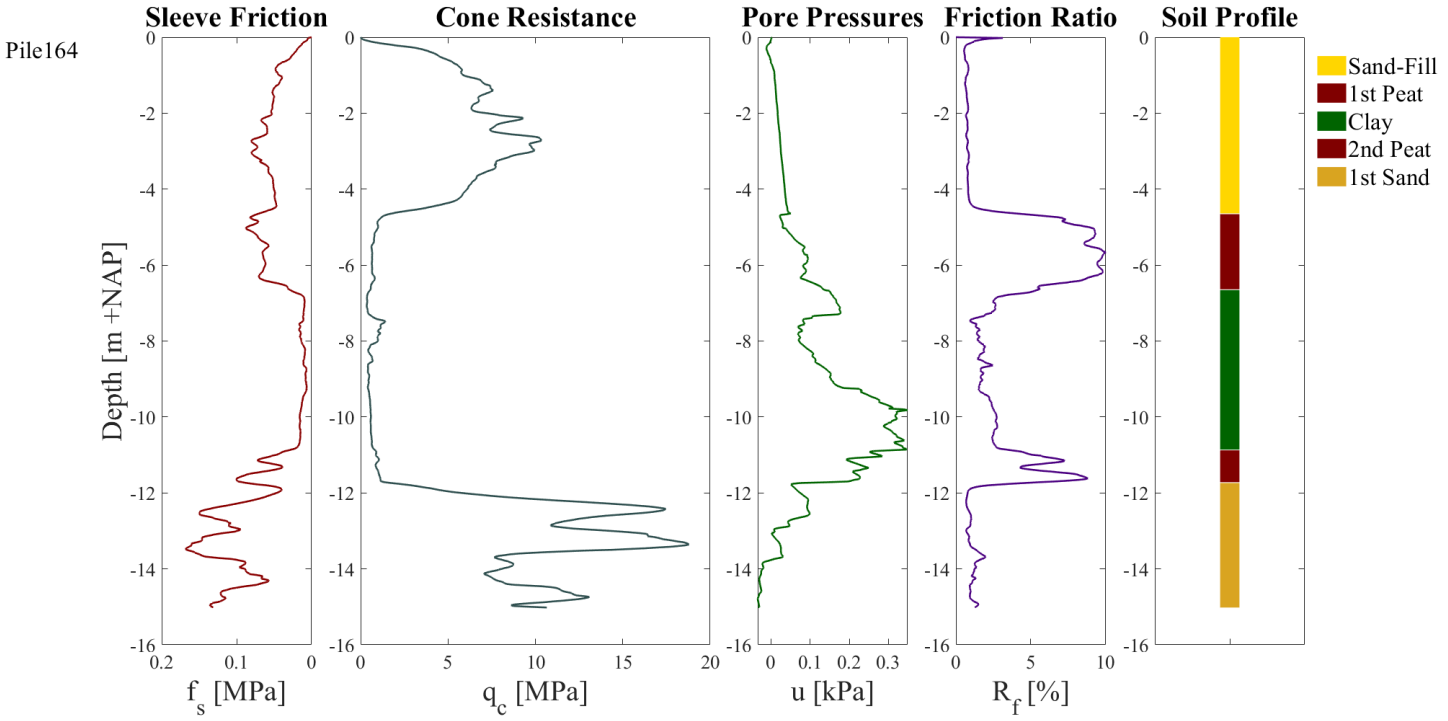

Figure B.3: CPT Pile 164

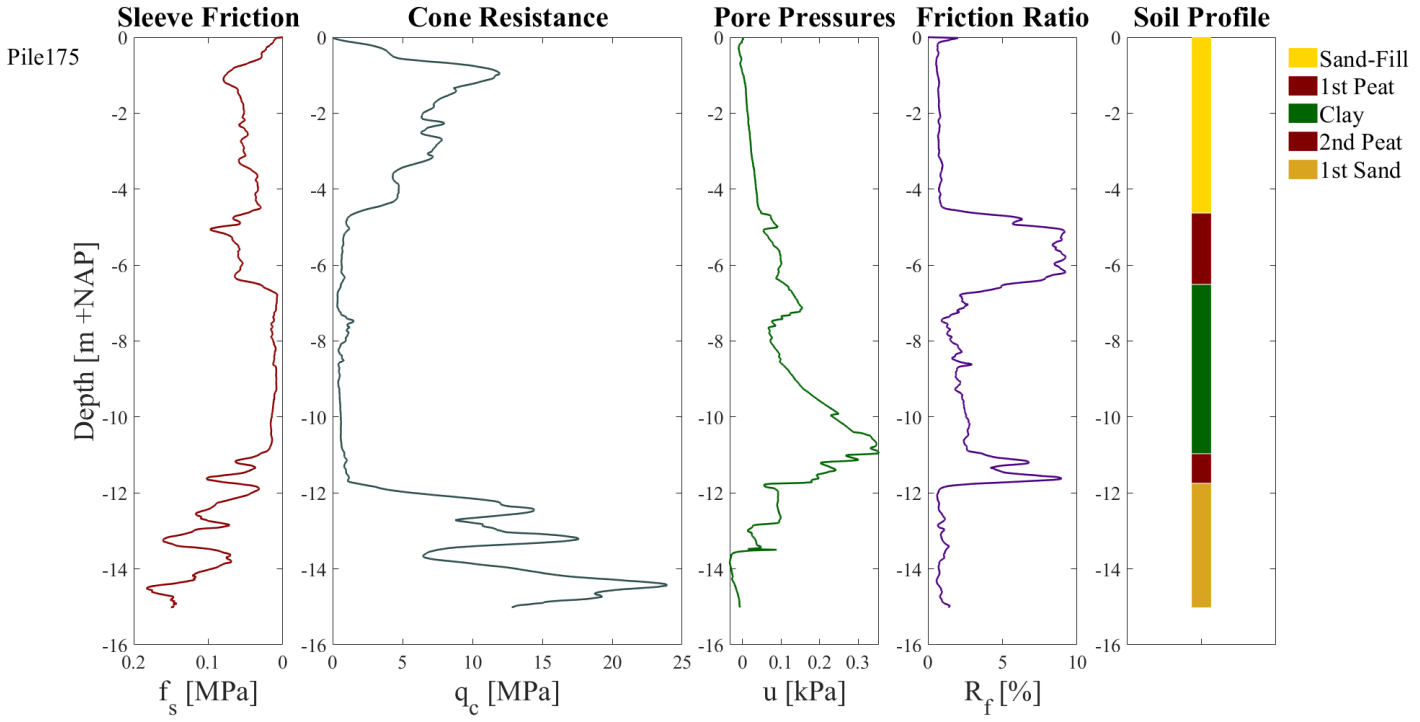

Figure B.4: CPT Pile 175

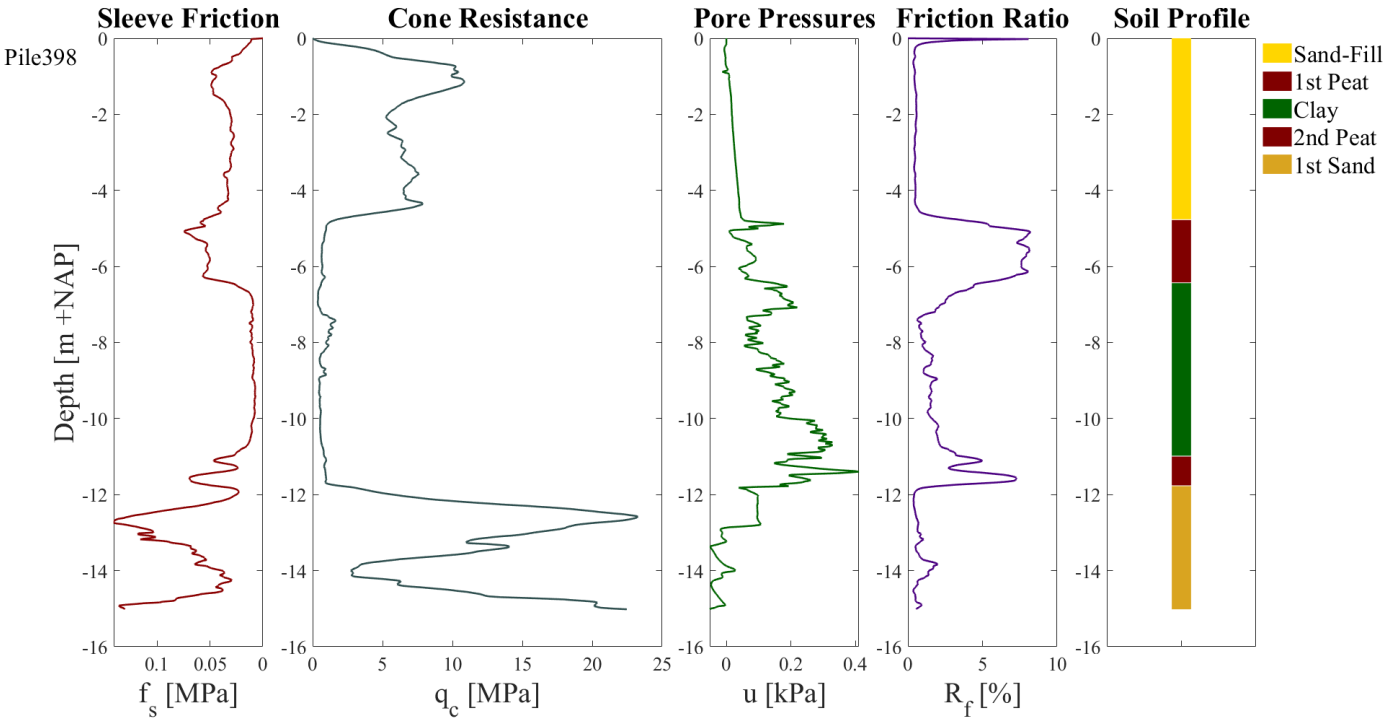

Figure B.5: CPT Pile 397

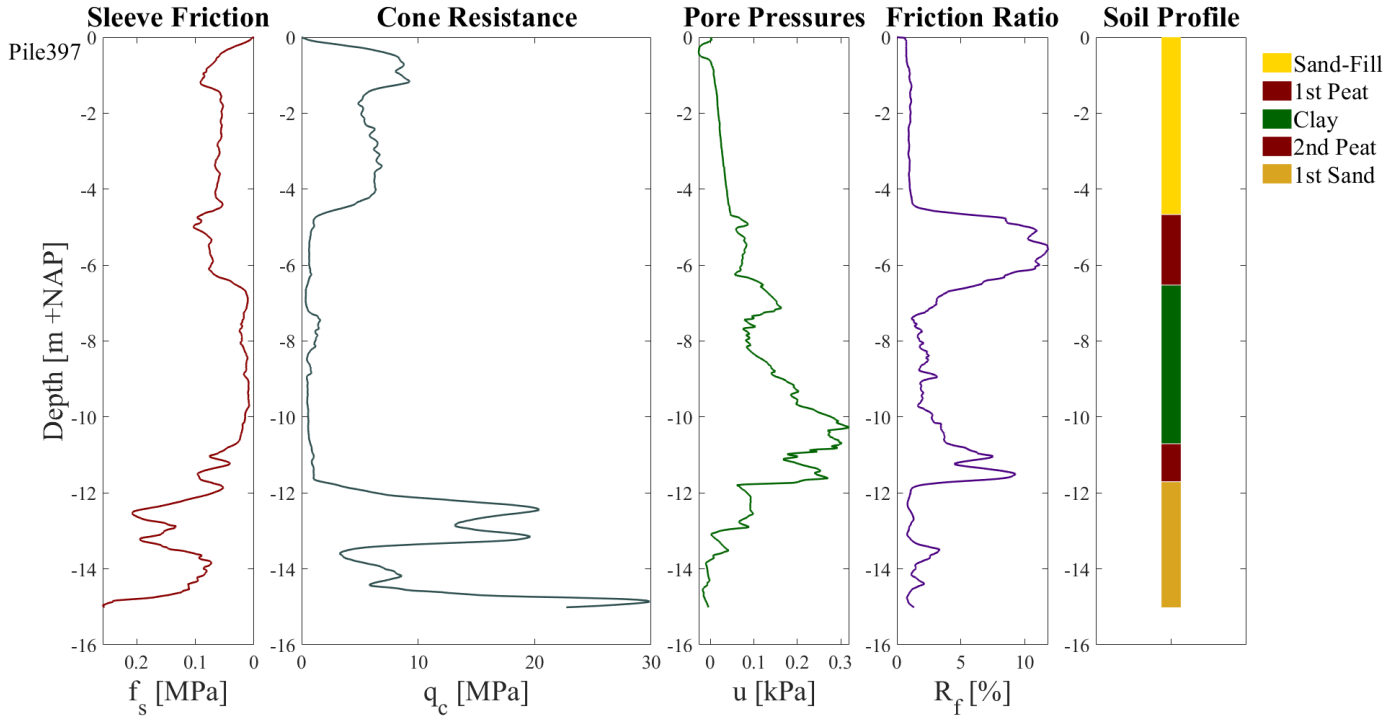

Figure B.6: CPT Pile 398

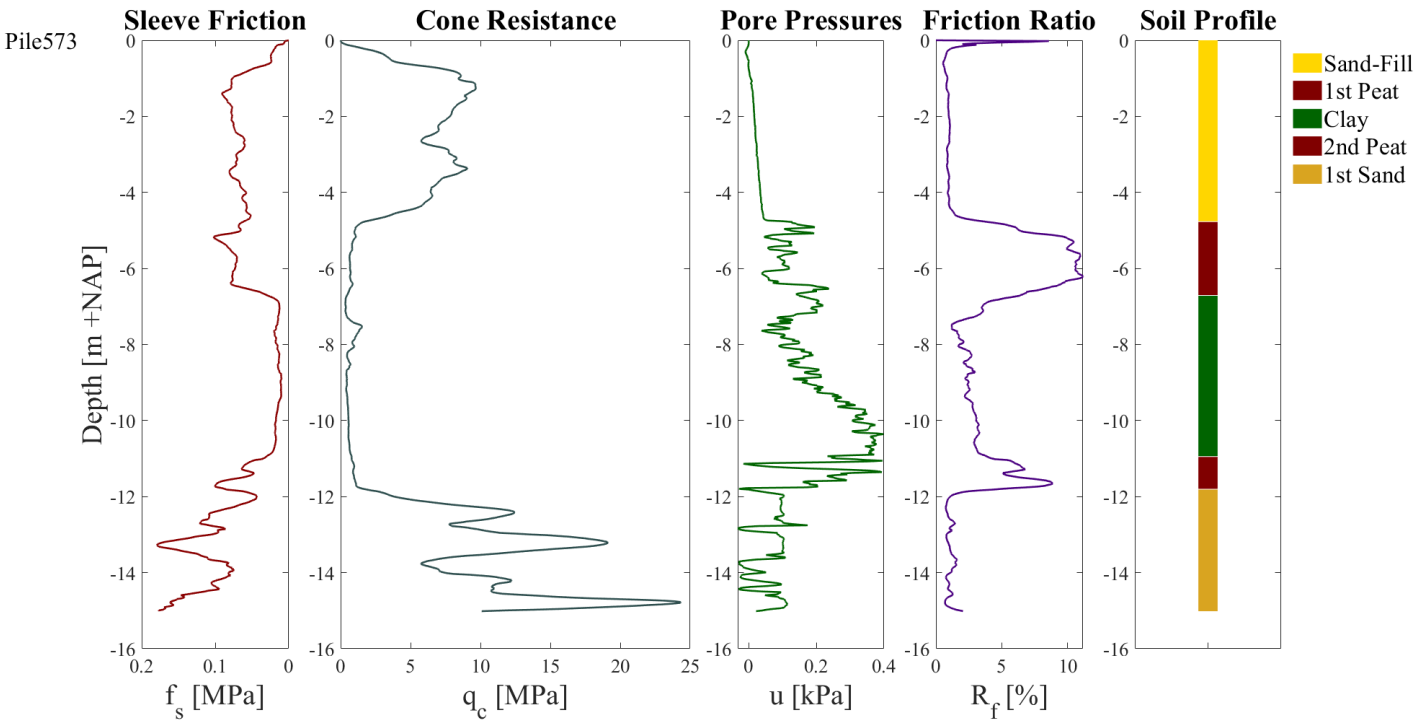

Figure B.7: CPT Pile 573

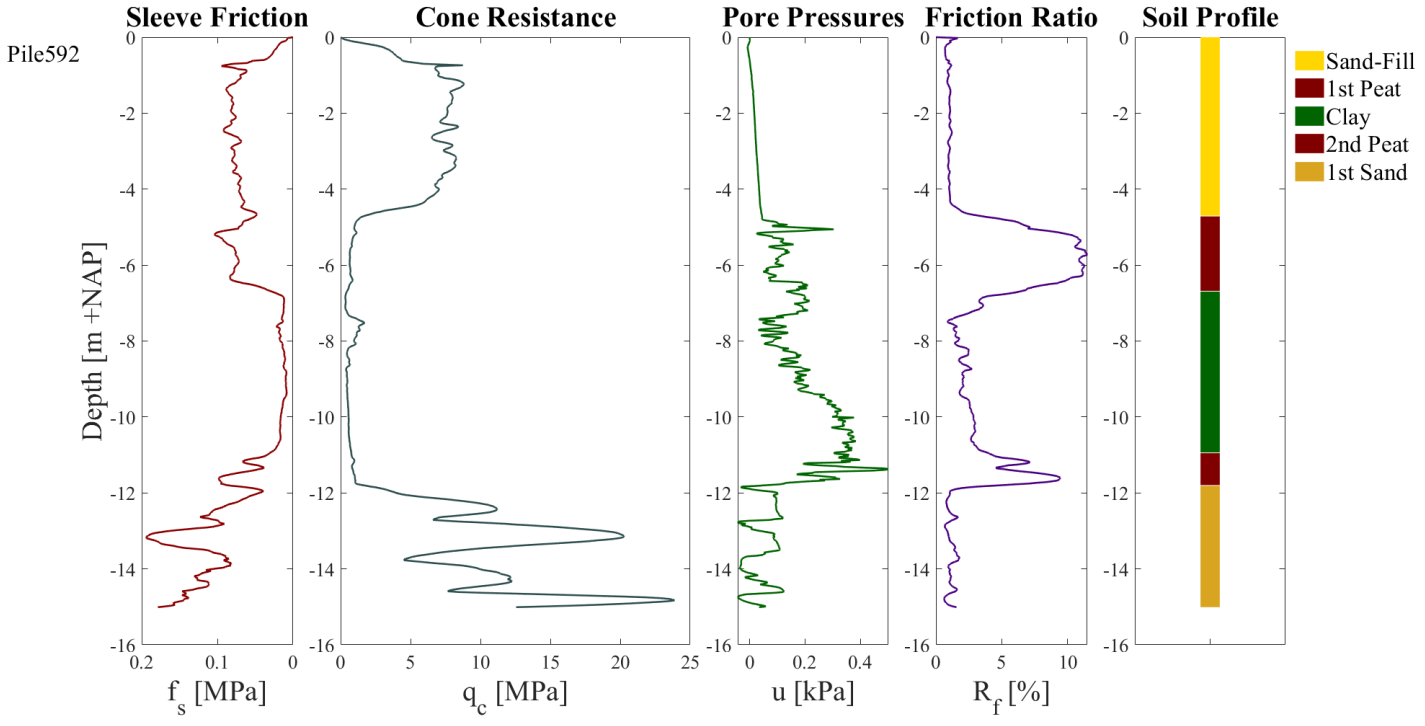

Figure B.8: CPT Pile 592

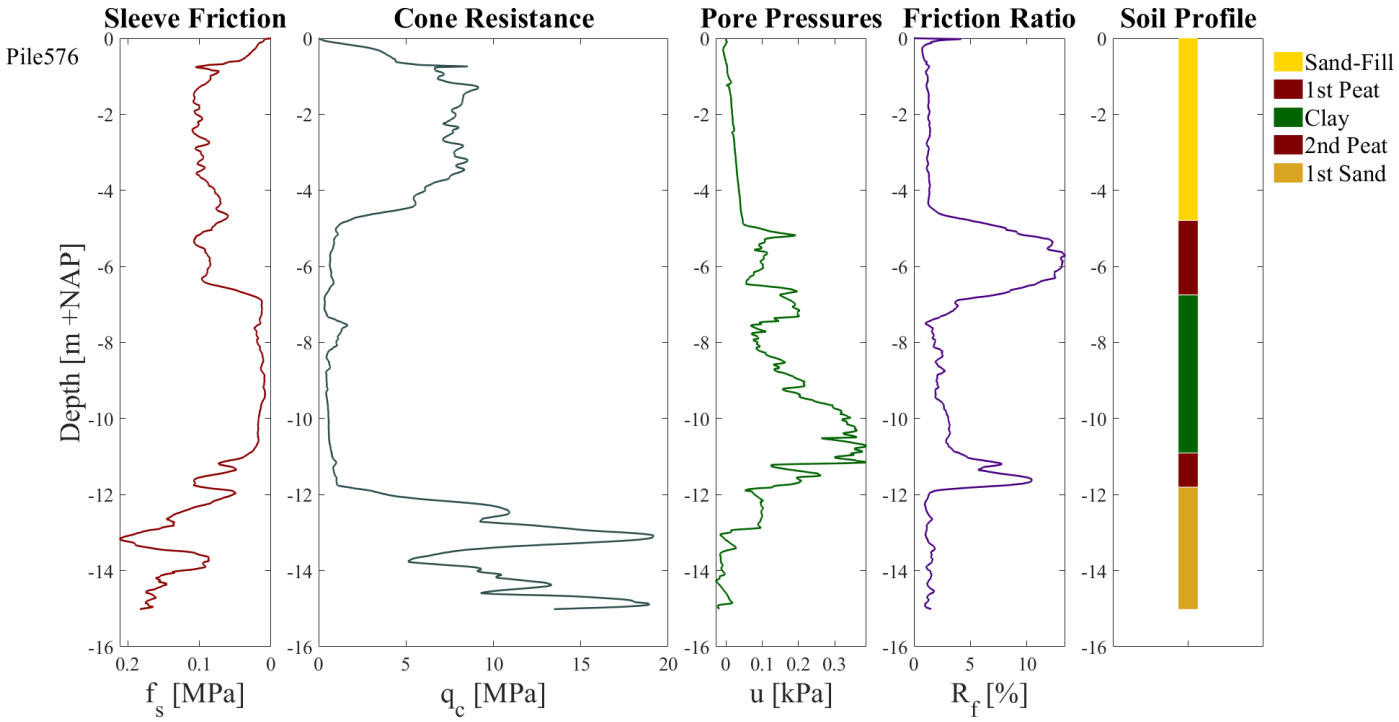

Figure B.9: CPT Pile 576

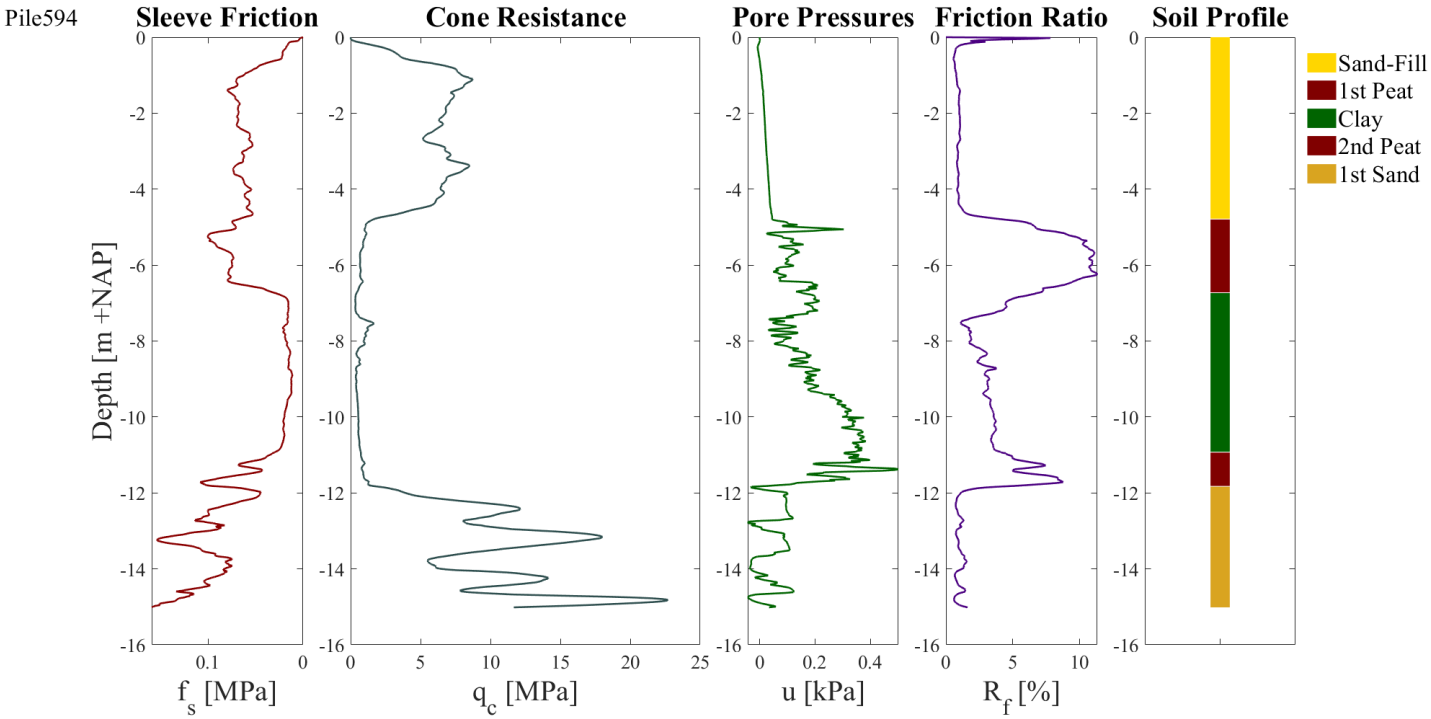

Figure B.10: CPT Pile 594

Appendix C

Results: All Analyzed Piles

C.1 Pile Geometry and Test Logistics

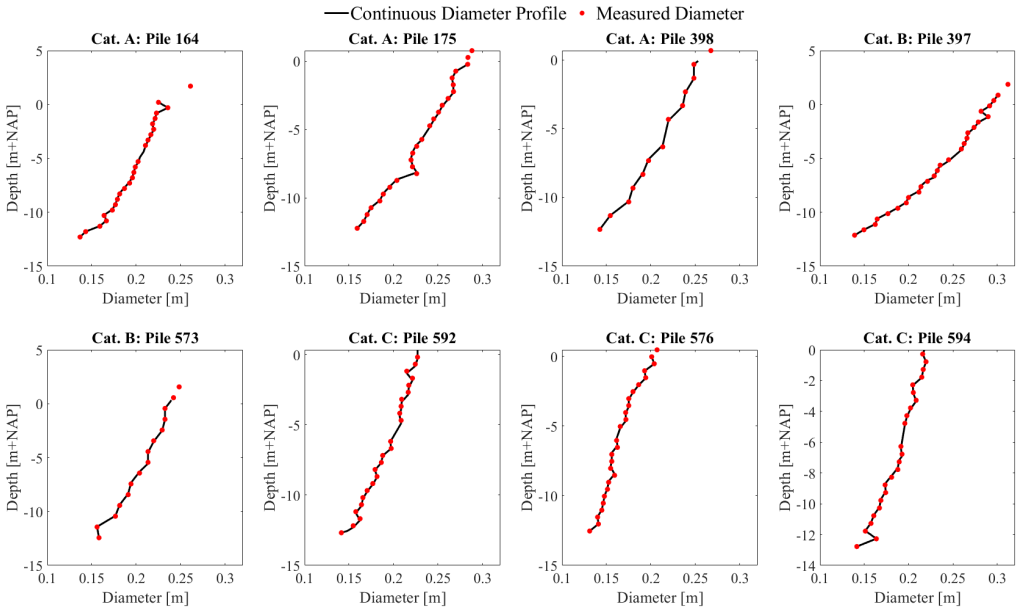

Figure C.1: Diameter Profile All Piles

Table C.1: Insertion Depth in Bearing Sand Layer

Pile	m in Sand Layer [cm]
164	55
175	47
398	55
397	41
573	62
592	86
576	72
594	94

C.2 Fiber Assessment

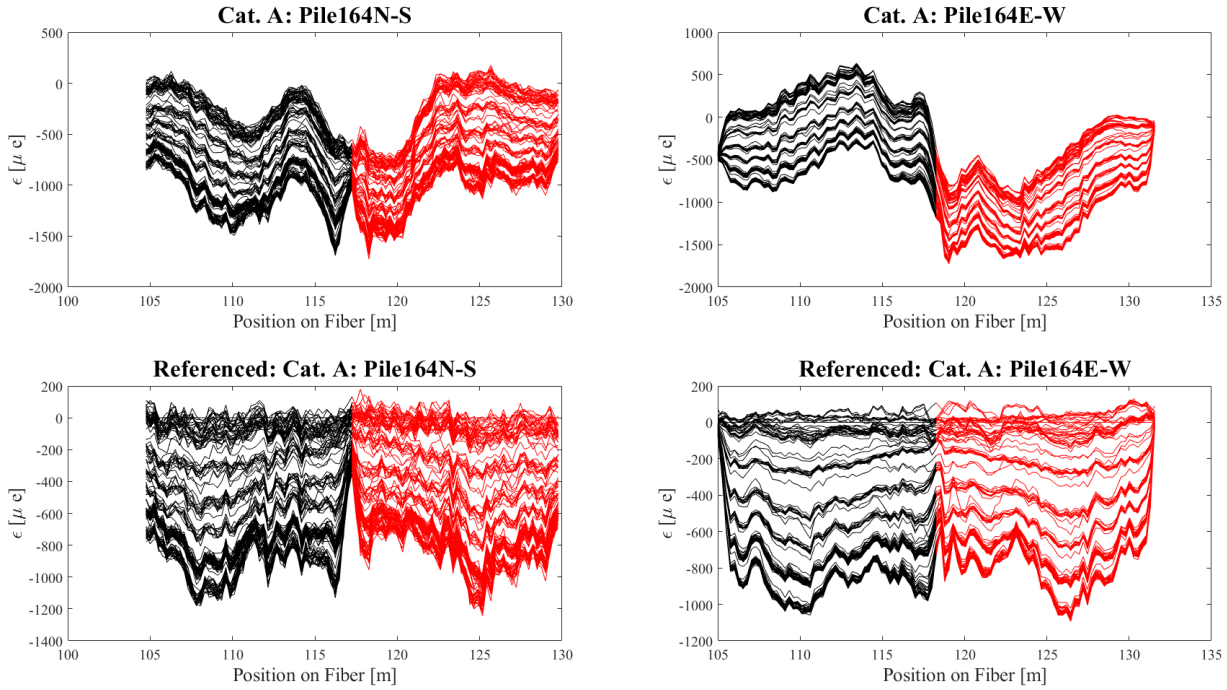

Figure C.2: Fiber Symmetry Pile 164

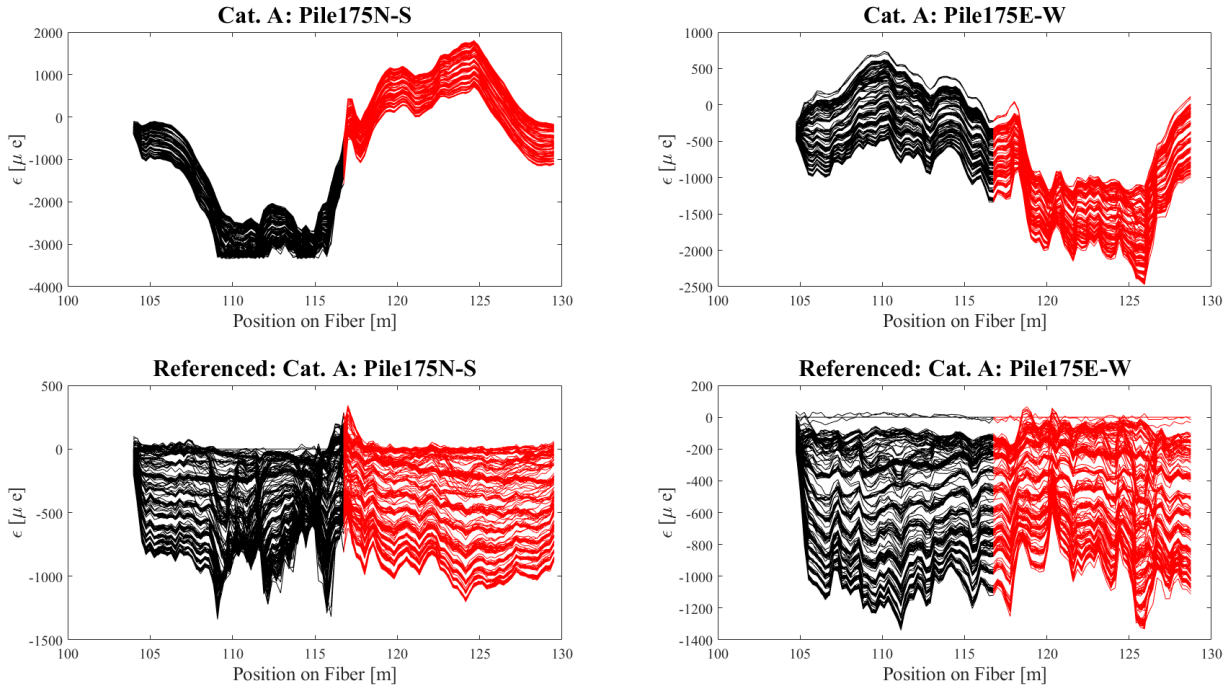

Figure C.3: Fiber Symmetry Pile 175

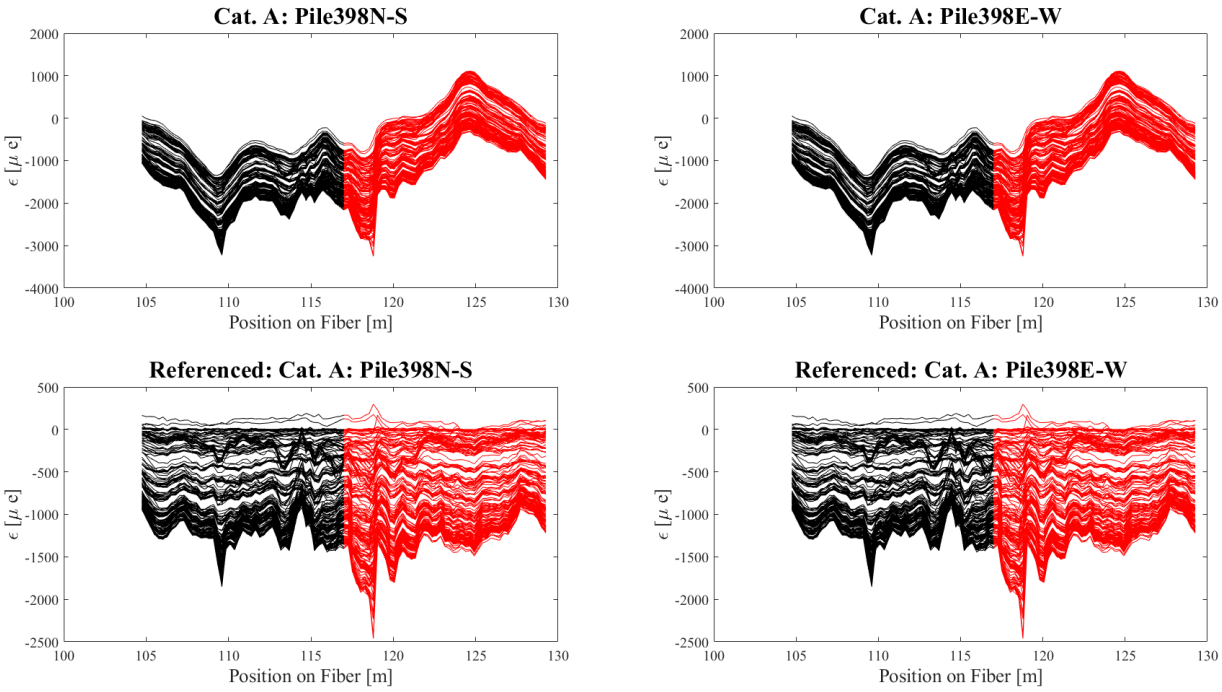

Figure C.4: Fiber Symmetry Pile 398

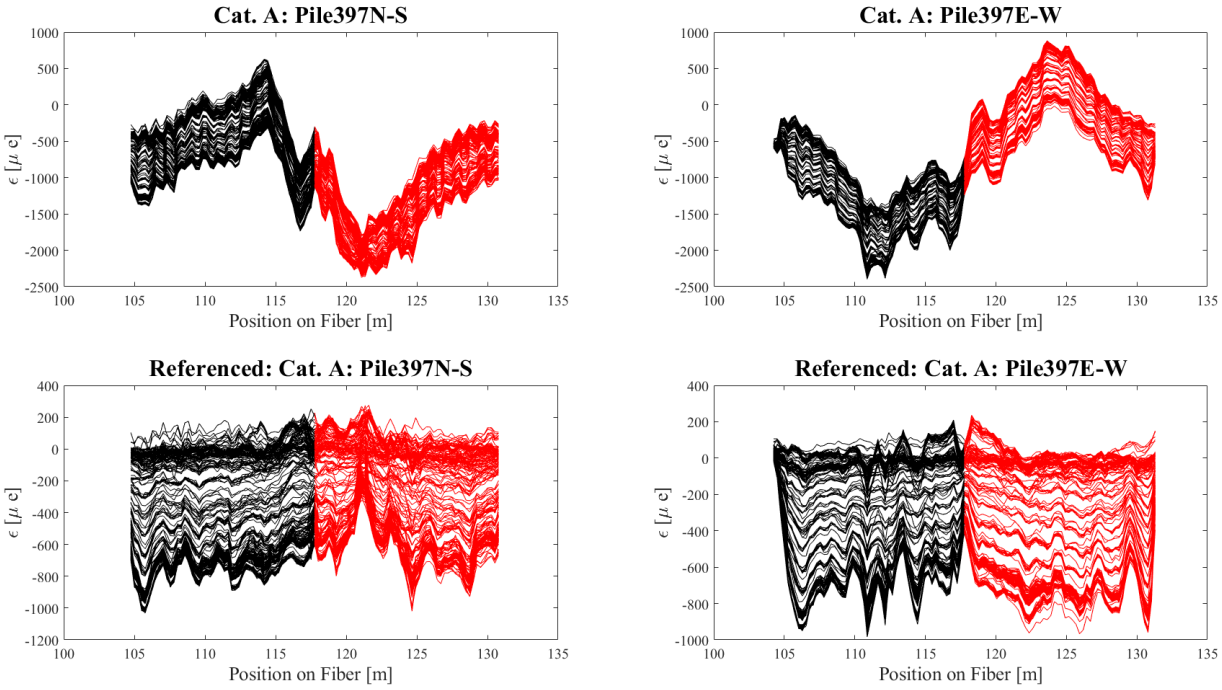

Figure C.5: Fiber Symmetry Pile 397

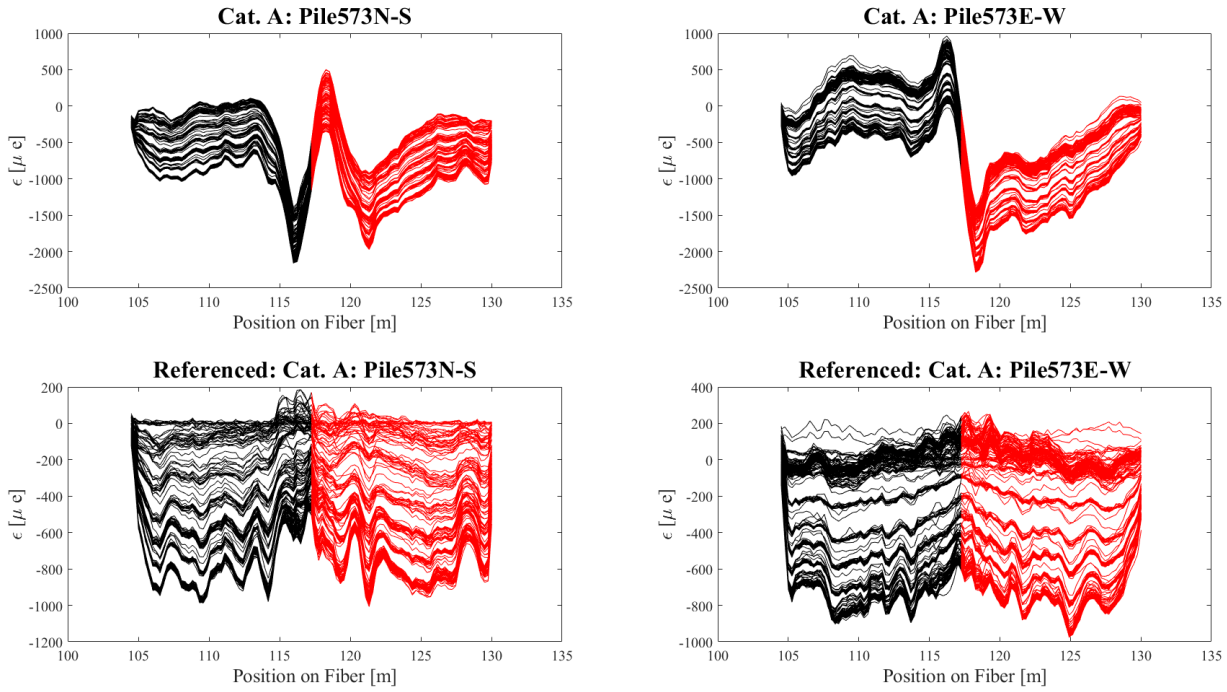

Figure C.6: Fiber Symmetry Pile 573

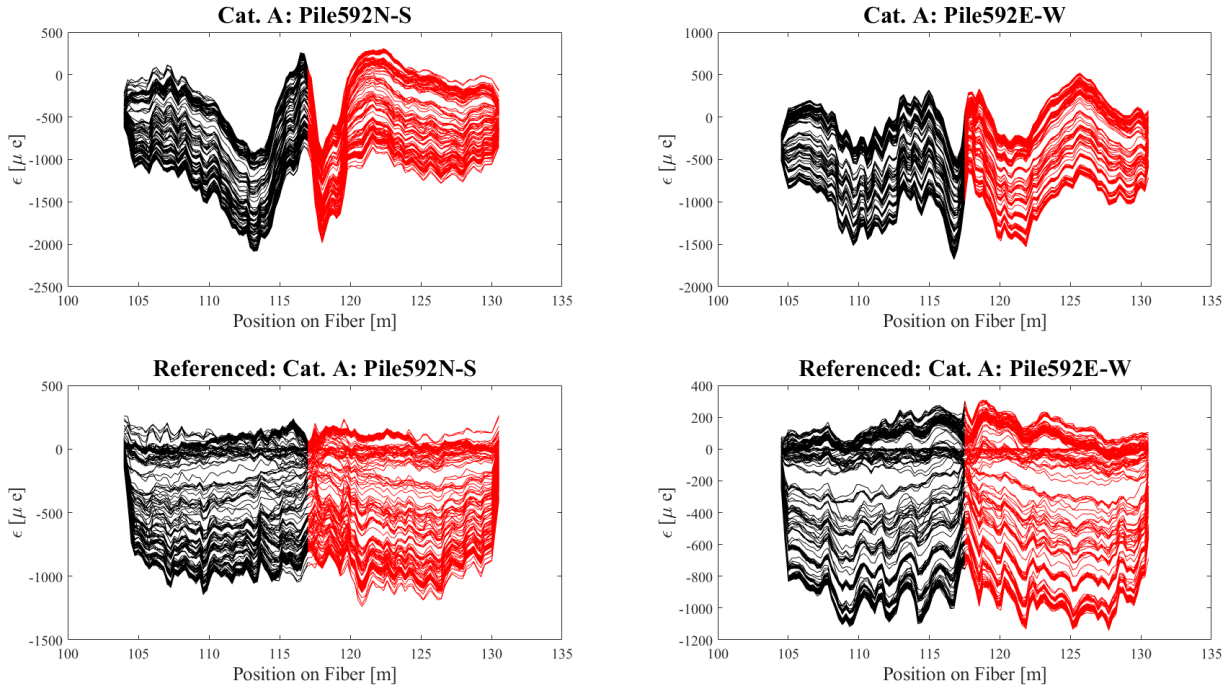

Figure C.7: Fiber Symmetry Pile 592

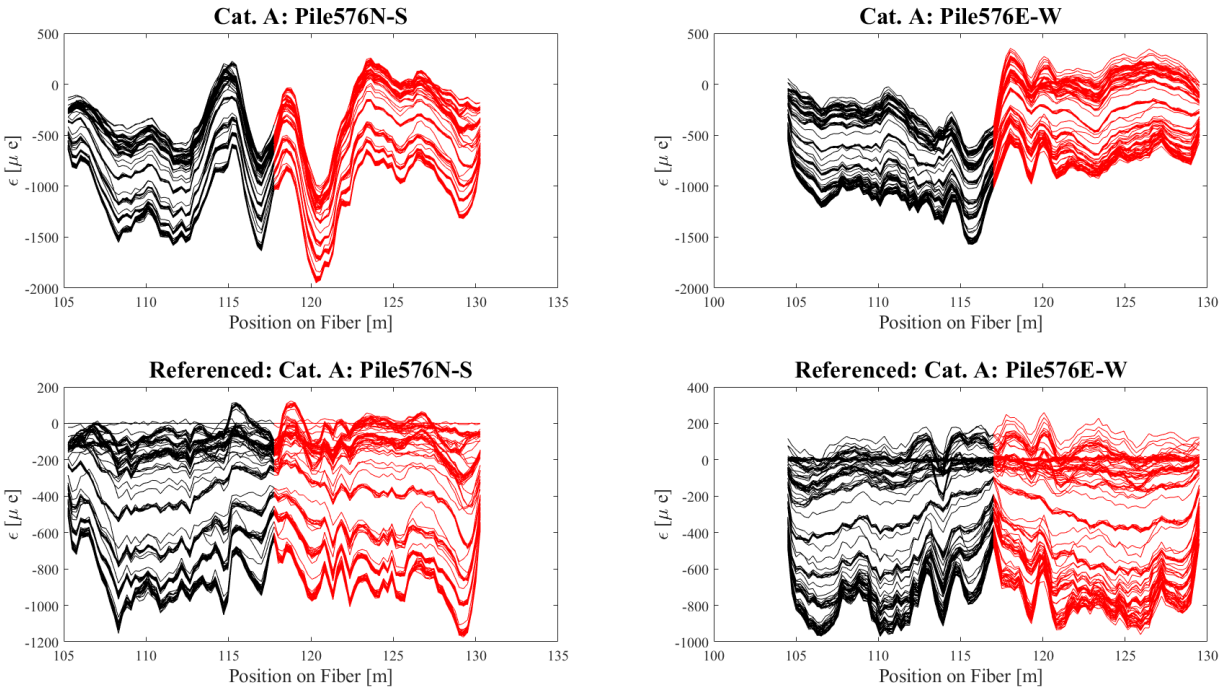

Figure C.8: Fiber Symmetry Pile 576

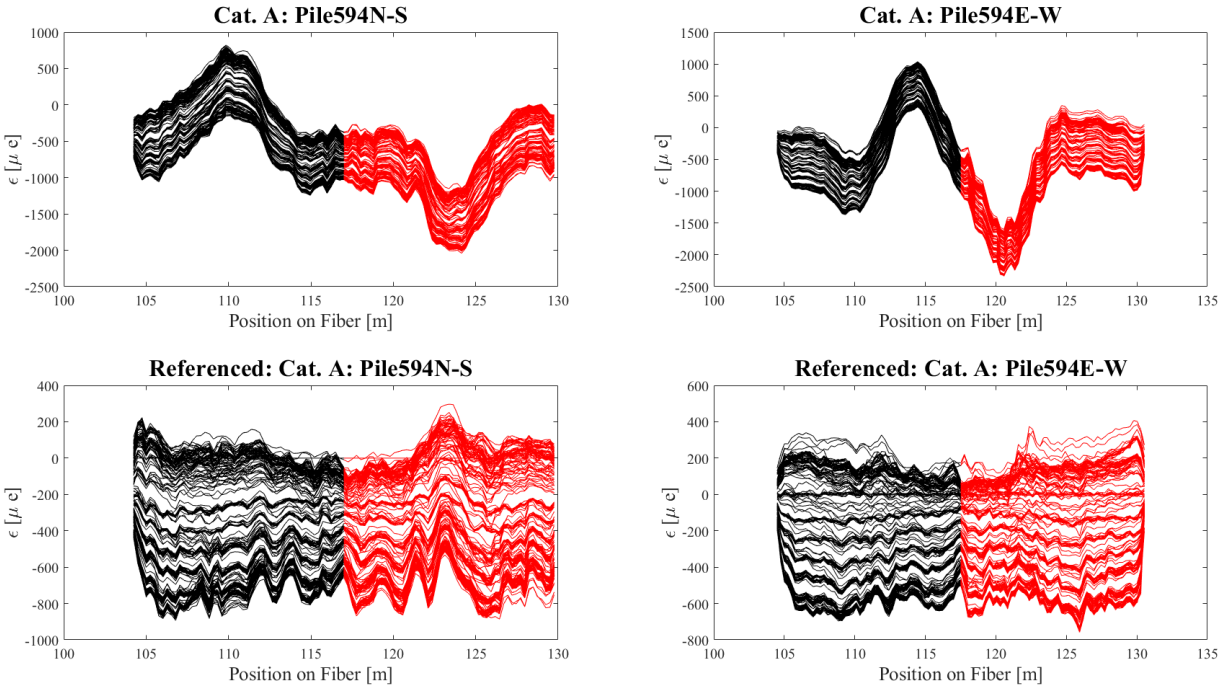

Figure C.9: Fiber Symmetry Pile 594

C.3 Correlation of Strains and Forces through Quadratic Fitting

The formulation illustrated in section 4.3 is illustrated here. The resultant coefficients for each quadratic relationship is summarized in table C.2.

$$F = a(\varepsilon \cdot A)^2 + b(\varepsilon \cdot A) \tag{C.1}$$

Table C.2: a and b Coefficients for Quadratic Fits

Pile ID	**a**	**b**
164	-0.1022	-14.7277
175	-0.0057	-9.1855
398	-0.0477	-10.9143
397	-0.0244	-9.7523
573	-0.063	-14.5199
592	-0.0540	-13.9517
576	0	-12.5107
594	-0.0100	-13.8126

These coefficients were averaged to obtain a singular relationship between strains and forces for each wood type.

C.4 Residual Loads

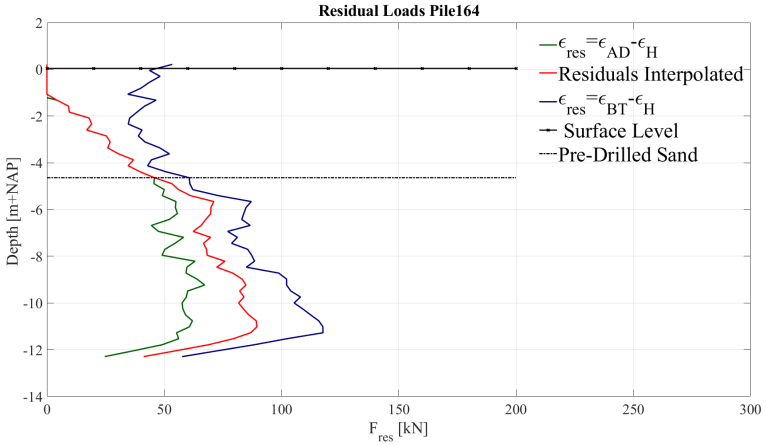

Figure C.10: Residual Loads Pile 164

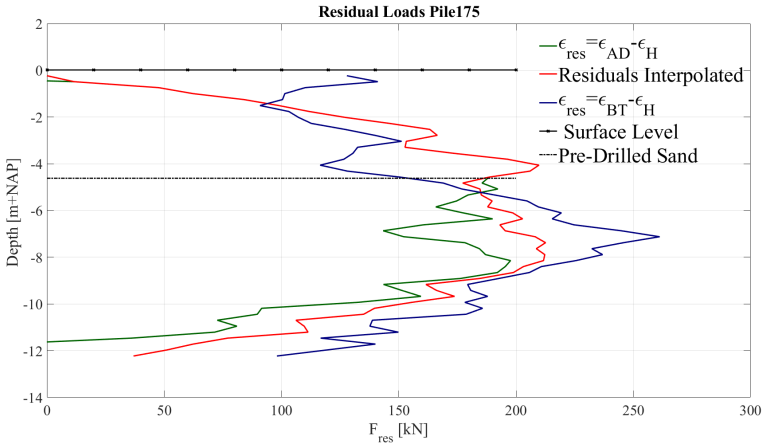

Figure C.11: Residual Loads Pile 175

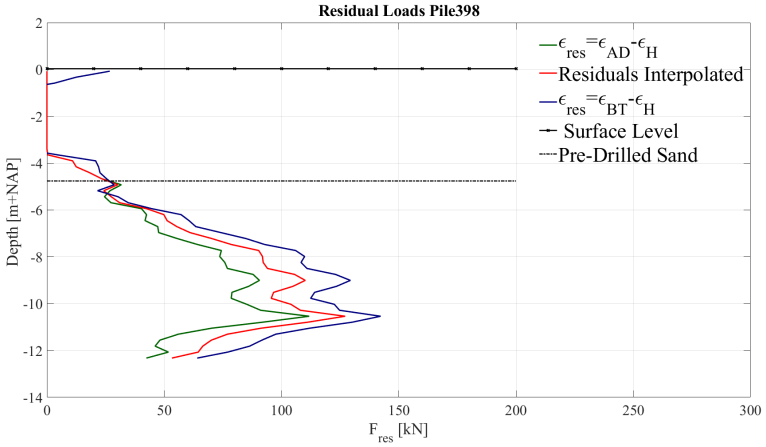

Figure C.12: Residual Loads Pile 398

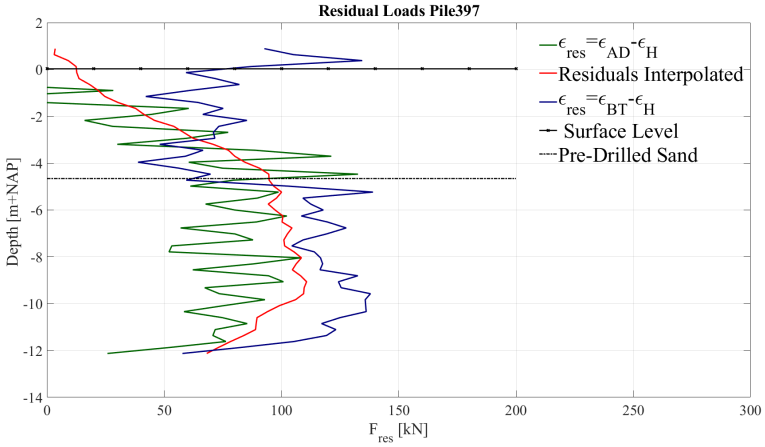

Figure C.13: Residual Loads Pile 397

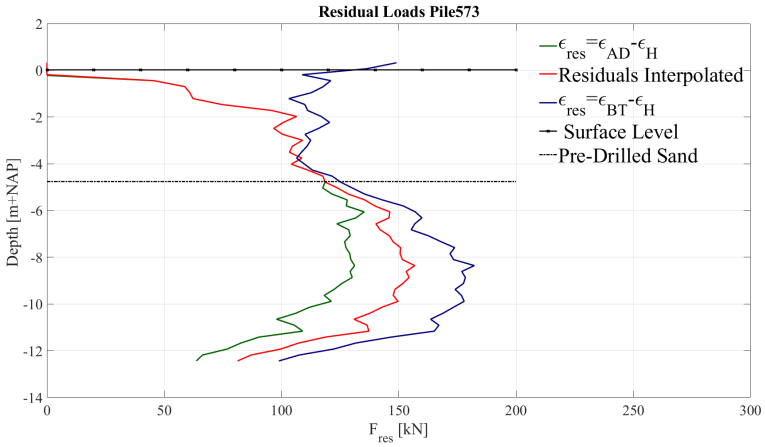

Figure C.14: Residual Loads Pile 573

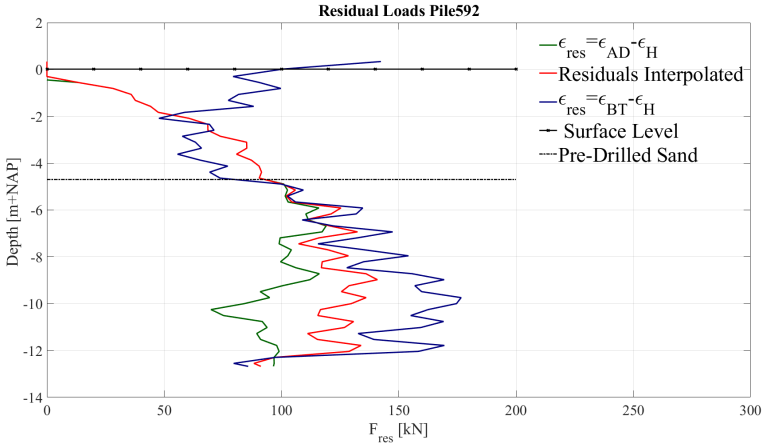

Figure C.15: Residual Loads Pile 592

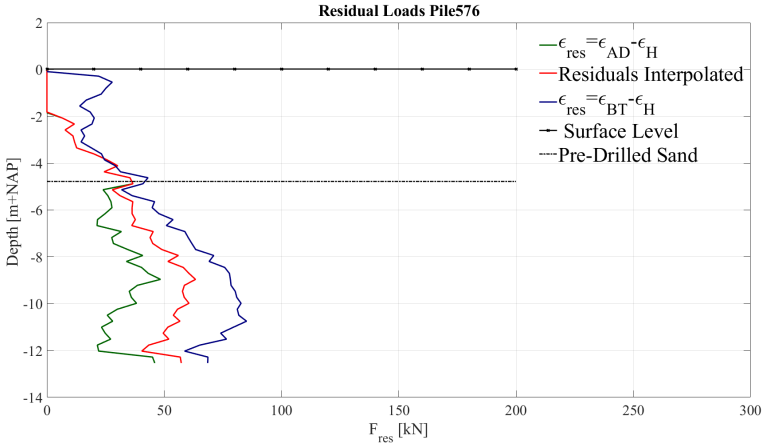

Figure C.16: Residual Loads Pile 576

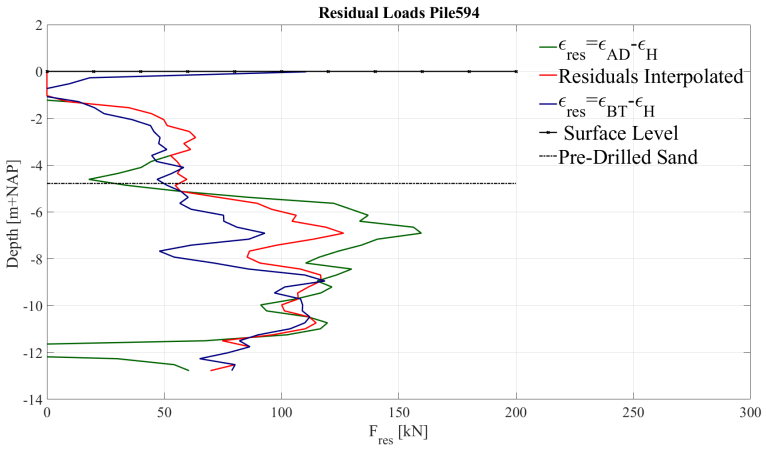

Figure C.17: Residual Loads Pile 594

C.5 Load Displacement Profiles

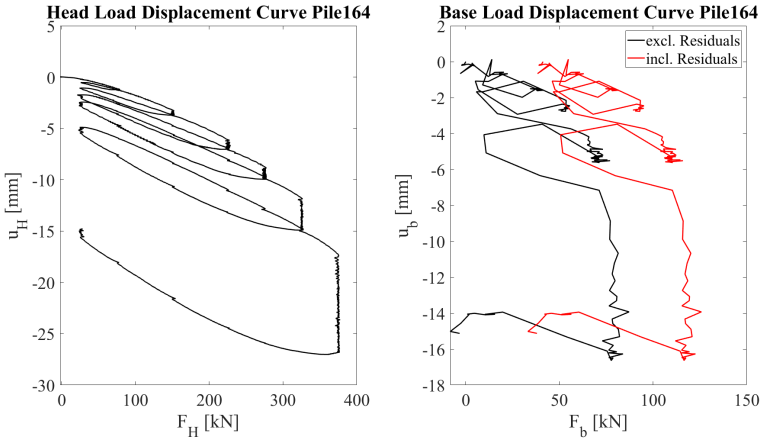

Figure C.18: Load Displacement Curves Pile 164

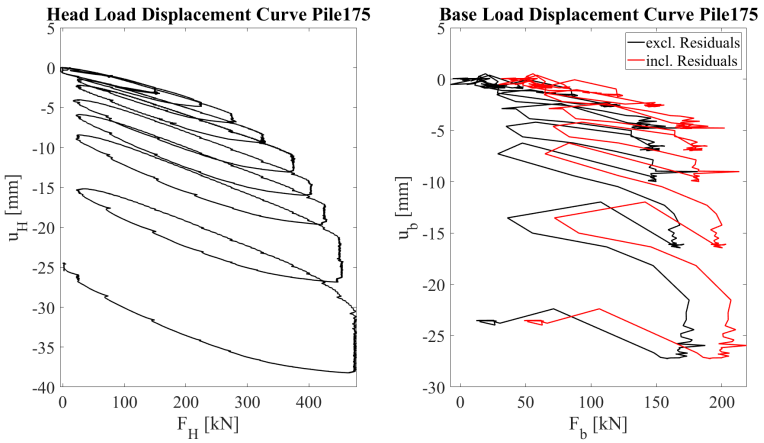

[
Load Displacement Curves Pile 175]Load Displacement Curves Pile 175

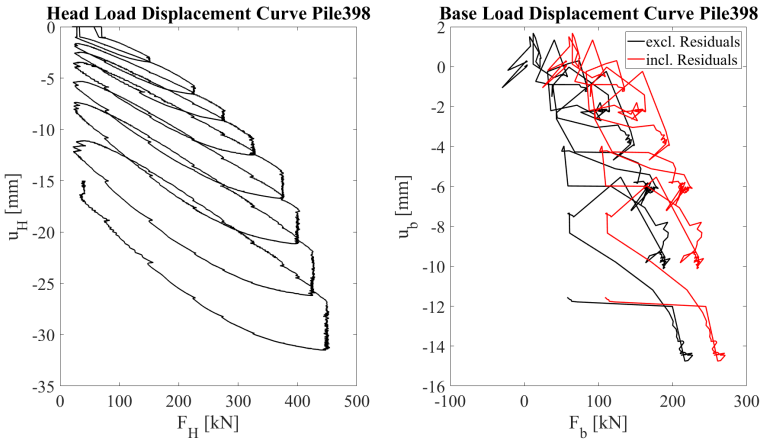

Figure C.19: Load Displacement Curves Pile 398

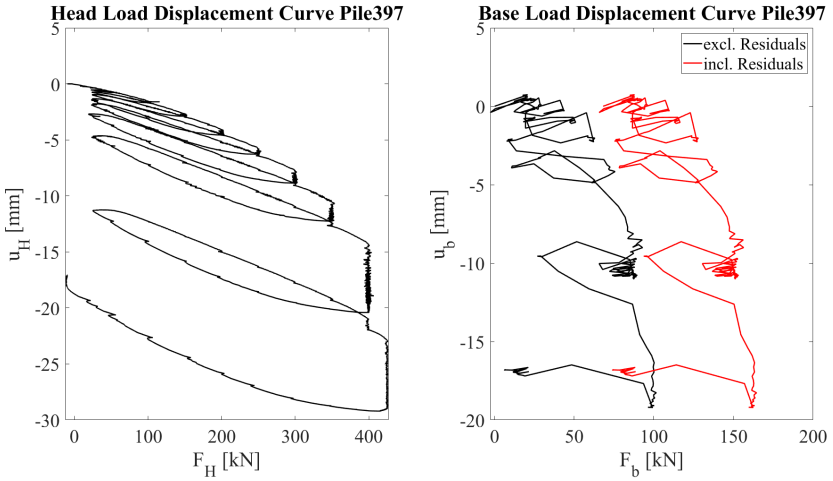

Figure C.20: Load Displacement Curves Pile 397

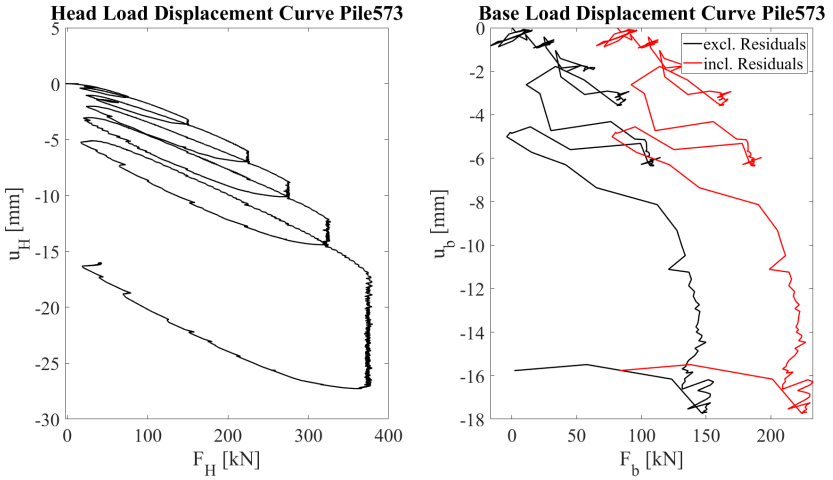

Figure C.21: Load Displacement Curves Pile 573

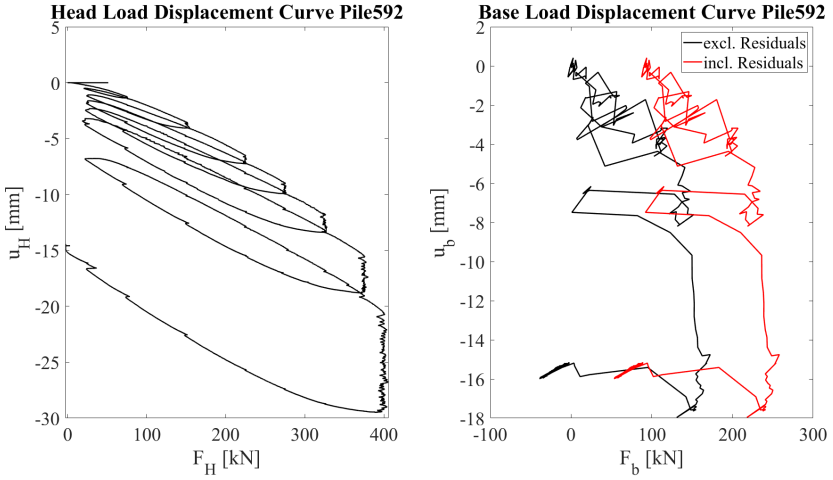

Figure C.22: Load Displacement Curves Pile 592

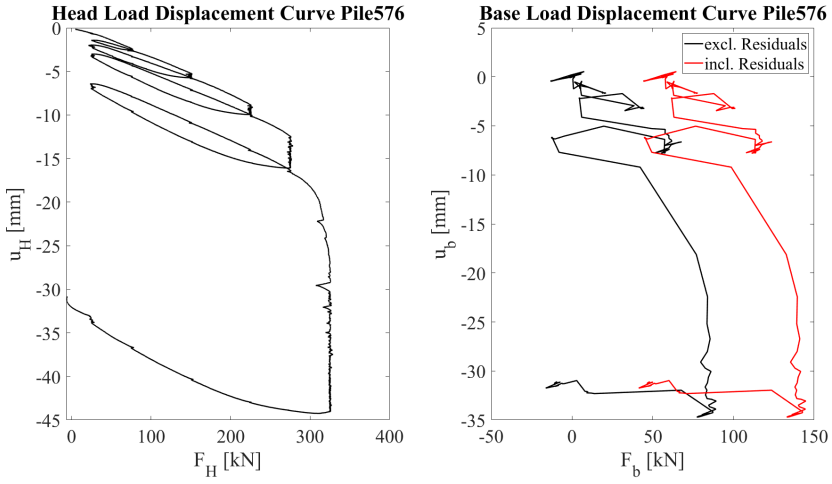

Figure C.23: Load Displacement Curves Pile 576

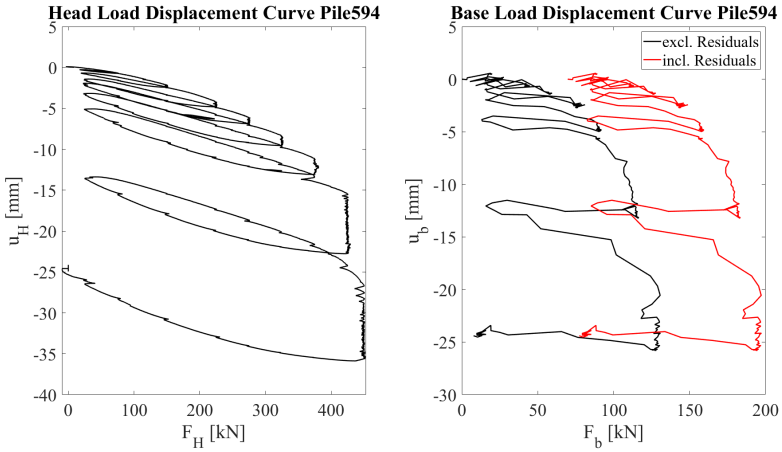

Figure C.24: Load Displacement Curves Pile 594

C.6 Resultant Load Distributions

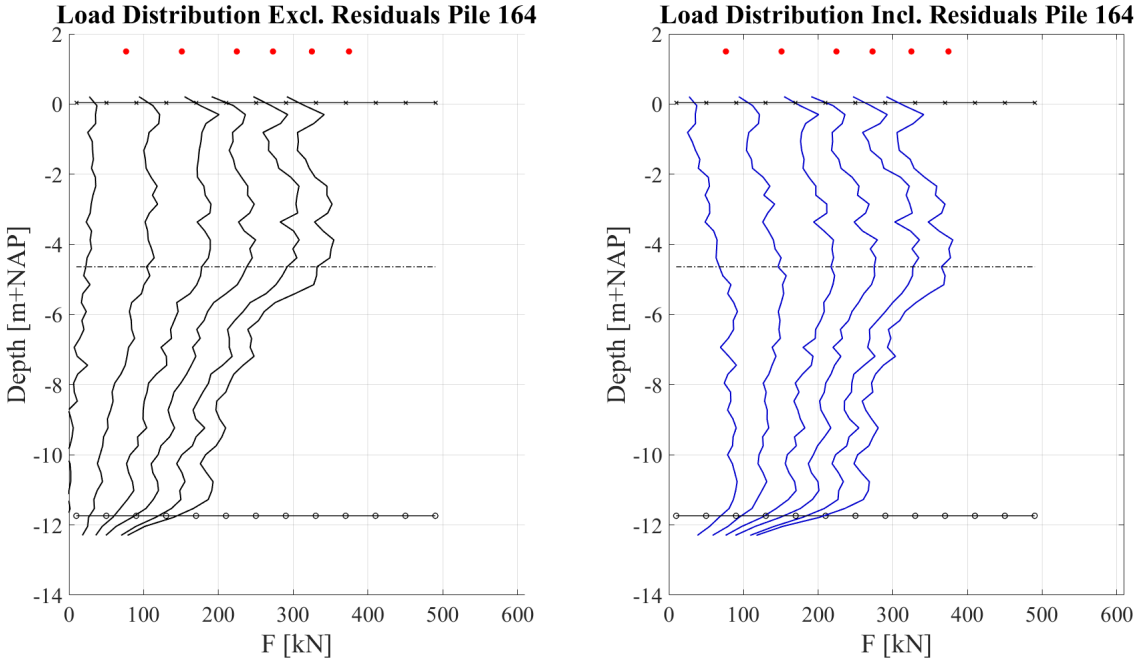

Figure C.25: Load Distribution Pile 164

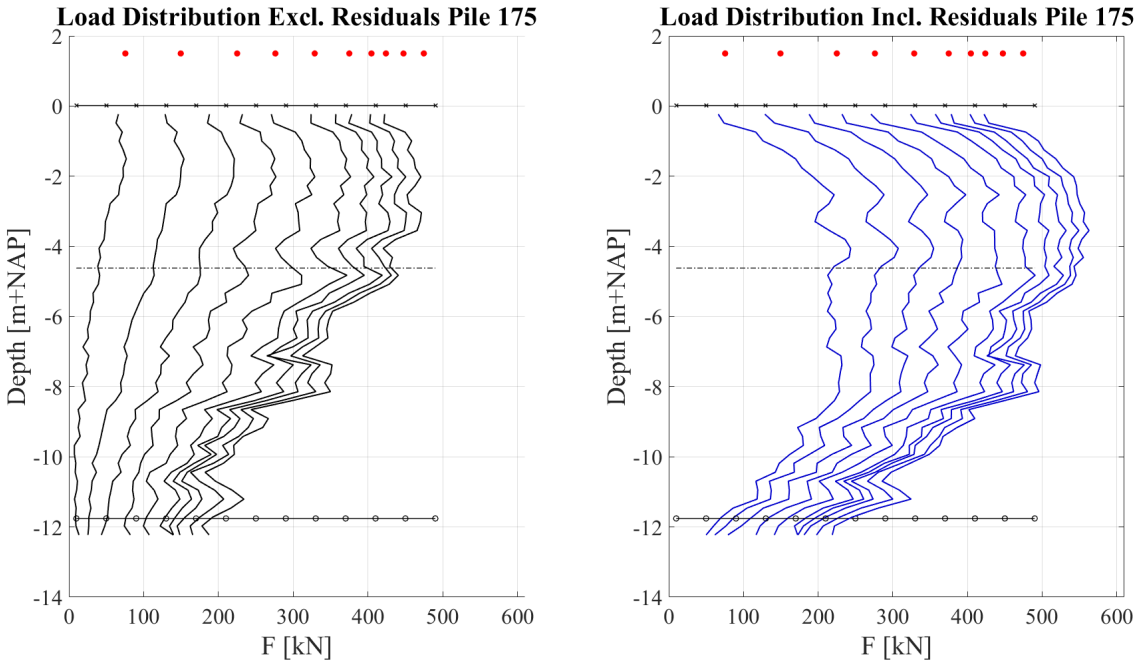

Figure C.26: Load Distribution Pile 175

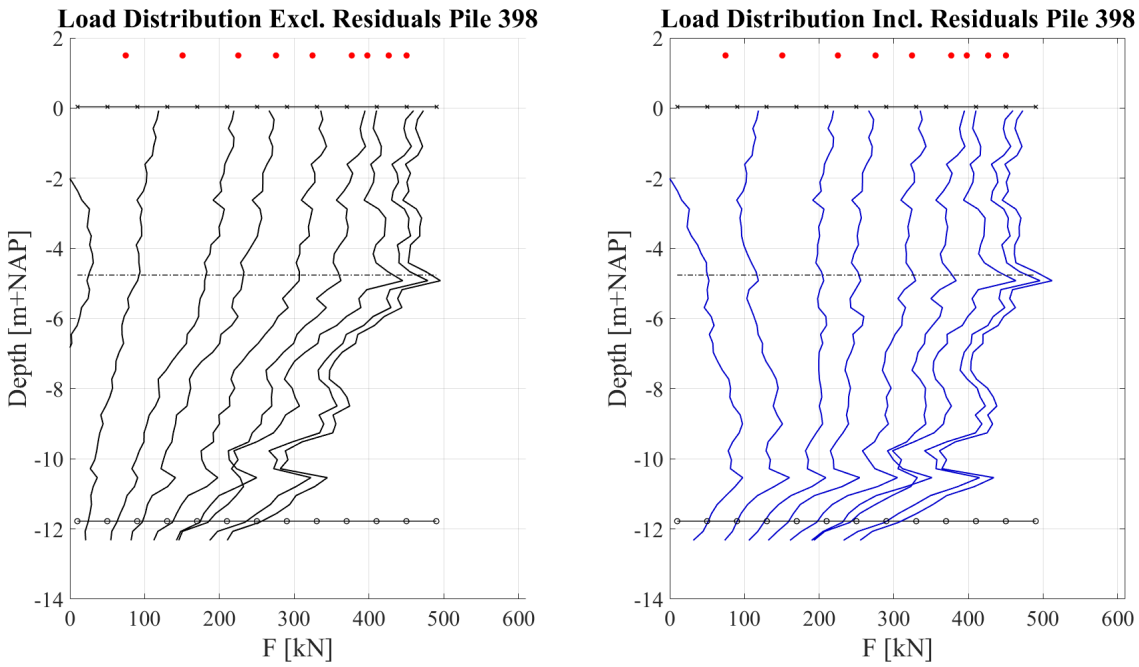

Figure C.27: Load Distribution Pile 398

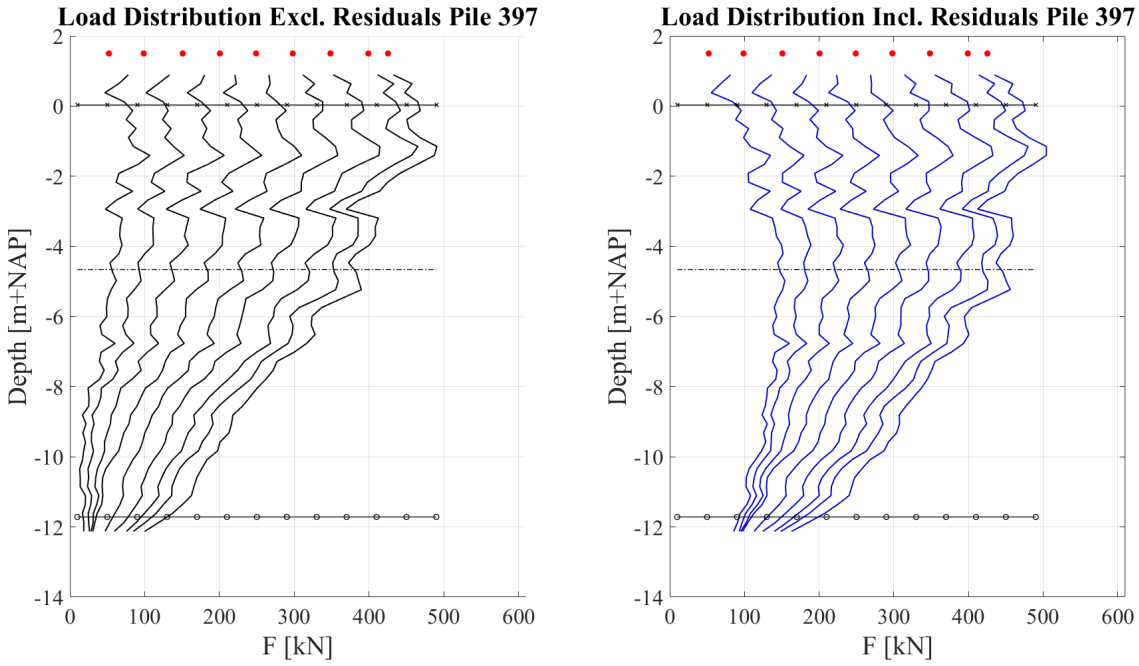

Figure C.28: Load Distribution Pile 397

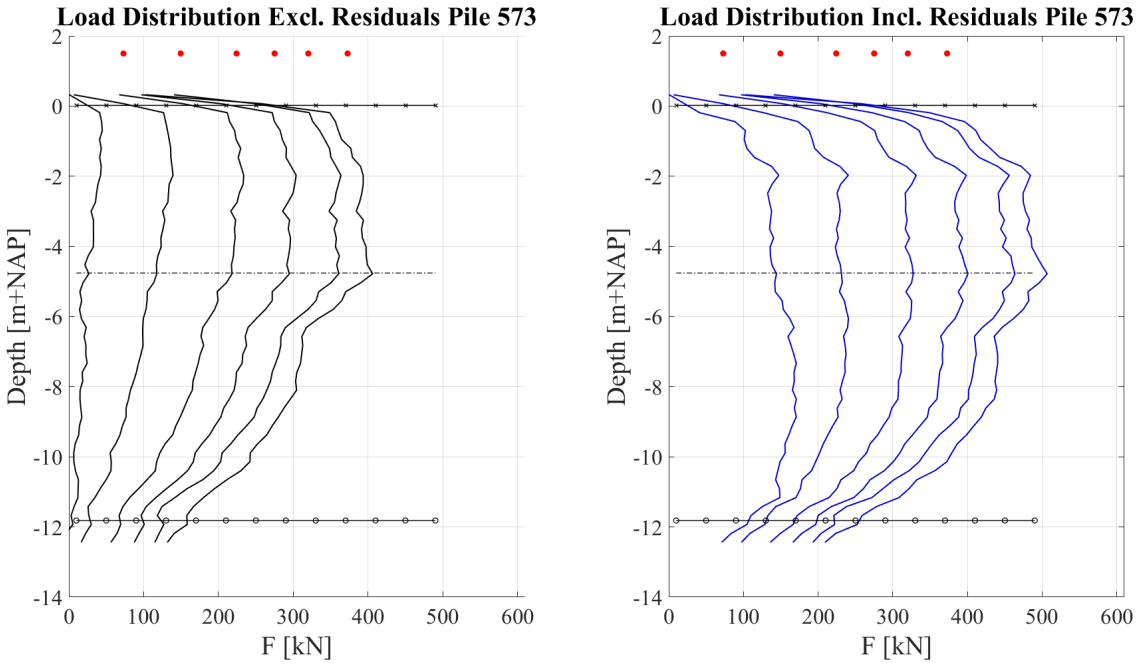

Figure C.29: Load Distribution Pile 573

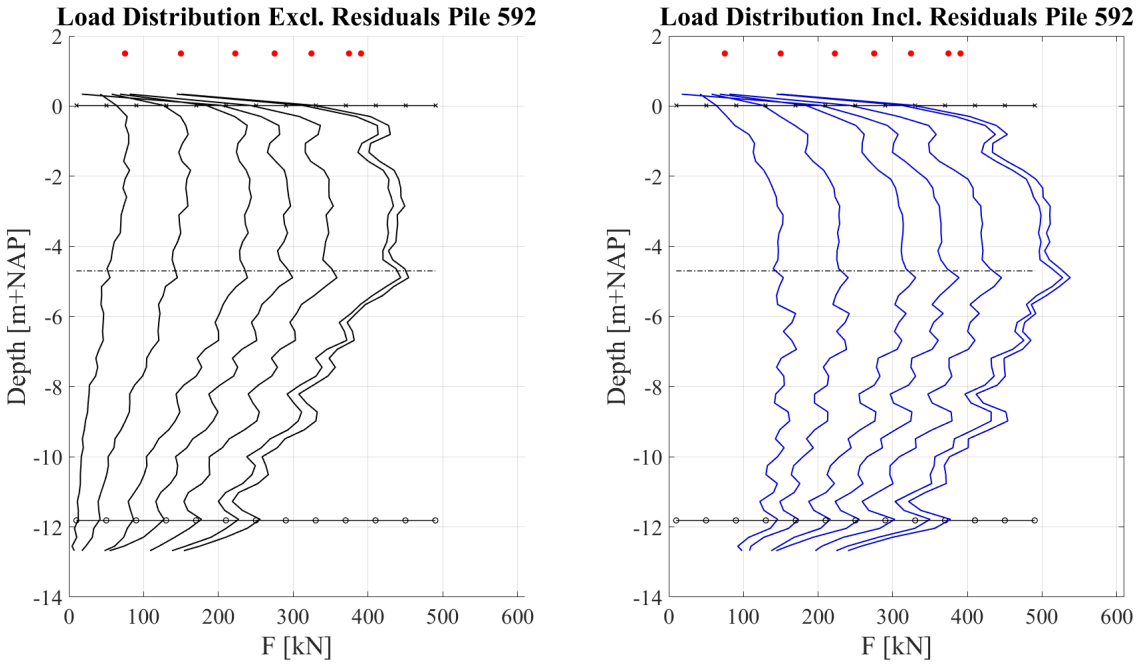

Figure C.30: Load Distribution Pile 592

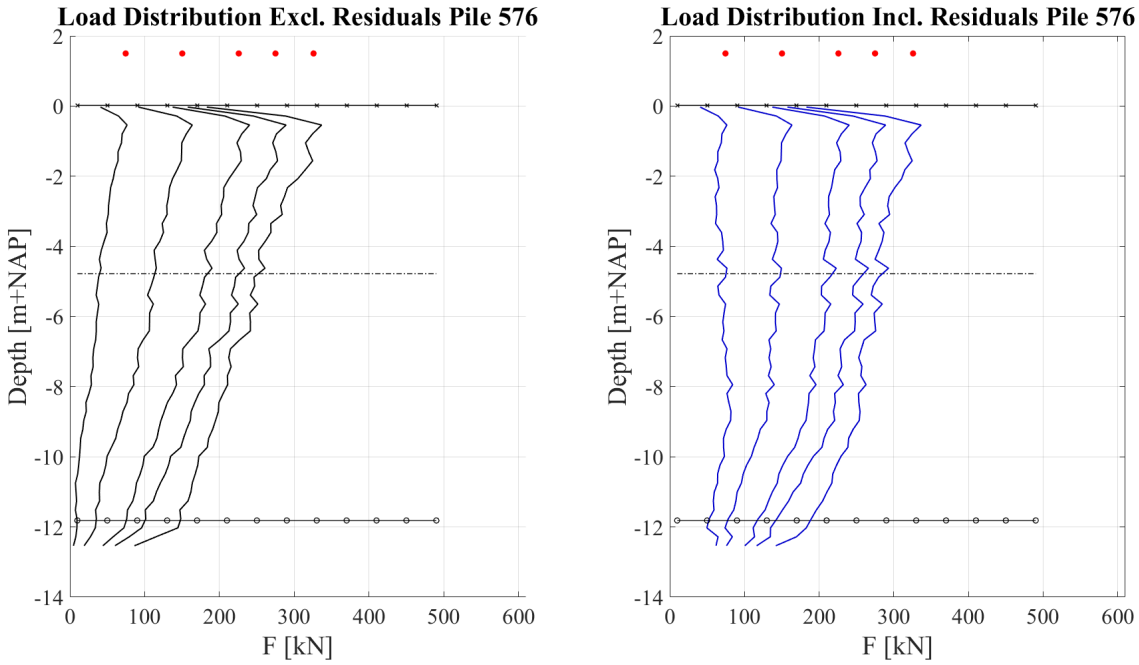

Figure C.31: Load Distribution Pile 576

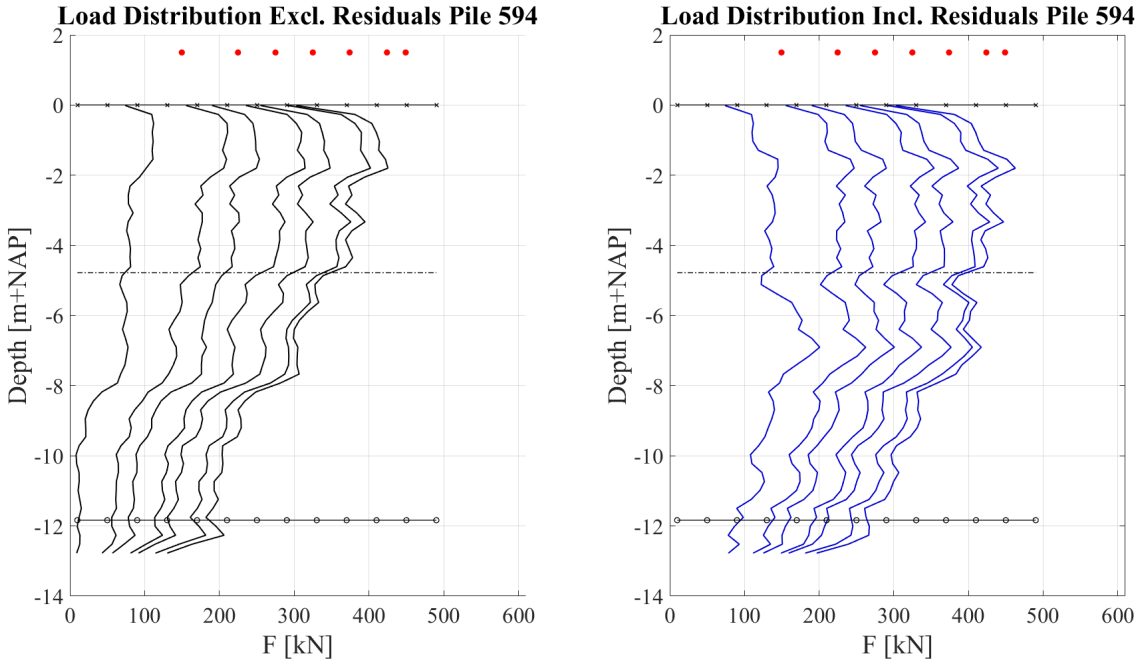

Figure C.32: Load Distribution Pile 594

C.7 Alpha Factors

C.7.1 Alpha-p

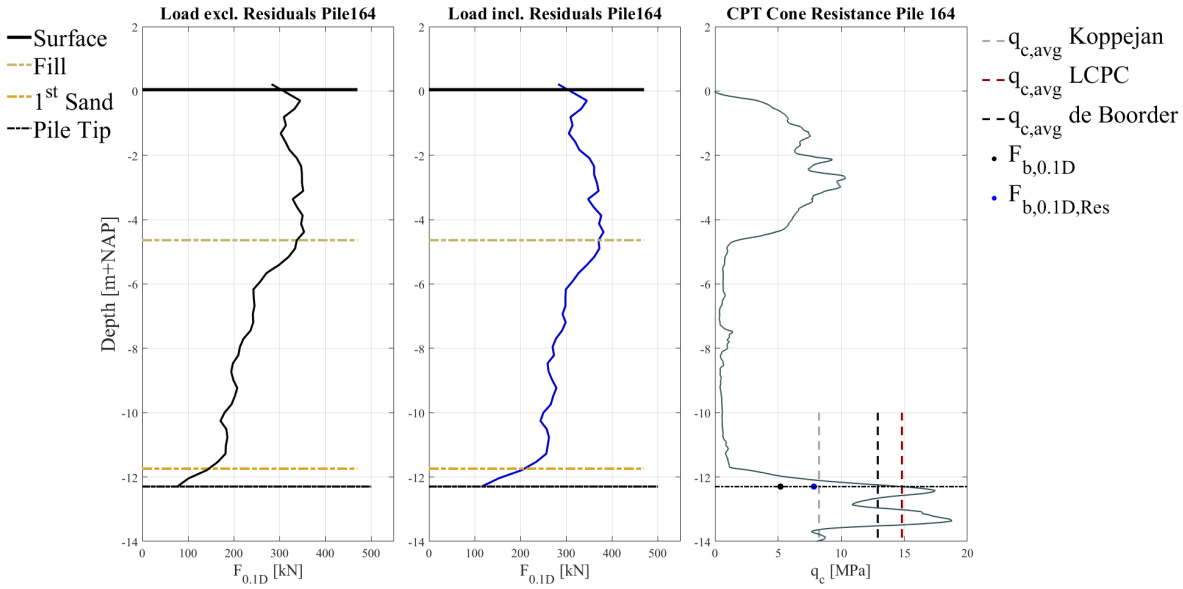

Figure C.33: α_p Pile 164

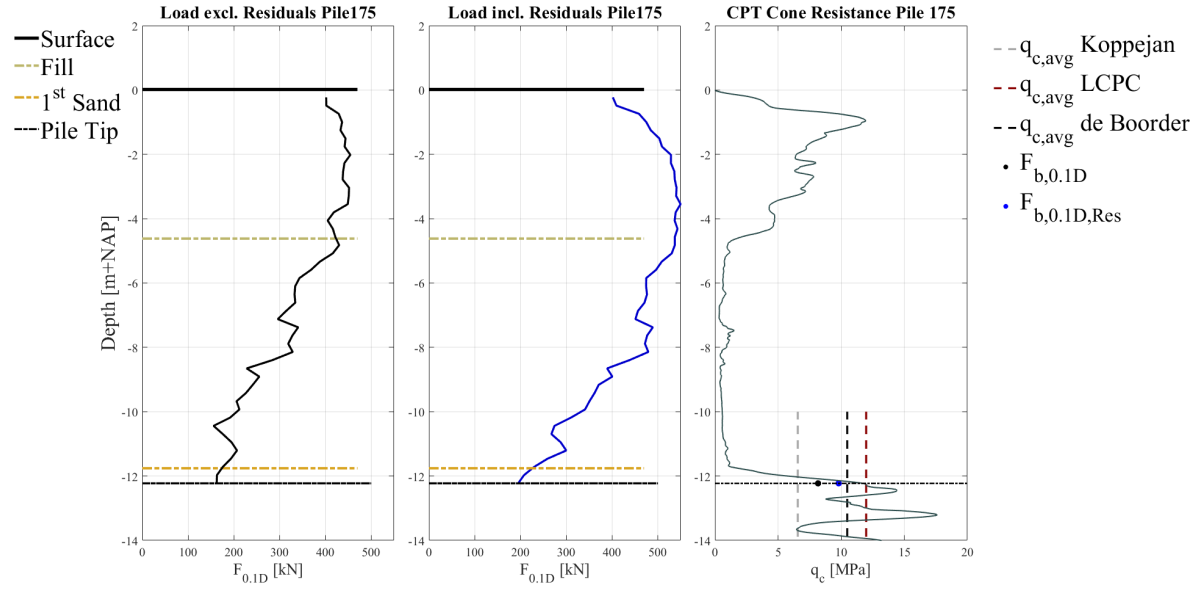

Figure C.34: α_p Pile 175

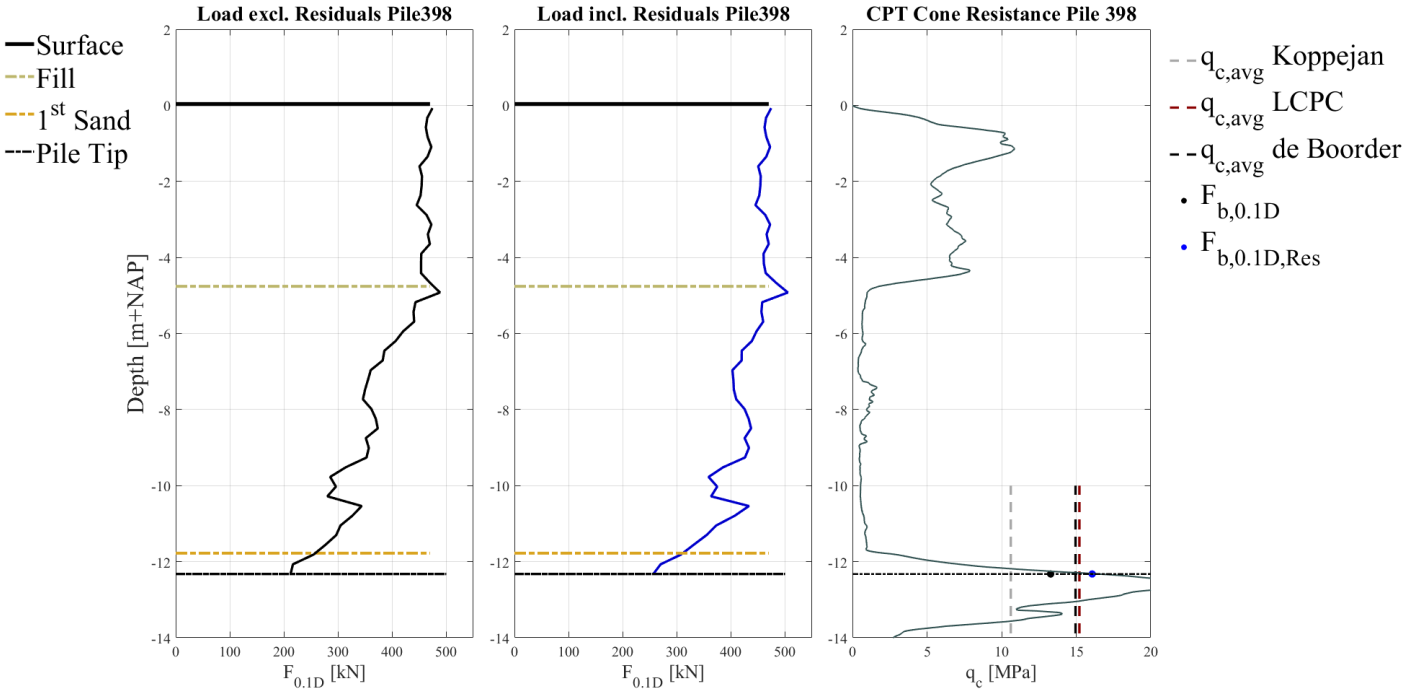

Figure C.35: α_p Pile 398

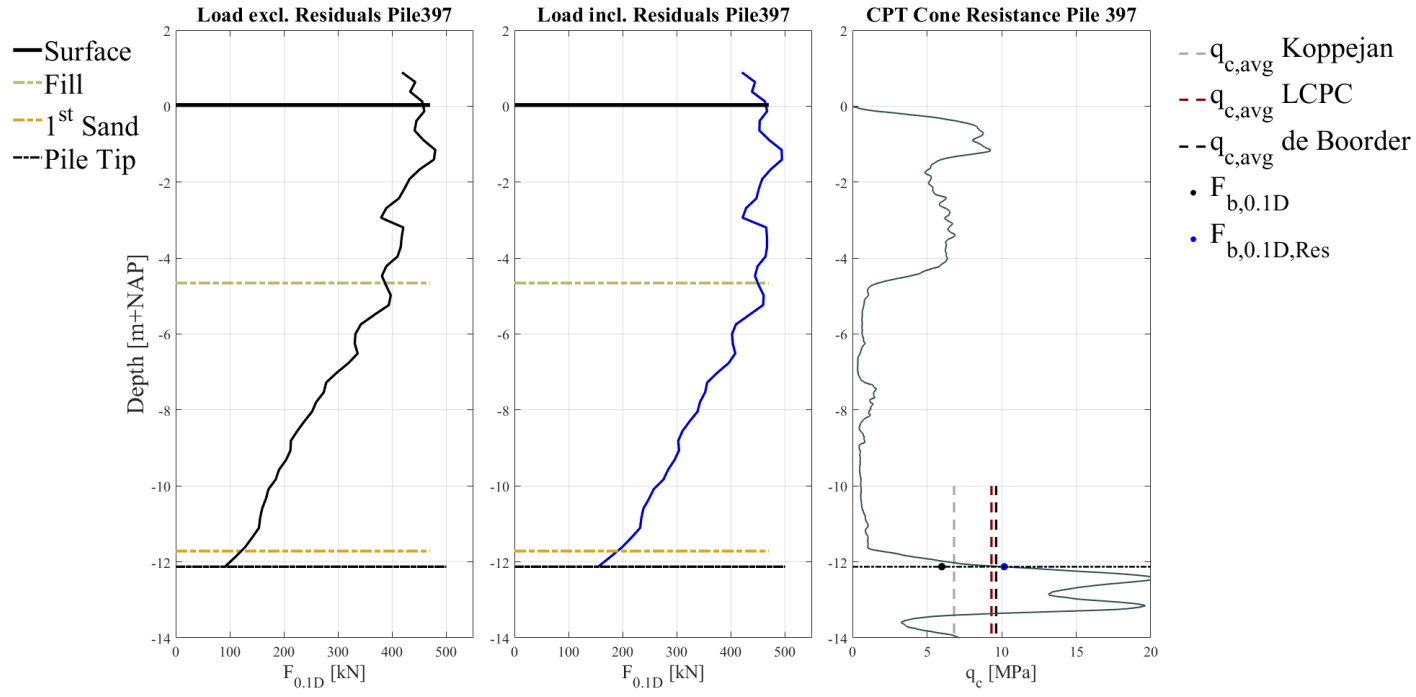

Figure C.36: α_p Pile 397

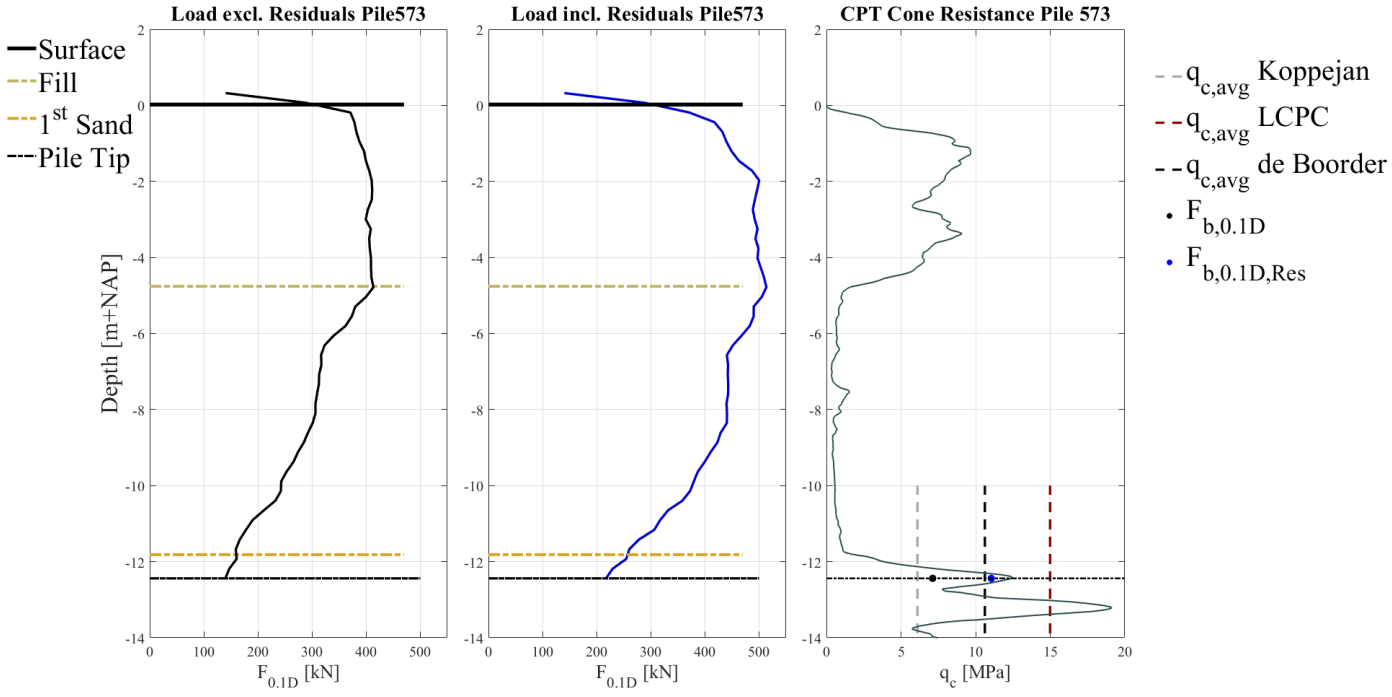

Figure C.37: α_p Pile 573

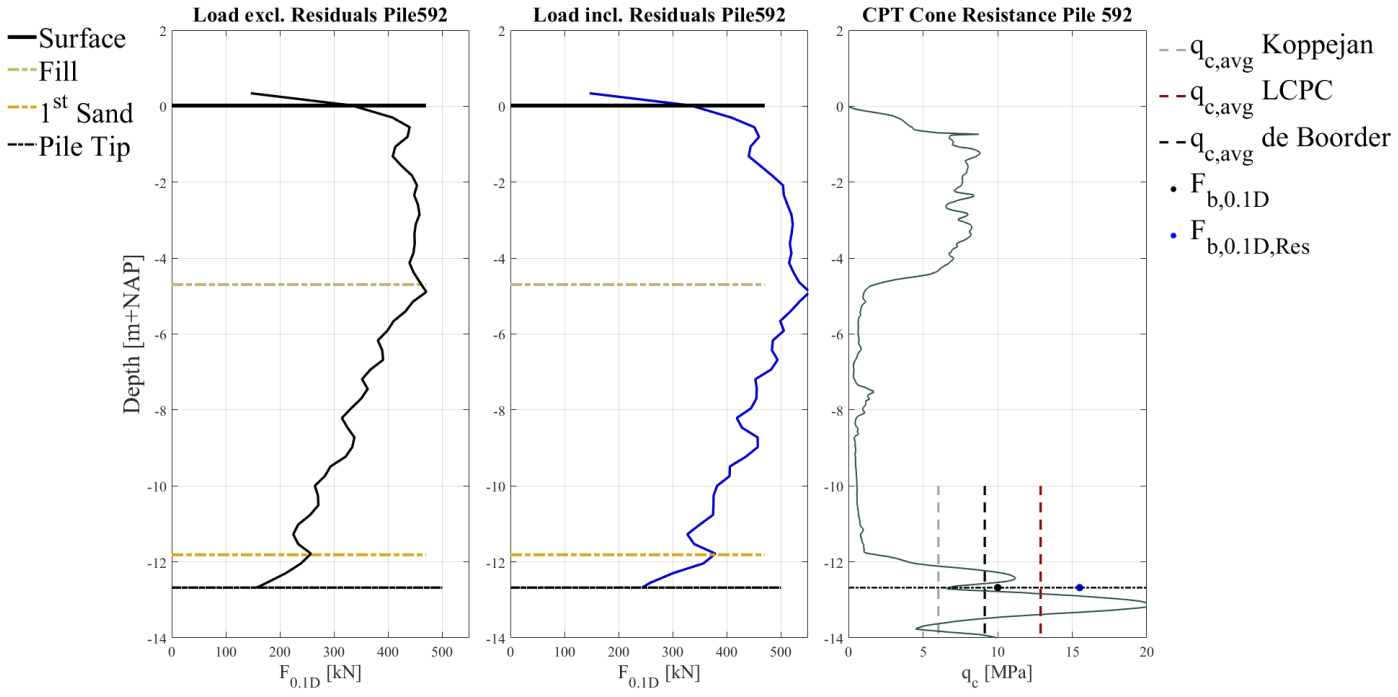

Figure C.38: α_p Pile 592

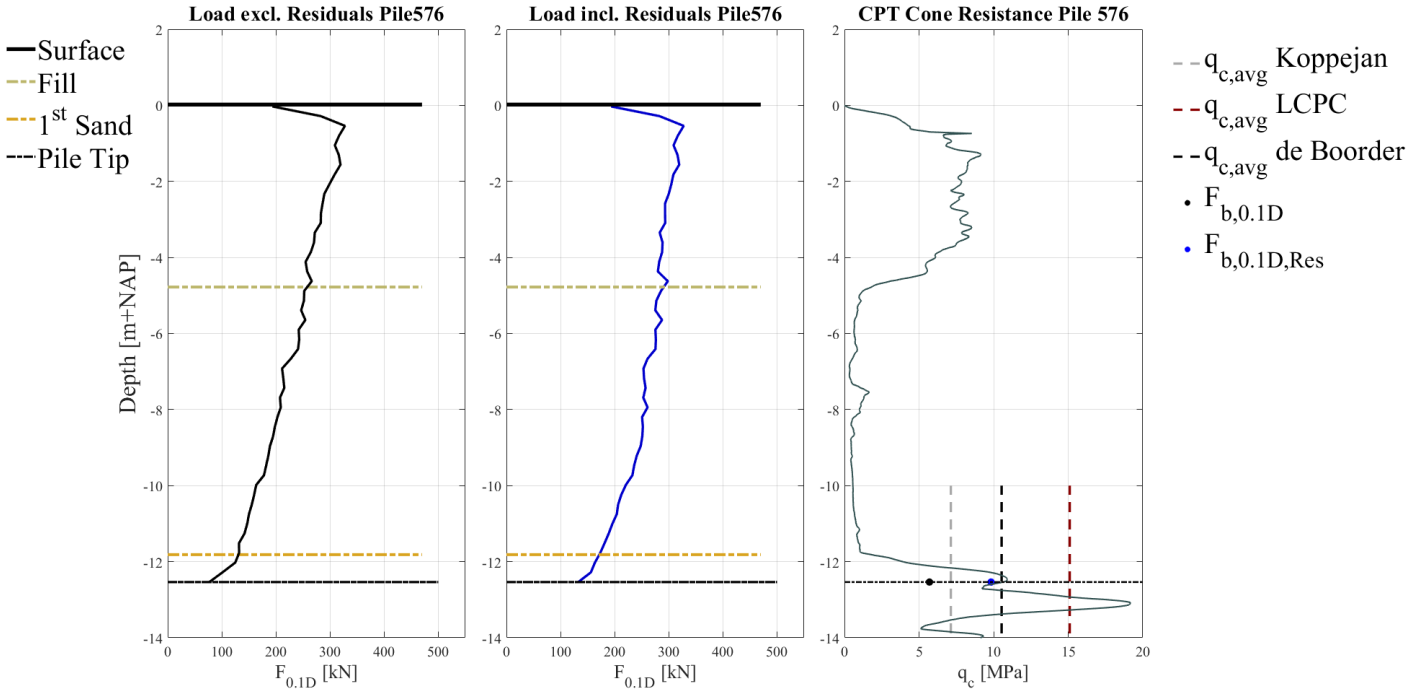

Figure C.39: α_p Pile 576

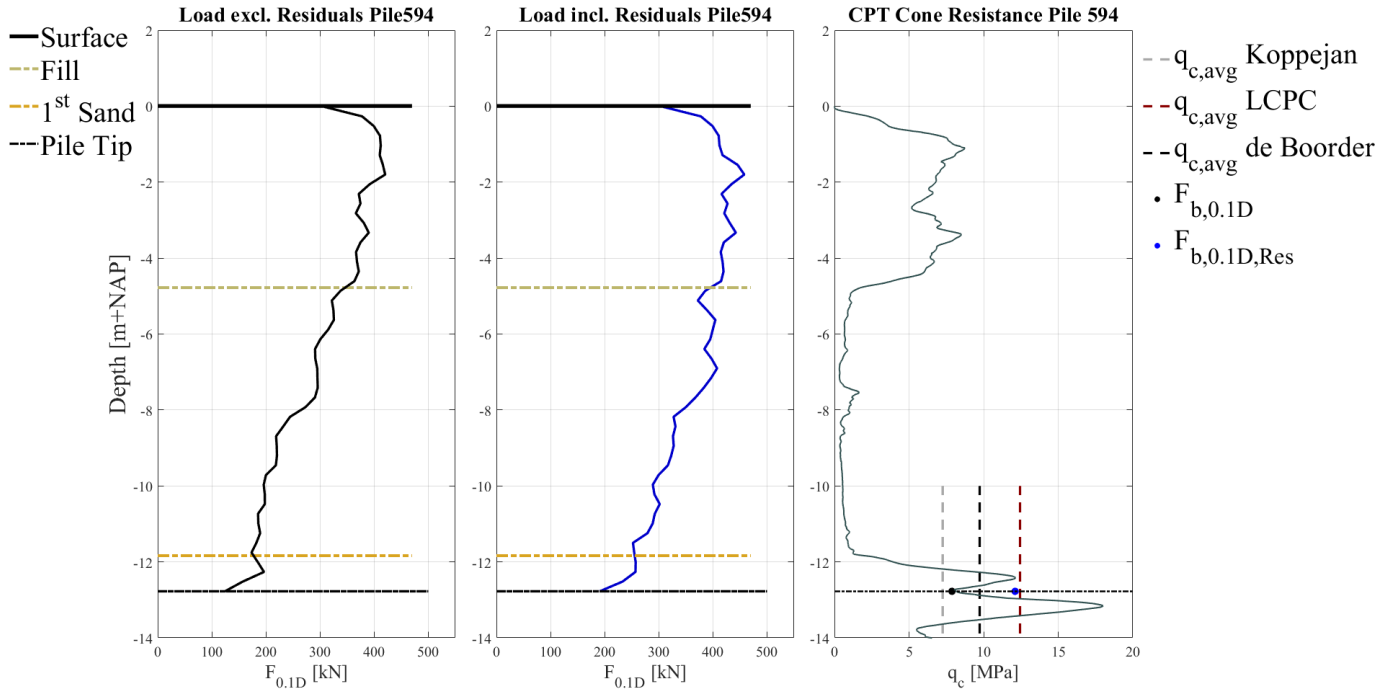

Figure C.40: α_p Pile 594

C.7.2 Alpha-s

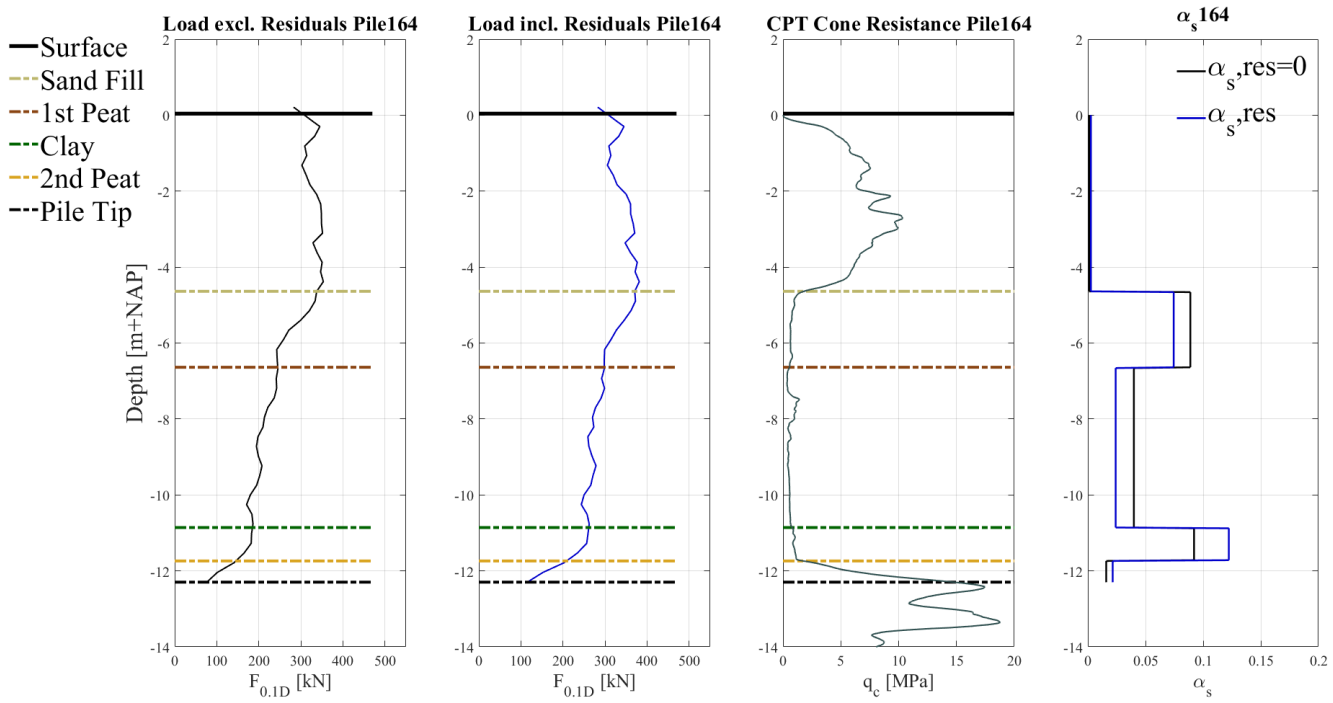

Figure C.41: α_s Pile 164

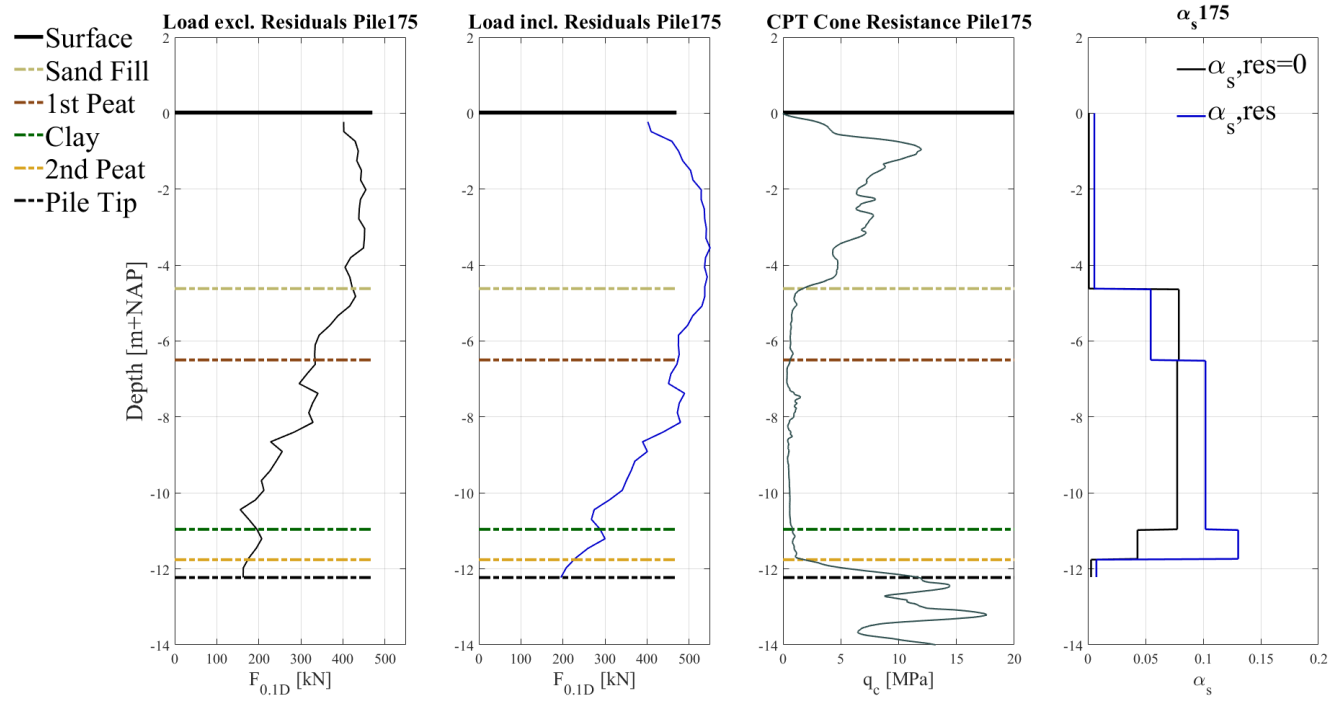

Figure C.42: α_s Pile 175

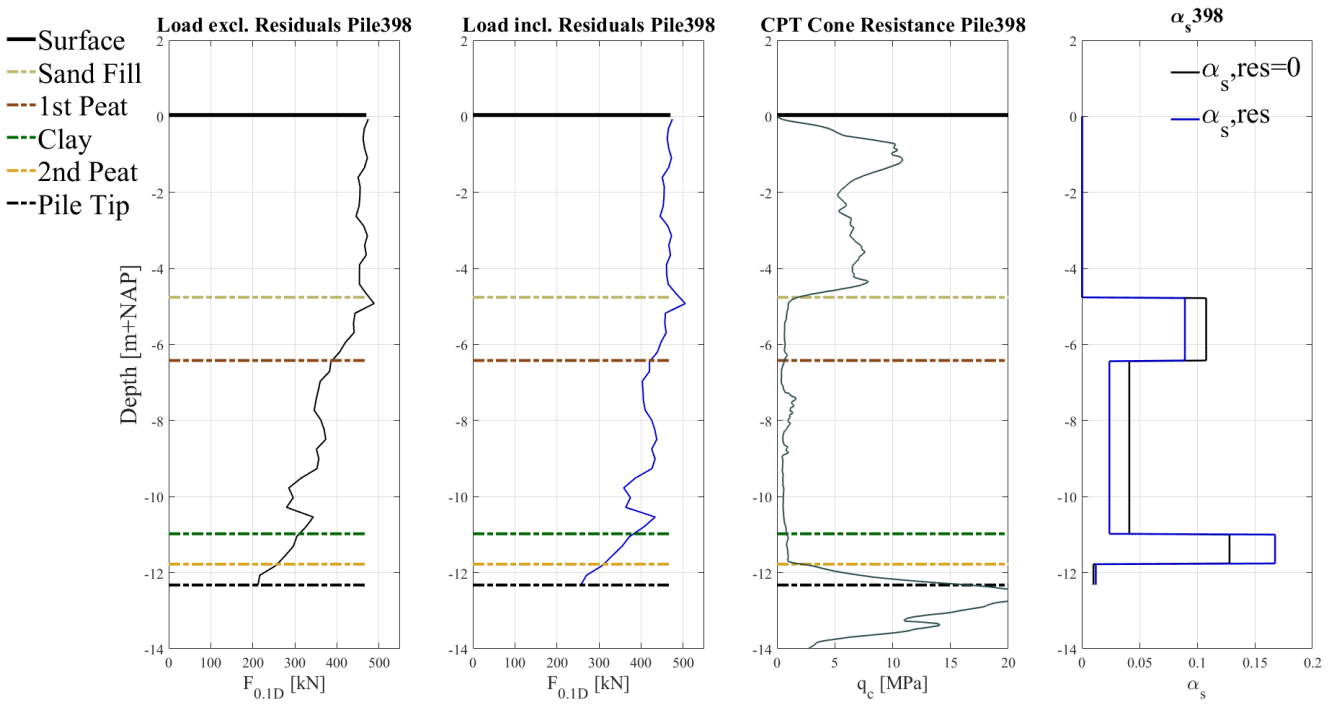

Figure C.43: α_s Pile 398

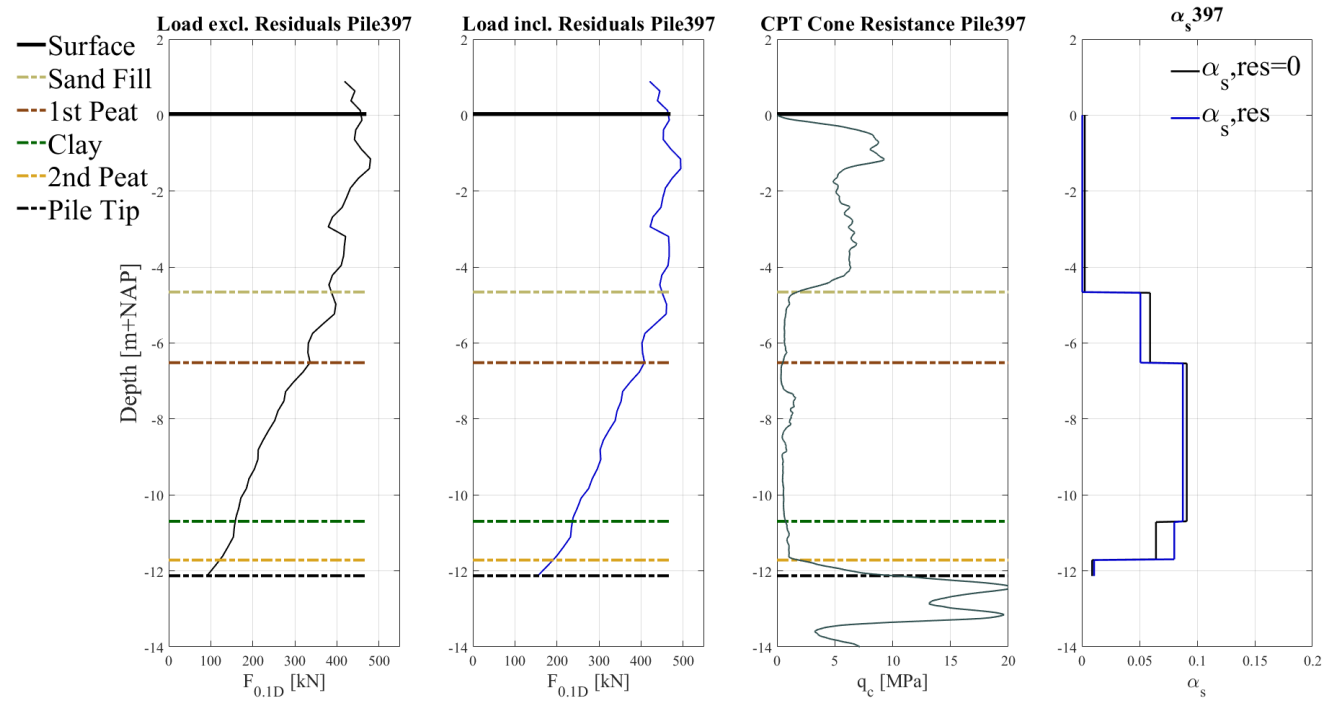

Figure C.44: α_s Pile 397

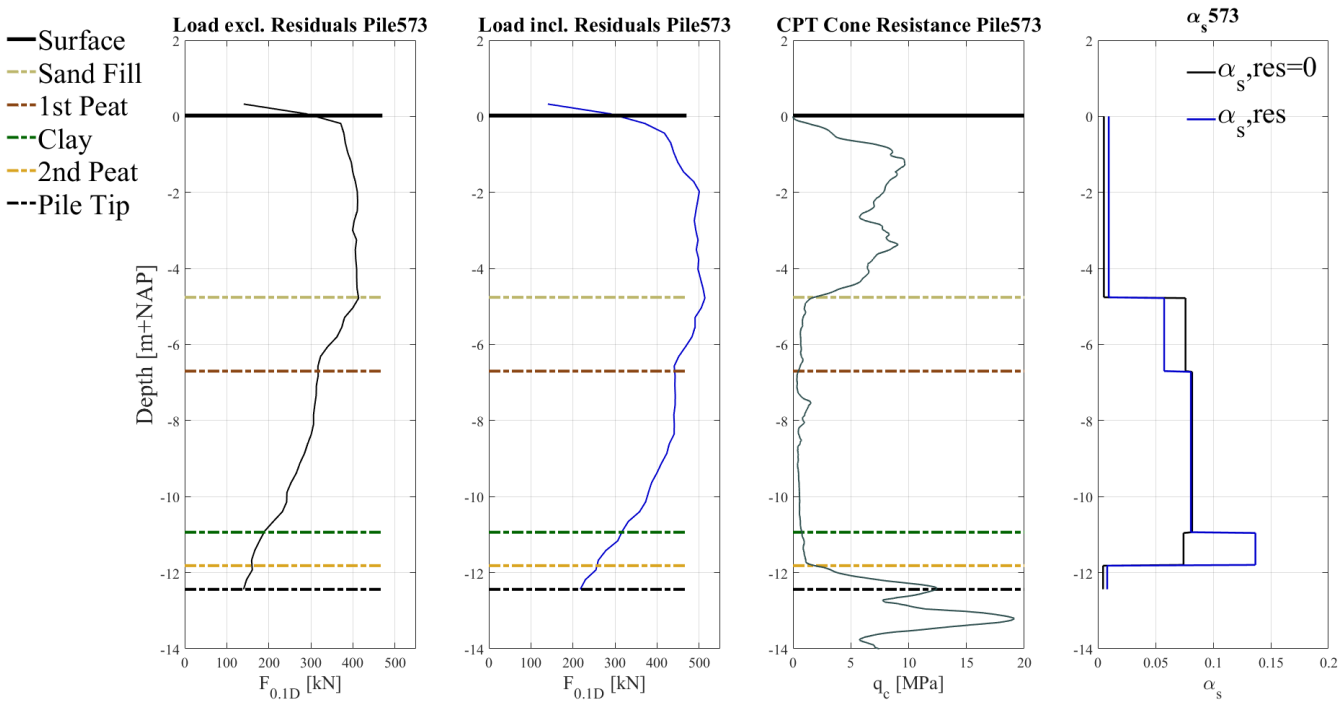

Figure C.45: α_s Pile 573

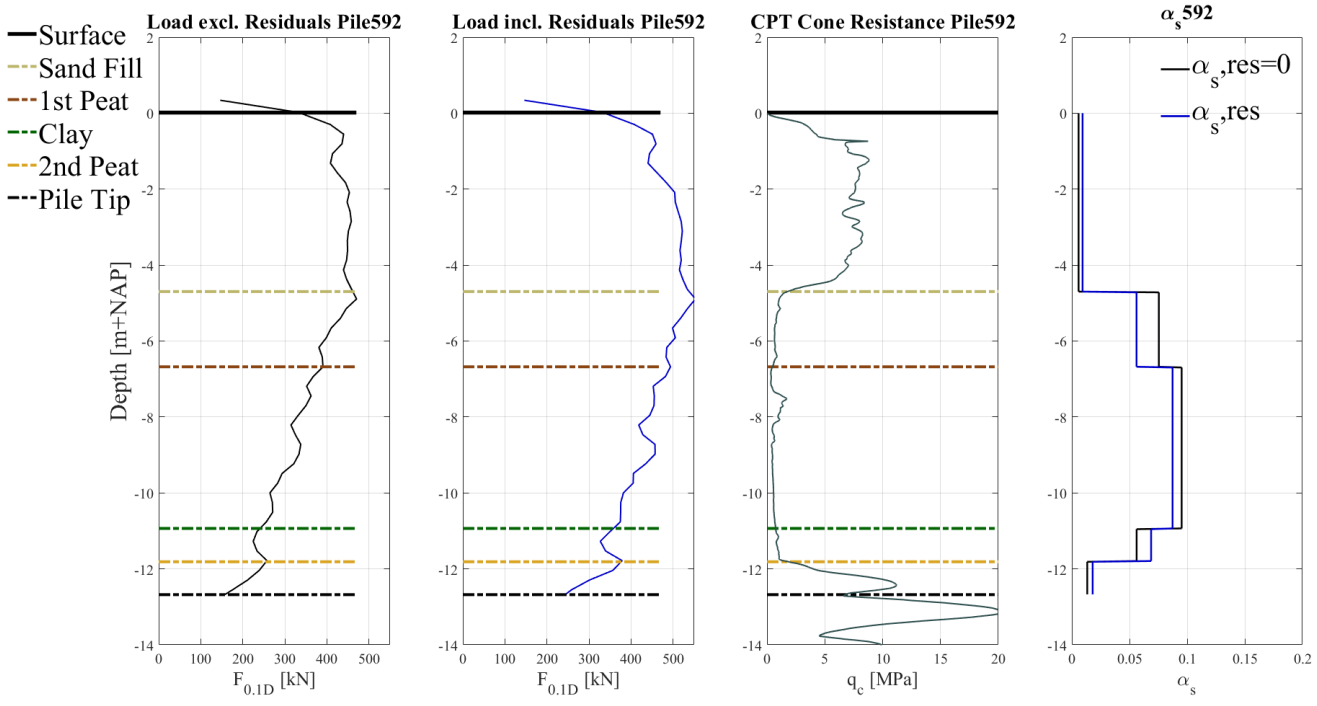

Figure C.46: α_s Pile 592

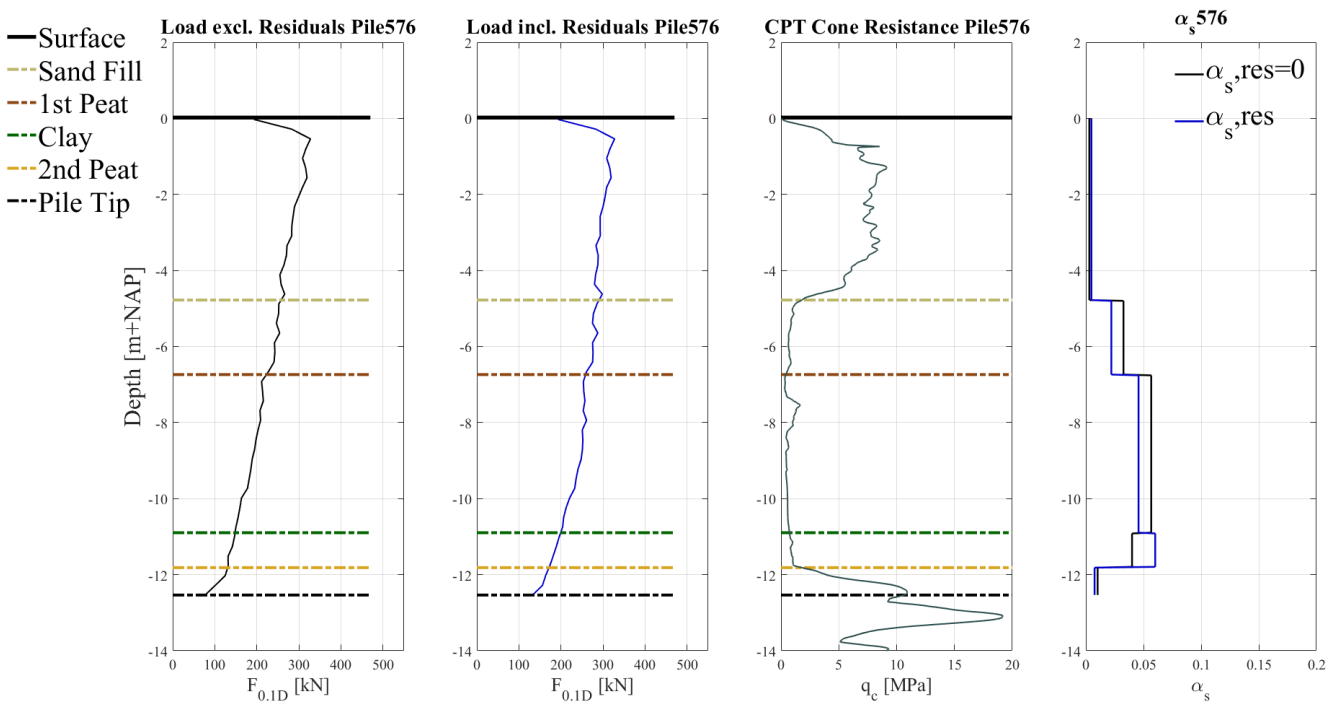

Figure C.47: α_s Pile 576

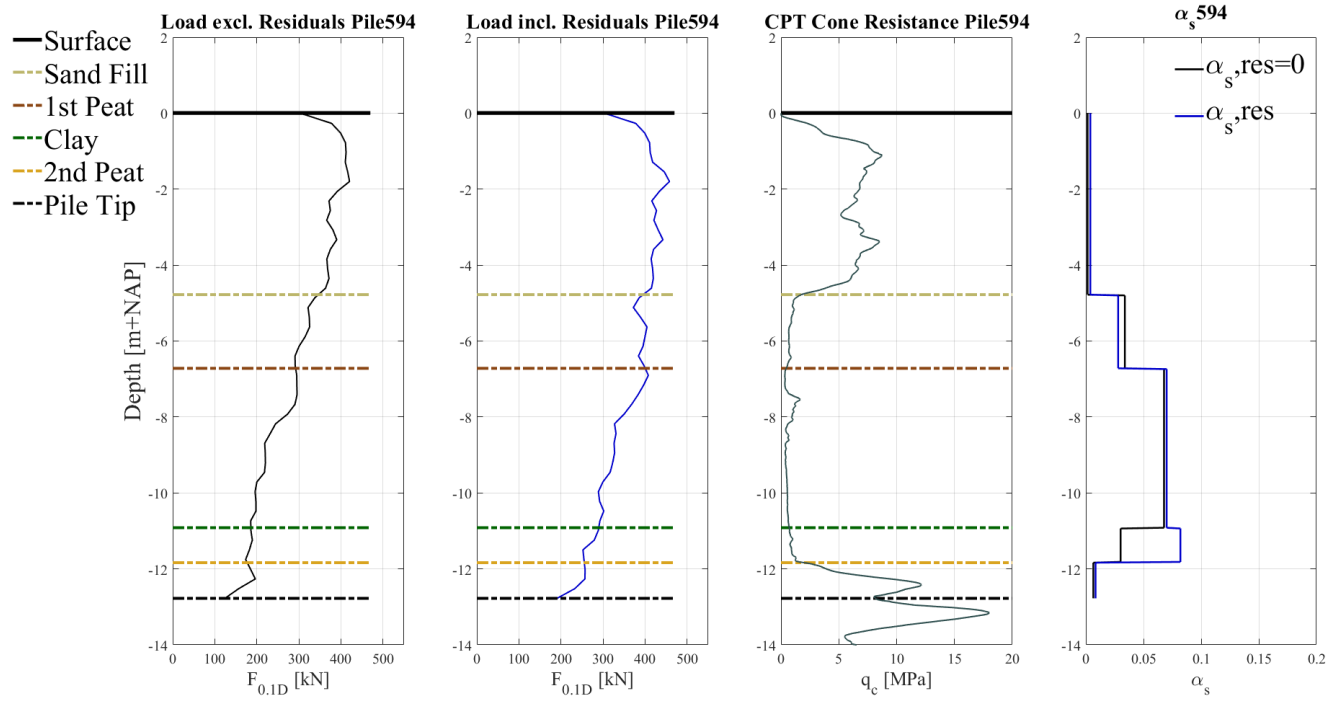

Figure C.48: α_s Pile 594

C.7.3 Relationship between Derived Factors and Pile Characteristics

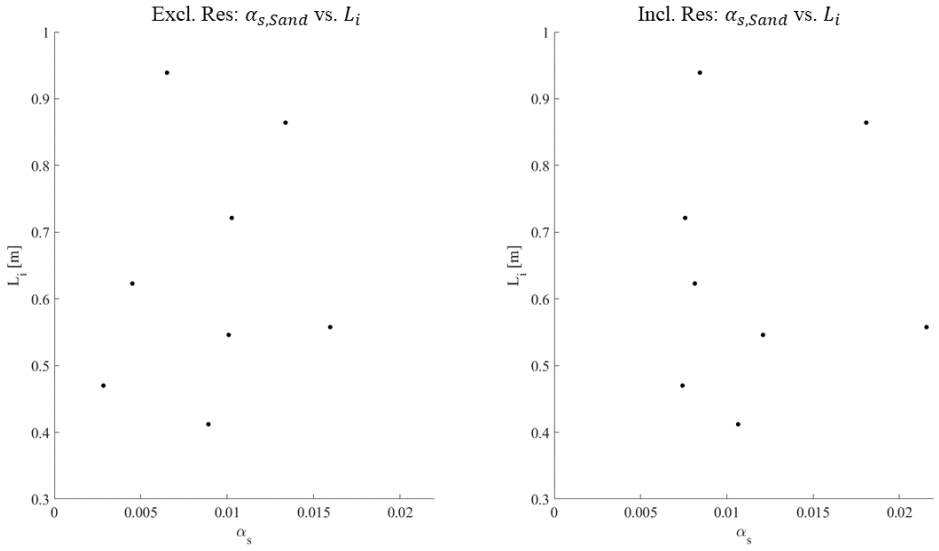

Figure C.49: α_s vs Insertion in Bearing Sand

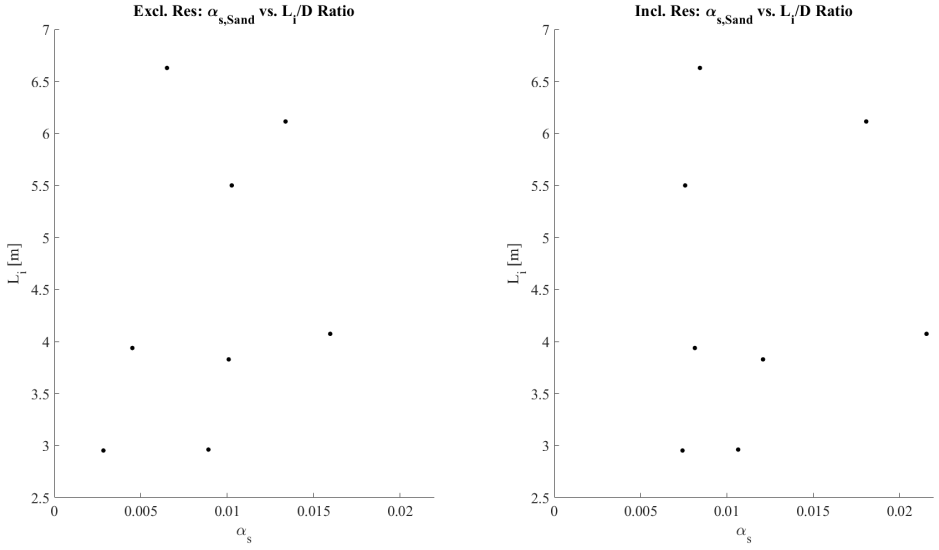

Figure C.50: α_s vs L_i/D

Appendix D

Complete Overview of Tested Piles

This page is intentionally left blank.

ID		DATA PRODUCTION SHEET												CATEGORY		
Pile ID	File ID	Wood Type	Debarking Method	E_lab (GPa)	Pile length after tip removal (m)	NAP Head (m)	NAP Tip (m)	Diameter Head (m)	Diameter Tip (m) After Cutting	Diameter Tip (m) Before Cutting	Tapering (mm/m)	NAP Sand Layer (m)	Insertion in Sand (m)	Tocht	A(1) Vuren 1 tocht	B(2) Vuren 2 tochten	C(3) Grenen 2 tochten
164	**P1**	V	M	15.4	14.3	2.004	-12.296	0.261	0.137	0.127	8.679	-11.96	0.6	1	A		
175	**P2**	V	H	17.0	13.91	1.683	-12.227	0.288	0.159	0.140	9.265	-11.86	0.5	1	A		
398	**P3**	V	H	12.1	13.82	1.496	-12.324	0.267	0.143	0.127	9.029	-11.76	0.6	2		B	
397	**P4**	V	H	16.6	14.41	2.283	-12.127	0.312	0.139	0.118	11.995	-11.64	0.4	2		B	
573	**P5**	G	M	14.0	14.3	1.861	-12.439	0.248	0.158	0.159	6.299	-11.96	0.6	2			C
592	**P6**	G	M	12.6	14.2	1.395	-12.805	0.227	0.141	0.140	6.032	-12.32	0.9	2			C
576	**P7**	G	M	14.5	14.12	1.584	-12.536	0.207	0.131	0.137	5.368	-11.93	0.7	2			C
594	**P10**	G	M	11.0	14.29	1.515	-12.775	0.227	0.142	0.124	5.976	-12.21	0.9	2			C
177	**ZP8**	V	H	14.0	14.25	2.055	-12.195	0.285	0.150	0.148	9.452	-11.83	0.365	1.46	A		
643	**P11**	G	M	12.1	14.45	2.052	-12.398	0.218	0.146	0.138	4.955	-11.8	0.598	2.39			C
177	**P3**	V	H	14.0	14.25	2.055	-12.195	0.285	0.150	0.148	9.452	-11.83	0.365	1.46	A		
183	**P12**	V	H	10.4	14.35	2.175	-12.175	0.283	0.155	0.143	8.899	-11.66	0.515	2.06		B	
179	**P13**	V	H	13.6	14.12	2.014	-12.106	0.267	0.156	0.135	7.882	-11.57	0.536	2.14		B	
195	**P14**	V	M	11.5	14.44	2.258	-12.182	0.241	0.132	0.124	7.562	-11.72	0.462	1.85		B	
564	**P15**	V	H	14.5	14.32	1.923	-12.397	0.273	0.142	0.130	9.148	-12.04	0.357	1.43	A		

Figure D.1: Data Production All Piles

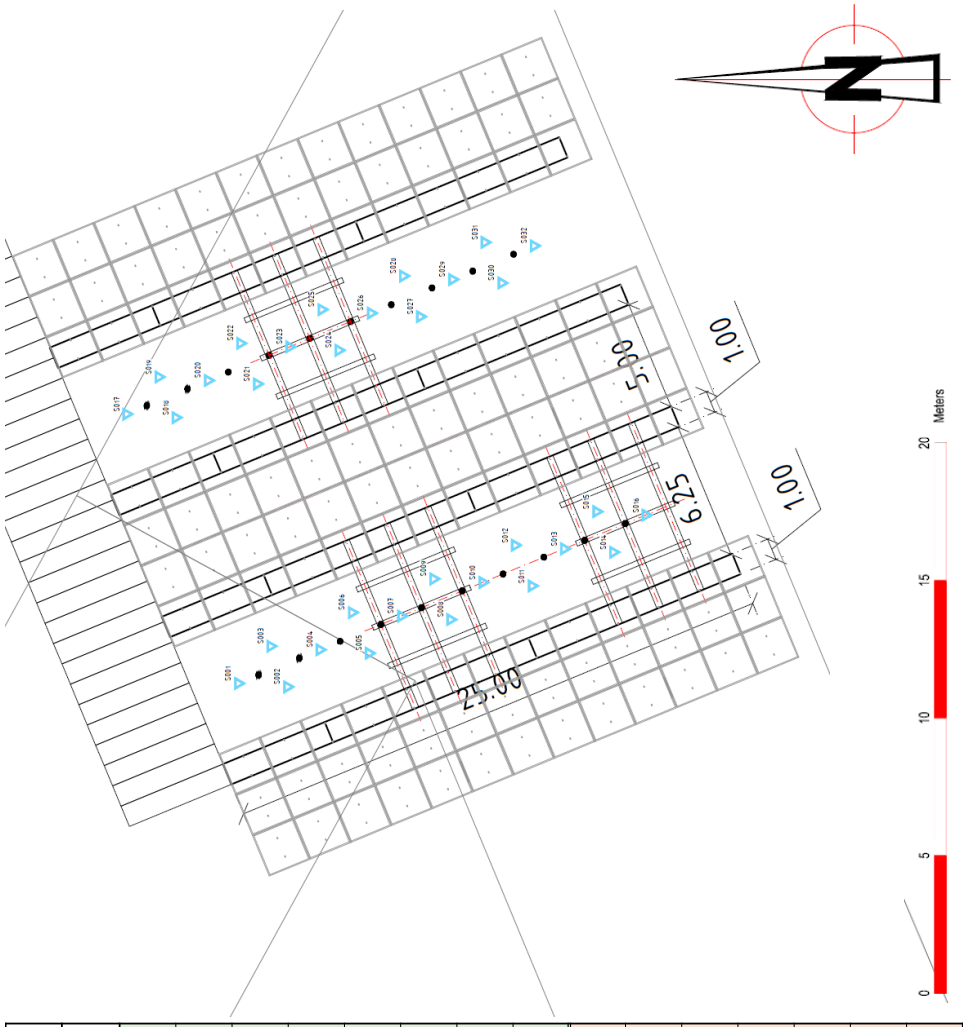

ID		CATEGORY			CPT's			
Pile ID	File ID	A(1) Vuren 1 tocht	B(2) Vuren 2 tochten	C(3) Grenen 2 tochten	CPTu	CPT		Maaiveld (m) NAP
164	**P1**	A			17	18	19	0.04
175	**P2**	A			23	24	25	0.015
398	**P3**		B		1	2	3	0.035
397	**P4**		B		7	6	5	0.03
573	**P5**			C	26	27	29	0.02
592	**P6**			C	29	30	31	0.015
576	**P7**			C	32	31	30	0.02
594	**P10**			C	29	28	27	0.005
177	**ZP8**	A			20	21	22	0.025
643	**P11**			C	26	25	24	0.015
177	**P3**	A			20	21	22	0.025
183	**P12**		B		10	9	8	0.04
179	**P13**		B		4	3	2	0.03
195	**P14**		B		7	8	9	0.035
564	**P15**	A			23	22	21	0.015

Figure D.2: Overview of piles and CPT's

ID		COMMENTS		
Pile ID	File ID	COMENTS ON LOAD CELL DATA	COMMENTS ON FIBER CHOICE	DATA STRUCTURE COMPLETE?
164	P1	CORRECT	AVG(NZ,OW)	YES
175	P2	CORRECT	AVG(NZ,OW)	YES
398	P3	CORRECT	only NZ since OW is broken at tip during loading	YES
397	P4	CORRECT	AVG(NZ,OW) For Hanging, Only OW is used due to irregularities in NZ during hang/stand	YES
573	P5	CORRECT	AVG(NZ,OW)	YES
592	P6	CORRECT	AVG(NZ,OW)	YES
576	P7	CORRECT	AVG(NZ,OW)	YES
594	P10	CORRECT	AVG(NZ,OW) For Reference Measure: Only OW	YES
177	ZP8	CORRECT	STRAINS DO NOT ALLIGN UPON REFERENCING TO INITIAL MEASUREMENT	YES
643	P11	MISSING DATA POINTS IN TIME	-	NO
177	P3	CORRECT	STRAINS DO NOT ALLIGN UPON REFERENCING TO INITIAL MEASUREMENT	YES
183	P12	MISMATCH BETWEEN TIME STAMPS OF LOADING/STRAINS	BOTDA HALF OF FIBER IS TOO NOISY	NO
179	P13	MISMATCH BETWEEN TIME STAMPS OF LOADING/STRAINS	half of each fiber is very noisy hence averaging doesn't make sense.	NO
195	P14	MISMATCH BETWEEN TIME STAMPS OF LOADING/STRAINS	Refrence measurements not available for both fibers -One side instrumented with BOTDA, the other BOTDR	NO
564	P15	CORRECT	BOTDA DOES NOT FIT WITHIN METHODLOGY OF DATA ANALYSIS	NO

Figure D.3: Data Assessment All Piles

ID		TEST INFO				FIBER NZ			FIBER OW		
Pile ID	File ID	Number of Load Steps	Highest Load Step (kN)	Lowest Load Step (kN)	Date of Test	Fiber length in use (m)	NAP start of fiber (m)	Ref./LT. Fiber NZ	Fiber length in use (m)	NAP start of fiber (m)	Ref./LT. Fiber OW
164	**P1**	6	375	75	14 October 2019	12.506	0.21	Ref:117.001 LT:117.256	13.018	0.722	Ref:118.277 LT:118.277
175	**P2**	10	475	75	30 September 2019	12.762	0.535	Ref:117.001 LT:116.746	11.996	-0.231	Ref:116.746 LT:116.746
398	**P3**	9	450	75	10 October 2019	12.762	0.438	Ref:117.001 LT:117.001	N/A	N/A	N/A
397	**P4**	9	425	50	25 September 2019	13.017	0.89	HANG:117.256 Ref:117.512 LT:117.767	13.017	0.89	HANG: 117.512 Ref:117.512 LT:117.767
573	**P5**	6	375	75	17 October 2019	12.762	0.323	Ref:117.001 LT:117.256	12.762	0.323	Ref:117.001 LT:117.256
592	**P6**	7	400	75	10 October 2019	13.272	0.467	Ref:117.256 LT:117.256	13.018	0.213	Ref:117.512 LT:117.512
576	**P7**	5	325	75	14 October 2019	12.507	-0.029	HANG=117.767 Ref:117.512 LT:117.767	12.507	-0.029	HANG=116.235 Ref:116.746 LT:117.001
594	**P10**	8	450	75	07 October 2019	12.762	-0.013	HANG=117.256 Ref:116.746 LT:117.001	13.018	0.243	HANG: =NZ Ref: =NZ LT:117.512

Figure D.4: Detailed Fiber Assessment of Analyzed Piles

Appendix E

Photographs of Test Conditions

Figure E.1: Location of Test Site Overamstel

Figure E.2: Test Site Overamstel

Figure E.3: Preparation: Sawing grooves for fiber installation

Figure E.4: Preparation: Drilling at tip for fiber loop

Figure E.5: Preparation: Soil Pre-drilling (left) and Pile Installation (right)

Figure E.6: Loading Frame

Figure E.7: Installed Piles with Load Cell and LVDT's

Appendix F

Data and Automatization

As part of this thesis, an automated script was developed in MATLAB alongside a user manual. For information on this code or the used data feel free to contact the author or the involved supervisors. The corresponding contact details are as below;

Siavash Honardar
E: siavashhonardar@gmail.com

Dirk de Lange
E: Dirk.deLange@deltares.nl

Mandy Korff
E: M.Korff@tudelft.nl

Siavash Honardar

Delft University of Technology
Faculty of Civil Engineering and Geosciences
Master Program Geotechnical Engineering
November 2020

Cover images: Taken by Rodriaan Spruit, Amsterdam 2019.

TU Delft